Fatigue in Mechanically Fastened Composite and Metallic Joints

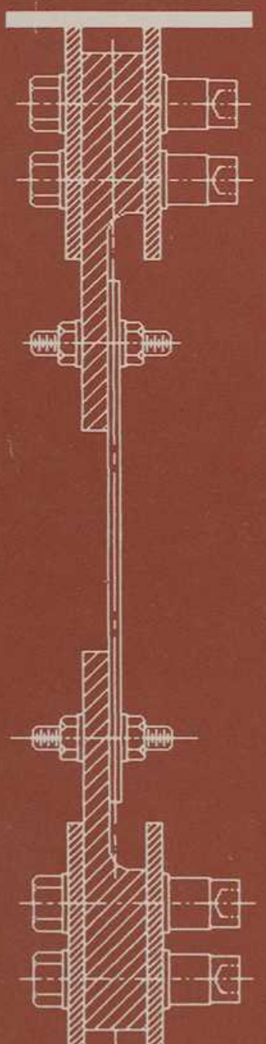

John M. Potter *editor*

ASTM STP 927

FATIGUE IN MECHANICALLY FASTENED COMPOSITE AND METALLIC JOINTS

A symposium
sponsored by ASTM
Committee E-9 on Fatigue
Charleston, SC, 18–19 March 1985

ASTM SPECIAL TECHNICAL PUBLICATION 927
John M. Potter, Air Force Wright Aeronautical
Laboratories, editor

ASTM Publication Code Number (PCN)
04-927000-30

1916 Race Street, Philadelphia, PA 19103

Library of Congress Cataloging-in-Publication Data

Fatigue in mechanically fastened composite and metallic joints.

(ASTM special technical publication; 927)
"ASTM publication code number (PCN) 04-927000-30."
Includes bibliographies and indexes.
1. Joints (Engineering)—Fatigue—Congresses. 2. Composite materials—Fatigue—Congresses. 3. Metals—Fatigue—Congresses. I. Potter, John M., 1943- . II. American Society for Testing and Materials. Committee E-9 on Fatigue. III. Series.
TA660.J64F38 1986 621.8′8 86-22288
ISBN 0-8031-0927-X

Library of Congress Catalog Card Number: 86-22288

NOTE

The Society is not responsible, as a body,
for the statements and opinions
advanced in this publication.

Printed in Ann Arbor, MI
November 1986

Foreword

The symposium on Fatigue in Mechanically Fastened Composite and Metallic Joints was held on 18–19 March 1985 in Charleston, South Carolina. The event was sponsored by ASTM Committee E-9 on Fatigue. John M. Potter, of the Air Force Wright Aeronautical Laboratories, presided as chairman of the symposium and also served as editor of this publication.

Related ASTM Publications

Automated Test Methods for Fracture and Fatigue Crack Growth, STP 877 (1985), 04-877000-30

Recent Advances in Composites in the United States and Japan, STP 864 (1985), 04-864000-33

Probabilistic Fracture Mechanics and Fatigue Methods: Applications for Structural Design and Maintenance, STP 798 (1983), 04-798000-30

A Note of Appreciation to Reviewers

The quality of the papers that appear in this publication reflects not only the obvious efforts of the authors but also the unheralded, though essential, work of the reviewers. On behalf of ASTM we acknowledge with appreciation their dedication to high professional standards and their sacrifice of time and effort.

ASTM Committee on Publications

ASTM Editorial Staff

Helen P. Mahy
Janet R. Schroeder
Kathleen A. Greene
William T. Benzing

Contents

Overview

The symposium on Fatigue in Mechanically Fastened Composite and Metallic Joints was organized to define the state of the art in durability of mechanically jointed structures.

Mechanically fastened joints are used in many critical engineering structures, including buildings, machinery, power plants, automobiles, and airframes. The joint is the magic part that turns a series of material forms into a structure. The joint between one piece of material and another is often blamed for causing the design to be heavier than desired or for being the point at which fatigue or fracture problems initiate. The study of stress, fatigue, and fracture at joints, then, is of significant interest for the structural designer, as well as those interested in the durability and damage tolerance of the resultant structure.

This volume will serve as a state of the art of joint fatigue. Its usefulness is enhanced by the range of the papers herein, since they run the gamut from basic research to the very applied, from bridge structures to airframes, from adhesive bonding to welding, and from metallic to composite materials. The broad range of the topics covered in this Special Technical Publication makes it an excellent resource for designers, analysts, students, and users of mechanically fastened structures.

The initial paper, by *Speakman*, covers the development of high-performance fasteners in airframe applications. He provides an excellent review of the development of new fasteners and other joining methods for reducing weight and improving fatigue life. The paper is filled with practicality in its approach to improved mechanical fastening systems through methods and fasteners that are "forgiving to the hole." To this author, "forgiving to the hole" means that the fastener system is a practical one in which the hole manufacturing tolerances and the joint materials are taken into account, which results in a mechanical joint that has a large degree of compatibility and, therefore, good fatigue performance. In this wide-ranging paper, Speakman covers fasteners, corrosion, fatigue, fretting, tapered fasteners, sleeved rivets, solid rivets, special nuts, and high-performance bushings and bearings.

The paper by *Champoux and Landy* covers the experimental evidence for structural bushed hole fatigue improvement by using a hole expansion method that includes the simultaneous installation of an interference-fitted bushing. This new bushed hole expansion method is shown to provide a threefold increase in bushed joint fatigue performance while decreasing installation costs, in comparison with the cryogenic shrink-fit installation methods commonly used.

The paper by *Ozelton and Coyle* covers the fatigue improvement of aluminum airframe structures through the use of cold hole expansion by the split-sleeve technique prior to fastener installation. The process of cold hole expansion is being utilized in many applications to improve the fatigue performance of joints. This paper not only covers the fatigue performance of properly cold-expanded fastened joints but also looks into the fatigue improvement of holes with preexisting cracks and also improper reaming during manufacture. The Ozelton and Coyle paper provides excellent evidence of fatigue performance improvements that can be realized.

The paper by *Albrecht and Sahli* covers the fatigue performance of adhesively bonded and bolted highway bridge joints. The paper covers bolted joints, bonded joints, and bolted and adhesively bonded joints in many configurations. These joints are shown to provide increased fatigue performance in typical highway bridge beam splices when compared with conventional joints.

The paper by *Lee* covers the study of load transfer and its effect on fatigue performance in aluminum joints. The Lee paper uses no-load, low-, medium-, and high-load transfer joint specimens to define experimentally the crack initiation and propagation behavior. The results provide an experimental basis for methodology for service life prediction of joints.

The paper by *Yang, Manning, and Rudd* reports on a study of crack growth at fastener holes. The authors have developed statistical evaluations from a very large data base of crack growth at fastened joints for cracks of an extremely small size [less than 2.54 mm (0.10 in.)]. This analytical approach allows excellent predictions of the safety and durability of complex mechanically fastened joints.

The paper by *Nicoletto* covers the application of frozen-stress photoelastic techniques in the stress intensity determination of cracks in open holes and pin-loaded lugs. Pin-loaded lugs are an important branch of mechanically fastened joints, for which the stress distribution is not well characterized. The techniques and measurements presented by Prof. Nicoletto provide considerable insight into stress effects on these joints.

The paper by *Ekvall* covers the fatigue performance of lap joint and butt joint specimens made from recently developed aluminum alloy materials. These fatigue performance results were compared with those of conventional aluminum alloy product forms to assist in the process of defining improvement for the new materials.

Landy, Armen, and Eidinoff address the cold hole expansion repair of cracked fastener holes in structural joints. In this study, residual stress distributions from the cold hole expansion process were analytically developed. The resultant residual stress distributions were then superimposed with applied-load stress intensity factors to give a prediction of crack growth during fatigue exposure following the stop-drill hole repair process. Experimental evidence from mechanically fastened joints supports the prediction of an improvement in fatigue performance. The data indicate that the fatigue life following the cold expansion repair process of cracked joints can exceed the basic as-manufactured fatigue performance.

The paper by *Huth* covers the effect of the fastener in the stress redistribution of a fastened multiple-row joint. Dr. Huth provides compelling experimental evidence of the effect of many primary joint and fastener parameters, including fastener rotation and flexibility, on the predicted load transfer and resultant fatigue performance in the joint and subsequent structure. In this paper, Huth has developed a formula for load transfer within multiple-row joints which includes fastener flexibility. The formula can be used with a variety of fastener systems and joint materials to improve the general predictability of stress and fatigue performance in mechanically fastened joints.

The paper by *Ramkumar and Tossavainen* covers the fatigue performance of composite-to-metal fastened joints. Joint parameters such as the fastener type, stacking sequences and thickness, fastener head type, and joint configuration were investigated to define their effects on fatigue performance. Also studied were the effects of moisture conditioning and load spectrum type.

The paper by *Mallick, Little, and Dunham* describes the fatigue performance of fastened joints where the joint was made from a composite material used in the automotive industry. The composite [continuous fiber sheet molding compound (CFSMC)] joints were prepared with conventional fasteners and subjected to fatigue loading. The authors were able to define several failure modes in the CFSMC fastened joints, including bearing and fretting failures. The variables covered include the bolt clamping pressure, fastener pattern, and specimen width in comparison with the fastener head size.

Mechanically fastened joints have been with us since the first use of assemblies. People have used dowels, rods, screws, pins, keys, glue, bolts, and rivets as mechanical means of fastening. These mechanical fastening methods will be with us for the foreseeable future wherever efficient and inexpensive methods of fastening are required to ensure that a structure will serve the purpose for which it was manufactured.

John M. Potter

Air Force Wright Aeronautical Laboratories, Wright-Patterson Air Force Base, OH 45433; symposium chariman and editor.

Eugene R. Speakman[1]

Advanced Fastener Technology for Composite and Metallic Joints

REFERENCE: Speakman, E. R., "**Advanced Fastener Technology for Composite and Metallic Joints,**" *Fatigue in Mechanically Fastened Composite and Metallic Joints, ASTM STP 927*, John M. Potter, Ed., American Society for Testing and Materials, Philadelphia, 1986, pp. 5–38.

ABSTRACT: The investigations described in this paper were conducted to develop new fasteners and joining methods to reduce the weight and improve the fatigue life of aircraft structures. Three major modes of structural failure—fatigue, fretting, and stress corrosion—are discussed along with recommendations for improvement. Stress-coining was developed to cold-work aircraft structures for fatigue improvement. Fretting fatigue failures have been reduced by using Teflon coatings on fasteners and in faying surfaces of splice joints. Standard stress corrosion test blocks have been designed for evaluation of this failure mode. A crown flush rivet configuration has been developed that does not require head shaving after installation. Qualification tests were performed in compliance with MIL-STD-1312 to obtain Federal Aviation Administration and military approval.

Various new fasteners have been developed for aluminum, carbon-fiber composite, and titanium structures. These fasteners were designed to be "forgiving to the hole" in that they fill and prestress the hole uniformly without being extremely sensitive to hole-preparation tolerances. New low-cost specimens have been designed to provide a basis for screening and comparing fastener tests conducted by fastener manufacturers and aircraft companies. These programs are directed toward creating technology for achieving a more balanced fatigue-resistant aircraft structure.

KEY WORDS: fatigue life, fretting, stress corrosion, fasteners, joining methods, stress-coining, weight reduction

The state of practice in fastener installation has changed from clearance-fit to interference-fit holes to improve structural fatigue performance (Fig. 1). Hole preparation for interference-fit fastener systems is more costly. Experience has shown that inadequately prepared holes, exceeding design tolerances, reduce service life. Therefore, in order to reduce installation costs without degrading fatigue life, fastener installation methods that are "forgiving to the hole" must be developed. The large number of joints and splices in aircraft structures contribute to increased cost not only of newly produced aircraft but also of reworking of in-service aircraft. The design

[1] Senior structural design engineer, Douglas Aircraft Co., Long Beach, CA 90846.

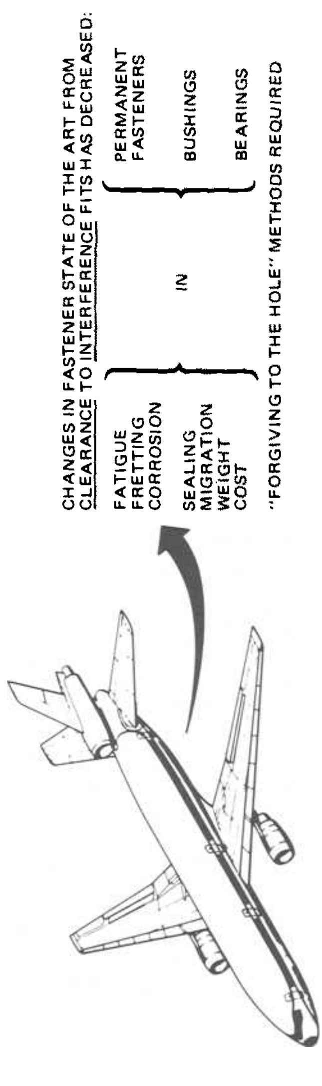

FIG. 1—*Advanced fastener technology.*

trend to higher stress levels and longer service lives also increases the need for high-performance and dependable fastening systems.

Fatigue Test Specimen Configurations

Fatigue specimens of various shapes and sizes are used throughout the industry to test new materials and attachments for new designs and rework of existing aircraft structures in the field. These specimens vary significantly and are usually tailored to determine the effect of a certain type of fastener on a specific structural design. These specimens are often more difficult to design and test than the full-scale structures they represent. It is practically impossible to simulate full-scale aircraft structure loading conditions with small test specimens (Fig. 2).

Specimen and end-grip premature failure due either to poor design or to sophisticated design techniques used in producing the test specimen is a costly and time-consuming hindrance to obtaining reliable test data. Coining and long-life-fatigue fasteners increase the cycle life of the specimen to a point at which fretting damage could initiate a premature failure. For these reasons, the present operating procedures used by fastener and airframe manufacturers to evaluate new fastener products are somewhat awkward and inefficient. Standard fatigue specimens (Fig. 3) have been designed to define a screening test and specimens that include the following criteria:

(*a*) specimen fabrication techniques to minimize manufacturing influence on the fatigue results,

(*b*) fastener installation using representative production equipment to

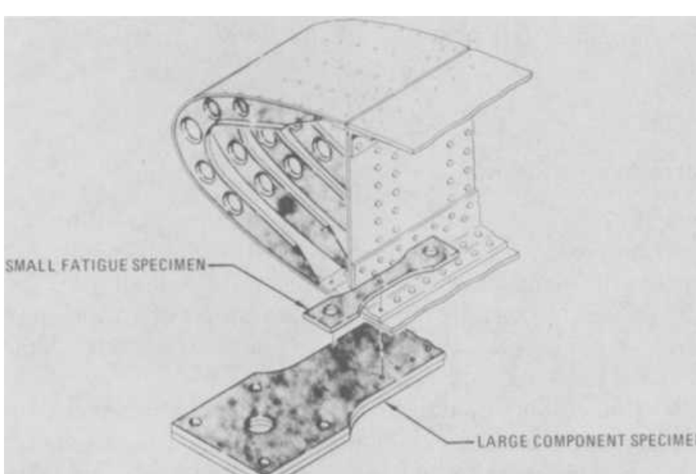

FIG. 2—*Application of test specimens to a full-scale aircraft structure.*

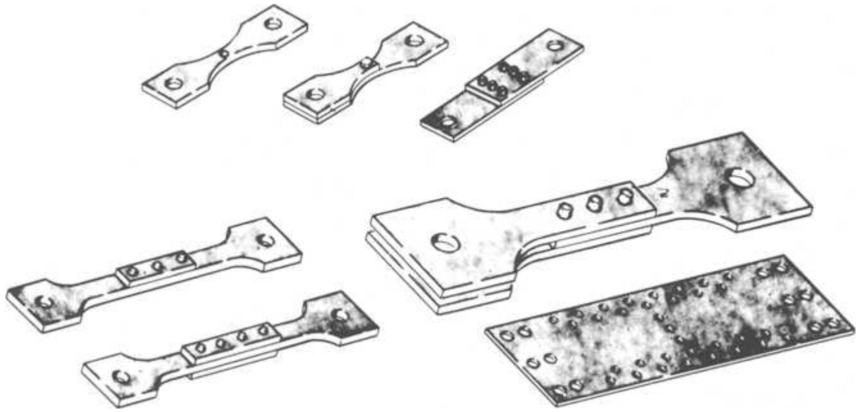

FIG. 3—*Various types of small, inexpensive fatigue specimens.*

obtain more accurate test data for the aircraft the specimens represent, and (*c*) definition of the test criteria, load spectrum, and data recording.

All major airframe manufacturers have their own fatigue specimens that they use to certify fastening methods for new designs and rework. Adoption of standard fatigue specimen designs would make it possible for fastener and aircraft companies to prepare and test specimens for direct comparison. The savings in time and money produced by such a proper approach would more than justify this program.

The small, standard fatigue specimen designs shown in Fig. 3 would also be the first step toward establishing the performance characteristics of the various types of fasteners and hole-preparation methods for possible inclusion in a design handbook such as MIL-HDBK-5. Fatigue data developed using these specimen designs would greatly aid designers in the aerospace industry.

Stress-Corrosion Test Blocks

A new test block configuration, designed to provide all three grain directions in one piece for comparative tests, is shown in Fig. 4. Fasteners are installed with identical interference fits, two-diameter edge distance, and four-diameter fastener spacing. Standardization of various test block configurations would provide industry with a practical method for comparing stress-corrosion test data.

Prestress from coining or interference fasteners, combined with a corrosive atmosphere, can cause a crack to originate in the hole and propagate in a direction parallel to the grain and loading directions of the part in the aircraft. This phenomenon, which causes the cracks to travel in 90-deg-

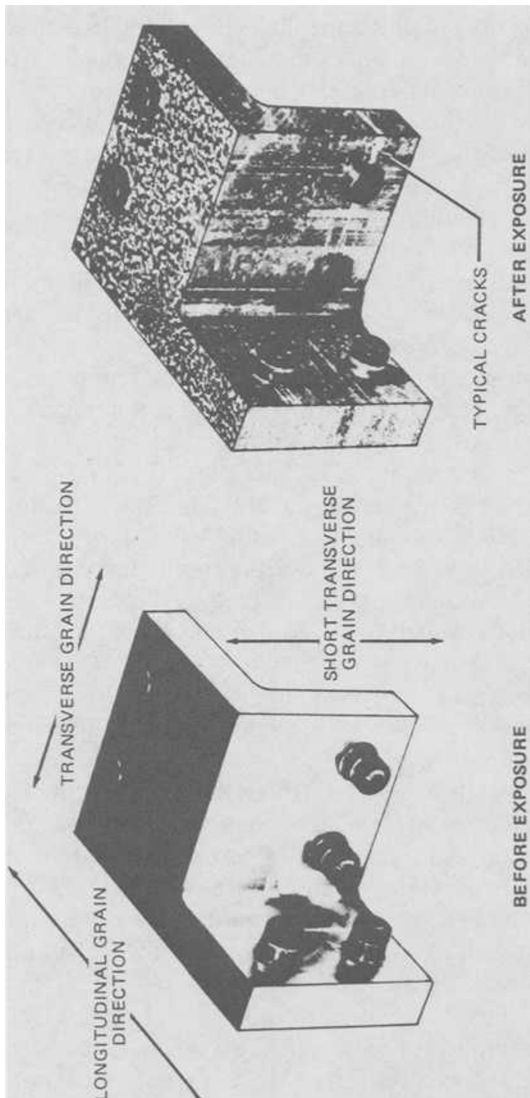

FIG. 4—Test blocks showing stress corrosion.

different directions, may be used to determine if the crack was caused by fatigue or stress corrosion.

Fretting Retardation in Aircraft Joints

Whenever surfaces of structural members are placed in contact with each other and subjected to small relative movements, a special form of corrosion is possible. This corrosion makes itself evident by the appearance of irregular patches of black oxide that will start under very low clamp-up pressures between the members and within the first few cycles of movement. This process is known as fretting corrosion and, if permitted to continue, usually results in a premature fatigue failure of the structural members. Observations of many fatigue test specimens indicate that fretting and stress corrosion account for at least 30% of the crack-induced failures reported on aircraft in service. The failures often occur before 50% of the design fatigue life of the aircraft has been expended.

In aircraft structures, fretting fatigue has initiated an increased number of crack failures, superseding stress corrosion and metal fatigue due to stress concentrations. There are two reasons for this change: interference fasteners and stress-coining, as shown in U.S. Patent No. 3,434,327, have reduced fatigue cracks in holes in structural elements; and the use of overage heat treatment of 7075 T6 to T73 aluminum alloy has reduced stress-corrosion cracks in the short-transverse grain direction in aluminum. Many types of coatings, tapes, and rub strips have been used to reduce fretting in aircraft structures. They have resulted in added cost and weight, however, and are unsatisfactory because they extrude out of a splice joint and reduce the clamp-up of the fastener. Figure 5, which shows three different crack failure modes and their different locations, might be useful in determining the cause of crack initiation.

The addition of material to reduce the stress level in fastener holes is a state-of-the-art design feature for large commercial aircraft today. As the service life of these aircraft grows, it is becoming apparent that fretting inside fastener holes and at the faying surfaces of splice joints is becoming a dominant factor in fatigue failures. Therefore, this failure mode must be prevented or greatly reduced so that the expected lifetime of aircraft structures can be substantially extended.

At Douglas, fatigue test specimens have been fabricated with the faying surface protected from fretting by applying a 0.0508-mm-thick (0.002-in.) film of tetrafluoroethylene (Teflon) on them. (When this is not convenient for rework of assembled aircraft, Teflon-coated shim stock may be inserted between the faying surfaces.) If the part is 7075 aluminum alloy, the Teflon compound is chosen to have a cure time and temperature to match the overage cycle heat treatment to T73; therefore, the cure and heat treatment can be accomplished at the same time. Fastener shanks and flush-headed

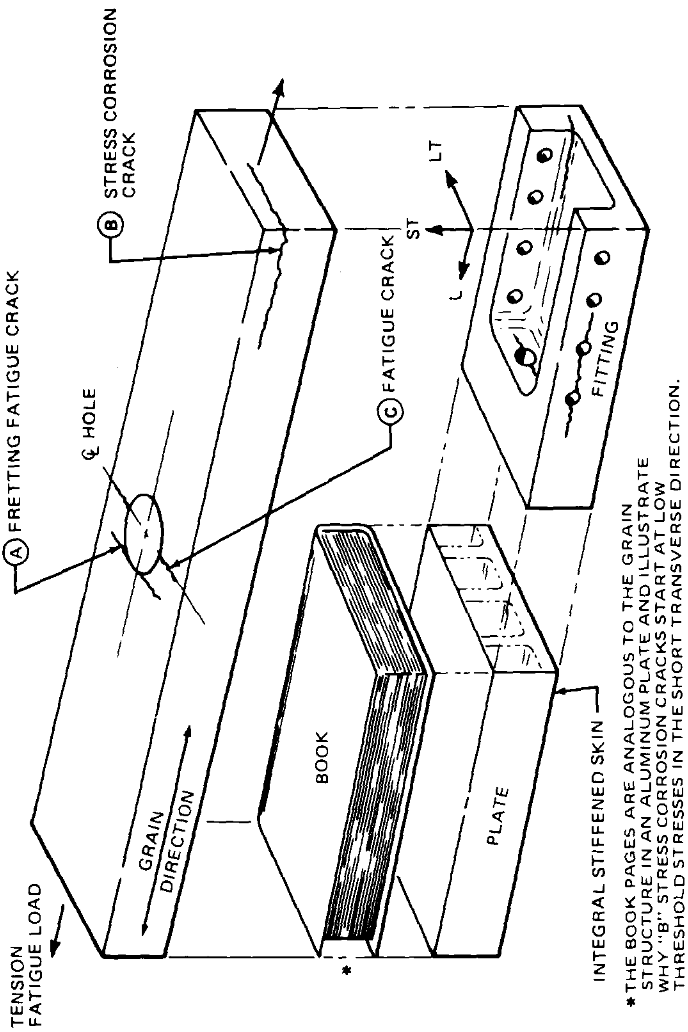

FIG. 5—*Three major crack types in aircraft structures.*

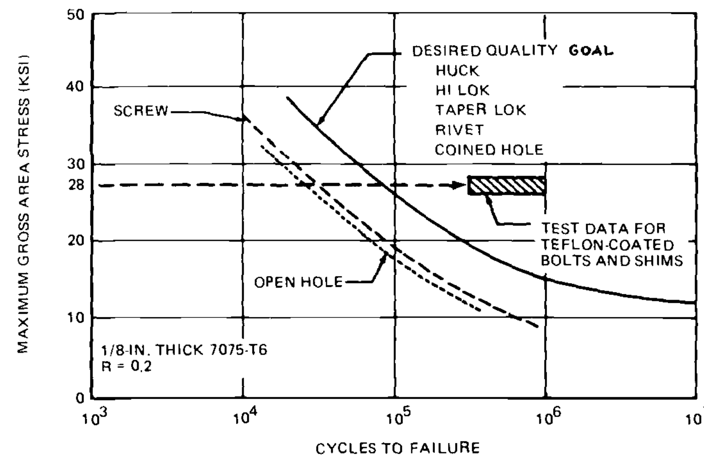

FIG. 6—*Basic structure fatigue improvement.*

fasteners also have been Teflon-coated to ease interference installation and retard fretting inside the hole.

Preliminary test data, shown in Fig. 6, indicate improved fatigue life for specimens with Teflon-coated fasteners and shims. The results for the splice joint specimen shown in Fig. 7 compare the fatigue life of Class A clearance-fit holes with that for both interference-fit holes and the addition of Teflon coating.

Fastener Weight Reduction

Modification of the threaded end of shear-loaded fasteners could reduce the installed weight 25% and balance the tensile strength of the shear bolt head with the reduced thread diameter. Figure 8 shows how this modification would be accomplished. The dashed-line portion of the tension-type bolt head was first removed more than 30 years ago to save weight; the reduced head height is referred to today as the shear head. Now it is pro-

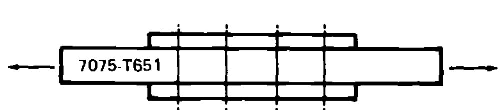

	25 KSI R = 0.2 FAILURE CYCLES
• STEEL BOLTS-CLASS "A" HOLES ANODIZED AND PRIMED PARTS	60,000
• LOCKBOLTS-INTERFERENCE HOLES ANODIZED AND PRIMED PARTS	230,000
• LOCKBOLTS-INTERFERENCE HOLES TEFLON-COATED SPLICE PLATES	2,500,000

FIG. 7—*Splice joint fatigue improvement.*

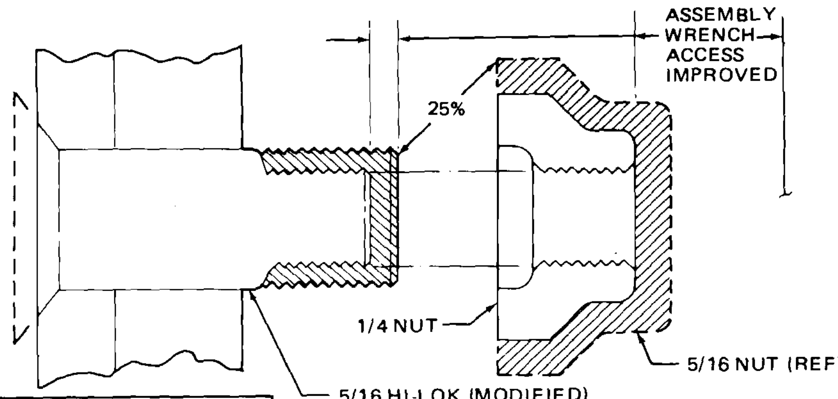

DIAMETER	TENSION STRENGTH (LB)	
	SHEAR HEAD	NUT
1/4	3700	5,820
5/16	5000	9,260
3/8	7200	14,000

FIG. 8—*Reduced bolt thread and nut size.*

posed that the threaded end and the nut be reduced one diameter size, as shown by the shaded areas, to accomplish a 25% weight reduction. These attachments could be located closer to a vertical web for increased loading capabilities without riding the fillet radius. When the thread diameter is reduced, so is the length of the bolt. This bolt, combined with a shorter-height nut, improves assembly access inside channels and tightly designed structures. The tension strength of the reduced thread remains greater than the tensile strength of the shear head. A reduced thread diameter does not scrape and damage the inside of the hole during interference installation or removal. The tension fatigue strength is not reduced for shear designed structural applications.

Crown-Flush Rivet System

A crown-flush rivet configuration has been developed that does not require head-shaving after installation. There are numerous other advantages to this design. The flat-top crown head of the rivet confines impact energy to the shank of the rivet instead of the surrounding structure; therefore less installation energy is required and structural distortion is reduced. The fatigue life is improved 100% because of increased hole and countersink filling, and replacement of head-shaving with the crown-flush rivet will provide a growing advantage as greater quantities of Monel and titanium rivets are required for future aircraft.

Common with each rivet configuration is a small center indent that remains after installation, permitting easier rivet removal for service repair. Qualification tests were performed in compliance with MIL-STD 1312 to obtain Federal Aviation Administration (FAA) and military approval. The crown-flush rivet system is self-inspecting, which has been demonstrated in several material and shape configurations. The rivets can be used to determine visually the countersink depth; thus, installation of the first rivet demonstrates proper or improper installation. An installation time average of 5 s per rivet is saved when head-shaving by hand is eliminated. The rate of automatic-machine-installed riveting can be increased from 6 to 8 rivets per minute when the shave cycle is eliminated. Comparisons of both rivet systems are shown in Figs. 9 and 10, and Fig. 11 and 12 illustrate the installation of conventional crown flush rivets, respectively.

With the conventional flush rivet, the edge of the rivet head that protrudes over the countersink diameter flares out between the rivet gun set and the structure, preventing optimum hole and countersink filling (Fig. 11). Additional driving forces increase the structural distortion and produce a wavy external skin surface.

Sixty Years of Flush Rivet History

During the 1930s, most metal airplanes were assembled with dome-head rivets that protruded above the external surface of the aircraft. A decade

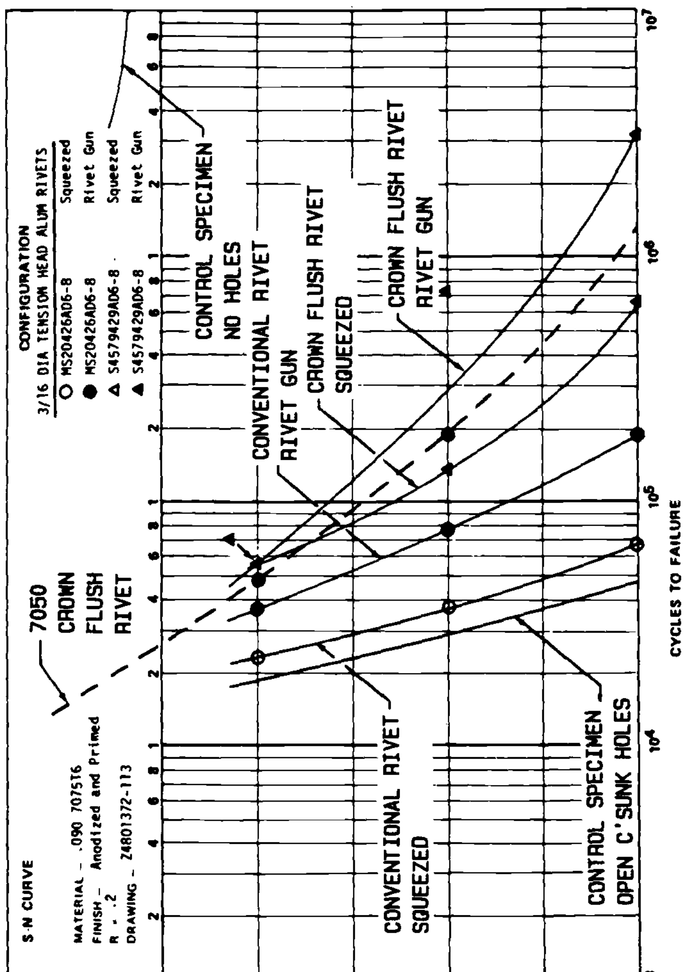

FIG. 9—*Crown flush rivet fatigue test results for 7050 aluminum alloy.*

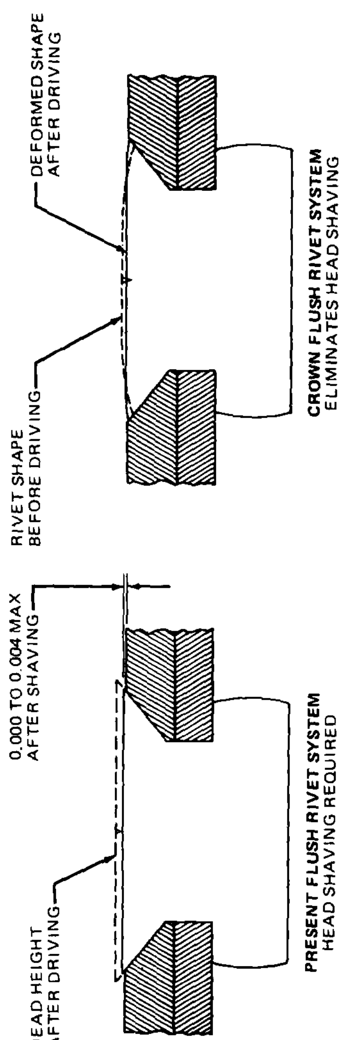

FIG. 10—*Comparison of solid rivet installations.*

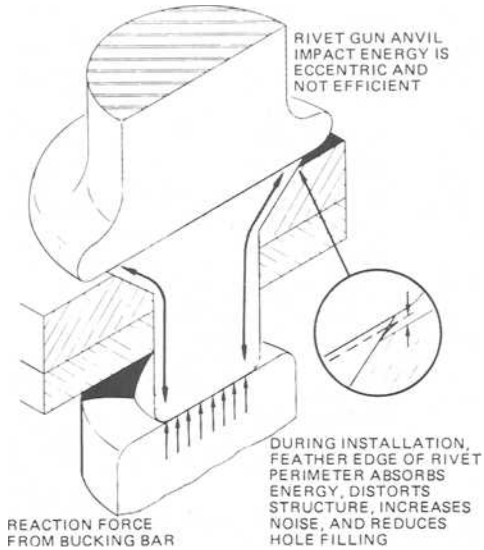

FIG. 11—*Conventional flush rivet installation.*

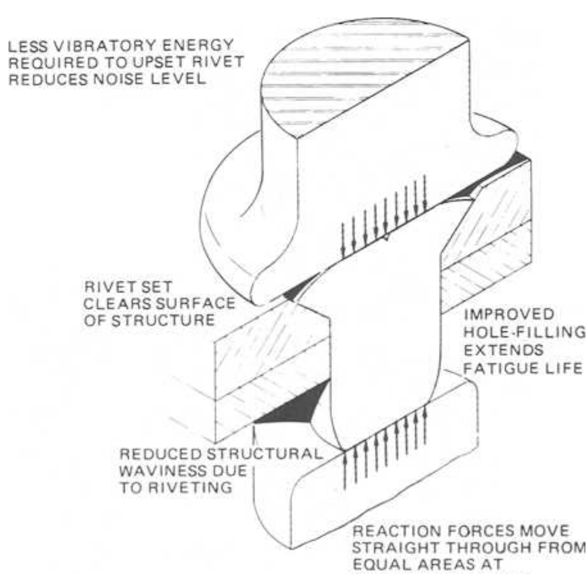

FIG. 12—*Crown flush rivet installation.*

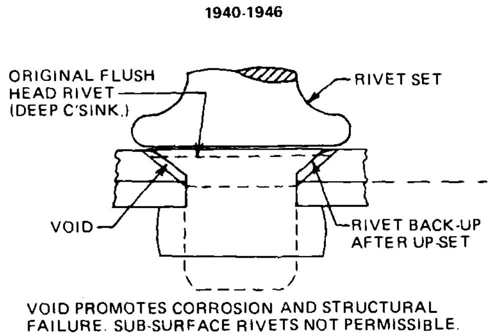

FIG. 13—*Early flush rivet heads, showing lack of fit.*

later almost all such aircraft changed to flush riveting to reduce aerodynamic drag. The following brief comments cover 60 years of flush riveting—from 1940 to what is expected by the year 2000.

The beginning of flush riveting on aircraft created many problems, including matching the countersink cavity to the flush rivet head (Fig. 13). The use of MS20426 tension head rivets in deep countersinks reduced clamp-up and fatigue life, and left a void for corrosion initiation. To overcome these deficiencies, controlled countersink diameters were established to ensure the rivet head remains high in order to fill the hole and countersink cavity (Fig. 14). This procedure required costly head shaving to obtain aerodynamic smoothness. Shear-head rivets (old Lockheed special) replaced tension-head rivets, thus eliminating knife-edge countersinks and improving the sealing and fatigue life. During the period 1970 to 1975, skin gages were reduced to save weight, and rivets were set deeper to eliminate head-shaving (Fig. 15). This practice returned aircraft assembly to the 1940s, with the associated problems of corrosion and fatigue failure.

The Douglas-designed crown-flush rivet and installation method eliminates many of the problems associated with conventional rivets. The crown-

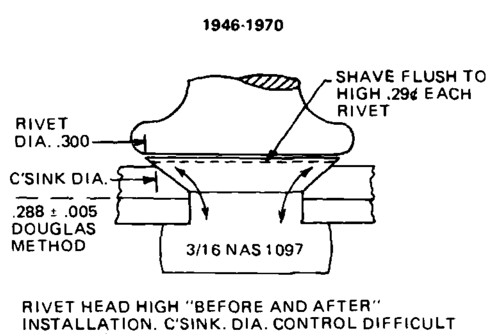

FIG. 14—*High rivet heads, requiring costly shaving.*

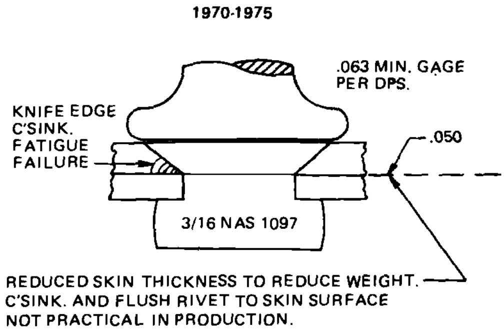

FIG. 15—*Flush rivet heads, which experience corrosion and fatigue problems.*

flush rivet is aerodynamically flush before and after installation. The 0.2032-mm-high (0.008-in.) flat-top crown provides vertical impact tolerance to offset variations in the depths and diameters of countersink cavities. Elimination of head-shaving on steel and titanium rivets for elevated-temperature aircraft will be an additional improvement by the year 2000 (Fig. 16).

Sleeved Aluminum Rivet

A further extension of aluminum rivet use is the application of rivets in graphite/epoxy structures. Conventional fasteners, aluminum rivets, and steel bolts corrode when in contact with graphite fiber ends in drilled holes. In the case of metal fasteners in intimate contact with graphite, aluminum rivets and cadmium-plated steel alloy fasteners corroded after only 24 h of exposure to a 5% salt spray environment. After 504 h of exposure, the aluminum rivets had almost completely disintegrated and the cadmium-plated steel bolts were extremely corroded. Identical aluminum rivets and steel fasteners inserted in aluminum panels and exposed to the identical environment showed almost no galvanic corrosion. However, titanium fasteners in contact with graphite showed no evidence of corrosion after 504

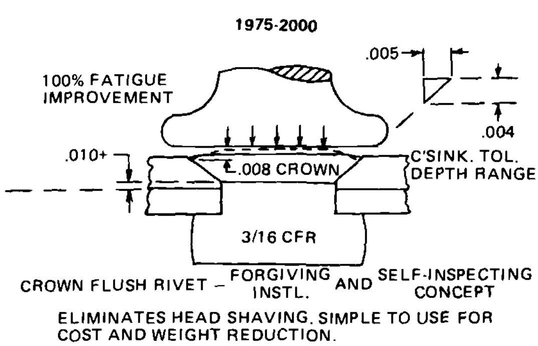

FIG. 16—*Crown flush rivets, which eliminate head shaving and cut weight and cost.*

h of salt spray exposure and are recommended, from a corrosion viewpoint, for use in contact with graphite/epoxy composite materials. Another possible solution to the problem would be a sleeved rivet assembly, in which the sleeve material of stainless steel or titanium would not corrode when in contact with graphite fiber ends (Fig. 17).

The shear and tension strength of sleeve rivets is greater than it is for solid one-piece aluminum rivets (Fig. 18). A shear strength design gap presently exists for aircraft designers—179 MPa (26 000 psi) for 2117-T4 (AD) aluminum rivets to 655 MPa (95 000 psi) for threaded fasteners. The available rivets to fill this gap are age-hardened 2017-T4 (D) rivets that often crack when installed and icebox 2024-T4 (DD) rivets that are expensive to install. Sleeve rivets would be cheaper and lighter than the threaded titanium fasteners presently used to fill this design gap (Fig. 19). The sleeve rivet can be made into flush, protruding head, and slug rivet configurations.

The sleeve rivet should not be confused with the old, and now obsolete, jacket rivets that had soft jackets around them to seal and protect against fuel tank leaks. The structural fatigue life will increase with the new sleeve rivet because of increased prestress inside the hole from the harder sleeve material. In addition, the countersink junction and hole edges are coldworked with the sleeve rivet. Sleeve rivets in graphite/epoxy structures will promote uniform loading in multiple-fastener joints. Solid titanium fasteners in graphite structures will not yield as aluminum fasteners do. This condition, coupled with loose holes in the graphite, causes unequal loading, thus reducing fatigue and static strength. All the sleeve rivet configurations discussed have been installed in aluminum and graphite/epoxy materials.

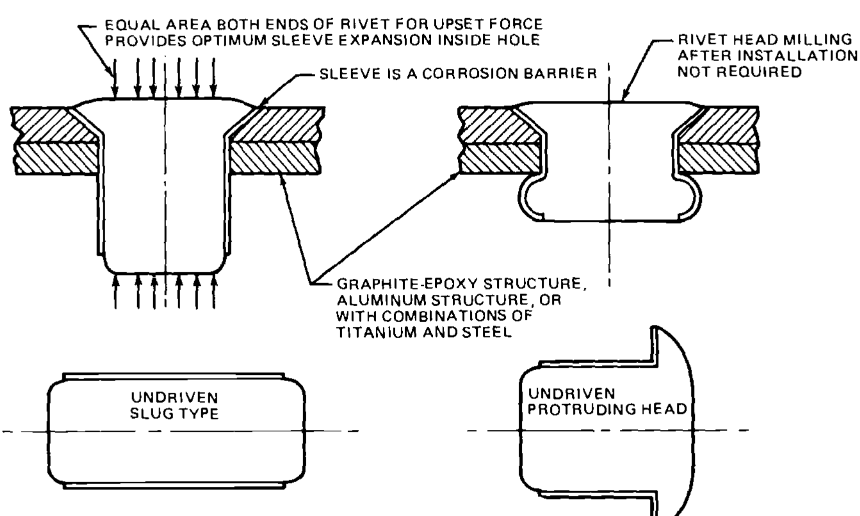

FIG. 17—*Sleeve rivet assembly before and after installation.*

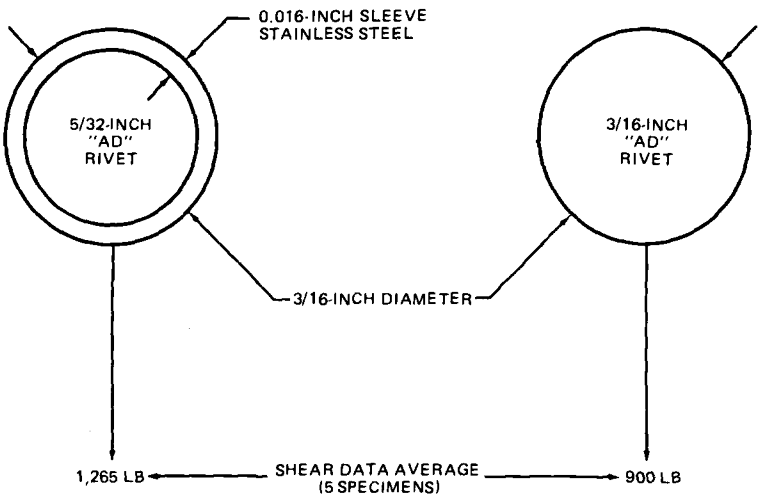

FIG. 18—*Ultimate shear test of sleeve and solid aluminum rivets.*

In addition to dealing with the shear strength gap problem, the aircraft designer must recognize the importance of cost and weight. Aluminum rivets are low-cost, lightweight fasteners when compared with lock-bolt and Hi-Lok attachments. If the rivet shear and tension allowables are not acceptable for a particular design, steel or titanium bolts are usually the next available choice. These fasteners weigh and cost more than aluminum rivets.

The hole preparation for lock-bolt-type fasteners is more expensive because installation is not forgiving to the hole. A rivet or sleeve rivet that is installed by squeeze or vibration upset swells inside the hole. Should the hole be tapered or slightly elongated, the rivets fill the shape of the hole when installed. This type of fastener installation is forgiving to hole variations following preparation. When fasteners do not properly fill the hole, fatigue, shear, and pressure resistance, as well as fuel sealing, are reduced.

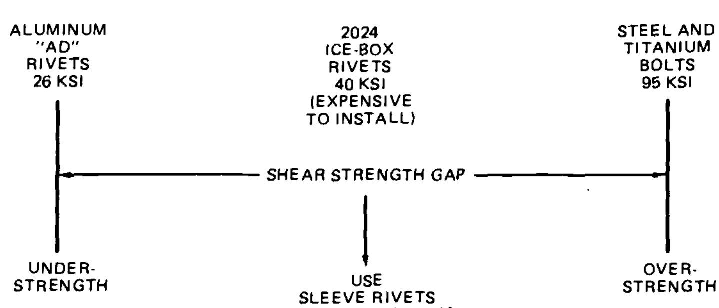

FIG. 19—*Aircraft design shear gap problem with fasteners.*

The sleeve rivet is installed as a one-piece assembly and is forgiving to normal hole fabrication methods and to tolerance variations.

Straight-Sleeve Bolt Fastener

Interference-fit fastener installation in thick combinations of aluminum and steel is very difficult, often even impossible. When cadmium-plated steel fasteners are used in dissimilar combinations, the plating is scraped off and the fastener corrodes. Stepped in-line holes, clearance in the steel, and interference in the aluminum are often impractical and costly. Titanium interference fasteners can seize partially installed inside the hole when the interference exceeds 0.0762 mm (0.003 in.).

The sleeve bolt assembly was designed for interference-fit installations and to overcome the problems noted. The correct grip length can first be assured by slipping the sleeve into a clearance-fit hole prior to core bolt installation. A standard 1 242 000-MPa (180 000-ksi) minimum Hi-Lok (HL-328) and self-aligning nut (S4933653) are used to clear up to 1.27-mm (0.050-in.) backside protrusion of the sleeve. Removal is simplified by first removing the Hi-Lok, which permits the outside diameter of the sleeve to contract. The sleeve can then be easily removed without damage to the hole. Figure 20 illustrates the assembly sequence of the straight-sleeve bolt. The advantages include interference fitting in a clearance hole, a metallic or graphite structure, an oversize service repair fastener, simple and hole-forgiving installation, and adaptability to dissimilar metals and composites.

Preliminary strength tests were performed to compare the strength properties of the sleeve bolts with the those of the solid fasteners presently used on aircraft. Double-shear tests were completed on conventional solid and sleeve bolt fasteners and the variations are shown in Table 1.

Fatigue specimens of steel and titanium were compared by being tested with both solid Hi-Lok fasteners and sleeve bolts. Results of limited testing indicated an equivalent fatigue life in the thinner gages tested, as shown in

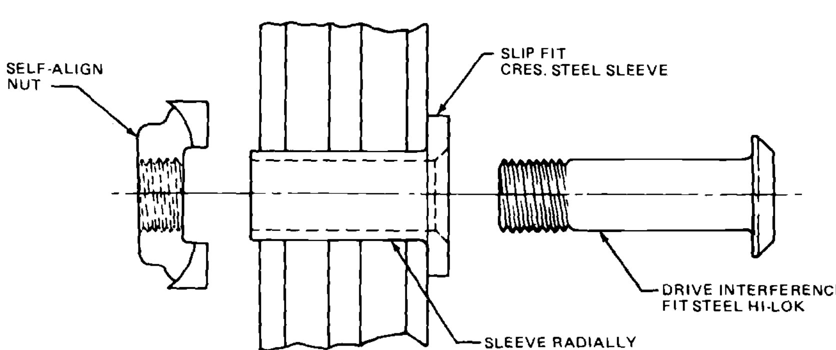

FIG. 20—*Straight-sleeve bolt.*

TABLE 1—*Sleeve bolt double-shear test.*[a]

Bolt[b]	Double-Shear Strength, lb[c]			
	Test 1	Test 2	Test 3	Average
Solid steel Hi-Lok	9 900	10 600	10 400	10 300
Solid titanium Hi-Lok	10 300	9 900	9 700	9 966
303 Steel sleeve bolt	10 900	10 800	10 700	10 800
17-4 Steel sleeve bolt	11 400	11 500	10 700	11 200

[a]9 300 lb (4218.48 kg) minimum shear acceptable.
[b]0.25-in. (6.35-mm) diameter.
[c]1 lb = 0.4536 kg.

Table 2. Trade-off cost studies are required to determine if the two-piece sleeve bolt assembly is sufficiently cost-effective to offset the low fatigue life and precision hole preparation required for single-piece Hi-Lok fasteners installed in thick joint assemblies.

To summarize the sleeve bolt test development, the thick-joint assembly criteria are shown in Fig. 21. Positive interference fit of 0.0254 mm (0.001 in.) or more is required for increased fatigue life. Hi-Lok seizure in the

TABLE 2—*Sleeve bolt fatigue test results.*

Bolt and Fit[a]	Cycles to Specimen Failure (Average of 4 Specimens)[b]	
	Low Load, 17-7 PH Steel[c]	High Load, 4130 Steel[d]
Hi-Lok 0.051 mm (0.002-in.) clearance fit	69 000	159 000
Hi-Lok, 0.051-mm (0.002-in.) interference fit	596 000	371 000
Sleeve bolt, 0.076-mm (0.003-in.) interference fit	570 000	493 000
Sleeve bolt, 0.152-mm (0.006-in.) interference fit	524 000	runout (>1 × 10^6)

[a]3/16-in. (4.76-mm) diameter.
[b]46-ksi (317.17-MPa) gross area stress, R = 0.05.

[c]Configuration:

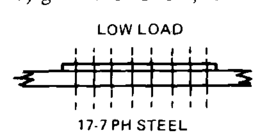

[d]Configuration:

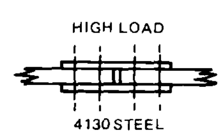

hole with 0.0508 to 0.0889-mm (0.002 to 0.0035-in.) interference fit compresses the assembly range below practical limits to assure a positive interference fit.

High-Fatigue-Life Bushing Design and Test

A new, improved fatigue-life bushing for control fittings has been developed to replace existing bushings (Fig. 22). A review of the record files from the process engineering and airline product support departments indicated that service failures were due to loose-fit bushing installations. This can occur when the hole in the fitting is at the maximum tolerance and the bushing outside diameter is at the low end of the tolerance range.

Alumium-bronze and steel bushings are cadmium-plated, which adds approximately 0.0254 mm (0.001 in.) to the outside diameter. With existing tolerances, press fits of less than 0.0254 mm (0.001 in.) are possible. In these situations, the soft cadmium plate scrapes off the bushing, and low prestressed installation is possible. Reversing loads in service with this condition would allow fretting to begin, causing early fatigue failure.

Disadvantages of Present Bushings

The disadvantages of the bushings presently used include the following:

- A sharp-edged chamfer scores material from inside the hole, causing a reduction in fatigue life.
- The bushing flange relief, external grease groove, and chamfer reduce the housing-bearing area. This design creates fatigue cracks due to high-stress concentrations and fretting from the grooves in contact with the housing.
- A flange groove and four holes make the present bushing more expensive to fabricate.
- Pivot joints on the aircraft could freeze up as a result of only four grease spots 3.175 mm in diameter (1/8 in.) coming in contact with the shaft.
- The bushing can rotate in the housing because of the low interference fit. This can occur when the smaller bushings, with only a 0.00254-mm (0.0001-in.) press fit, are line-reamed after installation.

Advantages of High-Fatigue-Life Bushings

The advantages of high-fatigue-life bushings are the following:

- The radius lead-in on a bushing installed with Parker-O-Lube eases installation without scoring the hole and provides corrosion protection.
- The bushing outside diameter provides 100% housing contact and improved fatigue strength.

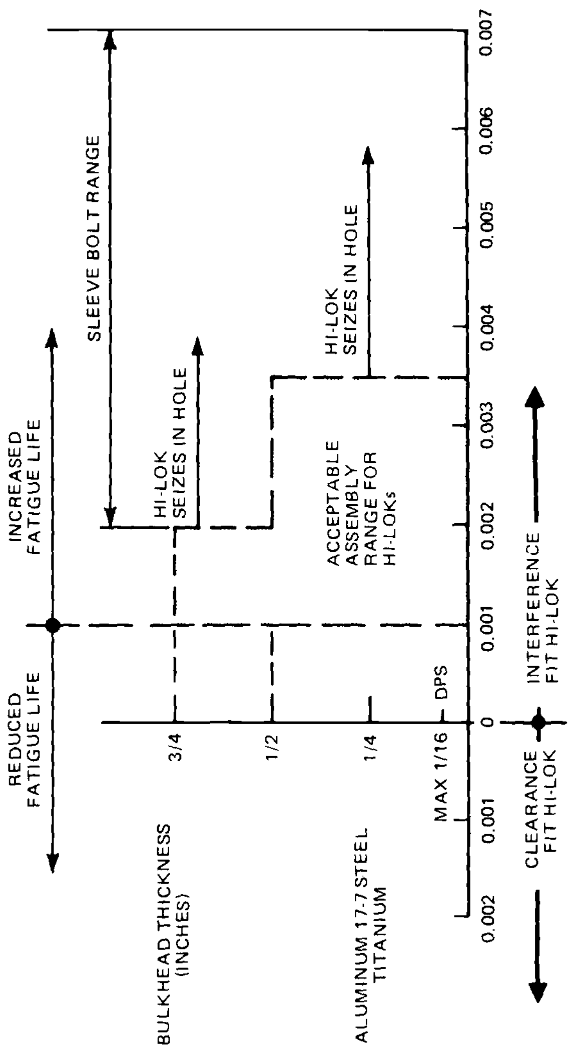

FIG. 21—*Thick-joint assembly.*

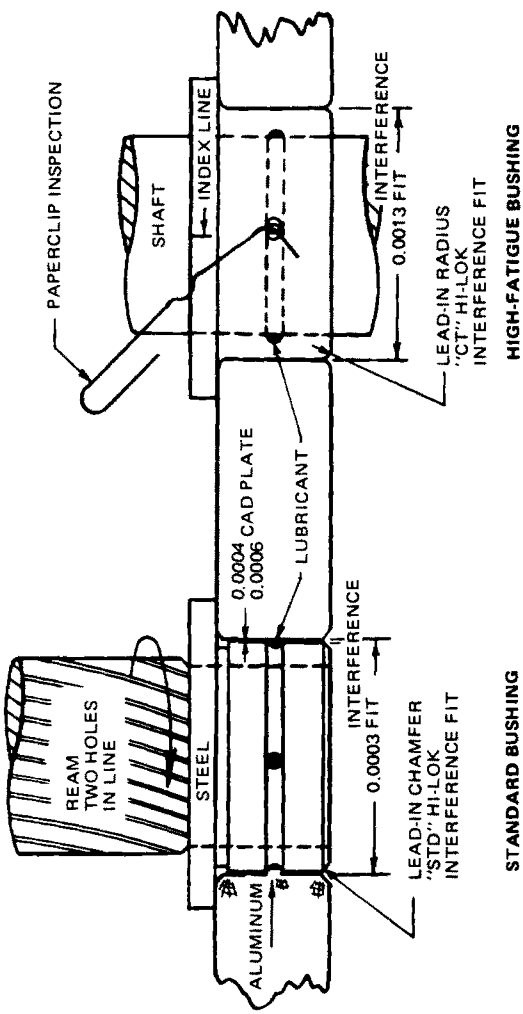

FIG. 22—*Comparison of standard and high-fatigue bushing designs.*

- The simplicity of the new-design bushing eliminates machining, thereby reducing fabrication costs.
- A continuous band of grease in contact with the shaft increases the lubricity to help prevent joint freeze-up.
- The bushing in the housing hole cannot rotate away from the grease hole in the bushing because the press fit has been increased to a positive interference fit. The increased press fit will not cause stress-corrosion cracking.

The low-cost tension fatigue specimen shown in Fig. 23 was developed to simulate fitting lug end shapes as well as to obtain two test failures from a single specimen. The fatigue test specimens were fabricated from 7075 T651 aluminum plate surface-machined to 12.7 mm (0.500 in.) thick. Variations in the interference fit and types of bushings installed were tested by comparison at a 124-MPa (18-ksi) net area stress, $R = 0.1$. Results from the test showed that the high-fatigue bushings improved the fatigue life approximately tenfold.

High-Fatigue-Life Bearings

Bearings are currently installed in their housings to a very low press interference fit to prevent the deformation of the outer race of the bearing, as well as binding and freezing of the movement of the ball inner race. This low press fit may permit axial movement of the bearing in the housing. Radial loads on the bearing tend to increase radial clearances. The combined effects of housing/bearing and inner/outer race tolerances potentially can result in short bearing and structure fatigue life.

A new bearing concept was developed; its principal feature is a predetermined larger radial clearance between the ball and outer race provided during manufacture. The radial clearance of 0.1016 to 0.4572 mm (0.004 to 0.018 in.), depending on diameter, shrinks to a sliding fit on the ball after interference press fit installation of the bearing in the housing. Figure 24 shows the new bearing before and after installation. This concept will improve fatigue life because of the lower-amplitude cyclic loads associated with interference-fit installation and will alleviate fretting, corrosion, and migration problems. The improvements in the concept are shown schematically in Fig. 25.

Present captive-ball-type spherical bearings are assembled with an outer race centered on the ball and then swaged down to the shape of the ball. It is thus unlikely that 100% area contact with the ball will be achieved. Elastic springback of the outer race is associated with an arching effect and can result in less than 50% contact with the ball. Bearing assembly practices generally provide a close sliding fit between the ball and outer edges, but the arched gap remains inside the bearing (Fig. 26, center picture).

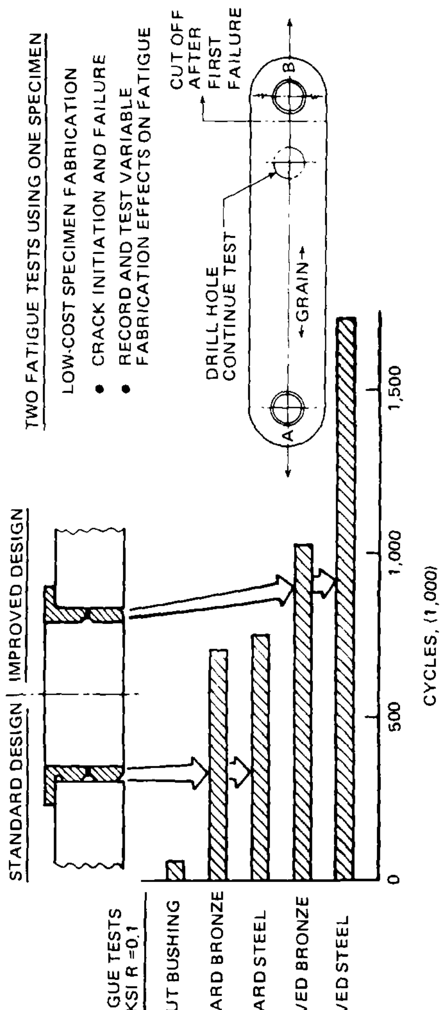

FIG. 23—*High-fatigue-bushing fatigue test results.*

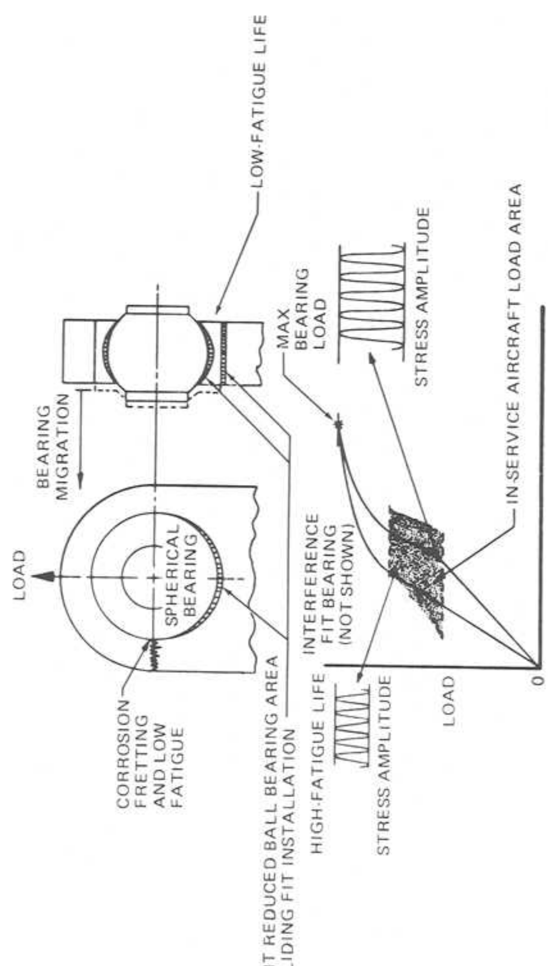

FIG. 24—*New high-faigue-life bearing design concept.*

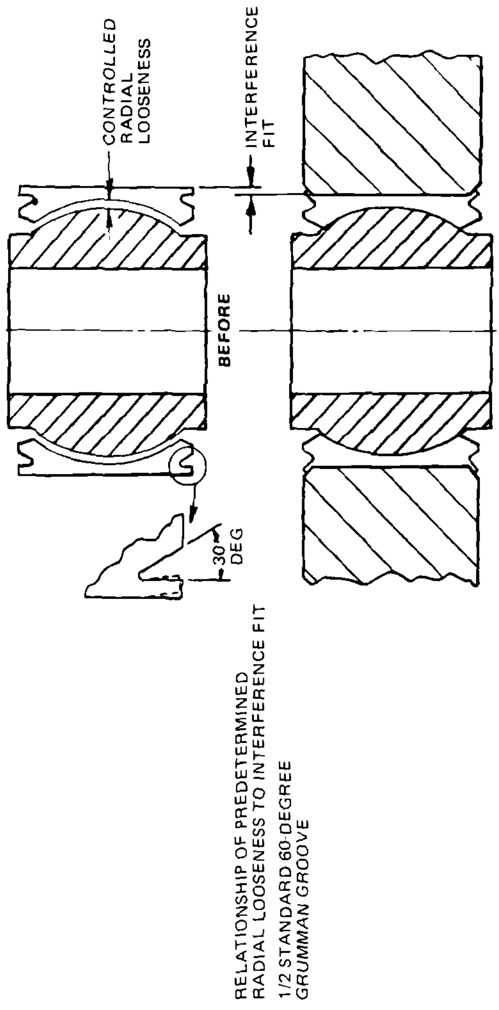

FIG. 25—*Comparison of present and new in-service high-fatigue-life bearing configurations.*

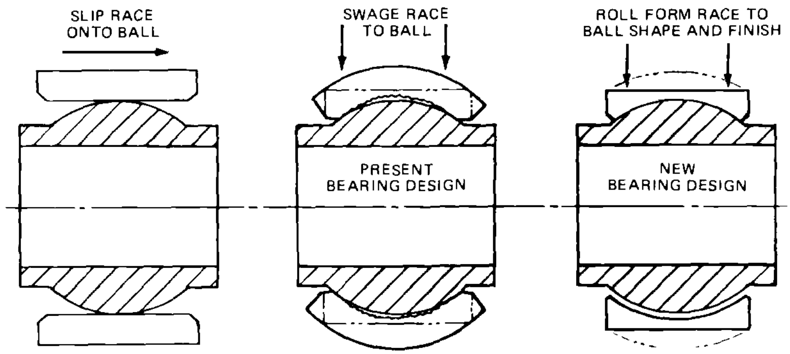

FIG. 26—*Spherical bearing cross sections.*

The increased interference press fit is generated by a larger bearing and, therefore, will permit interchange with existing bearings installed in standard hole sizes. Tests indicated that the fatigue performance of the new bearing installation sysem is 10 to 20 times better than that of present bearings (Figs. 27 and 28).

Stress-Coining Procedures for Fatigue Improvement

The stress-coining procedure controls the yielding of material inside holes and surrounding holes and slots. Stress-coining induces residual compressive stresses that affect load-induced tensile stresses concentrated around these load-carrying areas. These compressive stresses decrease the local mean stress at a point where cracking begins and increase the fatigue life of the structural component by an approximate factor of 4 (Figs. 29 and 30).

The tooling and equipment used in stress-coining have been designed with the skill level of the average airframe mechanic in mind. They are designed to be portable, for use both on new aircraft production lines or at remote locations for field service rework.

Stress-coining has proven extremely useful in extending the fatigue life of a structure when a large percentage of its service life has already been expended. Seven stress-coining methods and associated tooling (Fig. 31) have been developed for this purpose. It is possible that many expensive aircraft components found to be fatigue-prone could be repaired and salvaged by using relatively inexpensive stress-coining methods.

Method 1: Pin-Coining—Hole Expansion for Material Combinations Within 2.286 to 152.4 mm (0.090 to 6.00 in.) Thick—Expansion-pin stress-coining is performed in highly stressed areas to increase the fatigue life of structural members. The hole is expanded plastically to final dimensions by driving a lubricated expansion pin through the precoined (undersized) hole. Approximately one half of the interference between the precoined hole and the expanding pin will spring back to the final hole diameter.

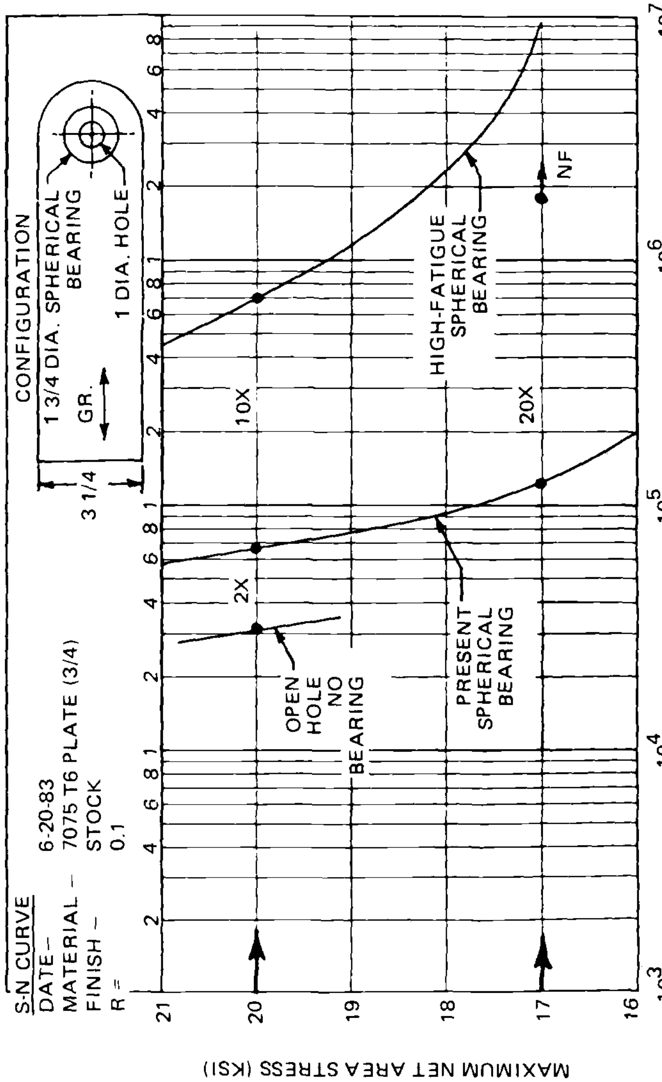

FIG. 27—*Fatigue-life test comparison of spherical bearings.*

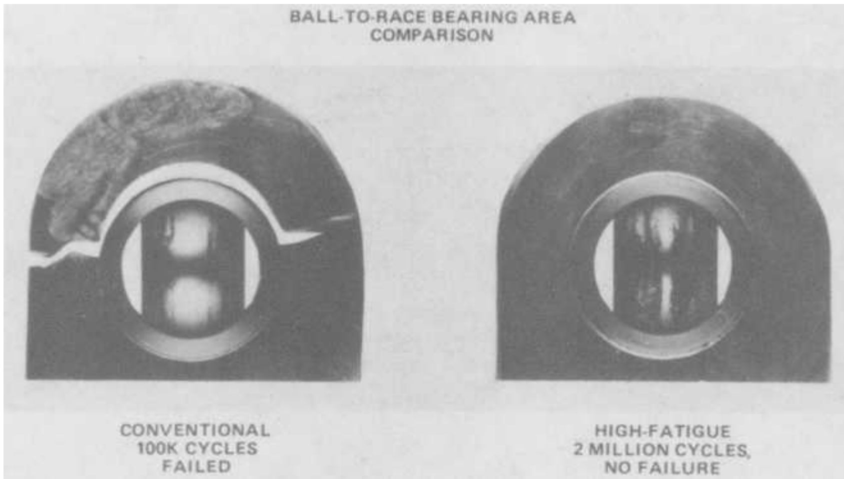

FIG. 28—*Fatigue-tested lug-end specimens.*

Control of the final hole preparation tolerances when using this method is superior to that of drilled and reamed hole preparation tolerances because of the consistency of the material springback after the expansion pin is driven through the undersized precoined hole. Unlike the drilling or reaming process, the final hole size in stress-coining is not affected by different operators.

Method 2: Countersink-Coining—Cold-Worked Countersink Cavity for Flush Attachments—The countersink for flush attachments is stress-coined by cold-working the juncture of the hole and countersink with a lubricated countersink coining tool. This cold-working leaves a smooth, polished juncture between the countersink and hole and induces residual compressive stresses around the countersink that offset load-induced tensile stresses. Stress-coining of the countersink is accomplished prior to pin-stress-coining of the hole.

Method 3: Radius Stress-Coined Interference Fit Holes for High-Fatigue Bushings—The fatigue life of aircraft linkage components can be extended by combining radius coining and a high-fatigue bushing installation. Radius-coining cold-works the edges of the hole to replace chamfering and hand edge-break procedures. The high-fatigue bushing is designed for a positive interference fit and a polished lead-in radius to ease installation.

Method 4: Radius-Coining—One-Side for Materials 1.27 to 2.286 mm (0.050 to 0.090 in.) Thick—One-sided radius-coining was developed for open-hole water drain applications and fatigue improvement of these holes.

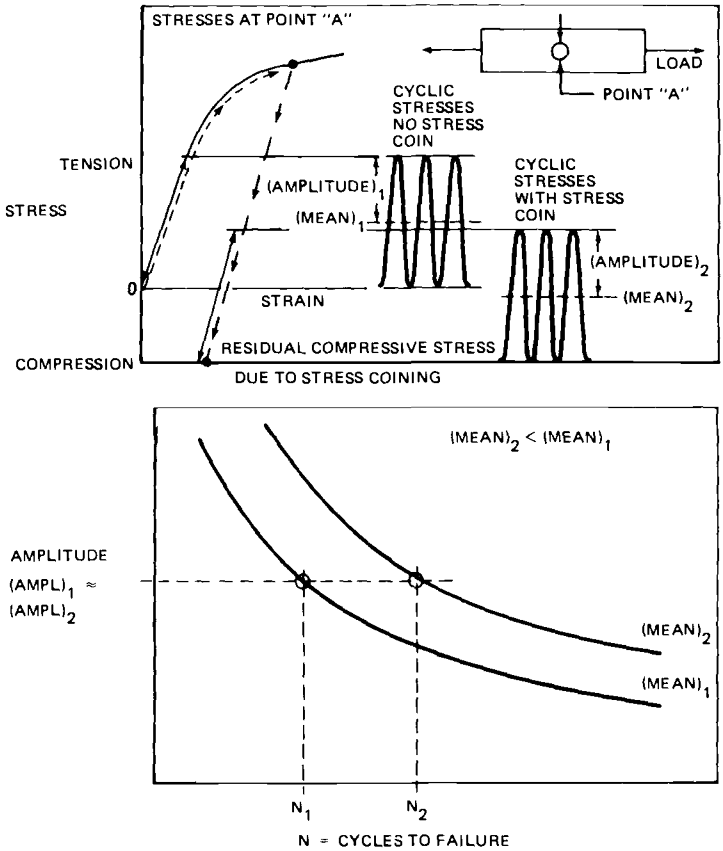

FIG. 29—*Stress-coining for fatigue improvement.*

Method 5: Pad-Coining Holes—Both Sides for Materials 2.286 to 13.97 mm (0.090 to 0.550 in.) Thick—Pad-stress-coining cold-works a 0.762-mm (0.030-in.) radius and a pad recess approximately 0.1016 mm (0.004 in.) deep around the surfaces of holes or slots in aluminum alloys from 2.286 to 13.97 mm (0.090 to 0.550 in.) thick. In this thickness range, the depth of the pad coin is increased with the increase in material thickness for optimum fatigue strength. This method is used for lower wing access door doublers and fuel transfer slots in wing stringers.

Method 6: Ring-Pad-Coining—Both Sides for Materials 0.8128 to 13.97 mm (0.032 to 0.550 in.) Thick—Ring-pad-coining has been demonstrated to be a satisfactory method of improving the fatigue resistance of holes for material thicknesses up to 13.97 (0.550 in.). Limited testing of specimens with a modest thermal history at both elevated and room temperatures has indicated that the ring-pad-coining technique is superior to several other

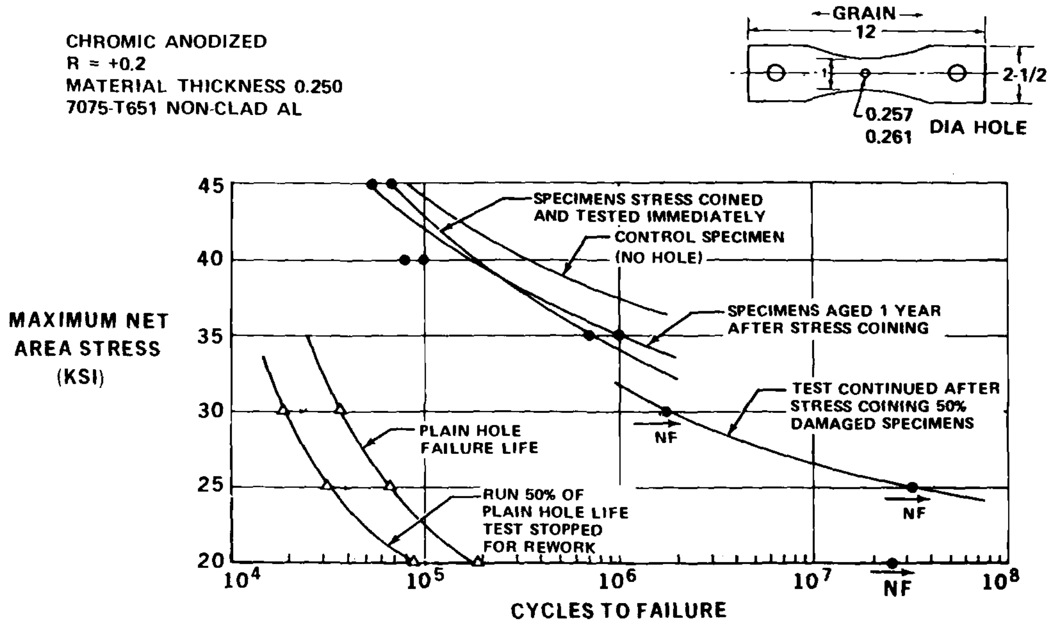

FIG. 30—*Comparison of fatigue for plain and stress-coined holes.*

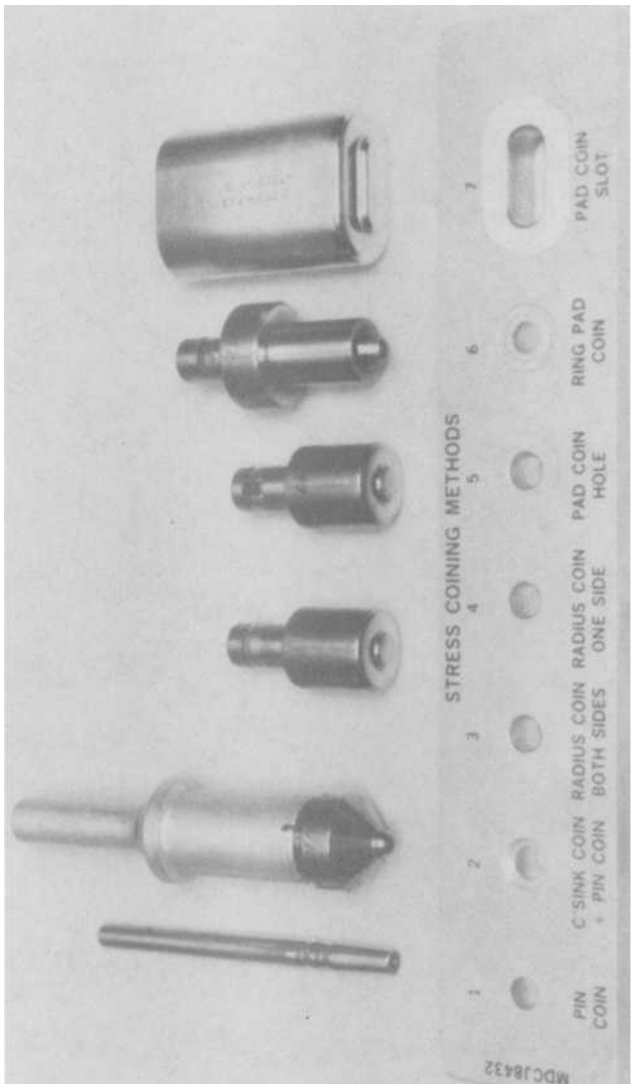

FIG. 31—*Seven stress-coining methods and associated tooling.*

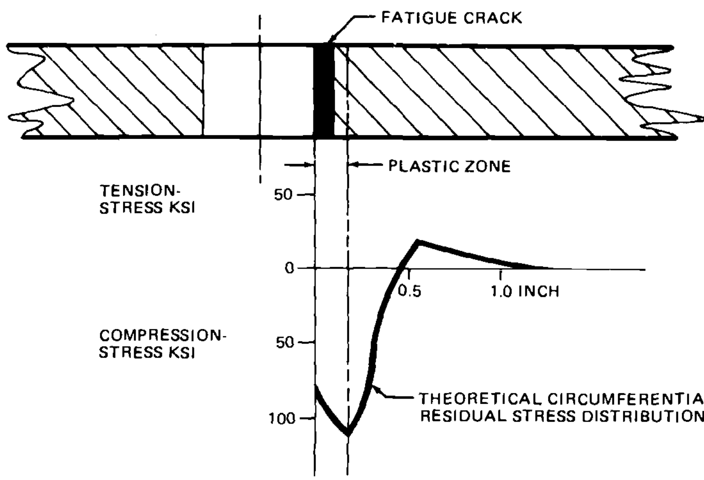

FIG. 32—*Effect of stress coining on cracked holes.*

methods of increasing fatigue resistance in this environment (aircraft jet engine parts).

Method 7: Pad-Coining Slots—Both Sides for Materials 2.286 to 12.7 mm (0.090 to 0.500 in.) Thick—Any open or loosely filled hole or slot in the lower surface of the wing has potential for fatigue failure due predominantly to tension stresses. For this reason most wing stress-coining applications are done on the lower surface rather than the upper surface where compressive stresses prevail. Fuel transfer slots in the lower wing stringers therefore must be pad-stress-coined to improve fatigue strength and reduce weight.

The seven stress-coining methods just described were developed to cold-work the many different fasteners, bushings, bearings and unfilled openings in aircraft structures. The design considerations were the materials and thicknesses to coin, the size and shape of the holes, and access to the aircraft using simple, reusable tools.

Retardation of Fatigue Cracks in Fastener Holes

Since most cracks start in fastener holes, it is difficult to ensure that all fatigue damage can or will be eliminated during rework. Reaming oversize cracked holes is limited by edge-distance restrictions; therefore, hairline cracks or fatigue damage remain out of sight in the hole. To obviate these limitations, fatigue tests have been conducted to evaluate the feasibility of cold-working cracked holes utilizing Douglas stress-coining procedures. The purpose of these tests was to determine if stress-coining procedures are adequate where known hairline cracks and minor damage exist inside the fastener holes.

Zero-load transfer specimens were cycled until a small crack was initiated either at the corner of or inside the hole. These holes [some with cracks up to 1.524 mm (0.060 in.) long] were then cold-worked by driving a stress-coin expander pin through the holes with a small rivet gun. The fatigue testing of the coined cracked holes was then resumed, and the results were very encouraging. The cracks were arrested from propagation and the improvement was threefold to fivefold in comparison with uncracked holes tested to uninterrupted failure.

The performance improvement thus demonstrated is due to residual stresses induced by interference between the hole and the expander pin, which plastically yields the crack tip. When the pin exits the far side of the hole, the crack tip springs back, inducing the beneficial residual compressive stresses that extend the fatigue life of cracked or uncracked holes (Fig. 32).

Conclusion

The advanced fastener technology described in this paper has been developed and tested for specific requirements on near-term aircraft. Many of the projects were developed for rework of in-serivce aircraft and design improvement of new-production aircraft. Aircraft design philosophy has drastically changed recently to emphasizing high-performance fastening systems, thus extending the life-cycle-to-cost ratio of future aircraft. The objective of the Douglas program reported in this paper has been aircraft improvement where material selection, fatigue life, and cost savings are design considerations.

Bibliography

Speakman, E. R., "Stress-Coining Procedures for Fatigue Improvement," Report MDC-J5588A, McDonnell Douglas Corp., Long Beach, CA, 22 Aug. 1977.

Speakman, E. R., "Crown Flush Rivet Development and Certification," Report MDC-J6628A, McDonnell Douglas Corp., Long Beach, CA, 27 March, 1981.

Speakman, E. R., "Advanced Fastener Technology," Report MDC-J2361, McDonnell Douglas Corp., Long Beach, CA, 15 Dec. 1981.

Robert L. Champoux[1] *and Michael A. Landy*[1]

Fatigue Life Enhancement and High Interference Bushing Installation Using the ForceMate Bushing Installation Technique

REFERENCE: Champoux, R. L. and Landy, M. A., **"Fatigue Life Enhancement and High Interference Bushing Installation Using the ForceMate Bushing Installation Technique,"** *Fatigue in Mechanically Fastened Composite and Metallic Joints, ASTM STP 927,* John M. Potter, Ed., American Society for Testing and Materials, Philadelphia, 1986, pp. 39–52.

ABSTRACT: The patented ForceMate bushing installation process, originally developed by McDonnell Aircraft, involves expansion of a hole and simultaneous installation of an interference fitted bushing. The process provides a significant improvement in the fatigue life of bushed holes in metallic structures and offers reduced bushing installation costs. Fatigue life improvement is attributed both to the creation of residual compressive stresses in the metal surrounding the hole and to the reduction in applied cyclic stress range caused by the interference fitted bushing. Installation is accomplished without loss of corrosion protection because of the initial clearance fit of the bushing in the hole. Installation costs are reduced by the elimination of liquid nitrogen needed for shrinkage of bushings, as well as the significant reduction in installation time and manpower.

This paper describes the ForceMate process in detail. Fatigue lives of simulated aluminum lug geometries with bushings installed using the ForceMate process were compared with lives of lugs with bushings installed using conventional shrink fit methods. Constant amplitude and flight-by-flight spectrum loading were used for cyclic testing. Life improvement factors of greater than 3:1 were shown. Bushing-to-hole interferences were significantly greater than those achievable with traditional shrink-fit installation techniques. The process was demonstrated effectively with bushings manufactured from beryllium-copper, aluminum-nickel-bronze, and steel alloys.

KEY WORDS: fatigue (materials), fatigue enhancement, bushings, aluminum alloys, lugs, cold working, cold expansion, interference fit, residual stress

Structural assemblies with bushed holes have historically been prone to fatigue problems. In particular, bushed holes in 100% load transfer joints (for example, lugs) are subject to premature fatigue crack initiation in the

[1] Vice president/general manager and engineering manager, respectively, Fatigue Technology, Inc., Seattle, WA 98188.
[2] U.S. Patent No. 4,164,807.

bushing-to-lug interface because of factors such as fretting or corrosion, or both. Subsequent fatigue crack growth is rapid owing to the high stress intensity factors associated with this geometry.

A common method for reducing fretting and providing fatigue life improvement of bushed holes is the installation of an interference fitted bushing. Bushing interference is defined as the degree to which the bushing outside diameter is greater than the hole inside diameter. Traditional techniques using a liquid nitrogen bath to "shrink" the bushing prior to installation are limited to diametrical interferences of 0.05 to 0.07 mm (0.002 to 0.003 in.). Attempts to install bushings at higher interferences often result in scoring and galling of the inside surface of the hole. Corrosion protection from cadmium plating is often scraped off or substantially lost during shrink-fit (SF) installation. The SF technique is labor-intensive and subject to frequent rework because of damage caused during bushing installation. Further, there are safety implications associated with the cryogenic temperatures of liquid nitrogen.

A new concept, the ForceMate (FM) bushing installation process,[2] provides fatigue enhancement by combining cold expansion of a hole with simultaneous high interference bushing installation. The initial clearance fit of the bushing in the hole allows installation to be accomplished without loss of corrosion protection. Installation of a bushing using the FM process involves only a few minutes of labor, in comparison with SF installation labor requirements of up to 45 min per bushing.

The bushing interference achievable with the FM process is far greater than is possible with SF techniques. Typically, 0.10 to 0.20-mm (0.004 to 0.008-in.) diametrical interference is achieveable for a nominal 25.4-mm-diameter (1.00-in.) FM bushing. The high bushing interferences associated with the FM process result in a significant reduction in fretting in the bushing-to-hole interface and preclude the intrusion of corrosive agents. The reduction in applied cyclic stress range of the interference fitted bushing and cold expansion of the hole provide significant retardation of fatigue crack growth and, as a consequence, allow longer inspection intervals. Since inspection of most bushed holes invariably involves dissassembly of a complicated structure, maintenance costs are reduced.

The FM process was originally conceived by Coughenour and Hoeckelman of McDonnell Aircraft Co. They subsequently developed tooling for specific beryllium-copper bushing installations in several U.S. military airframes. The fatigue life improvement and reduced bushing installation costs have been well proven with testing and in-service experience. The process is currently under advanced development at Fatigue Technology, Inc., where it is being systematized for other bushing materials and hole geometries and as a substitute for National Aerospace Standards (NAS) standard bushings.

The purpose of this paper is to describe the FM process. Fatigue lives of simulated lug geometries with bushings installed using the FM process are compared with lives of lugs with bushings installed using conventional techniques. Life improvement factors of better than 3:1 are shown with constant amplitude and flight-by-flight spectrum loaded cyclic testing. Process parameters, various FM bushing materials, manufacturing tolerances, and test data are discussed.

Process Overview

Installation of a bushing using the FM process is shown in Fig. 1. A specially sized bushing, with a proprietary dry film lubricant on the inside surface, is placed over a tapered expansion mandrel. The attachment end of the mandrel is inserted into a hydraulic puller unit; the mandrel/bushing assembly is inserted into the hole; and the puller unit is activated to pull the expansion mandrel through the bushing. The expansion of the bushing by the mandrel cold expands the hole material while the bushing is simultaneously installed with high interference. The inside surface of the bushing after FM processing has a tapered profile, with a slightly larger diameter at either end than in the middle. A subsequent reaming operation is per-

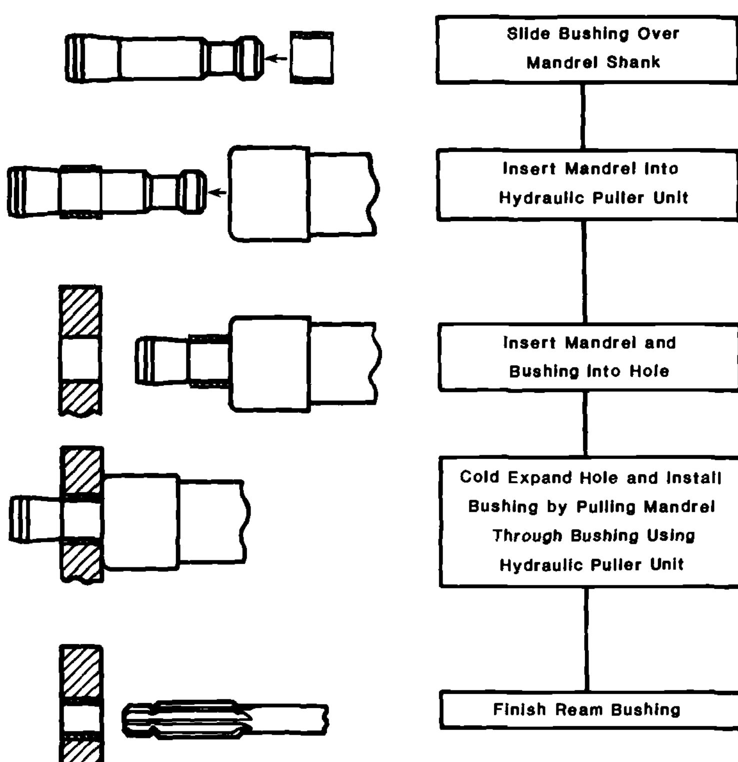

FIG. 1—*ForceMate process methodology.*

formed to size the bushing inside diameter to the final size and to remove lubricant residue. In multi-flanged lug assemblies, the final reaming operation also ensures alignment of the bushing inside diameters.

Cold expansion creates a zone of residual compressive stresses around a hole [*1,2*]. These compressive stresses effectively reduce the magnitude of applied cyclic tensile stresses and hence increase fatigue and crack growth life. There is exhaustive data available concerning the beneficial effects of cold expansion on fatigue life performance.

Similar to interference fitted pins, interference fitted bushings have also been shown to provide fatigue life enhancement of a bushed hole through a reduction in applied cyclic stress range at a hole [*3,4*]. The amount of improvement depends on the ratio of the bushing modulus to the material modulus and the bushing wall thickness.

Bushing inside diameters are expanded between 2 and 6%, depending on the bushing and lug materials and dimensions. Expansion is defined as the total expansion of the bushing during FM processing, expressed as a percentage of the initial bushing inside diameter. The presence of the bushing precludes the 100% transfer of applied radial expansion to the hole. Hence, the actual expansion of the lug material is less than the expansion of the bushing. In some cases, this reduced amount of applied expansion is less than the recommended minimum for effective cold expansion processing of typical hole geometries [*5*]. However, lower levels of applied expansion have been shown to provide significant fatigue improvement in lug geometries [*6–9*]. In general, thinner bushings or aluminum lugs will require less expansion than thicker bushings or titanium or high-strength steel lugs. An applied expansion of 2% was used for the bushing sizes and lug geometries in this test program.

Bushing-to-hole diametrical interferences ranged from 0.10 to 0.20 mm (0.004 to 0.008 in.) for the bushing sizes used in the fatigue test program. This measurement was taken by pressing the bushing out of the hole after FM processing and then comparing the bushing outside diameter and the hole inside diameter.

Bushing corrosion inhibitors such as cadmium plating applied to the outside of the bushing are unaffected by the FM process because of the initial clearance fit of the bushing in the starting hole. Protective coatings on SF bushings are often damaged by scraping action as the bushing is installed. The FM process also facilitates effective use of wet sealants applied to the inside of the hole.

Straight and flanged FM bushings have been manufactured from most typical aerospace bushing materials, including aluminum-nickel-bronze, beryllium-copper, and high-strength steel. Developmental testing is also being performed with other bushing alloys such as 410 stainless (modified) and precipitation-hardened steels.

Initial starting hole tolerance requirements for the FM process are ±0.025 mm (0.001 in.). This requirement is typically the same as, or less restrictive than, SF hole tolerance requirements and, in conjunction with the mandrel diametrical tolerance of ±0.010 mm (0.0004 in.), ensures that the minimum applied expansions are achieved. Additional manufacturing cost reductions are realized by elimination of the bushing and starting hole sorting required to achieve precise levels of bushing interference. This labor-intensive procedure involves measuring individual bushing outside diameters and matching them to measured hole diameters.

Bushing flushness requirements are achieved using a specially designed nosecap assembly that restricts bushing axial movement during cold expansion. Both recess (underflush) and protrusion (overflush) requirements can be satisfied.

Fatigue Test Program

The test program was designed to show fatigue life improvement in a typical aerospace attachment lug. The configuration selected is representative of a nacelle strut attachment lug on a strategic bomber. Both constant amplitude and flight-by-flight spectrum loading were used for cyclic testing.

The test plan is shown in Table 1. The test conditions were designed to show:

(*a*) process effectiveness,
(*b*) baseline fatigue design data (*S-N*), and
(*c*) representative service life improvement factors.

All the tests were performed with aluminum specimens.

TABLE 1—*Test conditions.*

Test Series	Bushing Installation Method	Bushing Alloy	Load Conditions (maximum net section stress, except where noted), MPa (ksi)
Basic process effectivity	shrink fit	Al—Ni—Br	85.5 (12.4), R = 0.05
	shrink fit	Be—Cu	85.5 (12.4), R = 0.05
	shrink fit	steel	85.5 (12.4), R = 0.05
	FmCx	Al—Ni—Br	85.5 (12.4), R = 0.05
	FmCx	Be—Cu	85.5 (12.4), R = 0.05
	FmCx	steel	85.5 (12.4), R = 0.05
Baseline design data development ($S - N$)	shrink fit	Be—Cu	51.7 (7.5), R = 0.05
	shrink fit	Be—Cu	68.9 (10), R = 0.05
	shrink fit	Be—Cu	110.3 (16), R = 0.05
	shrink fit	Be—Cu	137.9 (20), R = 0.05
	FmCx	Be—Cu	85.5 (12.4), R = 0.05
	FmCx	Be—Cu	110.3 (16), R = 0.05
	FmCx	Be—Cu	137.9 (20), R = 0.05
Service life improvement	shrink fit	Be—Cu	nacelle strut attachment
	FmCx	Be—Cu	load spectrum
	shrink fit	steel	nacelle strut attachment
	FmCx	steel	load spectrum

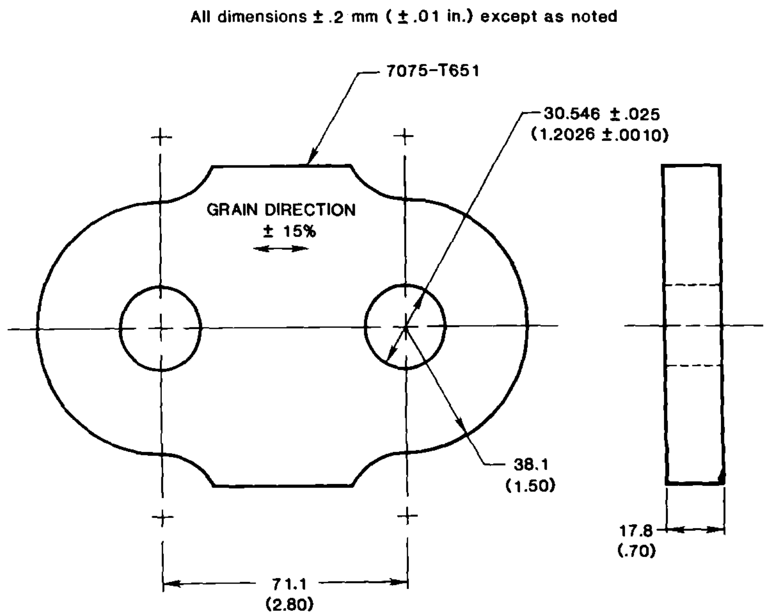

FIG. 2—*Fatigue test specimen.*

Process effectiveness tests compared SF and FM specimen fatigue lives at a single constant-amplitude load level, using beryllium-copper, aluminum-nickel-bronze, and steel bushings. Design data in the form of *S-N* curves were developed and compared for both SF and FM specimens with those for beryllium-copper bushings. Specimens with beryllium-copper and steel bushings were used to show service life improvement due to FM processing.

Specimens designed to simulate the attachment lug geometry were ma-

TABLE 2—*Test specimen material properties and chemical analysis for 7075-T651 aluminum plate.*

Material properties	
Yield strength, MPa (ksi)	560 (81.2)
Tensile strength, MPa (ksi)	607 (88.1)
Elongation, in 25.4 mm (1 in.), %	9
Chemical analysis, %	
Cu	1.48
Si	0.11
Fe	0.30
Mn	0.10
Mg	2.57
Zn	5.30
Cr	0.21
Ti + Zr	0.06
Other elements, each	−0.05
Other elements, total	−0.05
Al	balance

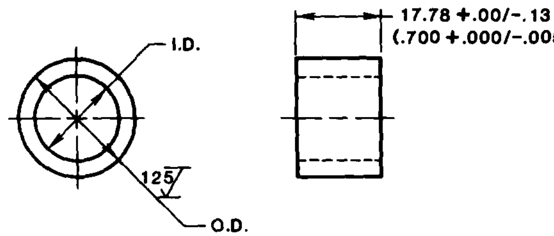

	I.D.	O.D.
SHRINK FIT	26.947 (1.0609)	30.594 (1.2045)
FmCx	25.811 (1.0162)	30.521 (1.2016)

All dimensions ±.013 mm (±.0005 in.) except as noted

FIG. 3—*Bushing dimensions.*

chined from 25.4-mm-thick (1.00-in.) 7075-T651 aluminum plate. Dimensions and material properties are shown in Fig. 2 and Table 2; bushing dimensions and material properties are shown in Fig. 3 and Table 3. No corrosion inhibitors were applied to the bushings for these tests.

The SF specimens were prepared by initially heating each specimen to 82°C (180°F), followed by installation of bushings previously cooled by submersion in a liquid nitrogen (LN_2) bath. The bushings were rapidly transferred from the LN_2 bath to the specimen, inserted into the hole, and pressed in with a hand vise. Bushing-to-hole diametrical interference ranged from 0.05 to 0.07 mm (0.002 to 0.003 in.).

FmCx specimens were prepared using the methodology shown in Fig. 1. The bushing applied expansion was 2% for these tests. The bushing inside diameters were reamed to 26.92 mm (1.060 in.) after FmCx processing.

The test specimen setup is shown in Fig. 4. A close-tolerance AISI 4340 steel pin, 26.861 mm (1.0575 in.) in diameter, was used to connect each end of the specimen to the clevis fittings. The pins were secured with soft rubber spacers between the retaining nut and the clevis grips so as to preclude any clamp-up effects.

All the specimens were cycled to failure in closed-loop servohydraulic fatigue test machines under load control. The test machines and associated equipment are calibrated semiannually using standards recommended by the National Bureau of Standards.

Constant amplitude loads were generated by digital function generators. Flight-by-flight loads were generated by a digital minicomputer from a load sequence supplied by the U.S. Air Force. The sequence consisted of a three-mission mix in quasi-random format representing the in-service load environment of a strategic bomber nacelle strut. The loads were arbitrarily

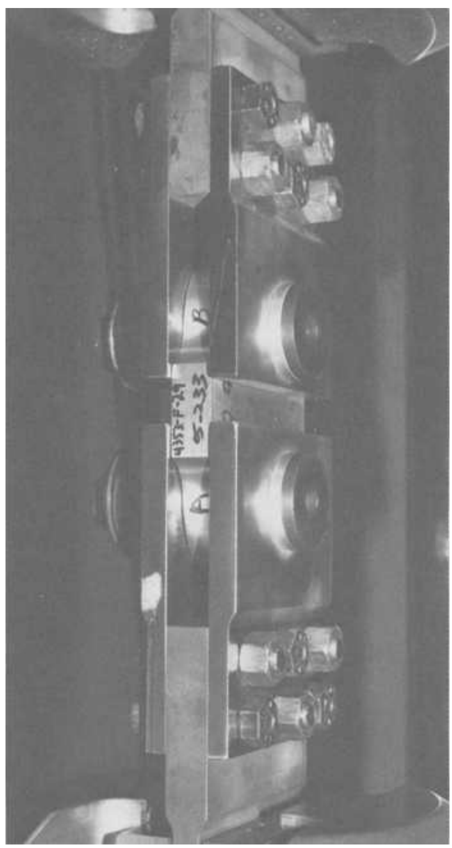

FIG. 4—*Fatigue test setup.*

TABLE 3—*Bushing material properties.*

Material	Material Specification	Minimum Yield Strength, MPa (ksi)	Minimum Tensile Strength, MPa (ksi)	Elongation in 50.8 mm (2 in.), %
Beryllium-copper	CA 172	1000 (145)	1138 (165)	3
Aluminum-nickel-bronze	CA 630	448 (65)	793 (115)	18
High-strength steel	AISI 4340	910 (132)	1034 (150)	14

increased so as to induce failures in a reasonable test period. Basic spectrum details are shown in Table 4.

Test Results and Discussion

Basic process effectivity test results are shown in Fig. 5 as cycles to failure for each specimen configuation. All tests were performed at a constant-amplitude maximum net section stress of 85.5 MPa (12.4 ksi), a stress ratio of 0.05, and a cyclic test frequency of 10 Hz. These results indicate that FM processing can be adapted to various bushing alloys. There were no failures of any FM specimens, which had test lives in excess of 10^6 cycles. This compares to minimum test lives of 2×10^5 cycles for aluminum-nickel-bronze and beryllium-copper bushed SF specimens, and 4×10^5 cycles for steel bushed specimens.

One FM specimen of each bushing type was successfully tested to 8×10^6 cycles without failure. An anticipated minimum life improvement of 3:1, based on other tests of cold expanded lugs, was exceeded [*6–9*].

Test lives of steel bushed FM and SF specimens were significantly longer than lives of comparable beryllium-copper or aluminum-nickel-bronze bushed specimens. This is because the stiffness of the steel bushing is significantly greater than that of the other two alloys and, hence, the load on the bearing area of the lug hole is more evenly distributed. Further, as noted by Crews, the tensile preloading benefit of an interference fitted pin (bushing) in-

TABLE 4—*Nacelle strut loading spectrum.*

		Maximum Net Spectrum Stress, ksi[a]			Minimum Net Spectrum Stress, ksi		
Mission	Missions per 1000 Flights	Once per Flight	Once per 10 Flights	Once per 100 Flights[b]	Once per Flight	Once per 10 Flights	Once per 100 Flights
1	846	22.7	25.4	28.1	4.7	8.1	8.1
2	65	27.1	30.5	35.0	4.3	2.7	2.7
3	89	17.7	18.0	19.1	9.6	9.6	9.6

[a] 1 ksi = 6.90 MPa.
[b] Maximum once per 100 flight stress is maximum spectrum stress.

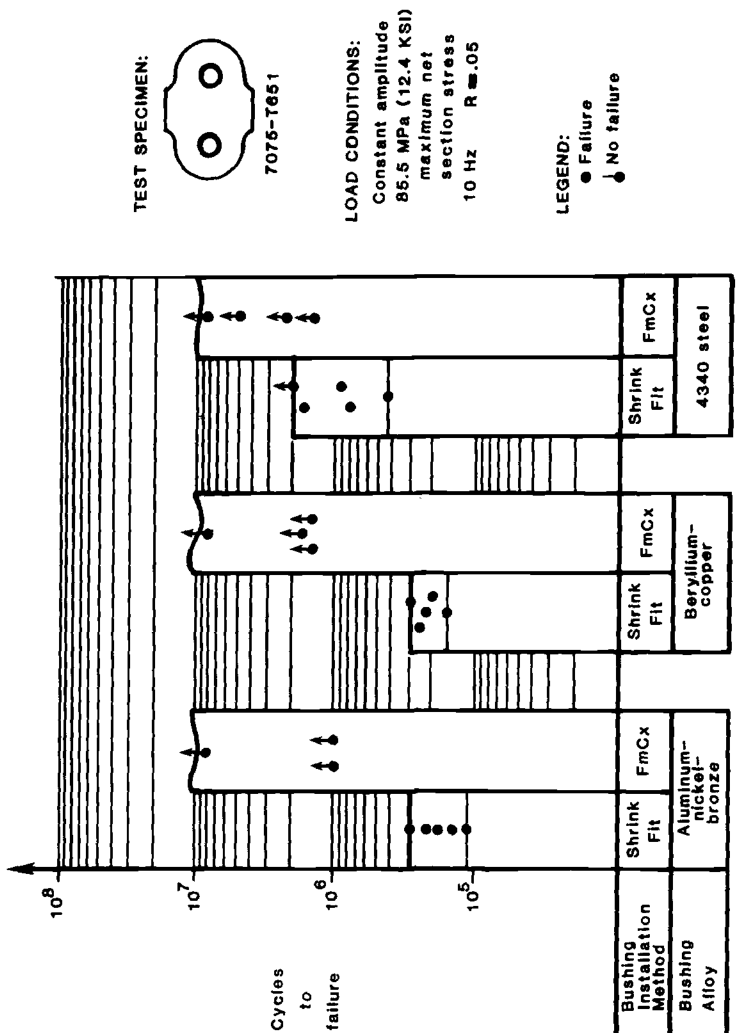

FIG. 5—*Test results: process effectiveness.*

creases as the ratio of the pin (bushing) modulus to the sheet modulus increases; the steel bushed specimens have the highest ratio for the geometries investigated [*10*].

Baseline fatigue design data were developed for beryllium-copper bushed specimens for comparison with unpublished McDonnell Aircraft test data. These results are shown in Fig. 6 as maximum net section stress versus cycles to failure (*S-N*). At the severe constant-amplitude load condition of 137.9 MPa (20 ksi), the minimum life improvement factor was 3:1. Life improvement factors increased significantly at lower, more realistic load levels. Conservatively, the endurance limit increased approximately 55%, from 51 MPa (7.5 ksi) for SF specimens to at least 79 MPa (11.5 ksi) for FM specimens.

Service life comparisons of SF and FM specimens are shown in Fig. 7 as flights to failure. These tests show that the FM process is effective under realistic usage conditions. Beryllium-copper bushed SF specimens failed in 250 to 450 flights, as compared to FM specimens that were tested to a minimum of 1100 flights, with only one failure. Steel bushed SF specimens failed in 400 to 1100 flights, as compared to FM specimens that did not fail after cycling to a minimum of 3100 flights. As noted during the constant amplitude tests, the inherent life improvement of the steel bushed specimens, as compared to the beryllium-copper bushed specimens, is also evident under spectrum loading conditions.

The fatigue life improvement due to the FM process can be attributed to the combination of cold expansion of the metal surrounding the hole and the high interference fit of the bushing. The synergistic effect of these two phenomena has been documented in other investigations of cold expansion in combination with interference fit fasteners [*11–13*].

All testing to date has demonstrated FM process effectiveness in 100% load transfer, lug-type geometries. It can be inferred from the tests of this "worst case" geometry that the process will also be effective with other types of bushed holes where fatigue life improvement is desired. Further, there are other applications where installation of an interference fit bushing in a nonfatigue critical structure is desirable but has been difficult to achieve; these include the following:

(*a*) access panel mounting holes, to maintain consistency of hole diamters;
(*b*) transfer holes through bulkheads, ribs, and other structures to facilitate hose and wire bundle routing; and
(*c*) oversized holes, to reduce hole diameters to the original size.

Further fatigue, crack growth, and corrosion testing is planned. The parameters to be studied include the effects of:

(*a*) manufacturing tolerance buildup,

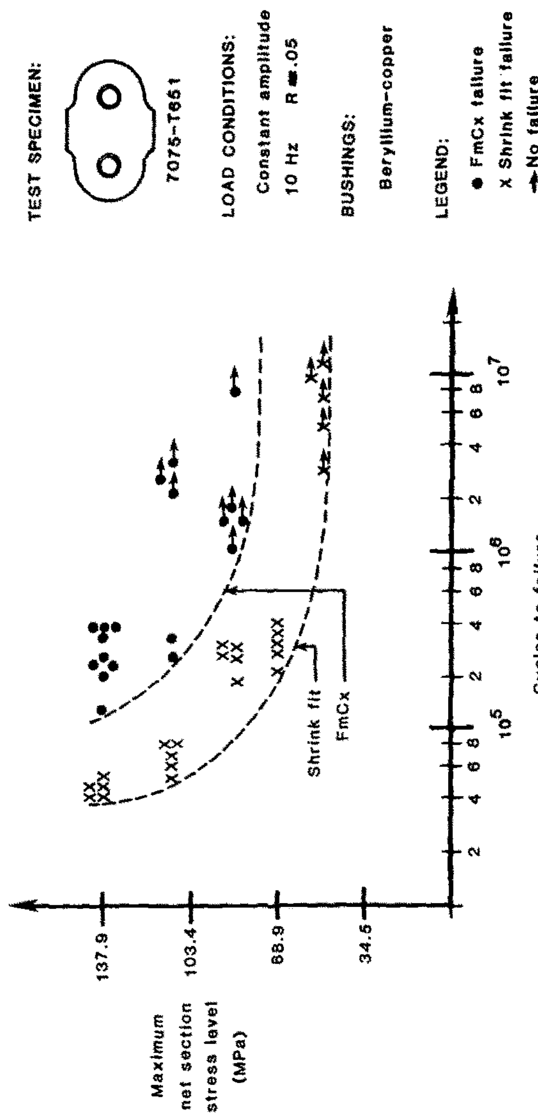

FIG. 6—Test results: design data.

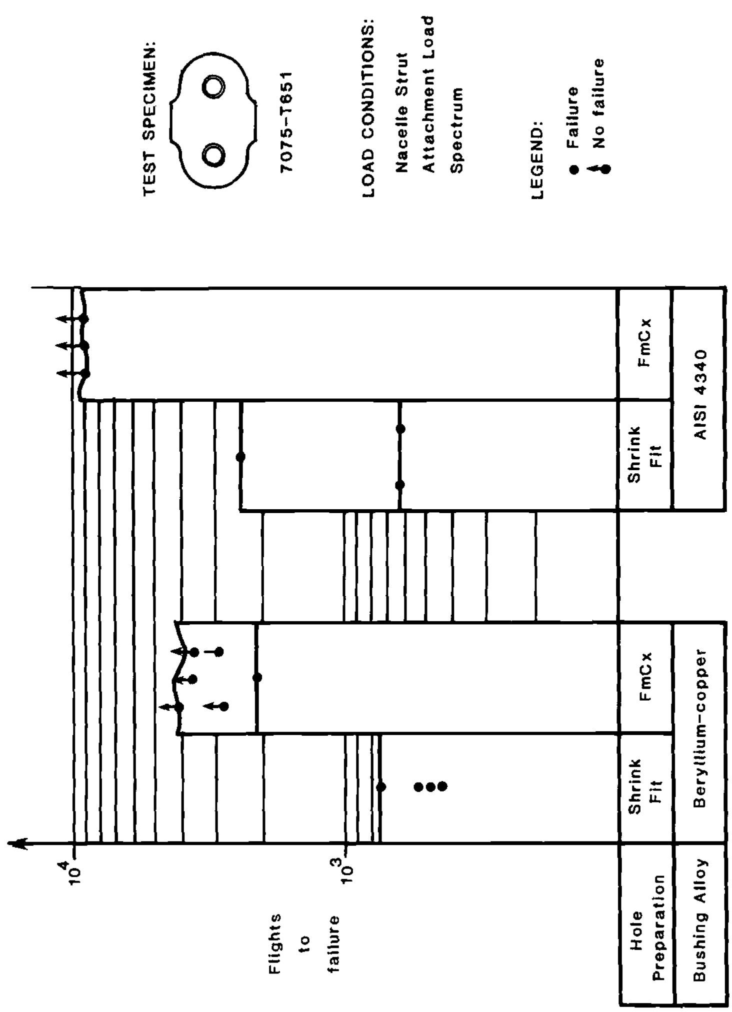

FIG. 7—*Test results: service life improvement.*

(*b*) bushing corrosion inhibiting coatings, and
(*c*) bushing wall thickness.

The use of other bushing alloys is currently being investigated.

Conclusions

1. A new process for simultaneous high interference bushing installation and cold expansion of holes has been demonstrated.

2. Constant-amplitude and spectrum-loaded cyclic testing shows minimum life improvement factors of 3:1 for specimens with bushings installed using the FM process—in comparison with specimens with bushings installed using SF techniques—for bushings made from beryllium-copper, aluminum-nickel-bronze, and 4340 steel alloys.

3. The FM process provides a bushing installation cost reduction when compared with the labor-intensive SF techniques.

References

[*1*] Dietrich, G. and Potter, J., "Stress Measurements on Cold-Worked Fastener Holes," *Advances in X-Ray Analysis*, Vol. 20, 1977.

[*2*] Cassatt, G. and Tenclay, M., "A Comparison of Residual Stresses Around Fastener Holes Produced by Three Different Methods of Mechanical Overstraining" *Proceedings*, Spring Meeting, Society for Experimental Stress Analysis, Honolulu, HI, 1982.

[*3*] Crews, J. H., "An Elastoplastic Analysis of a Uniaxially Loaded Sheet with an Interference Bolt," NASA TN D-7748, National Aeronautics and Space Administration, Washington, DC, October 1974.

[*4*] Crews, J. H., "Analytical and Experimental Investigation of Fatigue in a Sheet Specimen with an Interference-Fit Bolt," NASA TN D-7926, National Aeronautics and Space Administration, Washington, DC, July 1975.

[*5*] "Cold Expansion of Fastener and Other Holes Using the Split Sleeve System (Cx) and Countersink Cold Expansion Nosecap," Fatigue Technology, Inc., Engineering Process Specification No. FTI 8101B, Seattle, WA, 1 May 1984.

[*6*] Impellizzeri, L. F. and Rich, D. L., "Spectrum Fatigue Crack Growth in Lugs" *Fatigue Crack Growth Under Spectrum Loads, ASTM STP 595*, American Society for Testing and Materials, Philadelphia, 1976, pp. 320–336.

[*7*] Schijve, J., Jacobs, F. A., and Meulman, A. E., "Flight Simulation Fatigue Tests on Lugs with Holes Expanded According to the Split Sleeve Cold Work Method," NLR TR 78131U, National Aerospace Laboratory, The Netherlands, September 1978.

[*8*] "McDonnell Douglas DC-9 Spoiler Actuator Cold Expansion Evaluation," FTI Technical Note 2344-1A, Fatigue Technology, Inc., Seattle, WA, December 1982.

[*9*] Jongebreur, A. A. and de Koning, A. U., "Results of a Study of Residual Stresses and Fatigue Crack Growth in Lugs with Expanded Holes," presented at 12th International Committee on Aeronautical Fatigue Conference, Toulouse, France, May 1983.

[*10*] Crews, J. H., "Stresses in a Uniaxially Loaded Sheet Containing an Interference-Fit Bolt; An Elastic Analysis," NASA LWP-1055, National Aeronautics and Space Administration, Washington, DC, June 1972.

[*11*] Armen, H., Levy, A., and Eidenoff, H., "Elastic-Plastic Behavior of Coldworked Holes," AIAA Paper No. 83-0865-CP, presented at the 24th AAIA/ASME/ASCE/AHS Structures, Structural Dynamics and Materials Conference, Lake Tahoe, NV, May 1983.

[*12*] Schwarmann, L., "On Improving the Fatigue Strength of a Double-Shear Lap Joint," *International Journal of Fatigue*, Vol. 5, No. 2, April 1983.

[*13*] Derber, T., "Test Results: Verification of Fastener Hole Coldwork Benefits," Boeing Report No. D500-10199-1, The Boeing Military Airplane Co., Seattle, WA, September 1982.

Malcolm W. Ozelton[1] *and Timothy G. Coyle*[1]

Fatigue Life Improvement by Cold Working Fastener Holes in 7050 Aluminum

REFERENCE: Ozelton, M. W. and Coyle, T. G., "**Fatigue Life Improvement by Cold Working Fastener Holes in 7050 Aluminum,**" *Fatigue in Mechanically Fastened Composite and Metallic Joints, ASTM STP 927,* John M. Potter, Ed., American Society for Testing and Materials, Philadelphia, 1986, pp. 53–71.

ABSTRACT: The effect of cold working on the fatigue life of 7050-T7451 aluminum that contained fastener holes was investigated. The holes were cold worked using the split sleeve technique. The fatigue life improvement achieved by inserting interference fit fasteners in both cold worked and non-cold worked holes was also determined. Fatigue tests were conducted under constant amplitude loading conditions. Additional evaluations were conducted, including determinations of the effects of precracks emanating from the hole (introduced prior to cold working), specimen orientation, and the amount of material reamed from a hole following cold working. Fractographic and metallographic analyses were undertaken to determine typical crack initiation sites. Cold working of fastener holes in 7050-T7451 increased the fatigue life by a factor of up to five, depending upon the specific cold work and fatigue test parameters employed. The insertion of interference fit fasteners also significantly increased fatigue life. Contributions from interference fit fasteners and cold working of holes were synergistic. The introduction of a precrack prior to cold working the hole reduced fatigue life, though precracked material containing a cold worked hole exhibited a greater fatigue life than if the hole had not been cold worked. The optimum amount of material that should be reamed from a hole after split sleeve cold working to give the maximum fatigue life for given test parameters was determined.

KEY WORDS: 7050-T7451 aluminum, split sleeve cold working, fatigue life, interference fit fasteners, reaming, precracks, constant amplitude loading

Most aircraft assemblies are joined by inserting mechanical fasteners through holes. The fatigue life of a given material is reduced by the presence of a hole because of increased stress concentrations around its periphery. The hole drilling operation can introduce flaws which further aggravate the situation, and the resulting joint can have a significantly lower fatigue life than the parent material. One proven method to offset, at least partially, the fatigue life reduction is to introduce compressive stresses by cold working

[1] Engineering specialist and manufacturing technology specialist, respectively, Northrop Corp., Aircraft Division, Hawthorne, CA 90250.

the area around the hole [*1,2*]. These stresses counteract the applied tensile stress responsible for crack initiation and growth. Several techniques have been developed for introducing compressive stresses around a hole. Of the methods available, the split sleeve technique [*1*] is widely used in the aerospace industry and was used for the work described in this paper.

The material investigated during the program, 7050-T7451 aluminum, is a high strength alloy. It has a low quench sensitivity and is used for aircraft components that have thick sections, such as bulkheads. Alloy 7050 is a relatively new aluminum alloy for which little data exist on the effect of cold worked holes on fatigue life.

The objective of the program was to determine the influence of the following five parameters on the fatigue life of 7050-T7451:

(*a*) cold work expansion level,
(*b*) amount of post-cold work reaming,
(*c*) precracks before cold working,
(*d*) flaws introduced during split sleeve cold working, and
(*e*) interference fit fasteners.

Knowledge of the effect of different cold work expansion levels and post-cold work reaming amounts on fatigue life will enable the optimum split sleeve cold work parameters to be established for 7050-T7451 aluminum. Precracks were introduced in non-cold worked material to determine if the detrimental effect of the presence of a crack originating at a hole can be reduced by cold working the hole. Flaws can sometimes be introduced during split sleeve cold working where the hole intersects the specimen surface. A fractographic analysis was conducted to establish if these flaws influence the fatigue life. Finally, the fatigue life improvement due to interference fit fasteners was determined because this method is sometimes used to cold work holes in aircraft components that are not normally removed for inspection or service during the life of an aircraft.

All specimens were tested under constant amplitude loading. Fractography of selected specimens was undertaken to determine crack initiation and propagation characteristics. Except for those specimens specifically described as containing clearance or interference fit fasteners, tests were conducted with open-hole specimens.

Experimental Procedures

Test Specimen

The fatigue test specimen is illustrated in Fig. 1. Each specimen was initially prepared with a 3.18-mm-diameter pilot hole. The final target hole size, whether cold worked or non-cold worked, was 6.35 mm. All holes were enlarged from the 3.18 mm starting size to 5.54-mm diameter using a

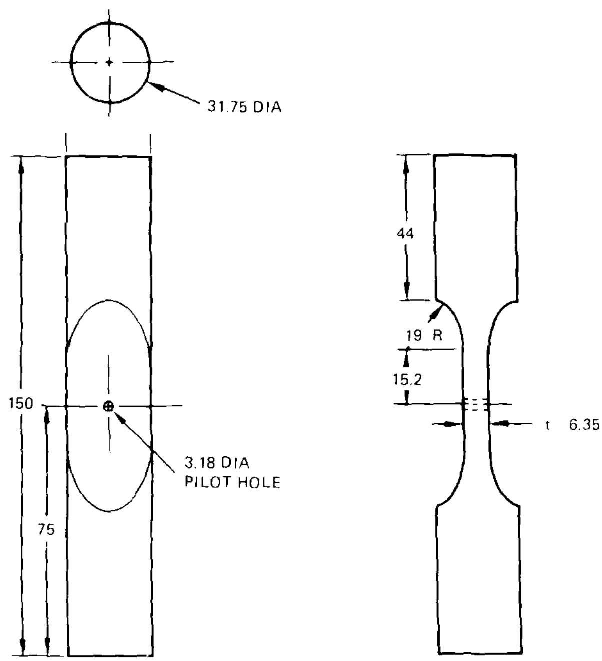

FIG. 1—*Fatigue specimen; dimensions are in mm.*

cobalt drill. Non-cold worked holes were reamed to 5.99-mm diameter and then to the final 6.35-mm diameter. Holes to be cold worked were enlarged to the pre-cold work diameter using cobalt reamers. A precision hole gage was used to measure hole diameters to the nearest 0.0025 mm. Drilling and reaming operations were conducted at 3000 rpm using Boelube lubricant, which was subsequently removed using methyl ethyl ketone (MEK).

Split Sleeve Cold Working

Several methods are available for introducing compressive stresses around the periphery of a hole. These include stress coining [*2*], shot peening, and split sleeve cold working [*1*]. The split sleeve method offers many advantages over other techniques, though other methods are used for some specific applications. The split sleeve method is schematically illustrated in Fig. 2. The amount of cold work is controlled by varying the mandrel diameter, sleeve thickness, and hole diameter. After cold working a hole, a small blemish or "pip" is formed, as is shown schematically in Fig. 3. The pip is due to the split in the sleeve. The area at the corner of the pip can be prone to the formation of small shear cracks as shown, particularly in alloys with low ductility. This region is usually reamed out following cold working so that many cracks are removed.

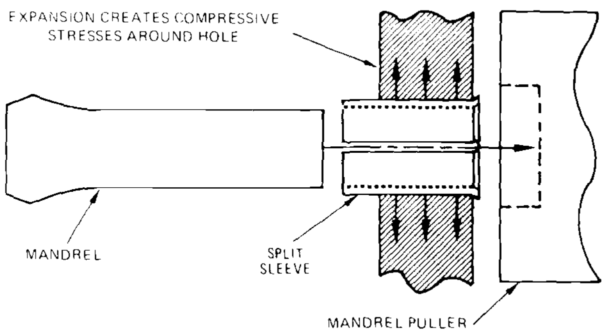

FIG. 2—*Split sleeve cold working method.*

The starting hole diameter for typical expansion levels is in the range of 5.97 to 6.04 mm for a 6.35-mm final hole diameter in aluminum. For this program, the target hole expansion for most of the work was 0.25 mm. The mandrel was 5.84-mm in diameter and the sleeve thickness was 0.20 mm. Thus, in order to achieve a 0.25-mm expansion, a starting hole of 5.99 mm was required. The following parameters describe the process:

Mandrel diameter:	5.84 mm
2 × sleeve thickness:	0.40 mm
Total tool diameter:	6.24 mm
Minus starting hole:	5.99 mm
Expansion:	0.25 mm

Cold expansion was achieved using a standard puller unit and hydraulic power pack, a 5.8-mm-diameter mandrel, and a prelubricated 0.20-mm-thick sleeve. Cold working was performed with one end of the specimen held in

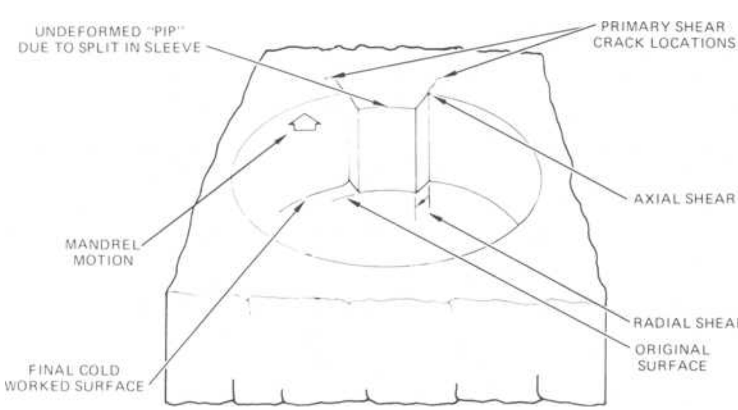

FIG. 3—*Hole configuration after split sleeve cold working.*

a vise. A dial gage was used to determine if specimen distortion occurred during the hole expansion operation, but none was observed. In most cases, the split in the sleeve was positioned at 90° to the direction of loading. For those specimens that were precracked, the split coincided with the crack. A limited number of tests were conducted with the pip in line with the applied load.

During the cold working process, the hole diameter increases by an amount equal to the cold work expansion, but then relaxes after the mandrel is withdrawn so that the "retained expansion" is less than the applied expansion. The retained expansion can vary according to the alloy being cold worked and the applied expansion. For a 0.25-mm hole expansion in 7050-T7451 aluminum, a typical retained expansion is 0.125 mm, that is, 50% of the initial hole expansion. Thus, for a total tool diameter of 6.24 mm and a 0.25-mm expansion, the cold worked hole diameter is 6.24 mm minus 0.125 mm, that is, 6.115 mm. To attain a final hole size of 6.35 mm, a further 0.235 mm was reamed from the hole diameter following cold working. The hole was then deburred by means of a hand-held tool with a 90° cutter.

Interference Fit Fasteners

Most tests were conducted using open-hole specimens. However, a limited amount of work was carried out to determine the effect of interference fit fasteners on fatigue life. The effect of split sleeve cold working the hole prior to fastener insertion was also determined. An interference level of 0.038 mm between the finished hole and fastener diameters was selected for determining the effect of interference fit fasteners on the fatigue life of 7050-T7451. Hi-Tigue titanium fasteners (HLT310) were used. For the holes that were cold worked, the following parameters were selected:

Mandrel diameter:	6.01 mm
2 × sleeve thickness:	0.40 mm
Total tool diameter:	6.41 mm
Minus starting hole diameter:	6.16 mm
Cold work expansion:	0.25 mm

The retained expansion was again 50%, and thus, the final hole size was 6.41 mm minus 0.125 mm, or 6.285 mm. The fasteners had a tolerance of 0.013 mm. To ensure that an installed fastener interference of 0.038 mm was achieved, fastener diameters were measured prior to installation.

For those interference fasteners installed after reaming a cold worked hole, the final hole was reamed to a diameter that was 0.038 mm smaller than that of the fastener in order to achieve the required interference.

Specimen Precracking Procedure

The fatigue life of specimens that had been precracked before cold working was determined. The following four-step procedure was followed to initiate and grow the cracks from a hole.

1. Both sides of the specimen gage length were polished using a buffing wheel so that the crack would be readily visible.
2. For crack initiation, a small groove was cut into the side of the 3.18-mm-diameter starting hole perpendicular to the loading direction. The groove was less than 1.59 mm deep to ensure that it would be totally removed when the hole was reamed to either its final size (non-cold worked) or to the diameter required for cold working. A jeweler's saw was used to cut the groove.
3. Cracks were grown using techniques covered by the ASTM Recommended Practice for Constant-Amplitude Low-Cycle Fatigue Testing (E 606-80) and the ASTM Test Method for Constant-Load-Amplitude Fatigue Crack Growth Rates Above 10^{-8} m/Cycle (E 647-83). The cracks were grown from the 3.18-mm pilot hole, which would later be enlarged to 6.35 mm. Therefore, the cracks were grown 1.59 mm longer than the required length from the final 6.35-mm hole.
4. All cracks emerged at both front and back surfaces of the gage section. Crack length data quoted in this paper are the average of the lengths measured on the two surfaces. Crack length was measured using a traveling microscope, accurate to 0.025 mm.

Fatigue Testing Procedures

Fatigue testing (constant amplitude) was conducted in laboratory air on a servohydraulic unit with digital-based electronic controls. Net stress values are quoted throughout this paper, that is, the hole diameter is subtracted from the gage section width to determine the required loads. All testing of the 7050-T7451 was conducted at a net maximum stress of 207 MPa and at a frequency of 10 Hz. A stress ratio of $R = 0.1$ was used, and a minimum of three and a maximum of five specimens were tested for each test condition. These parameters were selected as being typical of those used for testing aluminum aerospace structural alloys.

Material

The data described in this paper were obtained using 7050-T7451 aluminum procured in the form of 152-mm and 70 mm-thick plates. Plates of both thicknesses had similar properties and are typical for 7050-T7451. The property data are shown in Table 1.

TABLE 1—*Properties of 7050-T7451 aluminum plate.*

Specimen Orientation	Ultimate Tensile Strength, MPa (ksi)	Yield Strength, MPa (ksi)	Elongation, %	K_{Ic}, MPa $\sqrt{m}$ (ksi $\sqrt{in.}$)
		70-mm PLATE		
Longitudinal	545 (79)	483 (70)	10	. . .
Long transverse	545 (79)	476 (69)	9	. . .
Short transverse	497 (72)	435 (63)	5	. . .
		152-mm PLATE		
Longitudinal	531 (77)	476 (69)	11	L-T 32 (29)
Long transverse	538 (78)	496 (68)	10	T-L 29 (26)
Short transverse	510 (74)	434 (63)	6	S-T 25 (23)

Results and Discussion

Effect of Hole Expansion Level on Fatigue Life

The influence of cold work expansion level on the fatigue life of 7050-T7451 aluminum was determined using the 152-mm plate and is shown in Fig. 4 for the long transverse (T-S), longitudinal (L-S), and short transverse (S-T) specimen orientations [defined in the ASTM Test for Plane-Strain Fracture Toughness of Metallic Materials (E 399-83)]. Expansion levels in the range zero (non-cold worked) to 0.35 mm were investigated. The majority of the effort was on the T-S orientation because 7050-T7451 aluminum can have low ductility (2% minimum) in the short transverse direction. Each data point on the curves in Fig. 4 represents the average of five specimens.

For the T-S orientation, the fatigue life for 0.10-mm expansion was essentially the same as that for non-cold worked material. No improvement in the fatigue life of cold worked specimens compared with non-cold worked material was observed until an expansion of at least 0.20 mm was used. A further increase in fatigue life was noted for a cold work expansion of 0.28 mm. At an expansion of 0.35 mm it became difficult to insert the tool in the hole. No improvement in fatigue life in comparison with specimens containing holes with a 0.28-mm expansion was obtained.

The results of this investigation indicate that, for the T-S orientation, a hole expansion level below about 0.10 mm was insufficient to induce compression stress levels around the hole that are able to retard crack initiation and growth in comparison with non-cold worked material. Above 0.28-mm expansion, no further increase in fatigue life was observed.

The fatigue life for S-T orientation specimens was less than that for L-S and T-S orientations, as indicated by the data for non-cold worked speci-

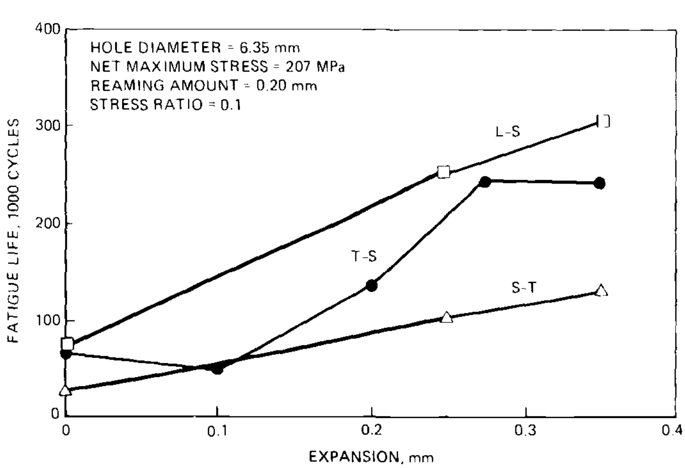

FIG. 4—*Cold work expansion versus fatigue life of 7050-T7451 aluminum.*

mens and for specimens that had been cold worked to expansion levels of 0.28 mm and 0.35 mm (Fig. 4). Therefore, it can be concluded that resistance to crack initiation and growth in the long transverse direction (under short transverse loading) is less than that in the short transverse direction in 7050-T7451 aluminum.

Effect of Post-Cold-Work Reaming on Fatigue Life

The effect of the amount of post-cold-work reaming on the fatigue life of 7050-T7451 aluminum was determined using specimens excised from the 152-mm plate and is shown in Fig. 5. All specimens were tested in the T-S orientation.

For specimens cold expanded by 0.28 mm and followed by a 0.20-mm ream, a life improvement factor (LIF) of 3.1 was obtained. The LIF is defined as the ratio of the fatigue life of cold worked to non-cold worked material. Additional reaming up to 0.50 mm improved the LIF to 5.1. This implies that the 0.20-mm ream is not sufficient to remove cold worked hole surface discontinuities completely, which can reduce fatigue life. Further reaming up to 1.00-mm diameter still resulted in a high LIF value (4.7). A post-cold-work ream of 2.00 mm resulted in a LIF of only 2.6. Therefore, a post-cold-work ream of up to 1.0 mm for 6.35-mm-diameter holes with a 0.28-mm expansion does not significantly reduce the fatigue life. Reaming is beneficial because hole surface discontinuities, introduced during cold working, are removed. However, a post-cold-work ream of 2.0 mm removes a large portion of the material that contains the beneficial residual compressive stresses created by the cold working and results in a lower LIF (2.6).

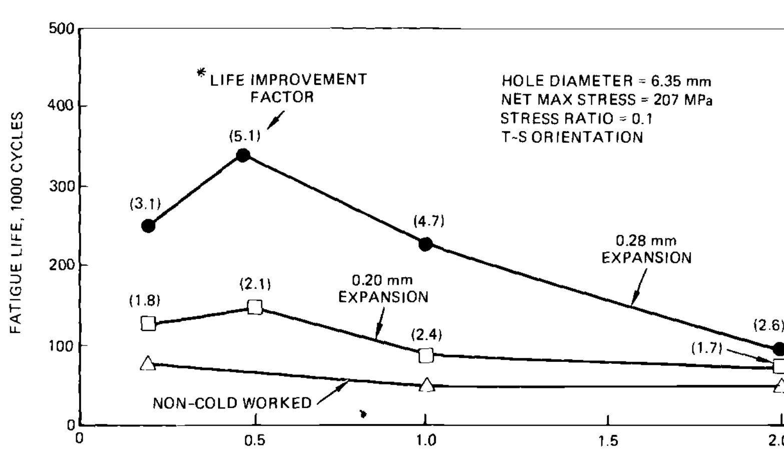

FIG. 5—*Effect of post-cold-work reaming on the fatigue life of 7050-T7451 aluminum. Note: a typical ream following production split sleeve cold working is 0.15–0.25 mm. The asterisk indicates the ratio of the fatigue life of cold worked to non-cold worked material.*

The trend for the 0.20-mm expansion was similar to that for 0.28 mm, although the fatigue life sensitivity to the amount of reaming was reduced and the peak for the 0.50-mm ream was less pronounced (Fig. 5).

In summary, the results indicate that, for both the 0.20-mm and 0.28-mm hole expansion levels, the fatigue life is greatest for a post-cold-work ream of about 0.50 mm. The optimum reaming amount probably represents a balance between removing cold worked material containing beneficial residual stresses and removing potential crack initiation sites. For example, the fatigue life for specimens with 0.20-mm and 0.28-mm expansion levels following a post-cold-work ream of 2.0 mm was similar to that for non-cold worked material.

Crack Initiation Sites

Using both optical and scanning electron microscopy (SEM) techniques, it was established that, as expected, crack initiation usually occurred at the corner where a hole emerges at the surface of a specimen. SEM fractographs showing a typical initiation site in a cold worked specimen are illustrated in Fig. 6. Crack initiation occurred at a burr that remained after the hole was deburred (evident by the chamfer around the hole). The crack initiation site depicted was typical for 7050-T7451 aluminum specimens that contained cold worked or non-cold worked holes.

Effect of Precrack on Fatigue Life of 7050-T7451

All specimens that were precracked were excised from 70-mm plate and were tested in the T-S orientation. The split sleeve pip was aligned at 90° to the applied load and coincided with the precrack. Specimens that contained precracks of nominal lengths, 0.50, 1.25, 2.0, and 3.0 mm, were tested at a net maximum stress of 207 MPa in both cold worked and non-cold worked conditions. The cracks in cold worked specimens were introduced prior to split sleeve cold working. Fatigue life results are plotted as a function of crack length in Fig. 7. The retained expansion averaged 0.13 mm, which is 2.2% of the average starting hole diameter (5.99 mm) or about 50% of the applied expansion (0.25 mm). A post-cold-working ream of 0.25 mm was used for each specimen to achieve the required 6.35-mm hole diameter.

Because all cracks were grown before the hole was cold worked, an investigation was carried out to determine if additional crack growth occurred during cold working, but none was apparent. The following trends are indicated:

1. Cold working of specimens that contained cracks increased the fatigue life.
2. The LIF for a specimen that contained a crack of a given length

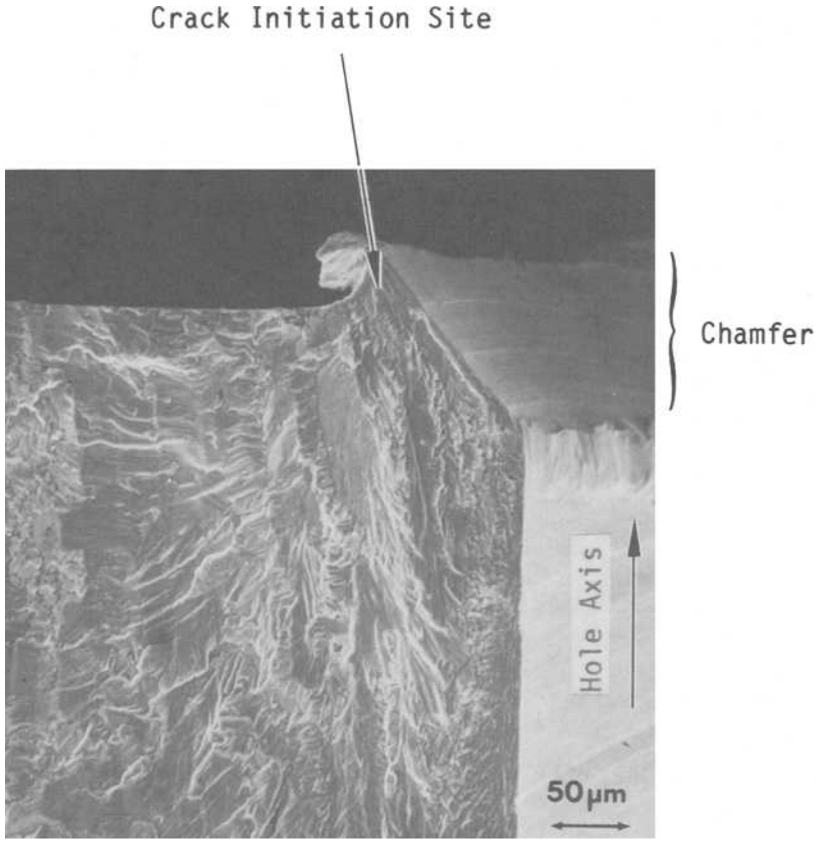

FIG. 6—*Typical fatigue crack initiation site at a cold worked hole in 7050-T7451 aluminum.*

increased significantly with decreasing crack length (from 1.6 to 8.6 as the crack decreased from 3.0 to 0.50 mm).

3. Cold worked material that contained a crack shorter than 0.50 mm had a greater fatigue life than non-cold worked, uncracked material.

It is clear from these results that the presence of a crack reduced the fatigue life of both cold worked and non-cold worked 7050-T7451 specimens. However, for a crack of a given length, specimens that contained a cold worked hole had a greater fatigue life than those containing non-cold worked holes.

If, during inspection of an aircraft, a crack is observed emanating from a hole, remedial action may be taken. One option is to ream the hole to remove cracked material and install an oversize fastener. The data from the program described herein suggest that, if the crack emanates from a non-cold worked hole and is less than 0.50 mm long, the hole could be cold

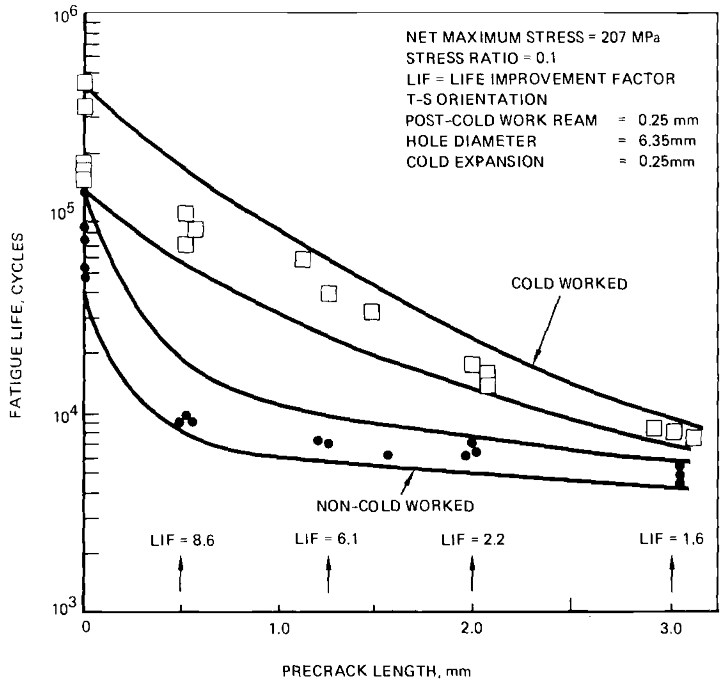

FIG. 7—*Effect of precrack length on fatigue life of 7050-T7451 aluminum.*

worked and the fatigue life improved to the level of uncracked, non-cold worked material, or better. The option of reaming the hole to remove the crack still remains, but there are potential concerns. For example, to remove a 0.50-mm crack, the diameter of a 6.35-mm hole will need to be increased to at least 7.35 mm. In fact, at least a 7.92-mm hole is required to be compatible with available fasteners. In some cases, for example, an aircraft skin fastened to a narrow component such as a spar, enlarging a hole could cause an unacceptable reduction in edge margin. Under these circumstances, it would be more beneficial to cold work the 6.35-mm hole and enlarge it by 0.40 mm to accept the next standard oversize fastener. Hence, a potential problem could be solved at a minimum cost.

The key issue is whether or not a crack 0.5 mm or less in length can be detected. Under laboratory conditions, detection of such a crack is feasible, particularly if the hole does not contain a fastener. However, under field conditions, detection may not be possible for cracks less than about 0.75 mm in length, even without a fastener. The presence of a fastener increases the minimum detectable crack length to about 2.5 mm. Thus, the potential use of the split sleeve method to improve the fatigue life of a non-cold worked hole from which a crack originates is limited by the sensitivity of the nondestructive inspection methods used for crack detection.

Interference Fit Fasteners

To determine the fatigue life improvement of 7050-T7451 aluminum due to an interference fit fastener and the effect of post-cold-work reaming prior to fastener installation, the following types of specimens were tested:

1. Cold worked, with a post-cold-work ream and a clearance fit fastener.
2. Cold worked, with a post-cold-work ream and a 0.038-mm interference fit fastener.
3. Cold worked, without a post-cold-work ream, but with a 0.038-mm interference fit fastener.
4. No cold work, but with a 0.038-mm interference fit fastener.

All specimens were excised from the 70-mm plate. The cold work expansion was 0.25 mm in each case. Five specimens were tested at a net maximum stress of 207 MPa for each of the four combinations of process conditions listed above. Results are shown in Table 2.

Data for the two sets of tests for cold worked specimens with interference fit fasteners showed a large amount of scatter. Two of the specimens that were reamed after split sleeve cold working failed in the grips. One of the cold worked specimens that had not been reamed was tested to 10 million cycles without failure, after which the test was terminated. Both the specimens that failed in the grips had long fatigue lives, and fretting was observed at the intersection of the edge of the grips and the specimen. However, the average fatigue life for cold worked specimens that contained interference fit fasteners was considerably higher than that for those containing clearance fit fasteners.

Crack initiation sites are shown in Fig. 8. Typical sites are (*a*) the corner where the hole intersects the surface of the specimen and (*b*) scratches in the bore of the hole caused during insertion of the fastener.

TABLE 2—*Effect of interference fit fasteners on the fatigue life of 7050-T7451 aluminum.*[a]

Fastener Installation	Fatigue life, cycles
Cold worked—clearance fit	167 000
Cold worked—interference fit (ream)	>574 000[b]
Cold worked—interference fit (no ream)	$>1.4 \times 10^{6}$[c]
No cold work—interference fit	370 000

[a]Net maximum stress = 207 MPa; stress ratio = 0.1; fastener interference = 0.038 mm; T-S orientation, fastener = HLT310 (Titanium Hi-Tigue).

[b]Two specimens broke in the grip area.

[c]One specimen did not fail after 10^7 cycles.

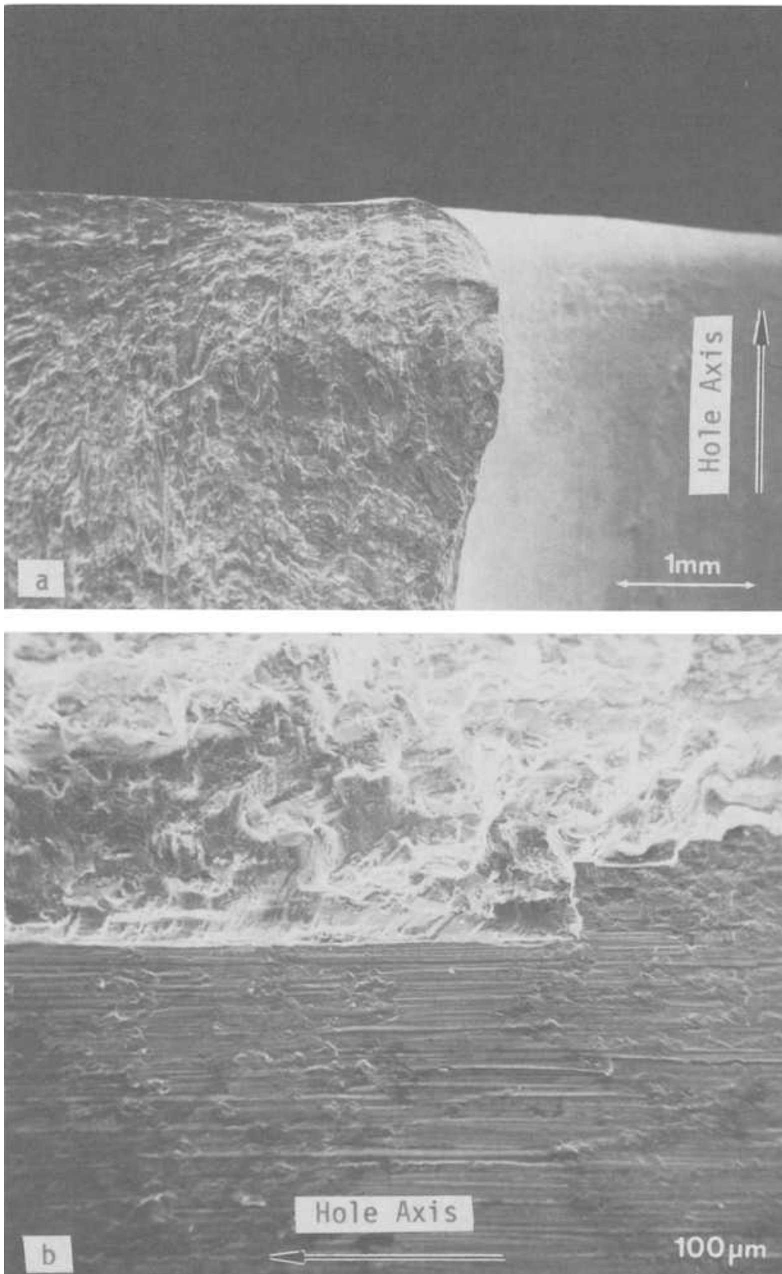

FIG. 8—*Fatigue crack initiation sites in a 7050-T7451 aluminum specimen that contained an interference fit fastener:* (a) *Intersection of the hole and specimen surface;* (b) *scratches caused by insertion of fastener.*

The average fatigue life for non-cold worked specimens containing 0.038-mm interference fit fasteners was 370 000 cycles, that is, a factor of 2.2 larger than that for clearance fit fastener specimens which had been split sleeve cold worked.

Flaws Due to Split Sleeve Cold Working

As the mandrel is pulled through the split sleeve, shear cracks can occur at the base of the pip, as shown in Fig. 3. A detailed analysis to determine the number and size of these flaws was undertaken using specimens taken from the 152-mm plate. The flaw analysis for specimens prior to fatigue testing is summarized in Table 3, according to specimen orientation, hole expansion level, and pip location with respect to the fatigue loading direction. The numbers of cracks 0.25, 0.50, and 0.75 mm in length are shown.

The normal split sleeve expansion range is from 0.20 to 0.30 mm. For the 100 specimens that were cold worked within this expansion range, 22 specimens were observed to have flaws after split sleeve cold working and reaming (22% percent of the total). Of these 22 specimens, three had cracks 0.75 mm long, eight had cracks 0.50 mm long, and eleven had cracks only 0.25 mm long. The deburring process removed approximately 0.25 mm of material around the hole. Hence, the 0.25-mm-long cracks created during cold working were removed. The remaining eleven specimens had cracks that were only 0.25 mm and 0.50 mm long after deburring.

For a 0.35-mm expansion level, 19 out of 40 specimens (or 48%) had cold work defects ranging up to 1.52 mm long. However, only one crack was 1.52 mm long, while all others were 0.75 mm or less in length. For split sleeve cold worked holes that received a low expansion level (0.10 mm), no cold work defects were observed; however, the fatigue life improvement due to cold working was zero.

Fracture analysis of 120 specimens was conducted to determine if the flaws introduced during cold working influenced fatigue crack initiation and growth. Although there were often multiple flaws due to cold working, almost all the fatigue cracks initiated at the mandrel *entrance* side of the hole. However, all the pip defects were observed at the mandrel *exit* side of the hole. Therefore, it was concluded that the pip flaws had little or no influence on the fatigue life of the specimens.

The pip flaws are caused by the discontinuous shear stresses applied to the wall of the hole by the sleeve. The mandrel causes the sleeve to be pulled toward the puller unit; consequently, the sleeve tends to pull the wall of the hole in the same direction. This phenomenon is uniform around the periphery of the hole, except at the split in the sleeve where there are no shear stresses applied to the hole. The shear discontinuity occurs at this juncture on the exit side of the hole, as shown in Fig. 3. The residual compressive stress created at the exit of the hole by split sleeve cold working

TABLE 3—*Defects in split sleeve cold worked 7050-T7451 aluminum.*

Specimen Orientation	Split Sleeve Interference, mm	Orientation of Pip, deg[a]	Number of Specimens	Number of Cracked Specimens	Number of Specimens with Crack Lengths 0.25 mm	0.50 mm	0.75 mm	Number of Cracked Specimens, % of total
Long	0.35	90	15	13[b]	7	2	3	87
transverse		in line	5	0				0
(T-S)	0.28	90	20	9	4	3	2	45
		in line	5	4	3	1	0	80
	0.25	90	10	1	0	1	0	10
	0.20	90	20	5	1	3	1	25
		in line	5	2	2	0	0	40
	0.10	90	20	0	0	0	0	0
		in line	5	0	0	0	0	0
Longitudinal	0.35	90	10	2	0	2	0	20
(L-S)	0.25	90	10	1	1	0	0	10
Short	0.35	90	10	4	0	4	0	40
transverse	0.25	90	20	0	0	0	0	0
(S-T)								

[a]Relative to load axis.
[b]One specimen had a crack 1.52-mm long.

probably retards fatigue crack initiation and growth at these flaws. It is not clear why failure initiated at the entrance of the hole where no flaws were detected. However, it may be possible that the residual compressive stresses were reduced in this area.

Conclusions

The main conclusions from the program on split sleeve cold working of holes in 7050-T7451 aluminum plate are as follows:

1. For a given hole expansion, the maximum fatigue life for 7050-T7451 aluminum containing 6.35-mm-diameter holes is obtained for a post-cold-work ream of about 0.50 mm.
2. The optimum expansion for a 6.35-mm-diameter hole is 0.28 mm. Although greater fatigue life might be possible at values above 0.28 mm, difficulties in inserting the tool into the hole can be encountered, making application of higher cold expansion impractical.
3. The flaws introduced during split sleeve cold working do not significantly influence fatigue life.
4. For material that contains a precrack less than 3 mm in length emanating from a hole, the fatigue life can be increased by cold working the hole.
5. Interference fit fasteners provide a greater fatigue life improvement than split sleeve cold working.
6. Fatigue life improvements due to cold working and to interference fit fasteners are synergistic.

Acknowledgments

The authors wish to recognize the support provided by the Naval Air Systems Command, which funded part of the work discussed in this paper under Contract N00019-82-0364. J. S. Bruce and G. Weaver were the project engineers. The support provided by A. P. Wijenayake and J. Boldt of the Northrop Corp. Manufacturing Technology Department is also recognized.

References

[1] Phillips, J. C., "Sleeve Cold Working Fastener Holes," Technical Report AFML-TR-74-10, Vol. 1, Air Force Materials Laboratory, Wright-Patterson Air Force Base, OH, February 1974.

[2] Speakman, E. R., "Fatigue Life Improvement Through Stress Coining Methods," *Achievement of High Fatigue Resistance in Metals and Alloys, ASTM STP 467,* American Society for Testing and Materials, Philadelphia 1970, pp. 209–237.

STP927-EB/Nov. 1986

DISCUSSION

A. Alpas[1] *and C. N. Reid*[1] (*written discussion*)—Examination of the surface of a hole cold expanded by the split sleeve process shows the presence of a step put in by the outer end of the spiral sleeve. The effect of the angular position of this step on the fatigue life of a cold expanded 6000 series aluminum alloy (British designation HE9) has been investigated, and the results obtained support the conclusions reported by the authors of this paper. Specimens containing a hole of 5-mm diameter drilled in their reduced gage section (100 by 19 by 1.67 mm) were solution treated at 520°C for 40 min, quenched, and then aged for 22 h at 170°C prior to cold expansion. During the cold expansion the position of the step was controlled and two orientations were used: (1) specimens with the angular position of the step coinciding with the longitudinal axis (designated the "12 o'clock" position) and (2) specimens with the angular position of the step in the transverse direction (the "3 o'clock" position). The amount of expansion was kept between 3 and 3.5%. Fatigue tests were conducted under a constant stress amplitude σ_a = 48 MPa and a stress ratio R = 0.05.

The fatigue lives of the specimens cold expanded at each of the step positions are summarized in Table 4. The table also includes the mean life of specimens subjected to an annealing treatment (170°C, 2 h) after the cold expansion. This was chosen to cause significant stress relief without overaging. Statistical analysis using the "Students's t test" showed that there is no significant difference between the mean lives of the two orientations of cold-worked specimens (t = 0.68). Similarly, there is no significant difference between the two orientations of stress-relieved test specimens, either (t = 0.65).

We conclude that the step constitutes an insignificant notch in the test piece. This is supported by the observation that in some of the CX3 and CXSR3 specimens, the fatigue crack did not even intersect the step. Furthermore, the first fatigue crack showed no preference for forming on the "stepped" side of the hole rather than on the opposite side—this happened in two out of five of the CX3 specimens and in three out of five of the CXSR3 test pieces. Fatigue cracks invariably nucleated at the intersection between the hole and one surface of the flat test piece.

M. W. Ozelton and T. G. Coyle (*authors' closure*)—The authors appreciate the comments of A. Alpas and C. N. Reid supporting our observations regarding the influence of the position of the pip on the fatigue life of split sleeved cold worked aluminum alloys. Though not specifically stated in our

[1] Faculty of Technology, The Open University, Milton Keynes, England MK 7 6AA.

TABLE 4—*Mean cycles to failure (5 tests in each case). The mean life of unworked holes under these conditions is 1.82 × 10^5 cycles.*

	3 o'Clock	12 o'Clock
Cold expanded (CX)	6.72 × 10^5	5.37 × 10^5
CX and stress-relieved (CXSR)	2.34 × 10^5	3.00 × 10^5

paper, it was also observed that failure frequently initiated on the side of the hole opposite to that at which the pip was located.

We were interested in the data shown in Table 4 that indicate that a significant fatigue life reduction results from stress relief due to elevated temperature exposure. This emphasizes the need to determine the effect of typical aircraft service temperatures on the fatigue life improvement due to cold working of holes. As aircraft performance requirements continue to increase, so do the temperatures, and the need for data of this type becomes significant.

Pedro Albrecht[1] *and Adnan H. Sahli*[2]

Fatigue Strength of Bolted and Adhesive Bonded Structural Steel Joints

REFERENCE: Albrecht, P. and Sahli, A. H., **"Fatigue Strength of Bolted and Adhesive Bonded Structural Steel Joints,"** *Fatigue in Mechanically Fastened Composite and Metallic Joints, ASTM STP 927,* John M. Potter, Ed., American Society for Testing and Materials, Philadelphia, 1986, pp. 72–94.

ABSTRACT: This study examines the feasibility of adhesive bonding and bolting tension splices, beam splices, and cover plates. The results show that bonding the contact surfaces significantly increased the fatigue life of high-strength bolted splices. Bonding cover plates to the tension flange of the beam increased the fatigue life by a factor of 20 as compared to that of conventionally welded cover plates. Replacing welds with adhesives and bolts virtually fatigue-proofs structural steel details subjected to highway bridge loading.

KEY WORDS: fatigue tests, steel, adhesives, bolts, splices, cover plates

The results of a recently completed study showed that attaching a cover plate to the tension flange of a steel beam with longitudinal welds along the central region, and with friction-type high-strength bolted connections at the nonwelded ends, increased the fatigue life by a factor of 21 over that of conventionally end-welded cover plates [*1,8*]. Accordingly, end-bolted cover plates have Category B fatigue strength, whereas end-welded cover plates have Category E strength [*7*]. The large increase in life is possible because friction-type bolted connections transfer force from one plate to another with much less stress concentration than would occur in rigid welded connections.

Similarly, one would expect an increase in the fatigue strength of structural details when adhesives help to distribute and transfer the load over a larger area, thus reducing the stress concentration. Two main applications come to mind. One deals with bolted joints, such as splices of tension and flexural members, and consists of reinforcing the joint by adhesive bonding the contact surfaces. In doing so, the force is transmitted by friction between

[1] Professor, Department of Civil Engineering, University of Maryland, College Park, MD 20742.
[2] Structural engineer, Dewberry & Davis Engineers, Fairfax, VA 22031.

the plates over the full contact surface, rather than either by friction in the regions surrounding the bolts (friction-type connection) or by bearing of the bolt shank against the plates (bearing-type connection). This could increase both the fatigue and static strength of the joints.

The second main application deals with the fatigue strength of attachments that currently are welded. The severity of the stress concentration and, hence, the fatigue strength depend on the length of the attachment. For example, the mean fatigue life of a Category B welded plate girder without attachments drops by a factor of 2.5 for Category C 50-mm-long (2-in.) attachments, by a factor of 7 for Category D 100-mm-long (4-in.) attachments, and by a factor of 16 for Category E 200-mm (8-in.) and longer attachments. Since end-bolting cover plates raised the fatigue strength from Category E to Category B, one can expect similar improvements when attachments are adhesive bonded.

The purpose of this study was to explore the feasibility of using adhesives, in combination with bolts, to (1) increase the fatigue strength of steel bridge members; (2) reduce the connection size without lowering the fatigue strength; and (3) eliminate welded details with low fatigue strength.

Experimental Procedure

The fatigue strength of adhesive bonded structural details for highway bridges was examined by testing Series A tension splices, Series B beam splices, and Series B beam cover plates.

Test Specimens

The Series A tension specimens, shown in Fig. 1, consisted of two main plates 64 by 16 mm (2½ by ⅝ in.) in cross section that were spliced with two plates 64 by 8 mm (2½ by 5⁄16 in.) in cross section. The splices had either one or two 16-mm-diameter (⅝-in.) A325 high-strength bolts in double shear on each side of the centerline of symmetry.

The Series B beam specimens, shown in Fig. 2, consisted of rolled beams of W 14x30 shape, 356 mm (14 in.) deep, weighing 438 N/m (30 lb/ft), which were tested on a 4574-mm (15-ft) span. The flanges were spliced at midspan with one plate 171 by 13 mm (6¾ by ½ in.) in cross section and either four or six 19-mm-diameter (¾-in.) A325 bolts in single shear on each side of the centerline. All webs were spliced with two 146 by 5 by 152-mm (5¼ by 3⁄16 by 6-in.) plates and two bolts. The splice was located between the two load points, in the region of constant bending moment. The redundant and undersized web splice was provided for ease of aligning the two beam halves and bonding and bolting the flanges. Accordingly, the flange splices carried the moment, while the web splice carried no shear. Except

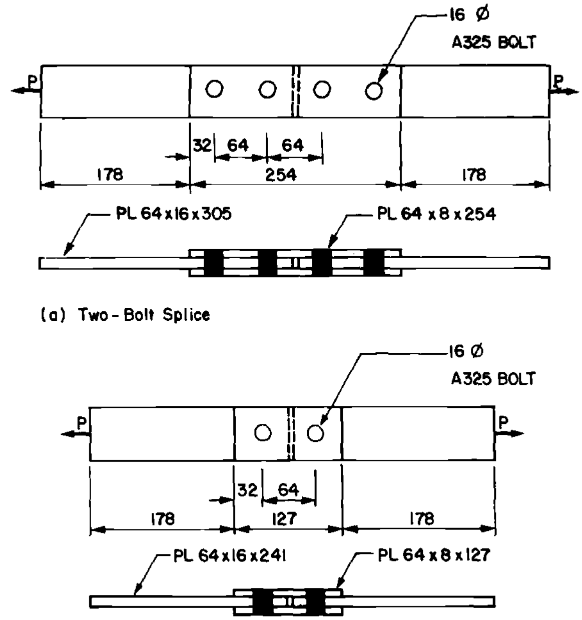

(b) One-Bolt Splice

FIG. 1—*Series A tension splices.*

for the control specimens, the contact surfaces of the Series A and B bolted splices were coated with adhesive prior to bolting.

In addition to the splice detail, the Series B beams had two 171 by 13 by 1143-mm-long (6¾ by ½ by 45-in.) cover plates bonded to the tension flange. The cover plate ends facing the midspan were clamped to the flange with two 19-mm-diameter (¾-in.) A325 bolts.

Bolts-to-Member Strength Ratio

The two-bolt tension specimens and the six-bolt beam specimens were designed on the basis of minimum tensile requirements so that the bolts and the member would fail at about the same calculated ultimate load. The number of bolts in the other specimens was reduced to determine experimentally the degree to which adhesive can replace bolts without lowering the fatigue strength (present study) and static strength [2] of the member.

The American Association of State Highway and Transportation Officials (AASHTO) [7] allowable bolts-to-member strength ratio allows one to compare the relative joint strength of the test specimens with that of bridge members. This ratio is, for the tension specimens:

$$\frac{P_b}{P_m} = \frac{mnF_vA_b}{F_tA} \tag{1}$$

where

P_b = allowable load carried by bolts,
P_m = allowable load carried by the tension specimen,
m = number of shearing planes,
n = number of bolts,
F_v = allowable bolt shear stress,
A_b = bolt gross area,
F_t = allowable plate tension stress, and
A = member cross-sectional area.

The calculated values were P_b/P_m = 0.72 and 0.36, respectively, for the tension specimens with two-bolt and one-bolt splices.

The AASHTO allowable bolts-to-member strength ratio for the beam specimens is

$$\frac{M_b}{M_m} = \frac{mnF_vA_bd}{S_nF_b} \tag{2}$$

where

M_b = allowable moment carried by bolts,
M_m = allowable moment carried by beam,
d = beam depth,
S_n = net section modulus, and
F_b = allowable bending stress.

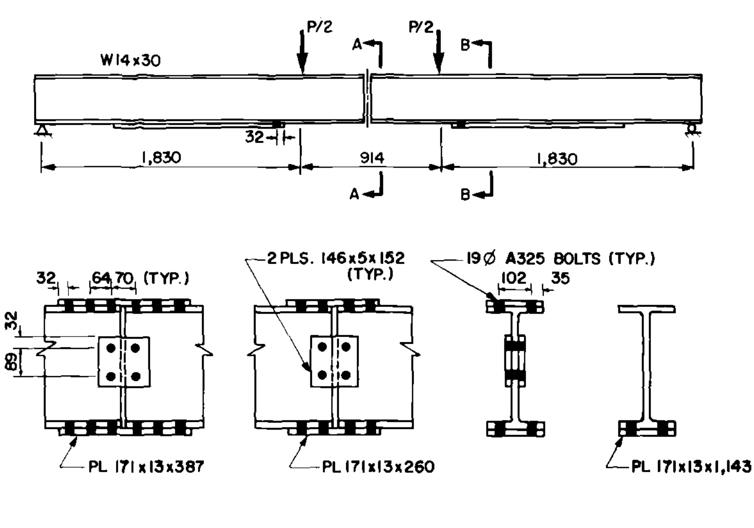

FIG. 2—*Series B beams with splice and cover plates.*

The values were $M_b/M_m = 0.87$ and 0.58, respectively, for the beams with six-bolt and four-bolt splices.

Because the AASHTO specifications require that a splice shall be designed for at least 75% of the member's strength, and assuming that the bolts are not overdesigned, the bolts-to-member strength ratio of bridge member splices falls in the range $0.75 \leq (P_b/P_m)$ or $(M_b/M_m) \leq 1.0$.

Material Properties

The steel for the plates and beams conformed to the requirements of the ASTM Specification for High-Strength Low-Alloy Steel with 345 MPa (50 ksi) Minimum Yield Point to 100 mm (4 in.) Thick (A588-82). The minimum tensile requirements for this steel are 345 MPa (50 ksi) yield point, 485 MPa (70 ksi) tensile strength, and 21% elongation.

The bolts conformed to the requirements of the ASTM Specification for High-Strength Bolts for Structural Steel Joints (A325-82). The minimum tensile requirements are 635 MPa (92 ksi) yield strength and 825 MPa (120 ksi) tensile strength for bolts up to 25 mm (1 in.) in diameter.

The specimens were bonded with Versilok 204, an acrylic structural adhesive for bonding metals, composites, and engineering thermoplastics. The adhesive consisted of two parts, a modified acrylic and accelerator No. 4. The adhesive begins to cure on contact with the accelerator. The bond becomes handleable after 8 to 16 min of curing at 24°C (75°F) and develops full strength after 24 h.

The mean shear strength of the adhesive, measured in the laboratory with 13 double-strap specimens under monotonically increasing load, was 27.3 MPa (3.96 ksi) with 2.2-MPa (0.32 ksi) standard deviation.

The Versilok 204 adhesive had been recommended in Ref *5* for its good shear and tension strengths under rapid loading, rapid cure at room temperature, and minimal requirements for surface preparation. In a recent study, structural adhesives were found that have much better creep strength in adverse environments than Versilok 204 [*10*].

Fabrication

All the specimens were fabricated by a structural steel fabricator to standards typical of bridge construction, shot-blasted to a near-white condition, and assembled for shipment with the bolts hand-tightened. The specimens were reassembled in the laboratory.

The nonbonded splices were bolted in the as-received condition. The bonded splices and cover plates were prepared as follows.

1. Both contact surfaces were wiped clean.
2. Accelerator No. 4 was applied on both contact surfaces.

3. After the accelerator had dried, the adhesive was applied on one of the two contact surfaces.
4. Glass beads 0.25 mm (0.010 in.) in diameter were sprinkled with a salt shaker on the contact surfaces to help control the bond line thickness away from the bolts.
5. The parts were brought together.
6. The bolts were installed and tensioned with a calibrated wrench to 70% of the minimum specified tensile strength.
7. Specimens were cured in the laboratory environment at least twice as long as the 24 h recommended by the supplier.

The tension specimens were assembled in a jig. The beam specimens were kept aligned by the bolted web splice.

Testing Procedure

The applied cyclic load was sinusoidal and of constant amplitude. It was applied at a rate of 4 to 10 Hz in the tension tests and 3 to 4 Hz in the beam tests, depending on the stress range. The Series A tension specimens were stress-cycled until the fatigue crack severed the specimen into two parts.

Each Series B beam had several details. When a fatigue crack caused one detail to fail, the beam was temporarily repaired with splice plates and high-strength C-clamps, and the test was then continued. In this manner, up to four data points were obtained per beam, one for each splice half and one for each cover plate end closest to the midspan. To enhance the likelihood of arresting a crack with a temporary repair splice, a beam detail was said to have failed when a bolt hole crack had emerged from under the nut or bolt head or when a fretting crack had grown through the thickness of the flange or splice plate and then to a surface length of about 50 mm (2 in.). Previous experience with testing bolted beam specimens had shown that the fatigue life so determined was at least 98% of the number of cycles to failure of the beam [*6,8*]. Testing of some details was discontinued when the crack extension at a previously failed detail could no longer be controlled or when a large number of load cycles produced no visible cracking.

Fatigue Strength of Tension Specimens

Experiment Design

Thirty-nine Series A tension specimens were fatigue tested in the three-way partial factorial, shown in Table 1, with four levels of stress range [124, 145, 159, and 207 MPa (18, 21, 23, and 30 ksi)], two-bolt and one-bolt splices, and nonbonded and bonded contact surfaces. There were two to

TABLE 1—*Fatigue test matrix for Series A tension specimens.*

Stress Range, MPa	Number of Specimens Tested			
	Two-Bolt Splices		One-Bolt Splices	
	Nonbonded	Bonded	Nonbonded	Bonded
124	2	...	4	4
145	2	...	3	4
159	4	4	2	2
207	4	4	...	...

four replicate tests per cell. The stress range was calculated with the expression

$$f_r = \frac{P_r}{A} \tag{3}$$

in which P_r is the load range, and A the gross area of plate.

Crack Initiation and Propagation

Two-Bolt Splices—Of the twelve nonbonded two-bolt splices, six failed from cracks that initiated at the first bolt hole in the main plate, one in the main plate by fretting ahead of the first bolt hole, and one at the second bolt hole in the splice plate. The remaining four specimens did not fail. Of the eight bonded two-bolt splices, six failed from cracks that initiated at the first bolt hole in the main plate, one failed from a crack at the second bolt hole in the splice plate, and one did not fail.

The bolt hole cracks initiated along the bore or at the intersection of the bore with the plate surface. They propagated at first as part-through or corner cracks, shown in Fig. 3, *a* and *b*, until their length along the bore was equal to the plate thickness. Thereafter, they propagated as through cracks across the plate until the net ligament ruptured in a ductile mode at stresses near the ultimate tensile strength of the plate. No brittle failures were observed. The bolt hole cracks initiated on either side of the lines where the normal plane intersects the edge of the hole. The fretting cracks initiated ahead of the bolt, by rubbing of the plates against each other (Fig. 3*c*).

The nonbonded and bonded two-bolt splices failed in equal numbers at the first bolt hole in the main plate (six each), and at the second bolt hole in the splice plate (one each). Only one splice failed from a fretting crack. Evidently, adding adhesive did not alter the mode of failure of the bolted splices. The cracking behaviors were similar, even though most nonbonded specimens slipped into bearing, whereas the bonded specimens remained in friction.

One-Bolt Splices—Of the nine nonbonded one-bolt splices, four failed from cracks that initiated at the bolt hole in the main plate, three at the bolt hole in the splice plate, one in the splice plate by fretting ahead of the bolt hole, and one in the bolt. Of the ten bonded one-bolt splices, three failed from cracks that initiated at the bolt hole in the main plate, six in the bolt, and one did not fail.

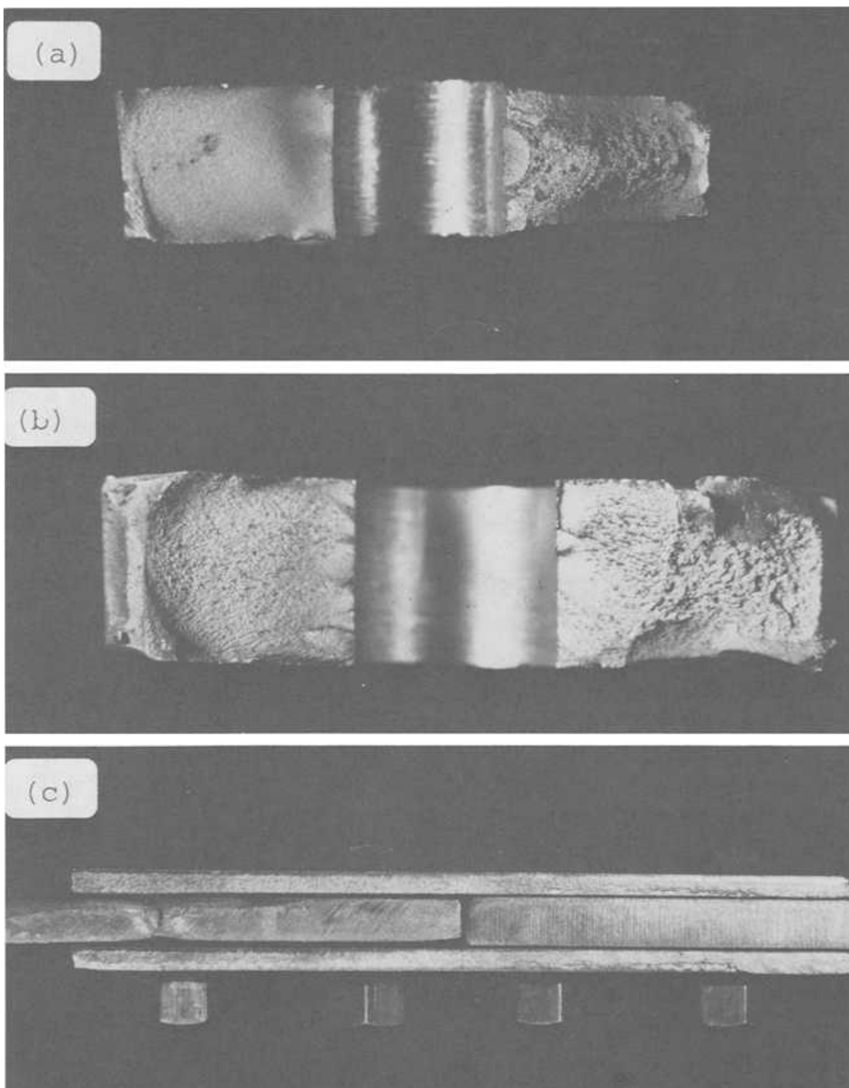

FIG. 3—*Typical fatigue cracks in two-bolt tension splices:* (a) *initiation along bore,* (b) *initiation at intersection of bore with plate surface,* (c) *initiation by fretting.*

The bolt hole cracks initiated and propagated in the same manner as those in the two-bolt splices.

The two shearing planes of the bolt were located at 8 mm (5/16 in.) and 24 mm (15/16 in.) from the bolt head. The first shearing plane was located in the body of the bolt (threads excluded) and was never the site of a fatigue crack. The second shearing plane was located at the runout of the last thread. Fractographic examination indicated that it was the site of fatigue cracks when the angular orientation caused the edge of the plate to bear on the bolt at the end of the last thread.

Bond breakage and connection slip into bearing always preceded the fatigue failure of a bolt. The bolts did not fatigue crack in the two-bolt splice because, for equal stress in the plate, the shear stress was only one-half of that in the one-bolt splice.

Fatigue Test Data

Two-Bolt Splices—The fatigue test data for the two-bolt splices were plotted in Fig. 4 on the basis of the gross area stress range in the plate, with open and solid triangles, respectively, for the nonbonded and bonded splices. The runouts were identified with an arrow. The specimen labeled "*F*" failed from a fretting crack. It had a relatively long life. One-half of the nonbonded splices slipped into bearing while the other half remained in friction. The data points for the former were labeled "*b*" in Fig. 4. All bonded splices behaved as friction-type joints.

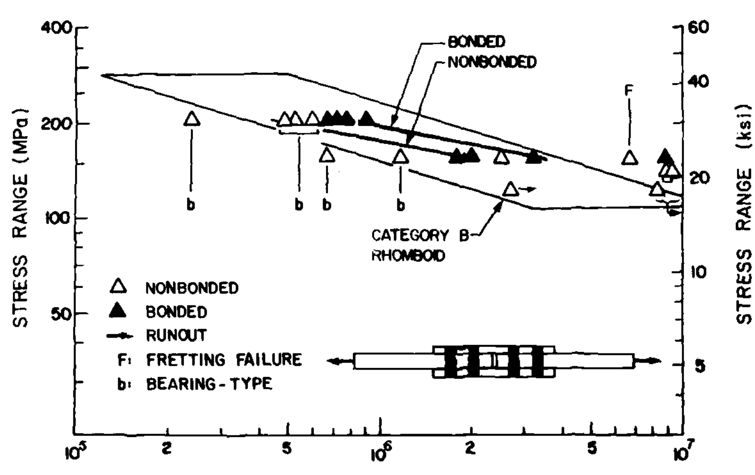

FIG. 4—*Fatigue test data for Series A two-bolt tension splices.*

The mean regression line for the S-N data is given by

$$\log N = b - m \log f_r \tag{4}$$

where

N = number of cycles,
b = intercept,
m = slope, and
f_r = stress range.

Table 2 lists the results of the regression analysis of the eight nonbonded and the eight bonded Series A two-bolt tension splices that were tested at 159 and 207-MPa (23 and 30-ksi) stress ranges. The horizontal shift between the two mean regression lines plotted in Fig. 4 reflects a factor-of-1.7 increase in the fatigue life of the bolted splices due to bonding. The increase in life was achieved by increasing the area of force transfer from a ring around each bolt hole of the splice to the 64 by 64-mm (2½ by 2½-in.) tributary bonded area per bolt when the splice was also bonded.

Also shown in Fig. 4, for purposes of comparison, is the Category B rhomboid, defined as the space containing 95.5% of the fatigue test data for the longitudinal flange-to-web weld of plate girders, from which the Category B allowable S-N line was derived [3]. The space is bound on the right and left by the mean plus and minus two standard deviations, $\log N = (13.697 \pm 2 \times 0.147) - 3.372 \log f_r$, on the bottom by the 110-MPa (16-ksi) fatigue limit for Category B, and on the top by the highest stress range at which the welded beams were tested. Most data points fell inside the rhomboid. The data points for the four splices that did not fail (runout) and for the splice with a fretting crack (F) fell above the rhomboid.

Only two data points, both for nonbonded bearing-type splices, fell below the rhomboid. Plotting them in terms of the net section stress range, as AASHTO specifies for bearing-type joints, would raise the points by a factor of $A/A_n = 1.43$ on the stress range to well within the rhomboid.

One-Bolt Splices—The fatigue test data for the one-bolt splices were plotted in Fig. 5 on the basis of the gross area stress range in the plate, with open and solid triangles for the nonbonded and bonded splices, respectively. Four additional points, for splices that failed by shearing of the bolt at very short lives, fell outside of the plot and are not shown. The other three splices with premature bolt failures were labeled "B."

The high cyclic shear deformations caused the adhesive of several bonded one-bolt splices to fail during the fatigue test. This changed the splice behavior from friction type to bearing type. In fact, the ten bonded splices behaved initially as friction-type joints, but six of them eventually failed by

TABLE 2—*Results of regression analysis of fatigue test data.*

Contact Surfaces	No. of Data Points	Regression Coefficients: Intercept, b^a	Regression Coefficients: Slope, m	Standard Deviation, s	Correlation Coefficient, r
Series A two-bolt tension splices					
Nonbonded	8	18.2821	5.456	0.3273	0.74
Bonded	8	18.4165	5.410	0.2445	0.83
Series B six-bolt beam splices					
Nonbonded	12	14.7020	3.898	0.2126	0.76
Bonded	12	26.0153	8.714	0.1801	0.95
Series B four-bolt beam splices					
Bonded	12	20.5276	6.527	0.1979	0.90
Series B beam cover plates					
Bonded and bolted	27	16.5715	4.571	0.1983	0.82

[a]Values of intercept are for stress range in MPa.

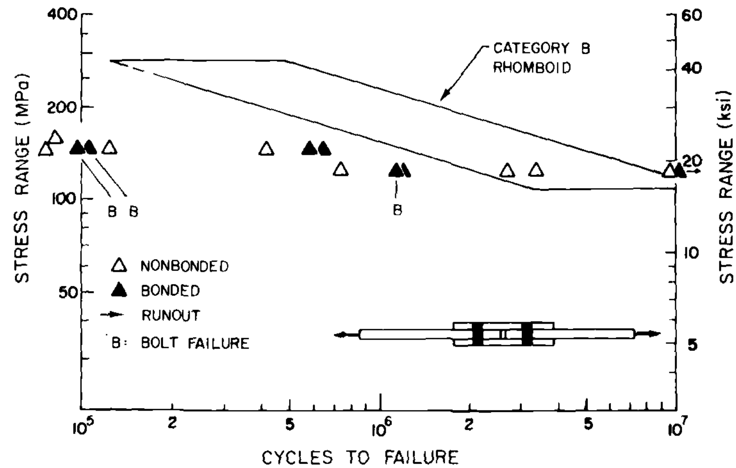

FIG. 5—*Fatigue test data for Series A one-bolt tension splices.*

shearing of the bolt when the thread runout was located in the second shearing plane.

Excluding the data for the splices with bolt failures, the data show an increase in fatigue life by a factor of 3.8 at 145-MPa (21 ksi) stress range and by a factor greater than 1.2 at 124-MPa (18 ksi) stress range. The sample sizes for one-bolt splices were too small for meaningful regression analysis.

Only four data points for splices tested at the 124-MPa (18 ksi) stress range fell inside or above the Category B rhomboid. All others fell below the rhomboid.

The bolts were deliberately underdesigned to determine the fatigue strength of a splice in which the bolts and adhesive shared in the load transfer. The one-bolt splice had a bolt-to-member strength ratio of 0.36, one half of the 0.72 ratio for the two-bolt splice. The AASHTO allowable stresses for A588 steel and A325 bolts are 186 MPa (27 ksi) for member axial tension, 172 MPa (25 ksi) for bolt shear, and 414 MPa (60 ksi) for bolt bearing. The ratio of the AASHTO allowable stresses is 1.0/0.93/2.22. The corresponding ratio of calculated stresses for the one-bolt splices was much higher, 1.0/2.55/4.00. Relative to the member axial stress, the bolts were overstressed by a factor of 2.55/0.93 = 2.74 on shear, and by a factor of 4.00/2.22 = 1.80 on bearing.

Comparison of Tension Splice Data

Figure 6 summarizes the fatigue test data for the Series A tension specimens. Each point represents the log mean fatigue life of a group of replicate tests. The data points for the specimens that failed by shearing of the bolt

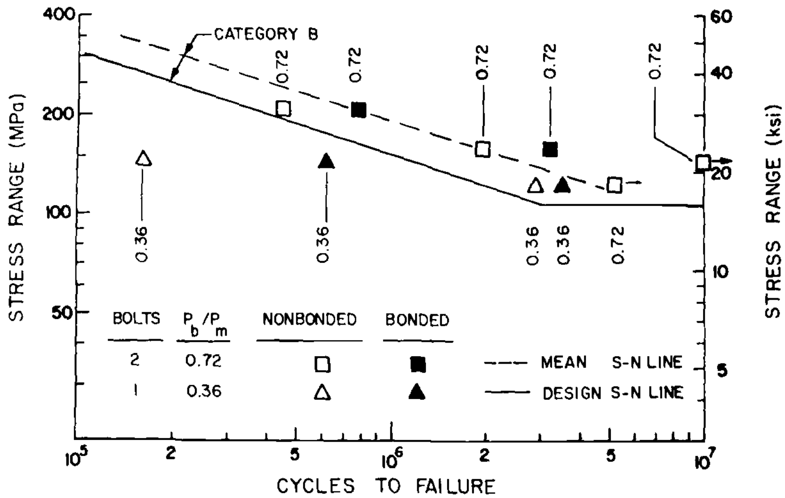

FIG. 6—*Comparison of all fatigue test data for Series A tension splices.*

were excluded. Also shown for purposes of comparison are the mean *S-N* line (dashed) and the AASHTO design *S-N* line (solid) for Category B. The latter is the same as the left and lower bounds of the Category B rhomboid. The results show that adhesive bonding, in addition to bolting, consistently increased the fatigue life. Furthermore, reducing the bolts-to-member strength ratio, from 0.72 for the two-bolt splices to 0.36 for the one-bolt splices, shortened the fatigue life to a degree that could not be recovered by bonding.

Fatigue Strength of Beam Splices

The Series B beam specimens, shown in Fig. 2, had three details: one splice at midspan and two cover plates in the moment gradient regions. The data for the splices are presented in this section.

Experiment Design

Eighteen Series B beam splices were fatigue tested in the three-way partial factorial, shown in Table 3, with two levels of stress range [159 and 207

TABLE 3—*Fatigue test matrix for Series B beam splices.*

Stress Range, MPa	Number of Specimens Tested			
	Six-Bolt Splices		Four-Bolt Splices	
	Nonbonded	Bonded	Nonbonded	Bonded
159	3	3	...	3
207	3	3	...	3

MPa (23 and 30 ksi)], six-bolt and four-bolt splices, and nonbonded and bonded contact surfaces. There were three replicate tests per cell. Nonbonded four-bolt splices were not tested. Because each crack was temporarily repaired and the test continued, fatigue test data were obtained for both halves of the splice, one left and one right of center. This raised the actual number of data points per cell to six. The stress range was calculated with the expression

$$f_r = \frac{M_r}{S} \tag{5}$$

where M_r is the moment range in the plane through the first bolt row (closest to support), and S is the gross section modulus of W 14x30 section without splice plates. The minimum stress was 7 MPa (1 ksi) in all tests.

Crack Initiation and Propagation

Three types of cracks were observed in the nonbonded and bonded splices:

(*a*) bolt hole cracks on the first row in the flange, closest to the support,
(*b*) bolt hole cracks on the last row in the splice plate, closest to the midspan point, and
(*c*) fretting cracks in the flange ahead of the first row.

No fretting cracks were found in the splice plates. The cracks in the beam splices initiated and propagated in the same way as those in the tension splices.

The type of crack was independent of the number of bolts in the splice, nonbonded and bonded contact surfaces, and friction-type and bearing-type behavior. Indeed, the number of cracks by type was similar for all groups.

Fatigue Test Data

Six-Bolt Splices—The fatigue test data for the six-bolt splices were plotted in Fig. 7 on the basis of the gross area stress range. The open and solid triangles represent the nonbonded and bonded splices, respectively. The runouts were identified with an arrow. The two splices labeled "*F*" in Fig. 7 failed from fretting cracks. They had longer lives than their counterparts tested at the same stress ranges. The nonbonded splices slipped into bearing during the first load cycle, whereas the bonded splices behaved as friction-type joints.

Table 2 lists the results of the regression analysis of the 12 nonbonded and the 12 bonded Series B six-bolt splices. The two regression lines were plotted in Fig. 7. Bonding the contact surfaces increased the mean fatigue life by a factor of more than 5.2 at the 159-MPa (23-ksi) stress range, from

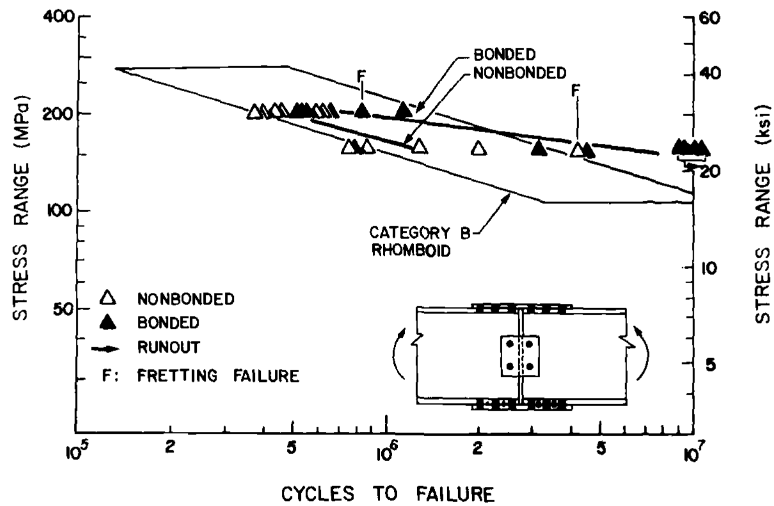

FIG. 7—*Fatigue test data for Series B six-bolt beam splices.*

1 335 000 to 6 950 000 cycles, and by a factor of 1.4 at the 207-MPa (30-ksi) stress range, from 474 000 to 686 000 cycles.

Figure 7 also compares the data with the Category B rhomboid. Nine of the twelve data points for nonbonded splices fell inside the rhomboid, even though the data points for the splices that slipped into bearing were plotted in terms of the gross area stress range. All data points for bonded splices fell inside or above the rhomboid. Bonding pushed five of six splices tested at the 159-MPa (23-ksi) stress range to runout. It appears that the fatigue limit is much higher than the value of 110 MPa (16 ksi) AASHTO specifies for Category B details.

Four Bolt Splices—The fatigue test data for the bonded four-bolt splices were plotted in Fig. 8 on the basis of the gross area stress range. The two splices labeled "*F*" in Fig. 8 failed from fretting cracks.

The splices tested at the 159-MPa (23-ksi) stress range behaved as friction-type joints. Their data points fell inside the Category B rhomboid. Those tested at the 207-MPa (30 ksi) stress range slipped into bearing, with four failure points falling below the rhomboid.

Table 2 lists the results of the regression analysis of the 12 bonded Series B four-bolt splices. The regression line was plotted in Fig. 8.

Comparison of Tension and Beam Splice Data—Figure 9 compares the data for Series A tension specimens with one-bolt and two-bolt splices (P_b/P_m = 0.36 and 0.72) with the data for Series B beams with four-bolt and

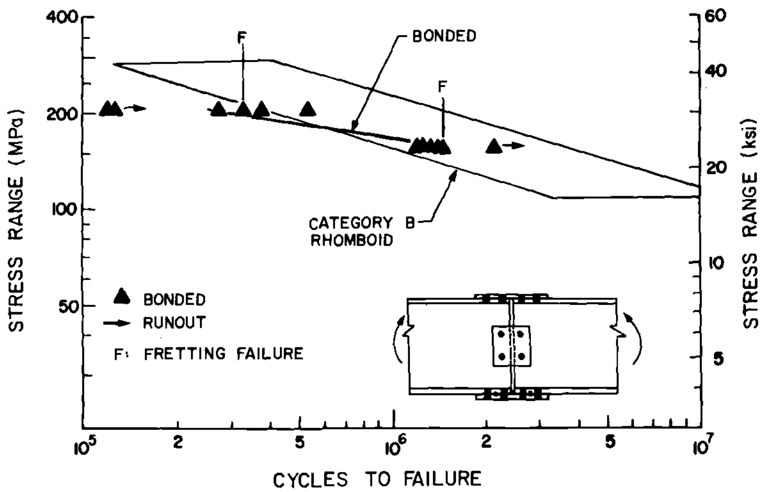

FIG. 8—*Fatigue test data for Series B four-bolt beam splices.*

six-bolt splices (M_b/M_m = 0.58 and 0.87). Each point corresponds to the mean life of a group of replicate tests. The mean *S-N* line (dashed) and the AASHTO design *S-N* line (solid) for Category B are also shown.

The data show good correlation between the two-bolt tension and the six-bolt beam splices with bolts-to-member strength ratios of 0.72 and 0.87, respectively. This finding applies to both the nonbonded and bonded specimens. The four-bolt beam splices (0.58) had a shorter fatigue life by about

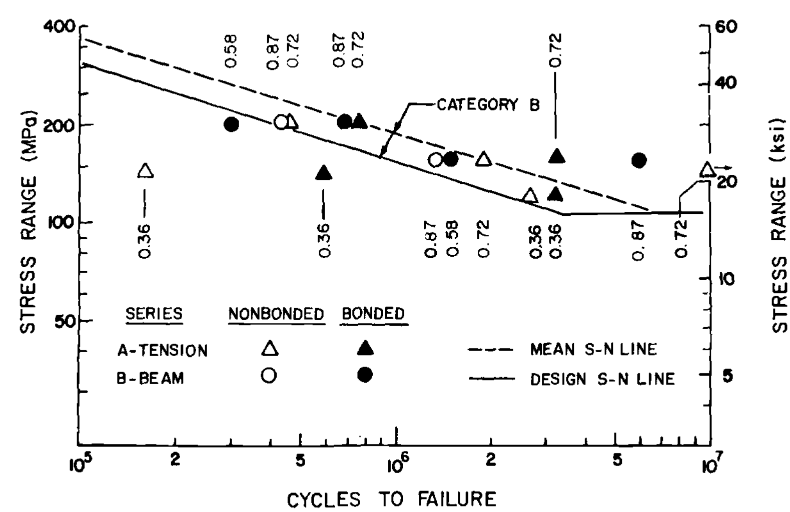

FIG. 9—*Comparison of all fatigue test data for Series A and B splices.*

a factor of 2.5. The one-bolt tension splices (0.36) were so severely underdesigned that they had very short lives even when bonded. Yet, for all values of the bolts-to-member strength ratio, bonding consistently increased the fatigue life. Figure 9 also shows that the use of adhesives in combination with bolts reduces to 72% the number of bolts needed for the splice still to develop the mean fatigue strength of Category B. Bolted joints without adhesives have Category B fatigue strength.

Fatigue Strength of Beam Cover Plates

Experiment Design

Two cover plates were adhesive bonded to the tension flange of 17 beams, giving a total of 34 data points, one for each cover plate end closest to the midspan of the beam.

The initial plan was to attach the cover plates to the flange with adhesive alone. However, because the cover plate ends had debonded on the three beams that were tested first, the cover plate ends of the remaining 13 beams were bolted to the flange, as shown in Section B of Fig. 2.

Twenty-six cover plates terminated 152 mm (6 in.) from the loading points and were cycled at stress ranges of 145 and 189 MPa (21 and 27.4 ksi). The other eight were extended 108 mm (4¼ in.) into the constant bending moment region and were cycled at stress ranges of 159 and 207 MPa (23 and 30 ksi), like the splices. The stress range was calculated with Eq 5.

Crack Initiation and Propagation

The six cover plates that were bonded but not bolted to the tension flange of three beams gradually debonded during stress cycling. For example, an ultrasonic compression wave scan of one cover plate showed the end had debonded over a length of about 125 mm (5 in.) after 2 000 000 cycles of 145-MPa (21-ksi) stress range. The debonded areas are shown dark in Fig. 10, with the bonded areas clear.

Nine of the 27 bonded and bolted cover plate ends failed from cracks that initiated at the bolt holes in the flange, 2 failed from fretting cracks in the flange between the bolts and the cover plate end, 16 were runouts, and one test was invalid. No cracks initiated in the cover plate, nor did flange cracks propagate across the bond line into the cover plate.

The bolt hole cracks and the fretting cracks initiated and propagated like those in the Series A tension splices. Figure 11 shows a typical bolt hole crack at the cover plate end. To continue the test at the other details on the same beam, the crack was temporarily repaired with splice plates and high-strength C clamps. The growth of the crack front in the web was arrested by drilling a hole at the crack tip, installing a bolt, and torquing the bolt to 70% of its tensile strength.

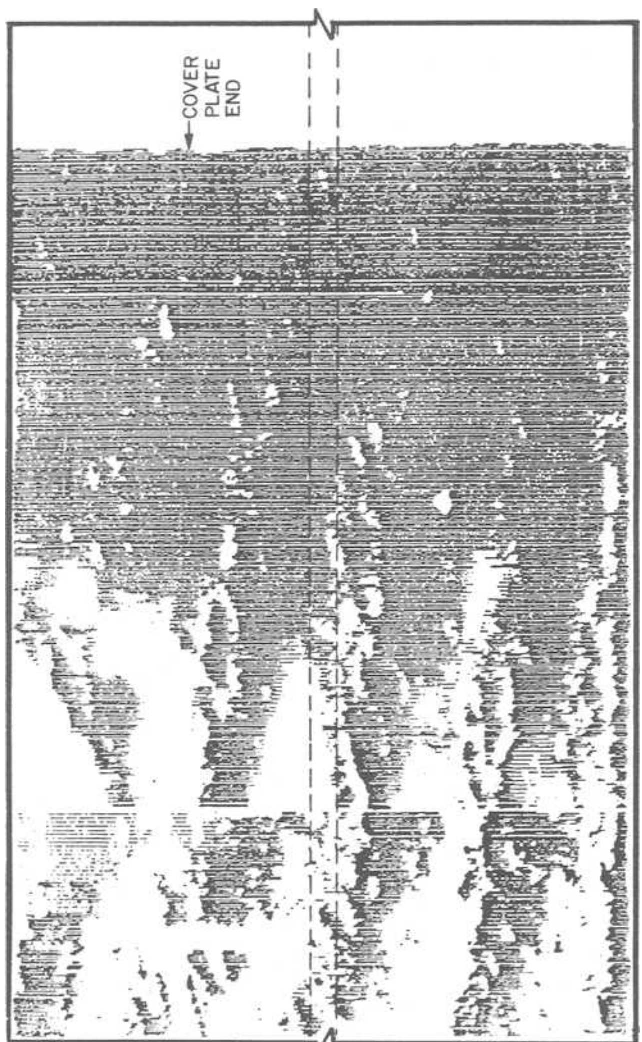

FIG. 10—*Compression wave scan of nonbolted cover plate end. Bonded areas are clear; debonded areas are dark.*

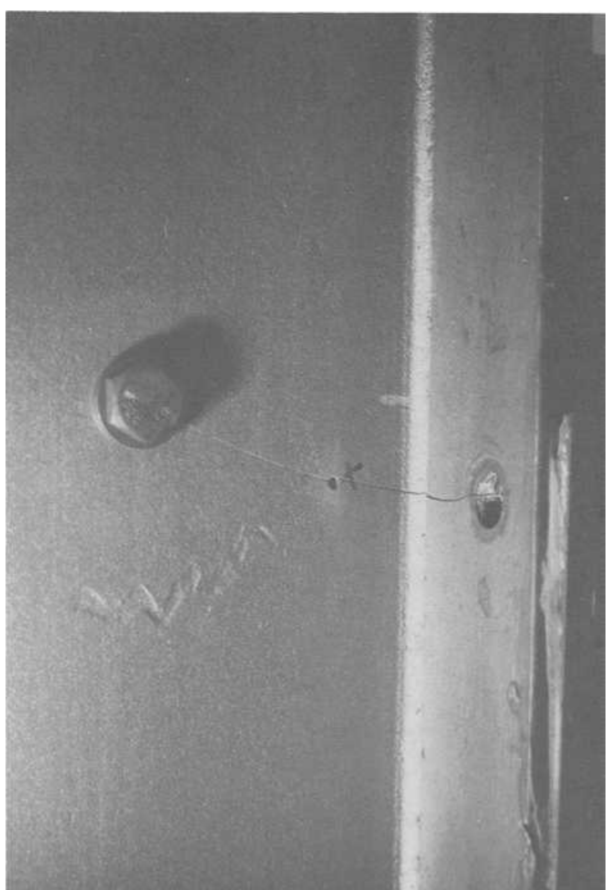

FIG. 11—*Typical bolt hole cracks at cover plate end; bolt at crack tip in web is part of temporary repair.*

Fatigue Test Data

The fatigue test data for the bonded cover plates were plotted in Fig. 12 in terms of the gross area stress range in the beam section. The data points for the cover plates on the beams, whose ends had not been bolted, are shown with open circles. These tests were considered to have run out because the steel section did not crack. However, the gradual debonding would eventually have separated the cover plate from the flange and limited the load carrying capacity to that of the W 14x30 beam alone. The number of cycles to failure is ambiguous in this case.

The 27 data points for the bonded cover plates with bolted ends are shown with solid triangles for the failures and with open triangles for the runouts. All points fell inside or above the Category B rhomboid. Table 2 gives the results of the regression analysis of the 27 data points for bonded and bolted cover plates. The corresponding mean *S-N* line is shown in Fig. 12. The data for nonbolted ends were excluded from the regression analysis.

Also shown in Fig. 12, for comparison, are the mean *S-N* line (dashed) and the AASHTO design *S-N* line (solid) for Category E welded cover plates. It was found that, at the stress ranges in the finite life regime, bonding and bolting cover plates increases the mean fatigue life by a factor of 20 over that of welded cover plates. At the lowest stress range of 145 MPa (21 ksi), six of eight details tested were runouts, suggesting that the fatigue limit may lie about halfway between the AASHTO fatigue limit for Category A [165 MPa (24 ksi)] and that for Category B [110 MPa (16 ksi)]. Clearly, bonding and bolting the ends have the potential of fatigue-proofing cover plates in typical bridge girders [*1*].

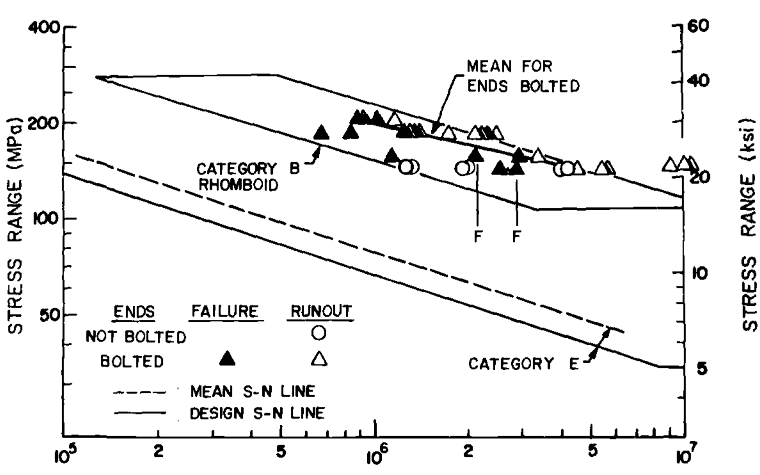

FIG. 12—*Fatigue test data for Series B beam cover plates.*

Comparison with Previous Work

Reference *1* summarizes the 755 fatigue tests of cover plates on steel beams that were reported since 1969. The more recent studies focused on improving the fatigue strength by the following processes: grinding, shot-peening, and tungsten-inert-gas (TIG) remelting the toe of the transverse end weld of the cover plate (Fig. 13*a*) [*4*]; end-welding and grinding the cover plate to a 1:3 taper (Fig. 13*b*) [*9*]; retrofitting the cover plate ends with bolted splices (Fig. 13*c*) [*6*]; and end-bolting the loose ends of longitudinally welded cover plates (Fig. 13*d*) [*8*].

The various strengthening methods increased the mean fatigue life over that of Category E for conventionally welded cover plates by the following factors: 1.5, 2.1 and 4.4 for ground, shot-peened, and TIG remelted toes of end welds, respectively; 6.5 for grinding the end weld of the cover plate to a 1:3 taper; 21 or more for end-bolting; and 18 and 13, respectively, for splicing the ends of noncracked and cracked cover plates. In comparison, bonding and bolting increased the mean fatigue life by a factor of 20 in the finite life regime and by a factor of 35 near the fatigue limit.

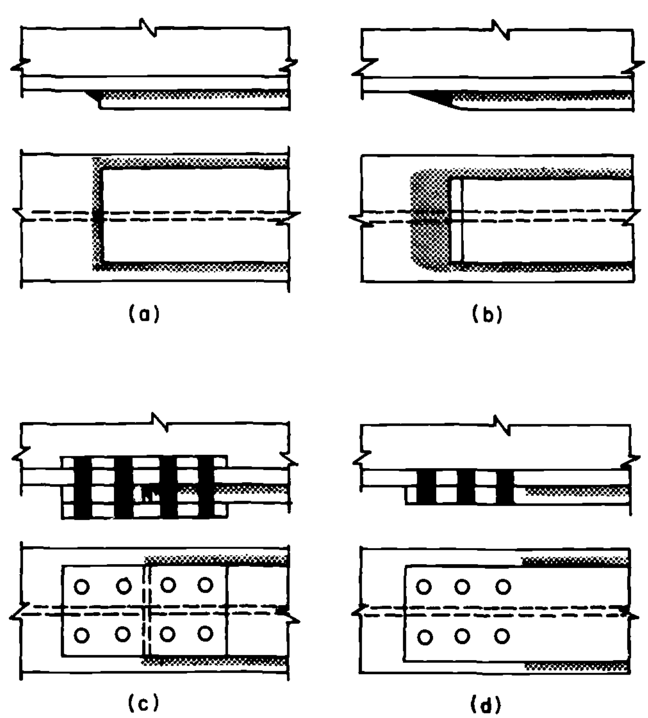

FIG. 13—*Configuration of cover plate ends tested in previous studies:* (a) *ground, shot-peened, and TIG remelted transverse end weld;* (b) *end weld ground to 1:3 taper;* (c) *spliced end;* (d) *bolted loose end.*

Conclusions

The results of the experimental work performed in this study and an analysis of related data reported in the literature yield the following important conclusions about the fatigue behavior of bonded and bolted joints:

1. The manner in which the cracks initiated and propagated was independent of (*a*) the number of bolts in the splice, (*b*) whether the contact surfaces were bonded or nonbonded, and (*c*) whether the joint behaved as a friction-type or bearing-type connection.
2. The joints with fretting cracks had generally longer fatigue lives than those with bolt hole cracks.
3. Bonding the contact surfaces of bolted joints consistently increased the fatigue strength at all bolts-to-member strength ratios.
4. The use of adhesives in combination with bolts reduces to 72% the number of bolts needed for the splice to still develop the mean fatigue strength of Category B. Bolted joints, without adhesive, have Category B fatigue strength.
5. Bonding and end-bolting cover plates increased the fatigue life by a factor of 20 over that of conventionally welded cover plates, from Category E to Category B.
6. The ends of a cover plate bonded to the outside of the tension flange of a steel beam must be clamped with bolts to prevent gradual debonding.

In general, the largest increase in the fatigue strength of structural steel details is obtained by replacing welded connections with bonded and bolted connections. When properly detailed, such connections can develop Category B fatigue strength. This virtually makes them fatigue-proof for highway bridge loading.

The authors emphasize that most epoxy and acrylic adhesives have low creep strength at ambient relative humidities and at temperatures that are high but still within the range of service environments [*10*]. The clamping force of high-strength bolts greatly reduces the creep susceptibility of bonded joints, but more durable adhesives are needed before they can be used alone in primary joints of highway bridges.

References

[*1*] Albrecht, P., Wattar, F., and Sahli, A. H., "Towards Fatigue-Proofing Cover Plate Ends," *Proceedings*, W. H. Munse Symposium on Metal Structures, Convention, American Society of Civil Engineers, Philadelphia, May 1983, pp. 24–44.

[*2*] Albrecht, P., Sahli, A. H., Crute, D., Albrecht, Ph., and Evans, B., "Application of Adhesives to Steel Bridges," Report FHWA/RD-84/037, Federal Highway Administration, Washington, DC, November 1984.

[*3*] Fisher, J. W., Frank, K. Y., Hirt, M. A., and McNamee, B. M., "Effects of Weldments on the Fatigue Strength of Steel Beams," NCHRP Report No. 102, Transportation Research Board, National Research Council, Washington, DC, 1970.

[4] Fisher, J. W., Hausammann, H., Sullivan, M. D., and Pense, A. W., "Detection and Repair of Fatigue Damage on Welded Highway Bridges," NCHRP Report No. 206, Transportation Research Board, National Research Council, Washington, DC, June 1979.

[5] Nara, H. and Gasparini, D., "Fatigue Resistance of Adhesively Bonded Structural Connections," Report No. 45K1-114, Department of Civil Engineering, Case Institute of Technology, OH, September 1981.

[6] Sahli, A. H., Albrecht, P., and Vannoy, D. W., "Fatigue Strength of Retrofitted Cover Plate Ends," *Journal of Structural Engineering,* American Society of Civil Engineers, Vol. 110, No. 6, June 1984, pp. 1374–1388.

[7] "Standard Specification for Highway Bridges," American Association of State Highway and Transportation Officials, Washington, DC, 1983.

[8] Wattar, F., Albrecht, P., and Sahli, A. H., "End-Bolted Cover Plates," *Journal of Structural Engineering,* American Society of Civil Engineers, Vol. 3, No. 6, June 1985, pp. 1235–1249.

[9] Yamada, K. and Albrecht, P., "Fatigue Behavior of Two Flange Details," *Journal of Structural Division,* American Society of Civil Engineers, Vol. 103, No. ST4, April 1977, pp. 781–791.

[10] Mecklenburg, M. F., Albrecht, P., and Evans, B. M., "Screening of Structural Adhesives for Application to Steel Bridges," Interim Report, Project No. DTFH 61-84-R-0027, Department of Civil Engineering, University of Maryland, College Park, MD, February 1985.

Eun U. Lee[1]

Effect of Load Transfer on Fatigue of Mechanically Fastened Metallic Joints

REFERENCE: Lee, E. U., "**Effect of Load Transfer on Fatigue of Mechanically Fastened Metallic Joints,**" *Fatigue in Mechanically Fastened Composite and Metallic Joints, ASTM STP 927*, John M. Potter, Ed., American Society for Testing and Materials, Philadelphia, 1986, pp. 95–117.

ABSTRACT: Mechanically fastened joints are highly susceptible to fatigue cracking especially when varying loads are applied. The fatigue cracking is influenced by load transfer through fasteners.

Tests were conducted using zero, low, medium, and high load transfer specimens of 7475-T7351 aluminum. The fatigue crack initiation and growth and the final fracture behaviors were investigated. The fatigue crack initiation life, N_i, and the total fatigue life, N_f, are reduced by increasing stress range, $\Delta\sigma$, and load transfer level, L. The relationship is defined by the equations of the form

$$\log N = C - B\Delta\sigma - DL^H$$

where C, B, D, and H are constants. The fatigue crack growth rate, da/dN, is related to the stress intensity factor range, ΔK, by the equation

$$da/dN = (2.36 \times 10^{-7}) \cdot (\Delta K)^{2.89} \text{ mm/cycle}$$

The crack initiation portion of the total fatigue life, N_i/N_f, is greater with lower stress range, $\Delta\sigma$, and longer total fatigue life, N_f, and it is reduced by load transfer.

KEY WORDS: mechanically fastened joints, load transfer, constant amplitude loading, fatigue, stress ratio, stress range, frequency, crack initiation, crack growth, fatigue life

An aircraft structure consists of many components connected mostly by mechanically fastened joints. Besides facilitating assembly and disassembly of structural components, mechanically fastened joints transfer and distribute loads. Many aircraft structural failures are induced by fatigue cracking of a mechanically fastened joint, originating at the fastener hole. The fastener hole is a common site of load transfer and stress concentration, both of which magnify the local stress and influence the fatigue behavior of the joint.

[1] Materials engineer, Naval Air Development Center, Warminster, PA 18974.

TABLE 1—*Chemical composition of 7475 aluminum.*

Element	Percent	
	Minimum	Maximum
Silicone	. . .	0.10
Iron	. . .	0.12
Copper	1.20	1.90
Manganese	. . .	0.06
Magnesium	1.90	2.60
Chromium	0.18	0.25
Zinc	5.20	6.20
Titanium	. . .	0.06
Others (each)	. . .	0.05
Others (total)	. . .	0.15
Aluminum	remainder	

To provide a technical basis for formulating a reliable service life prediction methodology of aircraft structure, it is essential to understand and quantify the load transfer effect on fatigue behavior of mechanically fastened joints. This study is aimed at characterizing the fatigue behavior of mechanically fastened joints and identifying the load transfer effect. With tests of zero, low, medium, and high load transfer specimens of 7475-T7351 aluminum, the fatigue crack initiation and growth and the final fracture behaviors were investigated, and the load transfer effect was defined quantitatively.

Experimental Procedure

Material and Specimen Preparation

As the specimen material, a 6.35-mm-thick (¼-in.) plate of 7475-T7351 aluminum was selected. The chemical composition and mechanical properties are presented in Tables 1 and 2. From the plate, open-hole dogbone, reverse dogbone joint, 1½ dogbone joint, and double lap shear joint specimens were prepared to have zero, low, medium, and high levels of load

TABLE 2—*Mechanical properties of 7475-T7351 aluminum.*

Test Axis	Ultimate Tensile Strength, MPa (ksi)	Yield Strength, MPa (ksi)	Elongation [50.8 mm (2 in.)], %
Longitudinal	493.0 (71.5)	412.3 (59.8)	11.0
Transverse	477.8 (69.3)	406.8 (59.0)	16.0
Short transverse	485.4 (70.4)	397.2 (57.6)	8.6

transfer, respectively (Figs. 1–4). The longitudinal axis of the specimen was in the original plate rolling direction. In each joint specimen, a steel fastener (MS20004) of 6.2916 ~ 6.3297-mm (0.2477 ~ 0.2492-in.) diameter was installed in holes of 6.3500 ~ 6.4008-mm (0.2500 ~ 0.2520-in.) diameter, drilled and reamed, with clamp-up torque of 2.26 N · m (20 lbf · in.).[2]

Determination of Load Transfer Level

Since the load transfer levels in the open-hole dogbone and double lap shear joint specimens are obviously 0 and 1, respectively, only those in the reverse dogbone joint and 1½ dogbone joint specimens were determined by means of strain gage measurement. Strain gages were glued at four spots along the mid-width lines, 38.1 mm (1½ in.) above and below the fastener center, on front and back surfaces (Figs. 5 and 6). (The strain gage, MA-06-062AP-120, was supplied by Micro-Measurement Division, Measurement Group, Raleigh, NC.) The surface strains were measured under sustained tensile loadings of various magnitudes. The strains at the interface were estimated by averaging the measured surface strains, and those at the mid-thickness points by averaging the interface and surface strains. The load transfer level, L, was calculated by employing the following equation:

$$L = \frac{\epsilon_a - \epsilon_c}{\epsilon_a} \quad (1)$$

where ϵ_a and ϵ_c are strains at mid-thickness points a and c (Figs. 5 and 6).

Fatigue Test

The fatigue test was performed in a controlled laboratory atmosphere of 24°C (75°F) and 45% relative humidity, employing a 88.96-kN (20-kip) closed-loop servohydraulic Materials Testing System (MTS) machine. In all tests, the fatigue crack was initiated and propagated under tension-to-tension haversine waveform loading with a stress ratio of 0.05 and frequency of 10 Hz.

Detection and Measurement of Fatigue Crack

At various intervals, fatigue loading was stopped and the specimen was disassembled.[3] Subsequently, the fastener hole was inspected with a Mag-

[2] The fastener manufacturer's specified torque for structural application is 5.65 ~ 6.78 N · m (50 ~ 60 lbf · in.).

[3] The test interruption for disassembly and reassembly of a joint specimen and detection and size measurement of crack may result in some difference in the fatigue crack growth rate and the fatigue life. However, it is not feasible to detect a crack in a joint specimen and measure its size accurately without test interruption.

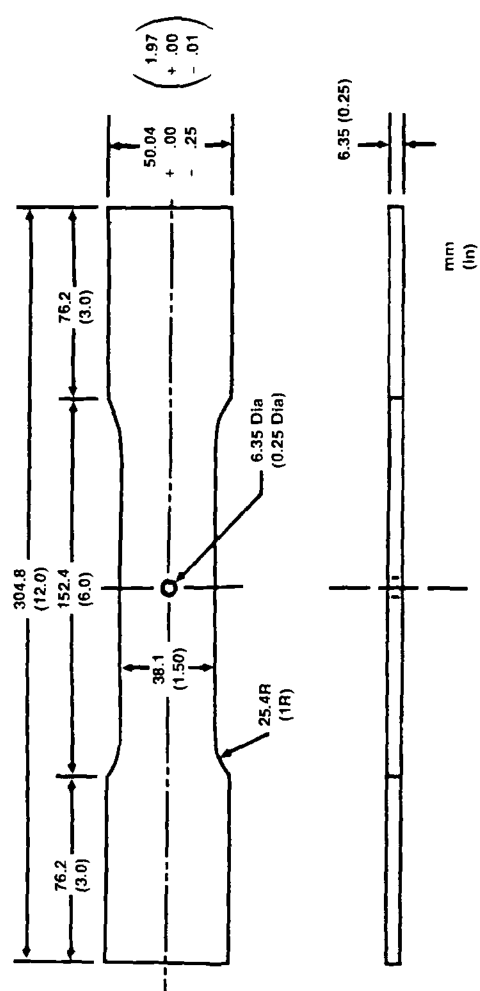

FIG. 1—Open-hole dogbone specimen.

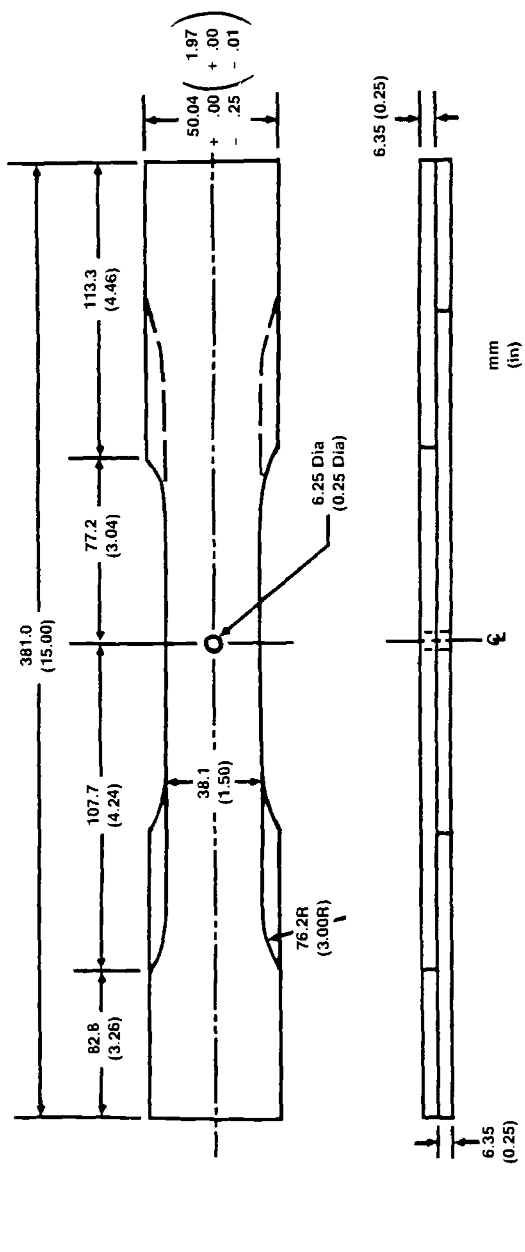

FIG. 2—*Reverse dogbone joint specimen (level of load transfer = 0.06).*

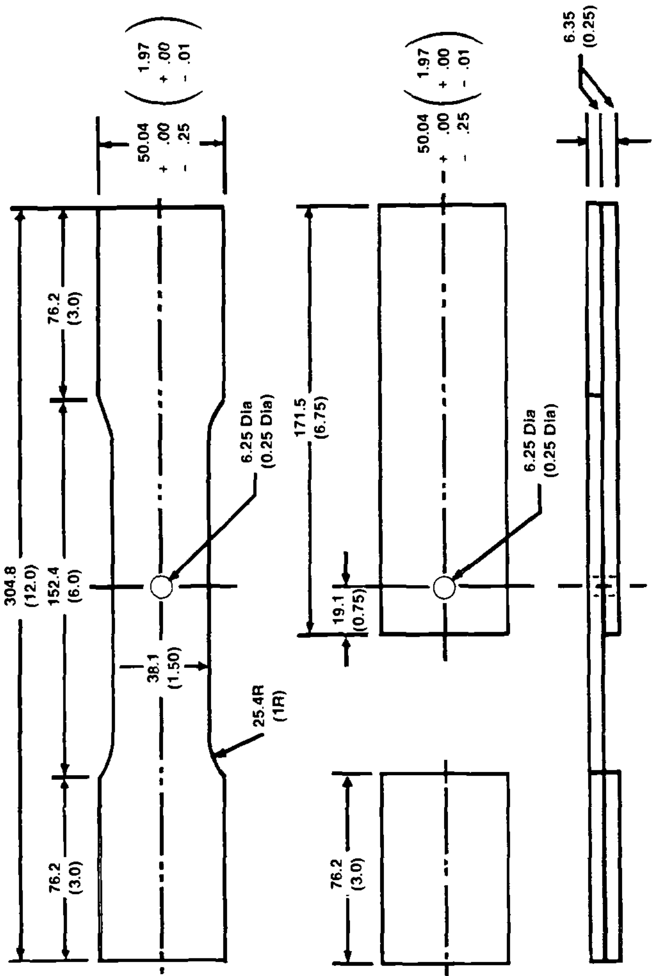

FIG. 3—1½ dogbone joint specimen (level of load transfer = 0.31).

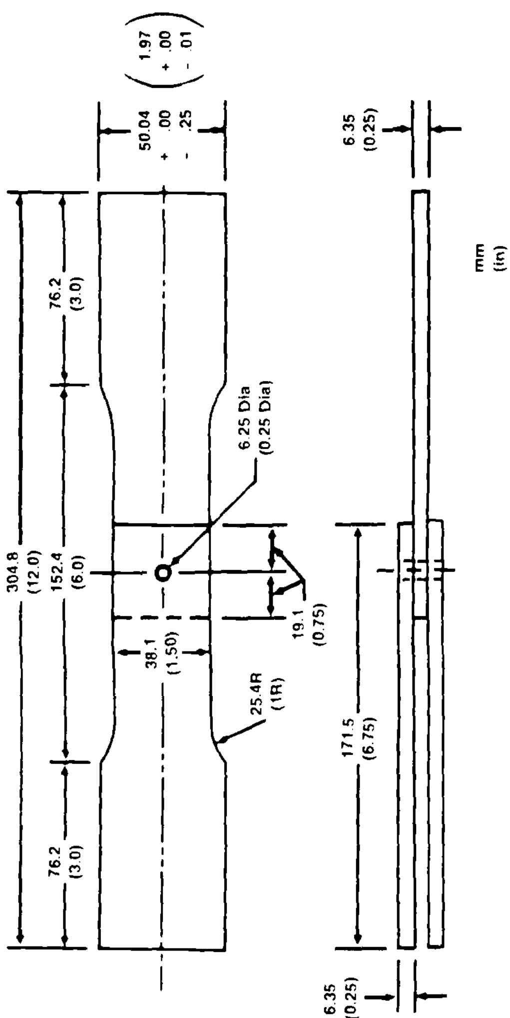

FIG. 4—*Double lap shear joint specimen (level of load transfer = 1).*

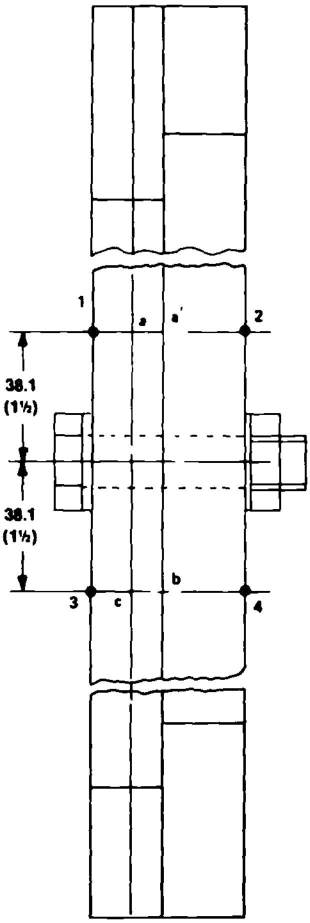

FIG. 5—*Strain gage locations in reverse dogbone joint specimen (strain gages at spots 1, 2, 3, and 4).*

naflux HT-100 eddy current hole scanner for possible crack initiation. Any crack presence is indicated by a group of eddy current signal spikes, whose heights are proportional to the depths at several crack tip points (Fig. 7). The greatest height was converted to the corresponding crack depth, using a calibration curve. The calibration curve was drawn with the spike heights of eddy current signal from EDM (electrical discharge machining) notches of known depths, 0.203 mm (0.008 in.), 0.381 mm (0.015 in.), 0.762 mm (0.030 in.), and 1.524 mm (0.060 in.), in a geometrically similar calibration standard of the same material. The determined crack depth was plotted against the corresponding number of loading cycles, and a crack growth curve was established. From this curve, a particular number of loading cycles

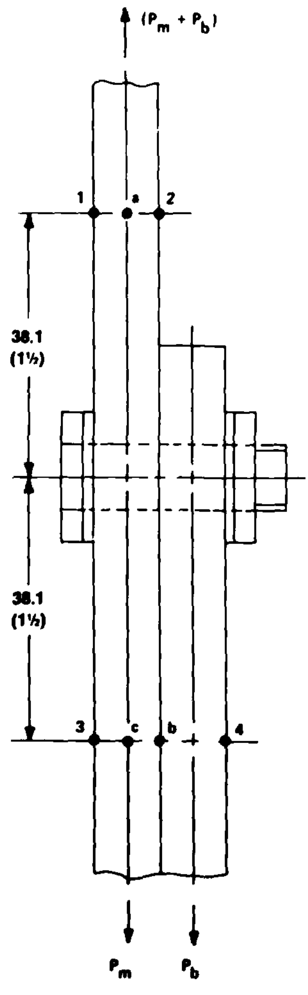

FIG. 6—*Strain gage locations in 1½ dogbone joint specimen (strain gages at spots 1, 2, 3, and 4).*

to produce a 0.254-mm-deep (0.01-in.) crack was taken and defined as the fatigue crack initiation life in this study. (Though the eddy current hole scanner is capable of finding smaller cracks, for example, 0.127-mm-deep (0.005-in.) crack, it can detect 0.254-mm-deep (0.01-in.) cracks more accurately and reliably.)

When the crack emanating from the fastener hole became visible, the fatigue loading was stopped, and the crack length was measured visually using a traveling microscope. This measurement was repeated at shorter loading intervals as the crack grew until its tip reached an edge of the

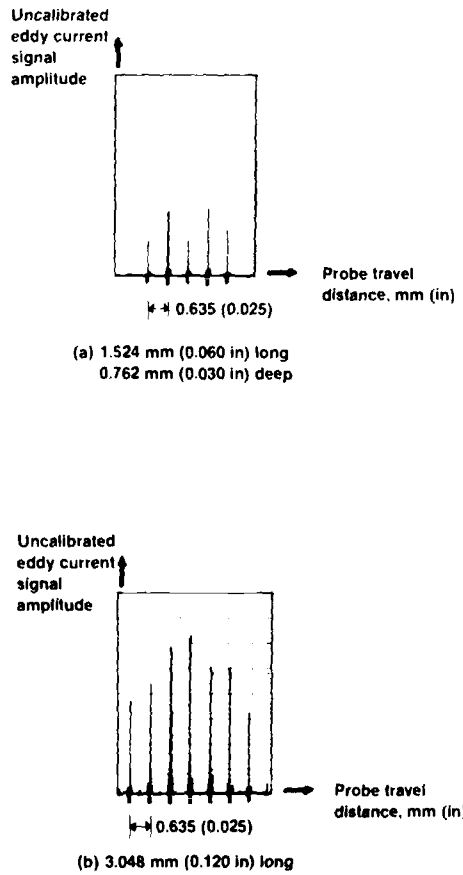

FIG. 7—*Eddy current signal spikes from* EDM *notches.*

specimen or the specimen was fractured. The rate of crack growth, da/dN, was then determined. The corresponding stress intensity factor range, ΔK, was calculated for a single or double crack emanating from the loaded fastener hole, employing the following equation [1–3]:

$$\Delta K = \frac{\Delta P}{t}\left[\left(\frac{1-L}{W}\right)\cdot F_n(a/r) + \frac{L}{2r}\cdot F_{nb}(a/r)\right] \sqrt{(\pi a)\cdot \sec\left\{\frac{\pi(na+2r)}{2W}\right\}} \quad (2)$$

where

ΔP = load range ($=P_{max} - P_{min}$), MPa,
P_{max} = maximum load, MPa,

P_{min} = minimum load, MPa,
t = specimen thickness, m
L = load transfer level,
W = specimen width, m,
$n = 1$ = for a single crack,
$n = 2$ = for a double crack
$F_{1,2}(a/r)$ = Bowie factor for a single crack or a double crack emanating from an open hole,
$F_{1b,2b}(a/r)$ = correction factor for a single crack or a double crack emanating from a loaded hole,
a = crack length, m, and
r = hole radius, m.

The derivation of the above equation is given in the Appendix.

Results

The obtained results consist of five parts: load transfer level, fatigue crack initiation, fatigue crack growth, fatigue fracture, and proportion of fatigue crack initiation and growth lives.

Load Transfer Level

The strains at four spots on the front and back surfaces of each specimen were measured. The strains at corresponding spots on the front and back surfaces are not equal, though those spots are located at an equal distance, 38.1 mm (1½ in.), from the fastener center. Such a discrepancy in strain is attributed to specimen bending under an applied tension. With the values of measured surface strains, the strains at the interface and mid-thickness were estimated. The load transfer level, L, was calculated with the values of mid-thickness strains, employing Eq 1. It ranges from 0.057 to 0.062 in the reverse dogbone joint specimen and from 0.307 to 0.314 in the 1½ dogbone joint specimen. In this study, the average values, 0.06 and 0.31, are taken as the load transfer levels in the reverse dogbone joint and 1½ dogbone joint specimens, respectively.

Fatigue Crack Initiation

Under fatigue loading, a single crack, not a double crack, was initiated at an edge of the fastener hole. Based on the results of the fatigue test and crack inspection, the applied stress range, $\Delta\sigma$, is plotted against the fatigue crack initiation life, N_i, in a semi-log scale (Fig. 8). The plot for the open-hole dogbone specimen has the feature of a typical *S-N* curve with a knee at $\Delta\sigma_{th}$ = 118.59 MPa (17.2 ksi). Below $\Delta\sigma_{th}$, no detectable crack was initiated within the limit number of loading cycles employed. On the other hand, the plots for the joint specimens are straight lines without any knee

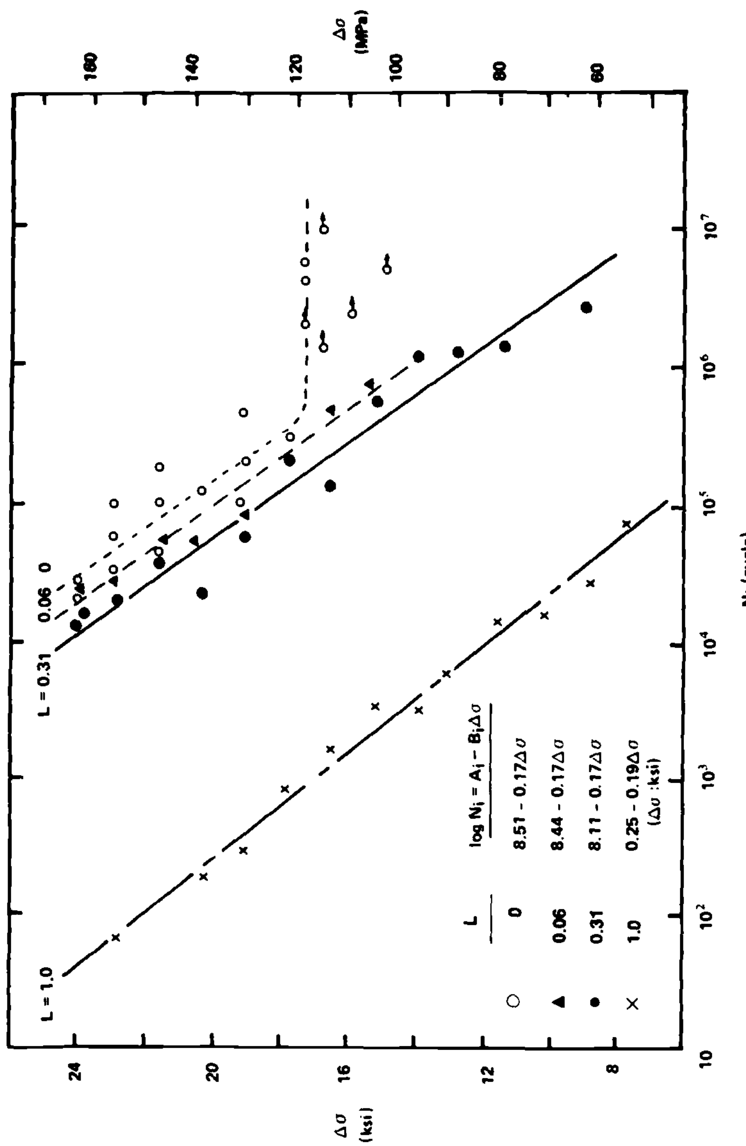

FIG. 8—*Variation of fatigue crack initiation life, N_i, with applied stress range, Δσ, in specimens of various load transfer levels.*

TABLE 3—*Parameters* A_i *and* B_i *in the fatigue crack initiation life equation,* $\log N_i = A_i - B_i\,\Delta\sigma$ ($\Delta\sigma$ = *ksi*).

Specimen	Load Transfer Level, *L*	A_i	B_i
Open-hole dogbone	0	8.51	0.17
Reverse dogbone joint	0.06	8.44	0.17
1½ dogbone joint	0.31	8.11	0.17
Double lap shear joint	1.0	6.25	0.19

within the limits of the applied stress range. The straight line plots, including that for $\Delta\sigma > \Delta\sigma_{th}$ in the open-hole dogbone specimen, can be defined by the equation

$$\log N_i = A_i - B_i\,\Delta\sigma \tag{3}$$

The parameters, A_i and B_i, are tabulated in Table 3.

Fatigue Crack Growth

The initiated single crack grew mostly alone in the open-hole dogbone, reverse dogbone joint, and 1½ dogbone joint specimens. Occasionally, before the crack reached an edge of the specimen, the second crack was initiated at the other edge of the fastener hole and began to grow. However, for the calculation of the stress intensity factor range, ΔK, it was assumed that only a single crack was initiated and grown. (This assumption is reasonably valid as long as the second crack is very small compared with the first one.) In the double lap shear joint specimen, shortly after the first crack was initiated at one edge of the fastener hole, the second crack was initiated at the other. The two cracks started to grow together. In this case, the stress intensity factor range, ΔK, was calculated for a double crack, using the average length of the two cracks. The fatigue crack growth rate, da/dN, is plotted against the stress intensity factor range, ΔK, in a log-log scale (Fig. 9). The log-linear portion of the curve takes a form of Paris' equation [*4*]:

$$da/dN = (2.36 \times 10^{-7}) \cdot (\Delta K)^{2.89} \text{ mm/cycle}$$

Fatigue Fracture

To evaluate the variation of total fatigue life or fatigue fracture life, N_f, with the applied stress range, $\Delta\sigma$, $\Delta\sigma$ is plotted against N_f in a semi-log scale (Fig. 10). As the plot of $\Delta\sigma$ versus $\log N_i$, the plot for the open-hole dogbone specimen has a form similar to a typical *S-N* curve and a knee at $\Delta\sigma_{th}$ = 118.59 MPa (17.2 ksi). On the other hand, the plots for the joint

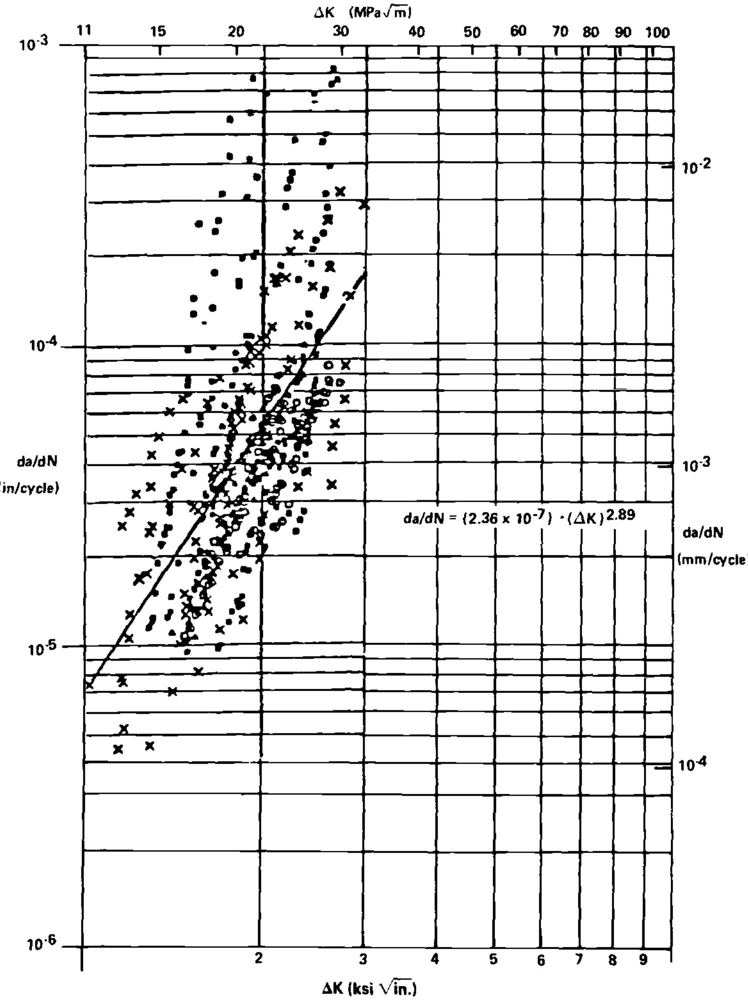

FIG. 9—*Variation of fatigue crack growth rate,* da/dN, *with stress intensity factor range,* ΔK, *in specimens of various load transfer levels.* ○, L = *0;* ▲, L = *0.06;* ●, L = *0.31; X,* L = *1.0.*

specimens are straight lines without any knee within the limits of the applied stress range. The straight line plots, including that for $\Delta\sigma > \Delta\sigma_{th}$ in the open-hole dogbone specimen, are defined by the equation

$$\log N_f = A_f - B_f \cdot \Delta\sigma \tag{4}$$

Parameters A_f and B_f are tabulated in Table 4.

Proportion of Fatigue Crack Initiation and Growth Lives

The crack initiation portion of the total fatigue life (or fatigue fracture life), N_i/N_f, was observed to decrease with increasing stress range and load

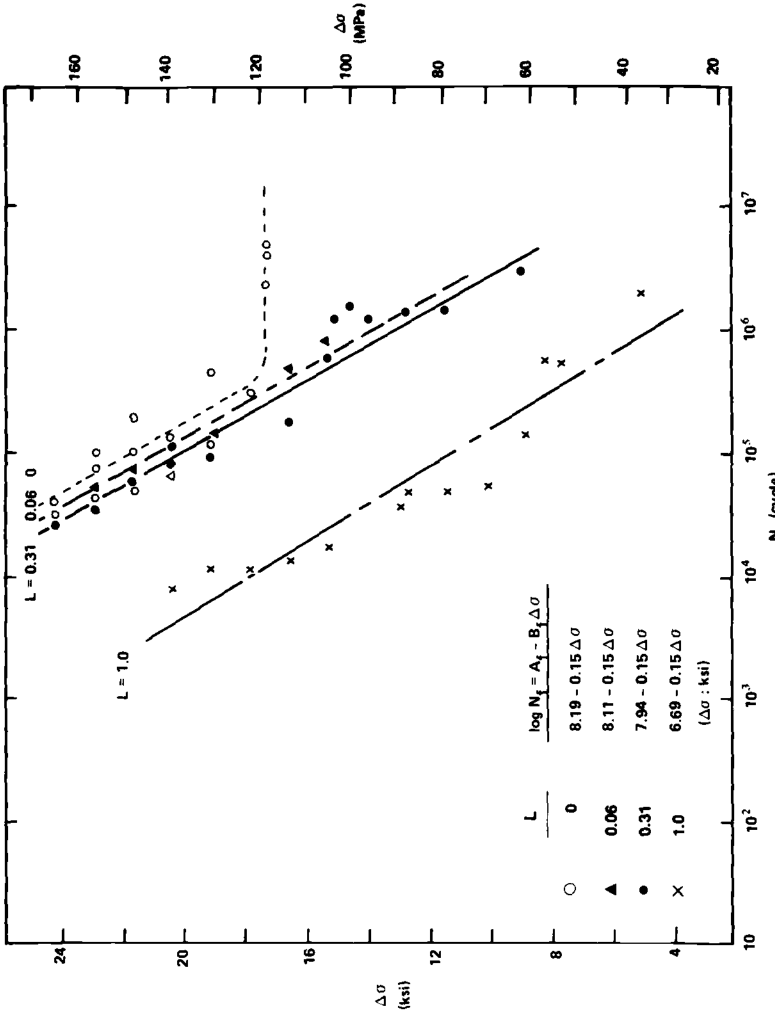

FIG. 10—*Variation of fatigue fracture life, N_f, with applied stress range, $\Delta\sigma$, in specimens of various load transfer levels.*

TABLE 4—*Parameters* A_f *and* B_f *in the fatigue fracture life equation,* $\log N_f = A_f - B_f \Delta\sigma$ ($\Delta\sigma$ = *ksi*).

Specimen	Load Transfer Level, L	A_f	B_f
Open-hole dogbone	0	8.19	0.15
Reverse dogbone joint	0.06	8.11	0.15
1½ dogbone joint	0.31	7.94	0.15
Double lap shear joint	1.0	6.69	0.15

transfer level. In Fig. 11, $\log (N_i/N_f)$ is plotted against the applied stress range, $\Delta\sigma$, for each group of specimens with a given level of load transfer. Those plots are straight and parallel lines, and can be defined by the following equation:

$$\log (N_i/N_f) = P - Q\,\Delta\sigma \tag{5}$$

Parameters P and Q are tabulated in Table 5. Parameter P decreases with increasing level of load transfer, whereas parameter $Q = 0.02$ remains constant.

The crack growth portion of total fatigue life, N_p/N_f, was observed to decrease with increasing total fatigue life. (Or, the crack initiation portion of total fatigue life, N_i/N_f, increases with increasing total fatigue life.) This variation is illustrated by the plots of N_p/N_f versus N_f on log–log coordinates in Fig. 12. Those plots are straight lines and are defined by the following equation:

$$N_p/N_f = 1 - N_i/N_f = U(N_f)^{-s} \tag{6}$$

or

$$N_i/N_f = 1 - U(N_f)^{-s} \tag{7}$$

Parameters U and S are tabulated in Table 6. Both parameters decrease with increasing level of load transfer.

Discussion

Fatigue Crack Initiation and Fracture

The $\Delta\sigma$ versus $\log N_i$ and $\Delta\sigma$ versus $\log N_f$ plots for the open-hole dogbone specimens of zero load transfer have knees at stress range $\Delta\sigma_{th}$ = 118.59 MPa (17.2 ksi), whereas those for the joint specimens are straight lines without any knee. This clearly indicates that a load transfer of not less than 0.06 in a joint specimen eliminates the knees of the $\Delta\sigma$ versus $\log N_i$ and $\Delta\sigma$ versus $\log N_f$ plots or the threshold stress range for fatigue crack initiation and fatigue limit stress range for fracture.

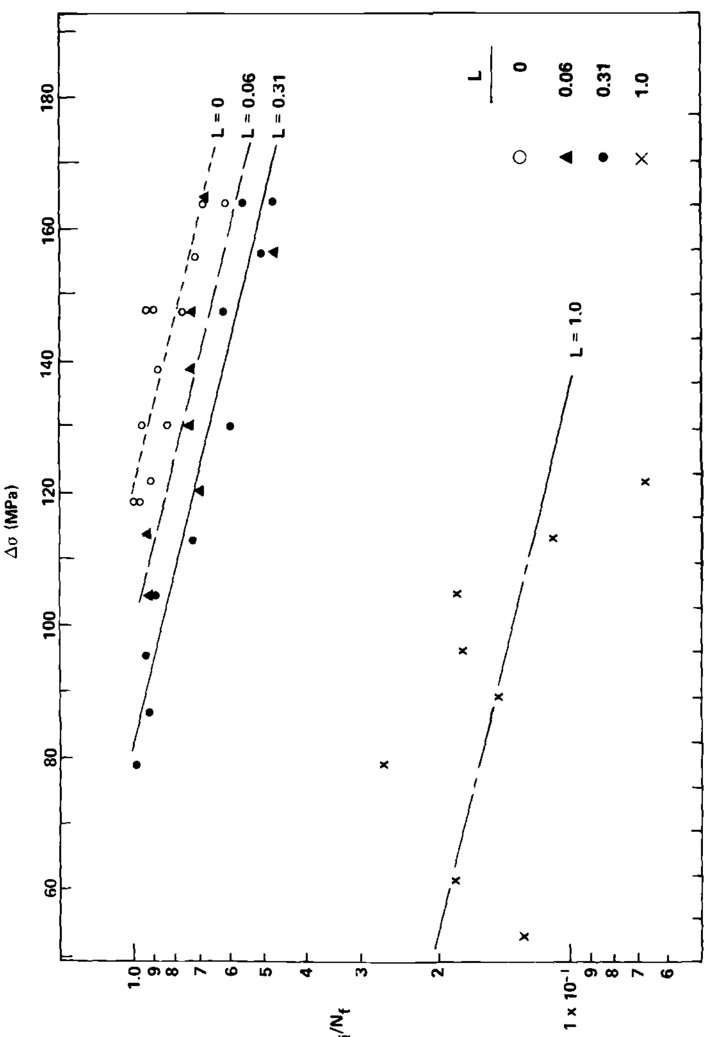

FIG. 11—*Variation of crack initiation portion of total fatigue life,* N_i/N_f*, with applied stress range,* $\Delta\sigma$.

TABLE 5—*Parameters* P *and* Q *in the equation for the crack initiation portion of total fatigue life, log* $(N_i/N_f) = P - Q\Delta\sigma$ $(\Delta\sigma = ksi)$.

Specimen	Load Transfer Level, L	P	Q
Open-hole dogbone	0	0.40	0.02
Reverse dogbone joint	0.06	0.33	0.02
1½ dogbone joint	0.31	0.28	0.02
Double lap shear joint	1.0	−0.51	0.02

The $\Delta\sigma$ versus log N_i and $\Delta\sigma$ versus log N_f plots for the joint specimens and the portions above the knees for the open-hole dogbone specimens are offset and parallel or nearly parallel. This is reflected in the values of parameters A_i and B_i of the fatigue crack initiation life equations, log $N_i = A_i - B_i\,\Delta\sigma$, and A_f and B_f of the fatigue fracture life equation, log $N_f = A_f - B_f\,\Delta\sigma$ (Tables 3 and 4). Parameters A_i and A_f decrease with increasing level of load transfer. On the other hand, Parameter B_i changes little and its average value is 0.18, and the parameter $B_f = 0.15$ does not change. The changes in the values of A_i and A_f with load transfer level, L, are illustrated in Figs. 13 and 14, and are defined by the following equations:

$$A_i = C_i - D_i L^{H_i} = 8.51 - 2.26\, L^{1.48} \tag{8}$$

$$A_f = C_f - D_f L^{H_f} = 8.19 - 1.50\, L^{1.53} \tag{9}$$

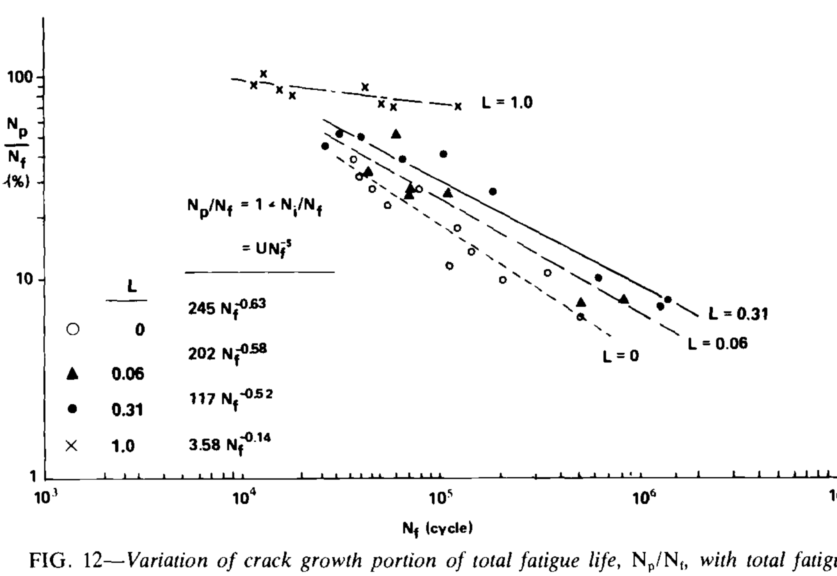

FIG. 12—*Variation of crack growth portion of total fatigue life,* N_p/N_f, *with total fatigue life,* N_f.

TABLE 6—*Parameters* U *and* S *in the equation for the crack growth portion of total fatigue life,* $N_p/N_f = U(N_f)^{-S}$

Specimen	Load Transfer Level, *L*	*U*	*S*
Open-hole dogbone	0	245	0.63
Reverse dogbone joint	0.06	202	0.58
1½ dogbone joint	0.31	117	0.52
Double lap shear joint	1.0	3.58	0.14

From Eqs 3, 4, 8, and 9, the fatigue crack initiation life, N_i, and the total fatigue life or fatigue fracture life, N_f, can be described as functions of stress range, $\Delta\sigma$ (ksi), and load transfer level, L, by the following equations.

$$\begin{aligned}\log N_i &= C_i - B_i\,\Delta\sigma - D_i L^{H_i}\\ &= 8.51 - 0.18\,\Delta\sigma - 22.6\,L^{1.48}\end{aligned} \tag{10}$$

$$\begin{aligned}\log N_f &= C_f - B_f\,\Delta\sigma - D_f L^{H_f}\\ &= 8.19 - 0.15\,\Delta\sigma - 1.50\,L^{1.53}\end{aligned} \tag{11}$$

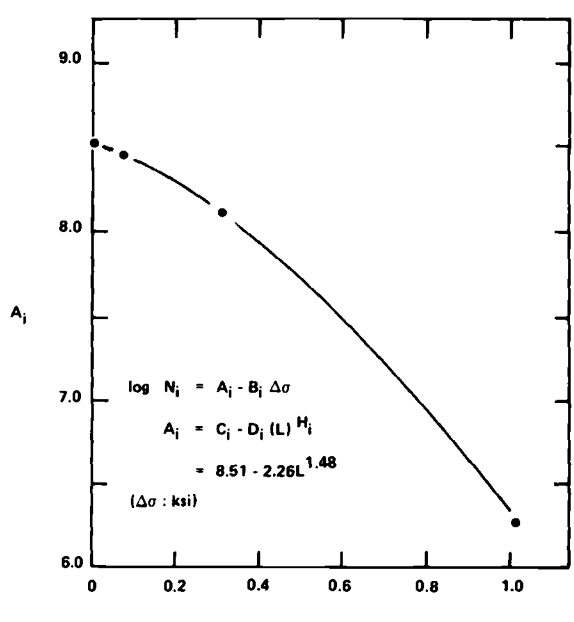

FIG. 13—*Variation of parameter,* A_i, *in fatigue crack initiation life equation, log* $N_i = A_i - B_i\,\Delta\sigma$, *with load transfer level,* L.

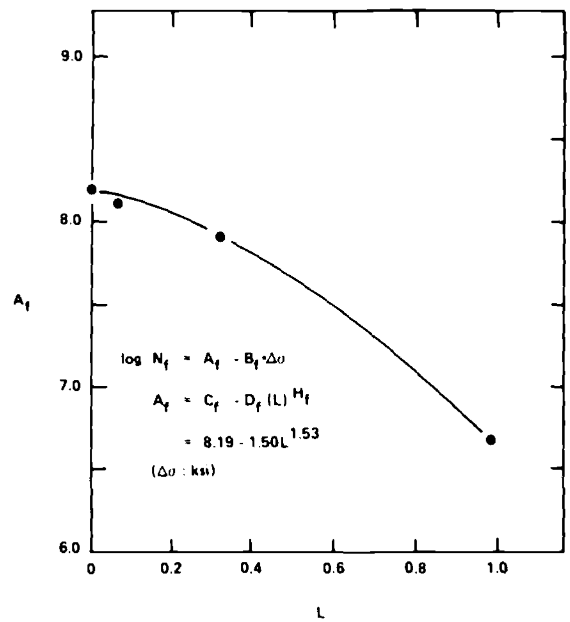

FIG. 14—*Variation of parameter,* A_f, *in fatigue fracture life equation, log* $N_f = A_f - B_f \Delta\sigma$, *with load transfer level,* L.

These equations show that the fatigue crack initiation and fracture lives decrease with increasing stress range and load transfer level.

Fatigue Crack Growth

The determined fatigue crack growth rate, $da/dN = (2.36 \times 10^{-7}) \cdot (\Delta K)^{2.89}$ mm/cycle, is not very different from the Margolis $da/dN = (5.41 \times 10^{-8}) \cdot (\Delta K)^{3.51}$ mm/cycle for an identical aluminum alloy [5]. The latter value was obtained by fatigue-testing compact tension specimens under the condition of stress ratio 0.5 and loading frequency 360 cpm in dry air [5].

Proportion of Fatigue Crack Initiation and Growth Lives

From the empirical equations for fatigue crack initiation and total fatigue lives, Eqs 7, 10, and 11, the crack initiation portion of total fatigue life, N_i/N_f, can be related with the stress range, $\Delta\sigma$, and the load transfer level, L, as

$$\begin{aligned} \log (N_i/N_f) &= [0.32 - (2.26 - 1.50\, L^{0.05})L^{1.48}] - 0.30\, \Delta\sigma \\ &= \log [1 - U(N_f)^{-s}] \end{aligned} \tag{12}$$

This equation indicates three things:

1. Log (N_i/N_f) decreases linearly with increasing stress range, $\Delta\sigma$, at a given level of load transfer, L.
2. N_i/N_f decreases with increasing level of load transfer, L, at a given stress range, $\Delta\sigma$.
3. N_i/N_f increases with increasing total fatigue life, N_f. Such variations are also observable in the plots of log (N_i/N_f) versus $\Delta\sigma$ in Fig. 11 and log (N_p/N_f) versus log N_f in Fig. 12.

The observed decrease of fatigue crack growth portion, N_p/N_f, with increasing total fatigue life, N_f, was also reported by Manson [*6*]. He investigated the fatigue behaviors of 410 stainless steel, 4130 steel, 2024-T4 aluminum alloy, pure aluminum, nickel, and polycarbonate resin, and related N_p/N_f and N_f as

$$N_p/N_f = 2.5\ N_f^{-1/3} \tag{14}$$

This equation is identical to Eq 6 in the form, but the parameters, or the intercept 2.5 and the slope $-⅓$ of the log-log plot, are different from those of Eq 6 in Table 6.

Summary

1. The load transfer levels are 0.06 for the reverse dogbone joint specimen and 0.31 for the 1½ dogbone joint specimen.

2. The fatigue crack initiation life, N_i, and the total fatigue life, N_f, decrease with increasing stress range, $\Delta\sigma$, and load transfer level, L. This relationship is defined by the equations

$$\log N_i = 8.51 - 0.18\ \Delta\sigma - 2.26\ L^{1.48}$$

$$\log N_f = 8.19 - 0.15\ \Delta\sigma - 1.50\ L^{1.53}$$

3. The fatigue crack growth rate, da/dN, as a function of the stress intensity factor range, ΔK, is

$$da/dN = (2.36 \times 10^{-7}) \cdot (\Delta K)^{2.89} \text{ mm/cycle}$$

4. The crack initiation portion of total fatigue life, N_i/N_f, decreases with increasing stress range, $\Delta\sigma$, and load transfer level, L, but increases with increasing total fatigue life, N_f. This relationship is defined by the equation

$$\log (N_i/N_f) = [0.32 - (2.26 - 1.50\ L^{0.05})L^{1.48}] - 0.03\ \Delta\sigma$$

$$= \log [1 - U(N_f)^{-s}]$$

APPENDIX

Stress Intensity Factor

The stress intensity factor, K, for a mechanically fastened joint with a fastener can be determined by superposition of two stress intensity factors, K_A and K_B, for an open-hole specimen and a loaded-hole specimen (Fig. 15).

The stress intensity factor, K_A MPa $\sqrt{m}$, for an open-hole specimen is

$$K_A = \frac{P_m}{Wt}\sqrt{\pi a}\cdot F_n(a/r)\sqrt{\sec\left\{\frac{\pi(na + 2r)}{2w}\right\}} \tag{15}$$

where

P_m = load bypassing fastener, N,
W = specimen width, m,
t = specimen thickness, m,
a = crack length, m,
n = 1 for a single crack,
n = 2 for a double crack,
$F_{1,2}(a/r)$ = Bowie factor for a single crack or a double crack emanating from an open-hole, and
$\sqrt{\sec\left\{\frac{\pi(na + 2r)}{2W}\right\}}$ = width correction factor.

In this equation, P_m/Wt N/m^2 is the gross stress away from the open hole.

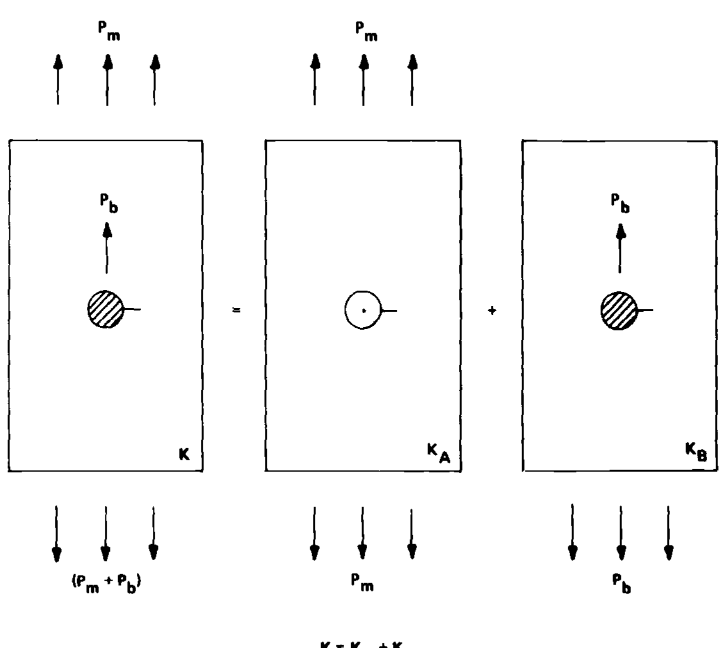

FIG. 15—*Stress intensity factor for a loaded-hole specimen.*

The stress intensity factor, K_B MPa $\sqrt{m}$, for a loaded-hole specimen is

$$K_B = \frac{P_b}{2rt} \cdot \sqrt{\pi a} \cdot F_{nb}(a/r) \cdot \sqrt{\sec\left\{\frac{\pi(na + 2r)}{2W}\right\}} \quad (16)$$

where P_b is the load transferring through fastener (N), and $F_{1b,2b}(a/r)$ is the correction factor for a single crack or a double crack emanating from a loaded hole. In this equation, $P_b/2rt$ N/m^2 is the bearing stress imposed on the fastener hole.

With Eqs 15 and 16, the stress intensity factor, K MPa $\sqrt{m}$, for a mechanically fastened joint with a fastener is determined as

$$K = K_A + K_B = \left[\frac{P_m}{Wt} \cdot F_n(a/r) + \frac{P_b}{2rt} \cdot F_{nb}(a/r)\right] \times \sqrt{(\pi a) \cdot \sec\left\{\frac{\pi(na + 2r)}{2W}\right\}} \quad (17)$$

Putting the total applied load, $P_m + P_b = P$, and the load transfer level, $L = P_b/P$, Eq 17 becomes

$$K = \frac{P}{t}\left[\left(\frac{1 - L}{W}\right) \cdot F_n(a/r) + \frac{L}{2r} \cdot F_{nb}(a/r)\right]\sqrt{(\pi a) \cdot \sec\left\{\frac{\pi(na + 2r)}{2W}\right\}} \quad (18)$$

Putting $\Delta P = P_{max} - P_{min}$, where P_{max} is the maximum applied load and P_{min} the minimum applied load, the range of stress intensity factor, ΔK, is

$$\Delta K = \frac{\Delta P}{t}\left[\left(\frac{1 - L}{W}\right) \cdot F_n(a/r) + \frac{L}{2r} \cdot F_{nb}(a/r)\right]\sqrt{(\pi a) \cdot \sec\left\{\frac{\pi(na + 2r)}{2W}\right\}} \quad (19)$$

References

[1] Bowie, O. L., *Journal of Mathematics and Physics*, Vol. 35, 1956, pp. 60–73.
[2] Isida, M., *Journal of Applied Mechanics*, Vol. 33, 1966, pp. 674–675.
[3] Hall, L. R., Shah, R. C., and Engstrom, W. L., "Fracture and Fatigue Crack Growth Behavior of Surface Flaws and Flaws Originating at Fastener Holes, Vol. I—Results and Discussion," Report No. AFFDL-TR-74-47, Air Force Flight Dynamics Laboratory, Wright-Patterson AFB, OH, May 1974.
[4] Paris, P. and Erdogan, F., *Journal of Basic Engineering*, Vol. 85, 1963, pp. 528–534.
[5] Margolis, W. S., "F-16 Material Test Allowables for Aluminum Alloy 7475, 3.0″ Plate –T7351 Temper, and 0.5″ Plate (92″ Width) –T7651 Temper and –T7351 Temper," Report No. 16PR926, General Dynamics, Fort Worth, TX, April 1978.
[6] Manson, S. S., *Experimental Mechanics*, Vol. 5, 1965, pp. 193–226.

Jann N. Yang,[1] Sherrell D. Manning,[2] and James L. Rudd[3]

Evaluation of a Stochastic Initial Fatigue Quality Model for Fastener Holes

REFERENCE: Yang, J. N., Manning, S. D., and Rudd, J. L., "**Evaluation of a Stochastic Initial Fatigue Quality Model for Fastener Holes,**" *Fatigue in Mechanically Fastened Composite and Metallic Joints, ASTM STP 927,* John M. Potter, Ed., American Society for Testing and Materials, Philadelphia, 1986, pp. 118–149.

ABSTRACT: An initial fatigue quality (IFQ) model, based on stochastic crack growth and the equivalent initial flaw size (EIFS) concept, is described and evaluated for the durability analysis of relatively small cracks in fastener holes [for example, <2.54 mm (0.10 in.)]. The IFQ model uses a stochastic crack growth rate model which accounts for crack growth rate dispersion. Procedures and concepts are also described and evaluated for optimizing initial flaw size distribution parameters based on pooled EIFS results. Fatigue crack growth test results for 7475-T7351 aluminum specimens subjected to fighter and bomber load spectra are used to evaluate the proposed IFQ model and model calibration procedures. The cumulative distribution of crack size at any given time and the cumulative distribution of the time-to-crack initiation (TTCI) at any given crack size are predicted using the derived EIFS distribution and a stochastic crack growth approach. The predictions compare well with the actual test results in the small-crack-size region. The methods described are very promising for durability analysis applications.

KEY WORDS: durability, fatigue, extent of damage, small crack size, equivalent initial flaw size (EIFS), crack size distribution, crack exceedance probability, stochastic crack growth, probabilistic fracture mechanics, initial fatigue quality (IFQ), time-to-crack initiation (TTCI)

Metallic airframes contain thousands of fastener holes which are susceptible to fatigue cracking in service. The accumulation of relatively small fatigue cracks in fastener holes [for example, 0.762 to 1.27 mm (0.03 to 0.05 in.)] must be accounted for in the design of aircraft structures to assure that the structures will be durable and can be economically maintained [*1*–*3*].

[1] Professor, School of Engineering and Applied Science, George Washington University, Washington, DC 20052.
[2] Engineering specialist senior, Structures Technology Staff, General Dynamics, Fort Worth, TX 76101.
[3] Aerospace engineer, Air Force Wright Aeronautical Laboratories, Flight Dynamics Laboratory, Wright-Patterson Air Force Base, OH 45433.

A durability analysis methodology has recently been developed for quantifying the extent of fatigue damage in fastener holes as a function of time and applicable design variables [*4–21*]. This methodology is based on a fracture mechanics philosophy, combining a probabilistic format with a deterministic crack growth approach. The initial fatigue quality (IFQ) of fastener holes is treated as a random variable and is represented by an equivalent initial flaw size (EIFS) distribution. The existing durability analysis methodology has been demonstrated for making crack exceedance predictions in the small-crack-size region [(for example, <2.54 mm (0.10 in.)] for a full-scale aircraft structure under both fighter and bomber load spectra [*10,13,19,21*].

Further research is now being conducted [*22*] to (1) extend the present durability analysis methodology to the large-crack-size region [(for example, >2.54 mm (0.10 in.)], (2) refine the methods for determining a generic EIFS distribution, (3) develop procedures for optimizing the equivalent initial flaw size distribution (EIFSD) parameters, and (4) develop a better understanding of the effects of crack growth rate dispersion on the EIFS distribution and on the accuracy of crack exceedance predictions in both the small- and large-crack-size regions.

In the current durability analysis methodology [*8,10,13,14*], the EIFS is determined by back-extrapolating available fractographic results [for example, Refs *11* and *23*] to time zero using a single deterministic crack growth equation, referred to as the EIFS master curve,

$$\frac{da(t)}{dt} = Q[a(t)]^b \tag{1}$$

where

$da(t)/dt$ = crack growth rate,
$a(t)$ = crack size at any time t, and
Q and b = empirical constants which are dependent upon the load spectrum and other design parameters.

The crack growth rate, however, involves statistical variability, which is not accounted for in back-extrapolation. Hence, the statistical distribution of EIFS thus established contains the statistical dispersion of the crack growth rate in the very small-crack-size region. This approach is quite reasonable if the resulting EIFS distribution is employed to predict the statistical crack growth damage accumulation in service using a deterministic service crack growth master curve in the small-crack-size region. This has been demonstrated in Refs *8, 10, 13,* and *14.* The main advantage of such an approach is that the durability analysis procedure can be simplified mathematically.

Another possible approach is to obtain the EIFS values by back-extrapolating available fractographic results stochastically. Thus, the statistical dispersion of the crack growth rate in the small-crack-size region is filtered out, and the resulting EIFS distribution represents the true initial fatigue quality (IFQ). Such an EIFS distribution will have a smaller dispersion than that obtained using a deterministic EIFS crack growth master curve. This EIFS model is referred to as the stochastic-based initial fatigue quality model. In predicting the statistical crack growth damage accumulation in service using the stochastic-based EIFS model, however, the stochastic crack growth rate equation should be used. As a result, the feasibility of such a stochastic approach depends essentially on the establishment of a reasonable but simple stochastic crack propagation model.

The objectives of this paper are twofold: to develop the durability analysis methodology using the stochastic-based IFQ model, and to evaluate proposed EIFS data pooling methods and procedures for optimizing the EIFS distribution parameters.

Analytical expressions are derived for the cumulative distributions of the time required to initiate a crack of any size, and for the crack size at any service life. These expressions are based on a stochastic transformation of the cumulative distribution of EIFS and the theorem of total probability. Actual crack propagation results for two fractographic data sets (7475-T7351 aluminum fastener hole specimens; fighter and bomber load spectra) in the small-crack-size region are used in the investigation [*23*]. A correlation study performed to compare the results of the stochastic-based IFQ model with actual fractographic results produced very reasonable correlations. The proposed procedures for EIFS data pooling and for optimizing the EIFS distribution parameters look promising for future durability analysis applications.

Stochastic Crack Growth Model

A simple stochastic crack growth approach has recently been developed [*24–28*] which accounts for the statistical dispersion of the crack growth rate for the growth of a single initial flaw. This approach is based on the randomization of the crack growth rate equation. In the case of the crack growth power law of Eq 1, the randomized crack growth rate equation is given by

$$\frac{da(t)}{dt} = X(t)Q[a(t)]^{b} \tag{2}$$

in which $X(t)$ is a stationary lognormal random process (positive stochastic process) taking values around unity. Thus, Eq 1 represents the central tendency of the crack growth behavior, whereas, in Eq 2 the statistical variability is taken care of by the random process $X(t)$. For the crack propagation in fastener holes, the lognormal stochastic process $X(t)$ is assumed to be totally correlated at any two time instants, indicating that $X(t)$ is a random variable, that is, $X(t) = X$

$$\frac{da(t)}{dt} = XQ[a(t)]^b \tag{3}$$

in which X is a lognormal random variable with a median of 1.0. Such a model is referred to as the lognormal random variable model [*26*], and it has been demonstrated to be very reasonable [*24–26*]. The model simplifies the stochastic crack growth analysis significantly and it will be used in this paper.

Taking the logarithm of both sides of Eq 3 yields

$$Y = bU + q + Z \tag{4}$$

where

$$\left.\begin{aligned} Y &= \log \frac{da(t)}{dt}, \\ q &= \log Q, \\ U &= \log a(t), \\ \text{and } Z &= \log X \end{aligned}\right\} \tag{5}$$

Since X is a lognormal random variable with a median of 1.0, it follows from Eq 5 that $Z = \log X$ is a normal random variable with zero mean and standard deviation σ_z. The crack growth rate parameters b and Q as well as the standard deviation, σ_z, of Z can be estimated from the log crack growth rate, $\log [da(t)/dt] = Y$, versus log crack length, $\log a(t) = U$, data, denoted (Y_i, U_i) for $i = 1, 2, \ldots, n$, using Eq 4 and the linear regression analysis. Since Eq 4 is linear, the results obtained from the method of linear regression are identical to those of the method of least-squares or the method of maximum likelihood [*24–28*]. Expressions for b, Q, and σ_z are given by

$$\left.\begin{aligned} b &= \frac{n\Sigma U_iY_i - (\Sigma U_i)(\Sigma Y_i)}{n\Sigma U_i^2 - (\Sigma U_i)^2} \\ Q &= 10^\lambda;\ \lambda = \frac{\Sigma Y_i - b\Sigma U_i}{n} \\ \sigma_z &= \left\{\frac{\Sigma[Y_i - (q - bU_i)]^2}{n - 1}\right\}^{1/2} \end{aligned}\right\} \tag{6}$$

in which n = number of samples (for example, crack growth rate data) and the other terms have been previously defined.

Yang et al [*24,26*] have investigated two extremes of the random process $X(t)$. At one extreme, $X(t)$ is totally uncorrelated (that is, a white noise process model) and at the other extreme, $X(t)$ is totally correlated at all times (that is, $X(t) = X$ is a random variable, referred to as the random variable model). It has been shown by Yang et al [*24,26*] that, for a given data set, the random variable model results in the largest statistical dispersion of fatigue crack growth accumulation in the class of random process $X(t)$.

The random process model $X(t)$ is mathematically complex. It requires a large fatigue crack growth data base and a simulation procedure to make crack growth accumulation predictions. On the other hand, the random variable model requires only a limited amount of fatigue crack growth data to implement and it is mathematically simple. Moreover, very reasonable fatigue crack growth accumulation predictions for fastener holes have been obtained using the random variable model [*24–26*]. For these reasons, the random variable crack growth model is attractive for the durability analysis of fatigue cracks in fastener holes in the small-crack-size region (for example, <2.54 mm (0.10 in.)) where large crack growth dispersions have been observed [*11,23,29*].

Stochastic Crack Growth Analysis

Expressions are derived for predicting the cumulative distributions of crack size at any given time, t, and of TTCI for any given crack size, a_1. Essential elements of the stochastic crack growth approach are described in Fig. 1 and details are provided later.

Equivalent Initial Flaw Size (EIFS) Concept

An equivalent initial flaw size (EIFS) is a hypothetical initial flaw assumed to exist in a structural detail which characterizes the equivalent effect of actual flaws produced by the manufacturing process. Such flaws must be consistently defined so that the EIFSs for different fractographic specimens are on the same baseline. EIFSs are defined by back-extrapolating suitable fractographic results to time zero (Fig. 1, Frame A). The objective is to define a statistical distribution of EIFS and then to verify that the derived distribution will provide reasonable predictions for the cumulative distributions of TTCI and $a(t)$ (Fig. 1, Frame D).

Analysis Procedures

1. EIFS is a random variable; each individual value is determined by back-extrapolating fractographic results for each individual crack (or specimen).

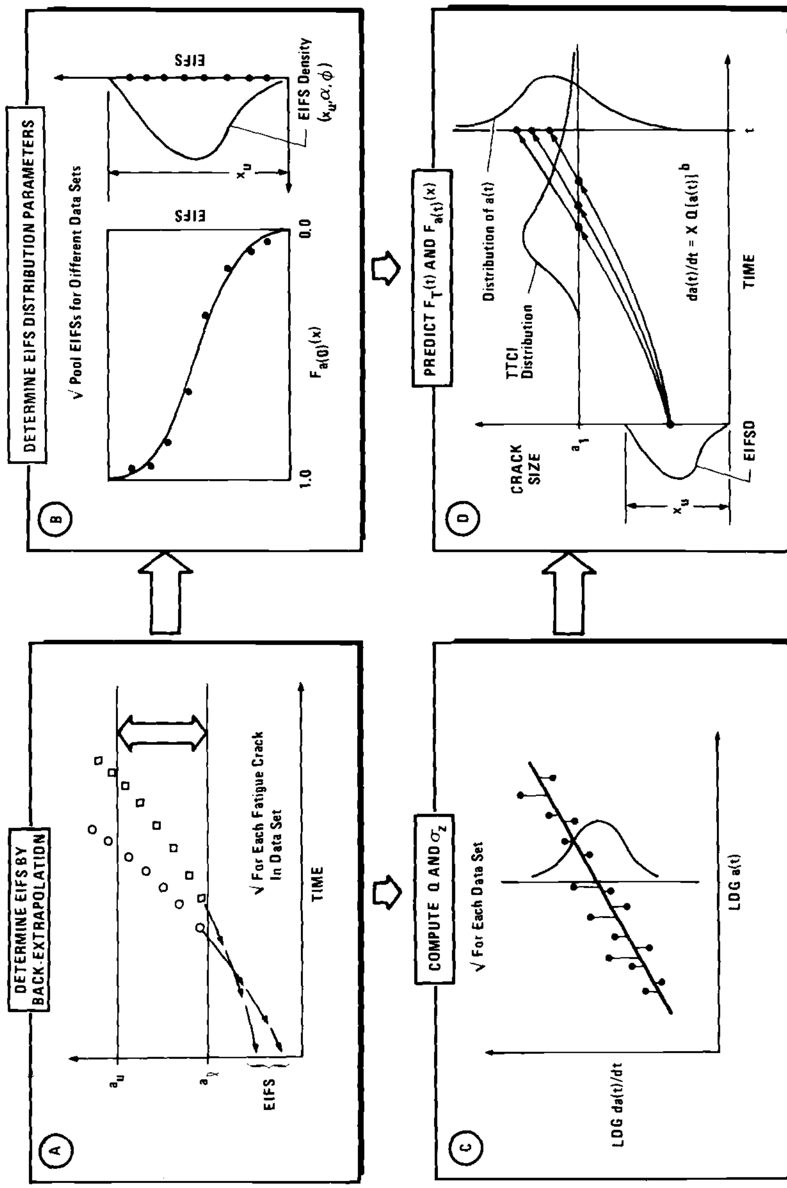

FIG. 1—*Essential elements of stochastic crack growth approach.*

2. The population of EIFSs is fitted by a suitable cumulative distribution, denoted $F_{a(0)}(x)$ (Fig. 1, Frame B).

3. A stochastic crack growth law, such as Eq 3, which accounts for the statistical dispersion of the crack growth rate (Fig. 1, Frame C), provides the basis for growing flaws backward and forward.

4. A stochastic transformation of $F_{a(0)}(x)$ is made using the crack growth law, Eq 3, to obtain expressions for the cumulative distributions of crack size, $F_{a(t)}(x)$, and of TTCI, $F_{T(a_1)}(t)$; see Fig. 2.

Crack Size-Time Relationships

Two different crack size-time relationships can be obtained by integrating Eq 3, considering $b = 1$ and $b \neq 1$, from $t = 0$ to any time, t. The resulting expressions for $b = 1$ and $b \neq 1$ are shown in Eqs 7 and 8, respectively:

$$a(t) = a(0) \exp [XQt] \qquad b = 1 \tag{7}$$

$$a(t) = \{[a(0)]^{-c} - cQtX\}^{-1/c} \qquad b \neq 1 \tag{8}$$

where

$a(t)$ = crack size at any time, t,
$a(0)$ = crack size at $t = 0$ (EIFS),
Q = crack growth rate constant, $c = b - 1$, and
X = lognormal random variable with median of 1.0.

Cumulative Distribution of EIFS

Various distribution functions defined in the positive domain may be used to fit the EIFS values, such as the Weibull, lognormal, and beta. The following distribution function, which is derived based on the three-parameter Weibull distribution for TTCI and the deterministic crack growth law of Eq 1 with $b = 1$, will be used herein:

$$F_{a(0)}(x) = \begin{cases} \exp\left\{-\left[\dfrac{\ell n\,(x_u/x)}{\phi}\right]^{\alpha}\right\} & 0 \leqq x \leqq x_u \\ = 1.0 & x \geqq x_u \end{cases} \tag{9}$$

in which $F_{a(0)}(x) = P[a(0) \leq x]$ is the cumulative distribution of EIFS, indicating the probability that the EIFS, $a(0)$, will be smaller than or equal to a value x. In Eq 9, x_u = the upper bound of EIFS and α and ϕ are two empirical constants [*13*]. In the original derivation of Eq 9 in Ref *13*, the notation "$Q\beta$" was used instead of "ϕ." To distinguish between the deterministic and stochastic crack growth approaches, the notation "ϕ" is used herein. The expression given by Eq 9 is considered to be reasonable for the distribution of the stochastic-based EIFS.

Cumulative Distribution of Crack Size

The conditional distribution function of the crack size, $a(t)$, denoted by $F_{a(t)}(x|z) = P[a(t) \leq x|X = z]$, given that the lognormal random variable X takes a value z, can be obtained from Eq 9 through a transformation of Eqs 7 and 8 for $b = 1$ and $b \neq 1$, respectively. Then, the unconditional cumulative distribution of crack size $a(t)$, $F_{a(t)}(x) = P[a(t) \leq x]$, is obtained from the conditional one, $F_{a(t)}(x|z)$, using the theorem of total probability. The results for $F_{a(t)}(x)$ are shown in Eqs 10 and 11 for $b = 1$ and $b \neq 1$, respectively.

$$F_{a(t)}(x) = \int_0^{\infty} \exp\left\{-\left[\frac{Qzt + \ell n\,(x_u/x)}{\phi}\right]^{\alpha}\right\} f_X(z)dz;\; b = 1 \quad (10)$$

$$F_{a(t)}(x) = \int_0^{\infty} \exp\left\{-\left[\frac{c\,\ell n\, x_u + \ell n\,(x^c + cQtz)}{c\phi}\right]^{\alpha}\right\} \times f_X(z)dz;\; b \neq 1 \quad (11)$$

In Eqs 10 and 11, $f_X(z)$ is the lognormal probability density function of X given by

$$f_X(z) = \frac{\log e}{\sqrt{2\pi}\, z\sigma_z} \exp\left\{-\frac{1}{2}\left(\frac{\log z}{\sigma_z}\right)^2\right\} \quad (12)$$

in which σ_z is the standard deviation of the normal random variable $Z = \log X$ given in Eq 5.

Cumulative Distribution of TTCI

Let $T(a_1)$ be the random time to initiate a crack size, a_1. Then, the distribution of $T(a_1)$, denoted $F_{T(a_1)}(t) = P[T(a_1) \leq t]$, can be derived from that of $a(t)$ as follows. Since the event $\{T(a_1) \leqslant t\}$ is the same as the event $\{a(t) \geq a_1\}$, one has

$$F_{T(a_1)}(t) = 1 - F_{a(t)}(a_1) \quad (13)$$

Substituting Eqs 10 and 11 into Eq 13, one obtains for $b = 1$ and $b \neq 1$, respectively,

$$F_{T(a_1)}(t) = 1 - \int_0^\infty \exp\left\{-\left[\frac{Qzt + \ell n\,(x_u/a_1)}{\phi}\right]^\alpha\right\} f_X(z)dz;\; b = 1 \quad (14)$$

$$F_{T(a_1)}(t) = 1 - \int_0^\infty \exp\left\{-\left[\frac{c\,\ell n\, x_u + \ell n\,(a_1^c + cQtz)}{c\phi}\right]^\alpha\right\} \times f_X(z)dz;\; b \neq 1 \quad (15)$$

in which $f_X(z)$ is given by Eq 12.

Equations 11 to 12 and 14 to 15 are not amenable to analytical integrations. However, these equations can easily be solved by a straightforward numerical integration.

Determination of EIFS Distribution Parameters

Procedures are described and discussed for determining EIFS values based on the stochastic crack growth approach and fractographic data. EIFS pooling concepts and justification are considered, and procedures are described for optimizing the EIFS distribution parameters in Eq 9, that is, x_u, α, and ϕ. For brevity, the discussion is limited to the $b = 1$ case.

Stochastic-Based EIFS

EIFS values are determined by back-extrapolating suitable fractographic data based on fatigue cracking results in fastener holes without intentional initial flaws. Such data are currently available for both straight-bore and countersunk fastener holes (for example, Refs *11* and *23*).

When the deterministic crack growth approach is used [*5,30,31*] to determine EIFSs, the same EIFS master curve is used to back-extrapolate to time zero for each fatigue crack in the fractographic data set. In this case the statistical dispersion of the crack growth rate is included in the resulting EIFS values.

When the crack growth rate is treated as a stochastic process, such as in Eq 3, the fractographic results should be back-extrapolated to time zero using the applicable crack growth records for a given fractographic sample (specimen). A stochastic-based EIFS value is obtained for each fractographic sample in the data set. In this case, the statistical dispersion of the crack growth rate is reflected in the random variable X, and hence it is filtered out from the EIFS.

A stochastic-based EIFS value can be obtained for a given fractographic sample, say the jth specimen, based on

$$a_j(0) = a_j(t) \exp\left[-X_j Q t\right] \tag{16}$$

in which X_j is the jth sample value of the lognormal random variable X, and $a_j(0)$ and $a_j(t)$ are the corresponding jth sample values of EIFS and the crack size at time t, respectively.

Using the least-squares criterion, one obtains the expression for $a_j(0)$

$$a_j(0) = \exp\left\{\frac{[\Sigma\, \ell n\, a_j(t_i)](\Sigma t_i^2) - (\Sigma t_i)[\Sigma(t_i)\, \ell n\, a_j(t_i)]}{N\Sigma t_i^2 - (\Sigma t_i)^2}\right\} \tag{17}$$

in which $a_j(t_i)$ is the crack size of the jth specimen at time t_i and N is the number of $[a_j(t_i), t_i]$ pairs for the jth fractographic sample. Thus, using Eq 17, $a_j(0)$ can be determined directly from $[a_j(t_i), t_i]$ pairs without computing the $X_j Q$ value in Eq 16.

It has been shown that the range of the fractographic crack size used affects the EIFS values [*10*]. Therefore, EIFS values should be determined using fractographic results in the same crack size range. For example, the upper and lower bounds of the crack size range are denoted a_u and a_ℓ, as shown in Fig. 1, Frame A.

EIFS Pooling Concepts

For practical durability analysis, an EIFS distribution is needed to represent the initial fatigue quality variation of the fastener holes. Ideally, such a distribution can be determined for a given material, fastener hole type (for example, straight-bore or countersunk), and drilling procedure from fractographic results reflecting different test variables (such as stress level, bolt load transfer percentage, and load spectra). The resulting EIFS distribution can be used to perform durability analyses for other conditions. In other words, an EIFS distribution (EIFSD), based on different fractographic results, is sought which is suitable for a broad range of durability analysis applications (for example, different stress levels, bolt load transfer percentages, and load spectra).

One way to justify using a given equivalent initial flaw size distribution (EIFSD) for a general durability analysis is to define the EIFSD parameters using pooled EIFS values obtained from different fractographic data sets. For example, fractographic results are available for the same material, fastener hole type/fit, and drilling procedure for different stress levels, bolt load transfer percentages, and load spectra [*11,23*]. If compatible EIFSs can be determined for different fractographic data sets, then the EIFSs can be pooled to determine the EIFSD parameters. Pooling the EIFSs is very

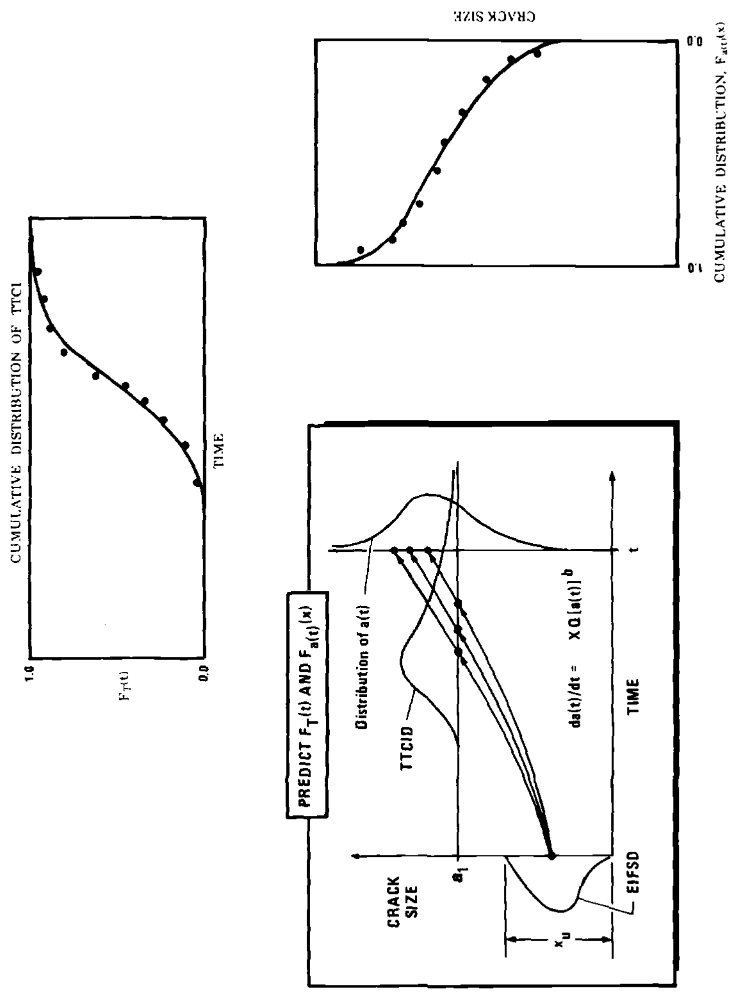

FIG. 2—*Stochastic crack growth of EIFSD.*

desirable because this increases the sample size and therefore the confidence in the EIFSD parameters. Also, since different fractographic data sets are used to determine the EIFSD parameters, it forces the derived EIFSD to cover a wider range of variables.

Optimization of EIFS Distribution Parameters

Once the EIFSs have been determined for selected fractographic data sets, they can be pooled and the parameters x_u, α, and ϕ can be optimized to "best fit" the pooled EIFSs and theoretical cumulative distribution of EIFS, $F_{a(0)}(x)$, shown in Eq 9. The optimization procedure described below is intended for Eq 9, but the same ideas can be applied to other $F_{a(0)}(x)$ distributions.

In Eq 9, x_u defines the EIFS upper-bound limit, that is, the maximum initial flaw size in $F_{a(0)}(x)$. A value of $x_u = 0.762$ mm (0.03 in.) is assumed to be a reasonable upper-bound limit for the EIFSD. This limit is arbitrarily based on the typical economical repair limit for fastener holes [*13,30,31*].

Another reason for limiting x_u to <0.762 mm (0.03 in.) is to eliminate the probability of exceeding a crack size of 0.762 mm (0.03 in.) at time zero. This is equivalent to assuming that no fastener hole will have an initial flaw size >0.762 mm (0.03 in.). If a larger x_u limit is used, then the probability of exceeding an initial flaw size of 0.762 mm (0.03 in.) will not be zero, which implies that some fastener holes could have an initial flaw size greater than the economical repair limit before the structure enters into service.

The EIFSD parameters x_u, α, and ϕ in Eq 9 are optimized using the following iterative procedure.

1. Assume a value of x_u; with the largest EIFS $\leq x_u \leq 0.762$ mm (0.03 in.).
2. Compute α and ϕ by least-squares fitting the pooled EIFSs to $F_{a(0)}(x)$ given in Eq 9. Equation 9 is transformed into the following linear least-squares fit form:

$$W = \alpha V + B \tag{18}$$

where

$$\left.\begin{aligned} W &= \ell n \{-\ell n\, F_{a(0)}(x)\} \\ V &= \ell n \{\ell n\, (x_u/x)\}, \text{ and} \\ B &= -\alpha\, \ell n\, \phi \end{aligned}\right\} \tag{19}$$

Let $x_i (i = 1, 2, \ldots, N)$ be the ith smallest EIFS value and N be the number of EIFS values pooled. The distribution function corresponding to

x_i is given by $F_{a(0)}(x_i) = i/(N + 1)$. Then the parameters α and ϕ in Eq 18 can be determined using the following least-squares fit equations:

$$\alpha = \frac{N\Sigma V_i W_i - (\Sigma V_i)(\Sigma W_i)}{N\Sigma V_i^2 - (\Sigma V_i)^2}; \qquad \phi = \exp\left(\frac{\alpha\Sigma V_i - \Sigma W_i}{\alpha N}\right) \tag{20}$$

where V_i and W_i are the sample values of V and W associated with x_i and $F_{a(0)}(x_i)$, respectively, as defined in Eq 18.

3. Compute the goodness-of-fit of the established $F_{a(0)}(x)$ for the given x_u, α, and ϕ. The standard error and Kolmogorov-Smirnov statistics (K-S value) are two reasonable measures of goodness-of-fit tests. The standard error, denoted σ_E, is expressed as

$$\sigma_E = \left\{\frac{\Sigma\left[\dfrac{k}{N + 1} - F_{a(0)}(x_k)\right]^2}{N}\right\}^{1/2} \tag{21}$$

in which all the EIFS sample values are arranged in an ascending order (x_1, x_2, . . . , x_k, . . . , x_N), k is the rank of EIFS value and N is the total number of pooled EIFS samples. The K-S value, denoted $D_{\max}$, is the maximum absolute difference between the ranked EIFS values (according to k/N and the theoretical $F_{a(0)}(x_k)$ values given by

$$D_{\max} = \max_{k=i}^{N}\left[\left|\frac{k}{N} - F_{a(0)}(x_k)\right|\right] \tag{22}$$

4. Steps 1 through 3 are repeated to minimize the standard error, σ_E, or K-S value, $D_{\max}$.

Determination and Normalization of Forward Crack Growth Rate Parameters

The statistical distribution of the crack growth damage in service, such as $F_{a(t)}(x)$ and $F_{T(a_1)}(t)$ given by Eqs 10 through 15, is derived using the EIFS distribution, $F_{a(0)}(x)$, and the forward stochastic crack growth rate equation, Eq 3. The parameters b, Q, and σ_z appearing in Eq 3 have been obtained in Eq 6 when the fractographic data for the applicable service environment are available. When the fractographic results are not available, however, these parameters should be determined from the general crack growth computer program. This subject will be discussed in another paper.

When pooled EIFS results are used to determine x_u, α, and ϕ in Eq 9, the Q value for a given fractographic data set should be normalized to the same baseline as the EIFSD. This is needed to ensure that $F_{a(t)}(x)$ and

$F_{T(a_1)}(t)$ predictions for a given data set are consistent with the basis for the EIFSD.

Let $(x_u, \alpha, \phi)_{\text{data set}}$ and $Q_{\text{data set}}$ be, respectively, the EIFSD parameters and the forward crack growth rate parameter using a given fractographic data set alone (without pooling procedures). Then, the normalized Q value for such a given data set, denoted $\hat{Q}_{\text{data set}}$, in the forward crack growth analysis is suggested to be

$$\hat{Q}_{\text{data set}} = \frac{\phi_{\text{pooled}}}{\phi_{\text{data set}}} (Q_{\text{data set}}) \tag{23}$$

Thus, when pooled EIFS results are used, the Q value appearing in Eqs 10 through 15 for a given fractographic data set should be replaced by $\hat{Q}_{\text{data set}}$. This approach will be illustrated in the following correlation study.

Correlation with Test Results

Fatigue crack growth results are available for fatigue cracking in fastener holes without the presence of intentional initial flaws (for example, Ref *23*). Two fractographic data sets from Ref *23* will be used to evaluate (1) the stochastic-based IFQ model developed, (2) the proposed EIFS data pooling procedure, (3) the procedure for optimizing the EIFSD parameters, and (4) the effectiveness of the derived EIFSD and stochastic crack growth approach for making $F_{a(t)}(x)$ and $F_{T(a_1)}(t)$ predictions. The distribution of the crack size, $F_{a(t)}(x)$, will be considered at two different service times and that of TTCI, $F_{T(a_1)}(t)$, will be considered at crack sizes $a_1 = 0.762$ mm (0.03 in.), 1.27 mm (0.05 in.), and 2.54 mm (0.10 in.). Predicted results will be compared with actual fractographic data.

Fractographic Data Sets

Two fractographic data sets, identified as "WPF" and "WPB," reflect 7475-T7351 aluminum replicate dogbone specimens with a 6.35-mm-diameter, ($\frac{1}{4}$-in.) straight-bore, centered hole containing an unloaded protruding head steel bolt (NAS6204) with a clearance fit. The WPF and WPB data sets were fatigue-tested in a laboratory air environment using a fighter spectrum and bomber spectrum, respectively. A maximum gross section stress of 234.4 MPa (34 ksi) was selected for each spectrum. The test specimens were fatigue-tested without intentional flaws in the fastener hole and natural fatigue cracks were allowed to occur. Following the fatigue test, the largest fatigue crack in each fastener hole was evaluated fractographically. Fractographic results [that is, $a(t)$ versus t records] were presented in Ref *23*. The number of fatigue cracks used in this investigation is 33 for the WPF data set and 32 for the WPB data set.

TABLE 1—*EIFSs for data sets WPF and WPB based on stochastic crack growth.*

Rank	WPF EIFS		WPB EIFS	
	mm	(in.)	mm	(in.)
1	0.0055	(0.00022)	0.0015	(0.000060)
2	0.0093	(0.00037)	0.0031	(0.000124)
3	0.0098	(0.00039)	0.0032	(0.000126)
4	0.0098	(0.00039)	0.0042	(0.000165)
5	0.0117	(0.00046)	0.0046	(0.000183)
6	0.0121	(0.00048)	0.0048	(0.000187)
7	0.0123	(0.00049)	0.0049	(0.000191)
8	0.0125	(0.00049)	0.0053	(0.000210)
9	0.0133	(0.00052)	0.0057	(0.000224)
10	0.0136	(0.00053)	0.0062	(0.000246)
11	0.0148	(0.00058)	0.0067	(0.000264)
12	0.0158	(0.00062)	0.0068	(0.000266)
13	0.0159	(0.00063)	0.0069	(0.000275)
14	0.0167	(0.00066)	0.0075	(0.000297)
15	0.0181	(0.00071)	0.0085	(0.000336)
16	0.0232	(0.00091)	0.0086	(0.000339)
17	0.0244	(0.00096)	0.0093	(0.000366)
18	0.0252	(0.00099)	0.0097	(0.000382)
19	0.0254	(0.00100)	0.0099	(0.000388)
20	0.0260	(0.00102)	0.0101	(0.000396)
21	0.0264	(0.00104)	0.0110	(0.000434)
22	0.0268	(0.00106)	0.0112	(0.000442)
23	0.0273	(0.00108)	0.0114	(0.000451)
24	0.0337	(0.00132)	0.0118	(0.000467)
25	0.0353	(0.00139)	0.0127	(0.000502)
26	0.0372	(0.00147)	0.0129	(0.000507)
27	0.0456	(0.00179)	0.0179	(0.000706)
28	0.0475	(0.00187)	0.0193	(0.000759)
29	0.0480	(0.00189)	0.0220	(0.000868)
30	0.0612	(0.00241)	0.0261	(0.001027)
31	0.0620	(0.00244)	0.0262	(0.001031)
31	0.0865	(0.00341)	0.0528	(0.002077)
33	0.0981	(0.00386)	...	...

[a]Fractographic crack size range used: 0.254 mm (0.01 in.) $\leqq a(t) \leqq$ 1.27 mm (0.05 in.).

EIFS Parameters

EIFSs for each fatigue crack in the WPF and WPB data sets were computed using Eq 17 and the fractographic results in the crack size range from 0.254 mm (0.01 in.) to 1.27 mm (0.05 in.). The ranked EIFSs for the WPF and WPB data sets are summarized in Table 1 in an ascending order of crack size.

EIFSD parameters x_u, α, and ϕ were determined using the EIFS values for the WPF, WPB, and combined WPF and WPB data sets. Different values were assumed for x_u, and the corresponding α, ϕ, standard error σ_E, and $D_{\max}$ (K-S) values were determined using Eqs 19 through 22, respectively. The results are summarized in Table 2.

Goodness-of-Fit Plots

EIFSD parameters based on x_u = 0.762 mm (0.03 in.) were used to make predictions for $F_{a(t)}(x)$ and $F_{T(a_1)}(t)$ based on Eqs 10 and 14, respectively. The upper-bound value of x_u = 0.762 mm (0.03 in.) was used because the standard error, σ_E, and the K-S value, D_{max}, "indicators" for the EIFSD goodness-of-fit, given in Table 2, were smaller than those values for $x_u <$ 0.762 mm (0.03 in.).

The forward crack growth parameter, Q, in Eqs 3, 10, and 14, and the standard deviation of the crack growth rate, σ_z, were estimated for each data set (that is, WPF and WPB) using the applicable log $da(t)/dt$ versus log $a(t)$ data and Eq 6 with b = 1. Crack growth rates, $da(t)/dt$, were determined for each fatigue crack in each fractographic data set based on the five-point incremental polynomial method [ASTM Standard Test Method for Constant-Load-Amplitude Fatigue Crack Growth Rates Above 10^{-8} m/Cycle (E 647-83)]. A typical plot of log $da(t)/dt$ versus log $a(t)$ is shown in Fig. 3 for the WPB data set.

Normalized Q values, denoted $\hat{Q}$, were determined for each data set using Eq 23 for individual and pooled EIFS data sets with the following results: $\hat{Q} = 2.708 \times 10^{-4}$ (WPF) and $\hat{Q} = 1.272 \times 10^{-4}$ (WPB). Results of Q, $\hat{Q}$, and σ_z are summarized in Table 3.

With the durability analysis approach using the stochastic-based EIFS model described above and the parameters presented in Table 3 for the six

TABLE 2—*Summary of EIFSD parameters based on stochastic crack growth.*[a]

Data Sets	x_u, mm (in.)	α	ϕ	Standard Error	Maximum Difference (K-S)
WPF (N = 33)	0.762 (0.030)	5.409	3.801	0.0323	0.0829
	0.508 (0.020)	4.705	3.392	0.0330	0.0886
	0.330 (0.013)	3.939	2.956	0.0349	0.0969
	0.254 (0.010)	3.458	2.691	0.0371	0.1039
	0.099 (0.0039)	0.928	2.039	0.1331	0.2575
WPB (N = 32)	0.762 (0.030)	6.684	4.775	0.0367	0.1075
	0.508 (0.020)	6.013	4.367	0.0372	0.1106
	0.330 (0.013)	5.287	3.935	0.0383	0.1149
	0.254 (0.010)	4.835	3.671	0.0396	0.1186
	0.099 (0.0039)	3.079	2.739	0.0541	0.1446
	0.076 (0.0030)	2.479	2.478	0.0677	0.1620
	0.069 (0.0027)	2.193	2.414	0.0774	0.1729
WPF + WPB (N = 65)	0.762 (0.030)	5.240	4.319	0.0231	0.0562
	0.508 (0.020)	4.633	3.908	0.0237	0.0601
	0.330 (0.013)	3.968	3.472	0.0256	0.0663
	0.254 (0.010)	3.547	3.206	0.0279	0.0720
	0.099 (0.0039)	1.199	2.556	0.1186	0.2135

[a]Fractographic crack size range used: 0.254 mm (0.01 in.) $\leqq a(t) \leqq$ 1.27 mm (0.05 in.).

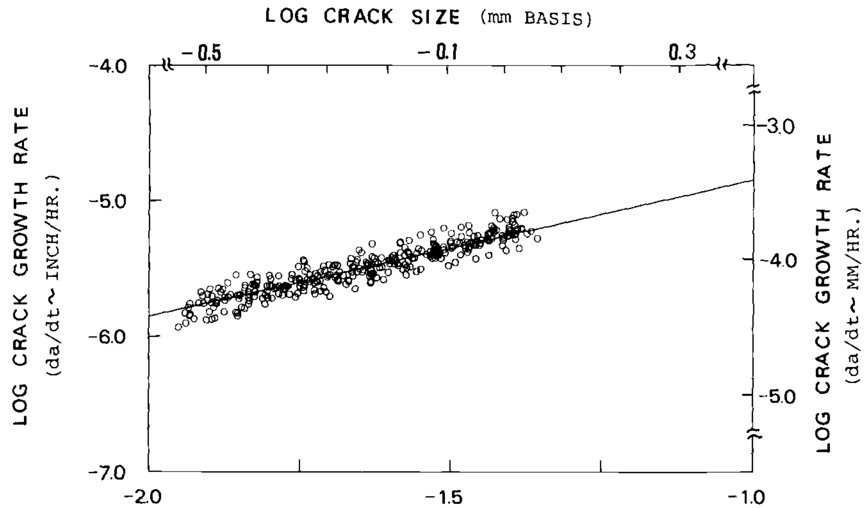

FIG. 3—*Log crack growth rate versus log crack size for WPB data set.*

cases considered, the distributions of the crack size at any service life, $F_{a(t)}(x)$, and the TTCI at any crack size can be predicted theoretically (Eqs 10 and 14).

The cumulative distribution of crack size at two different service times (WPF at 9200 and 14 800 flight hours, and WPB at 29 109 and 35 438 flight hours) are plotted in Figs. 4 to 9 as a solid curve for the theoretical predictions. The experimental test results are also plotted in these figures using selected symbols. For example, in Fig. 4 the results for t = 0, 9200, and 14 800 flight hours are denoted by an open circle, a triangle and a square, respectively. In Figs. 5 and 6, an open circle and a solid circle denote the EIFS values at t = 0 for the WPF and WPB data sets, respectively.

Plots of theoretical predictions of the cumulative distribution of TTCI at crack sizes of 0.762 mm (0.03 in.), 1.27 mm (0.05 in.), and 2.54 mm (0.1 in.) are shown as solid curves in Figs. 10 to 12 and Figs. 13 to 15 for the WPF and WPB data sets, respectively. The corresponding ranked TTCI test results are displayed in these figures as a circle, star, and square, respectively. Symbols for the WPF data set are open and those for the WPB data set are solid.

The following observations are based on Figs. 4 to 9:

1. The theoretical predictions for $F_{a(t)}(x)$ generally fit the overall test results better when the EIFSs for a given data set are used (for example, see Figs. 4 and 7).
2. When the EIFSD parameters are based on the pooled EIFSs for the

TABLE 3—*Summary of parameters used in correlation plots.*[a,b]

Case	EIFS Basis	x_u, mm	α[c]	ϕ[c]	$Q \times 10^4$, per flight hour	σ_z[d]	b	t, flight hours	t, flight hours
I	WPF	0.762	5.409	3.801	2.383	0.0839	1.0	9200	14800
II	WPF + WPB	0.762	5.240	4.319	2.383	0.0839	1.0	9200	14800
III	WPF + WPB	0.762	5.240	4.319	2.708[e]	0.0839	1.0	9200	14800
IV	WPB	0.762	6.684	4.775	1.406	0.0669	1.0	29109	35438
V	WPF + WPB	0.762	5.240	4.319	1.406	0.0669	1.0	29109	35438
VI	WPF + WPB	0.762	5.240	4.319	1.272[e]	0.0669	1.0	29109	35438

[a] Fractographic crack size range used: 0.254 mm (0.01 in.) $\leqq a(t) \leqq$ 1.27 mm (0.05 in.).
[b] a_l = 0.762 mm (0.03 in); 1.27 mm (0.05 in.); 2.54 mm (0.10 in.).
[c] See Eqs 19 and 20.
[d] See Eq 6.
[e] Normalized Q value, $\hat{Q}$ (see Eq 24).

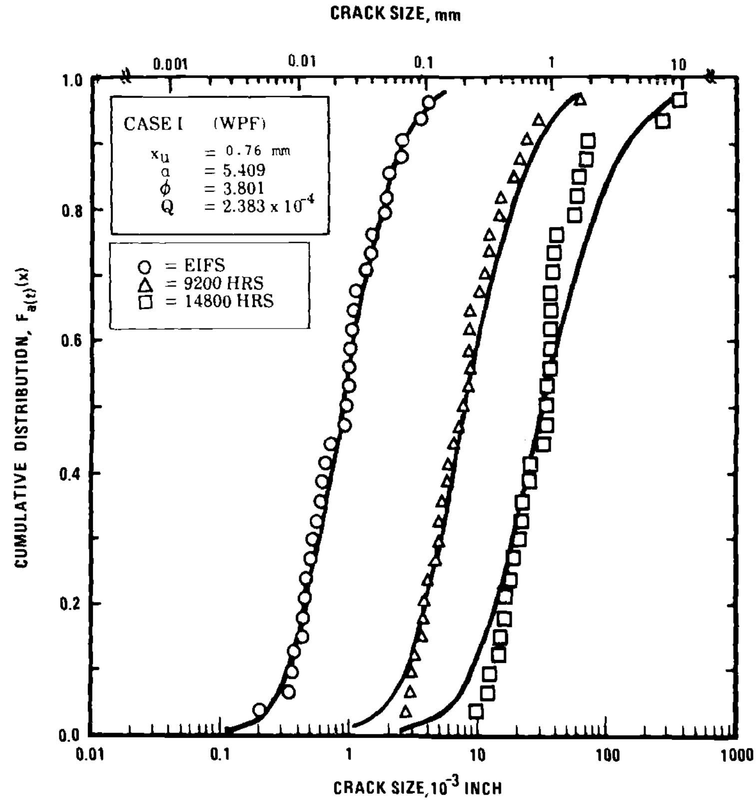

FIG. 4—*Correlation between predictions and test results for cumulative distribution of crack size at 9200 and 14 800 flight hours for WPF data set (Case I: EIFSs for WPF; unnormalized Q value).*

WPF and WPB data sets, the theoretical predictions for $F_{a(t)}(x)$ for a given data set generally correlate better with the ranked experimental results when the crack growth parameter, Q, is normalized using Eq 23. For example, compare the plots shown in Figs. 5 and 6 and Figs. 8 and 9 for the WPF and WPB data sets, respectively.

3. The upper tail of $F_{a(t)}(x)$ (that is, the largest crack sizes) is of most interest for durability analysis. For all the cases considered herein, the theoretical predictions for crack exceedance [that is, $p(i, \tau) = 1 - F_{a(t)}(x)$] in the upper tail generally fit the ranked experimental results very well. In Fig. 8 the theoretical predictions for $F_{a(t)}(x)$ for the WPB data set are conservative in the upper tail (that is, the predicted crack exceedance is larger than the ranked test result). In this case, the Q value is not normalized. The goodness-of-fit improves significantly when Q is normalized as shown in Fig. 9.

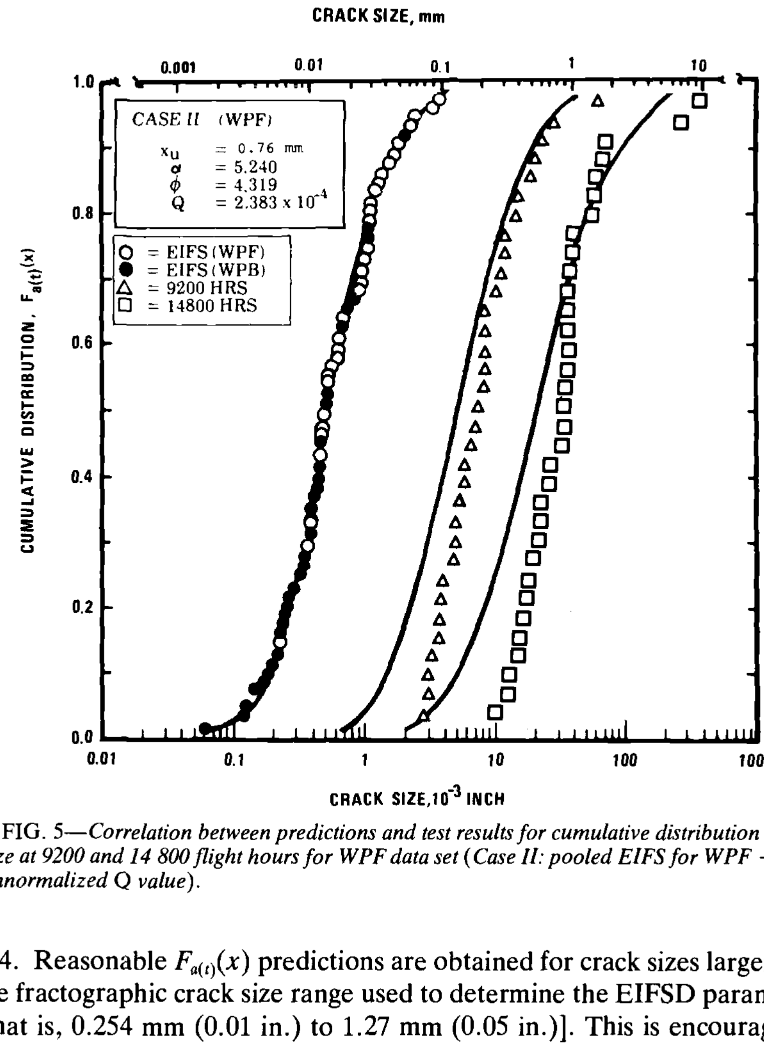

FIG. 5—*Correlation between predictions and test results for cumulative distribution of crack size at 9200 and 14 800 flight hours for WPF data set (Case II: pooled EIFS for WPF + WPB; unnormalized Q value).*

4. Reasonable $F_{a(t)}(x)$ predictions are obtained for crack sizes larger than the fractographic crack size range used to determine the EIFSD parameters [that is, 0.254 mm (0.01 in.) to 1.27 mm (0.05 in.)]. This is encouraging.

The following observations are based on Figs. 10 to 15.

1. The lower tail (that is, the smallest TTCIs) of the TTCI cumulative distribution, $F_{T(a_1)}(t)$, is generally the area of most interest for durability analysis. As shown in Figs. 10 to 15, the theoretical predictions for $F_{T(a_1)}(t)$ correlate very well with the ranked experimental results.
2. The overall fit is generally improved when Q is normalized. For example, compare results for Figs. 11 and 12 and Figs. 14 and 15 for the WPF and WPB data sets, respectively.
3. Reasonable $F_{T(a_1)}(t)$ predictions for the WPF and WPB data sets are

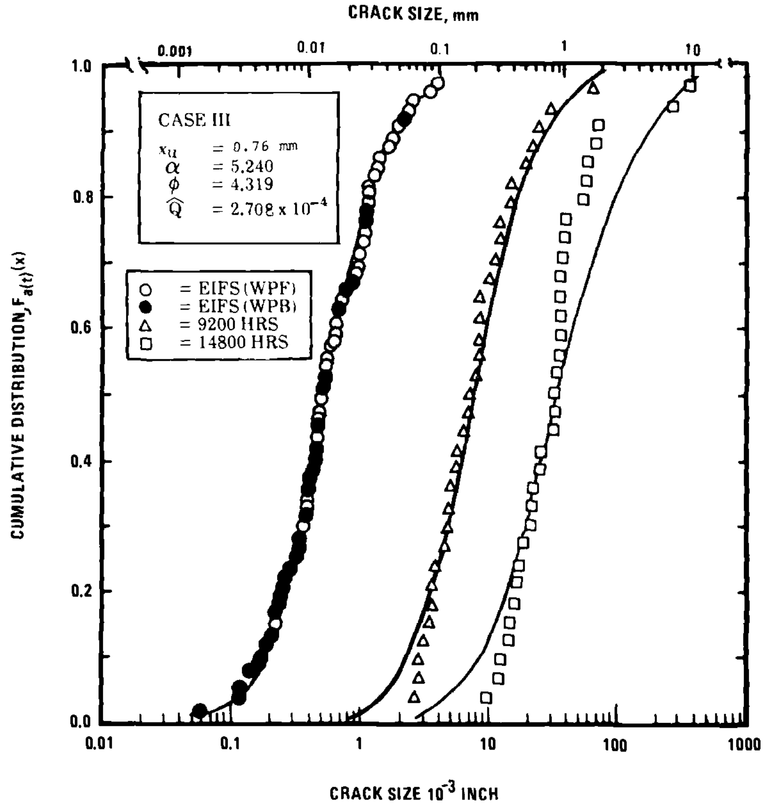

FIG. 6—*Correlation between predictions and test results for cumulative distribution of crack size at 9200 and 14 800 flight hours for WPF data set (Case III: pooled EIFSs for WPF + WPB; normalized Q value).*

obtained in the lower tail for a_1 = 2.54 mm (0.10 in.); for example, see Figs. 12 and 15. Thus, reasonable $F_{T(a_1)}(t)$ predictions are obtained for a crack size outside the fractographic crack size range used to define the EIFSD parameters.

Conclusions

Expressions have been developed for predicting the cumulative distribution of crack size at any given time, and the cumulative distribution of times to reach any given crack size using the stochastic-based EIFS model. These expressions, based on a stochastic crack growth approach, have been evaluated for the durability analysis of fastener holes in the small-crack-size region [for example, <2.54 mm (0.10 in.)]. The analytical expressions

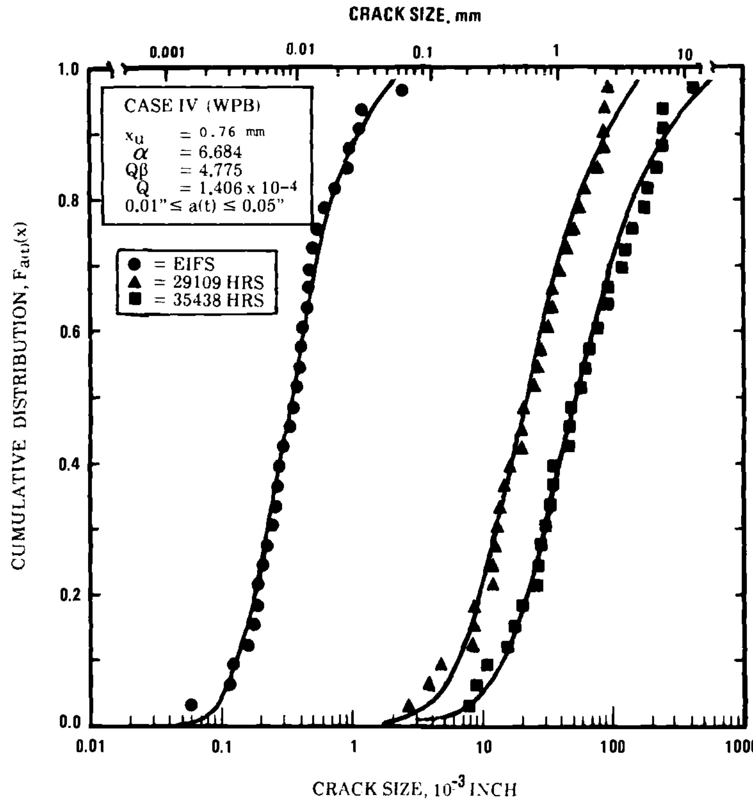

FIG. 7—*Correlation between predictions and test results for cumulative distribution of crack size at 29 109 and 35 438 flight hours for WPB data set (Case IV: EIFSs for WPB; unnormalized Q value).*

for $F_{a(t)}(x)$ and $F_{T(a_1)}(t)$ are derived based on a stochastic transformation of the theoretical EIFSD. EIFS data pooling concepts and procedures for optimizing the distribution parameters have been presented and evaluated.

Theoretical predictions for $F_{a(t)}(x)$ and $F_{T(a_1)}(t)$ compared reasonably well with ranked experimental results when both the WPF and WPB data sets were considered separately. Overall fits based on pooled EIFS values for both WPF and WPB data sets were improved when the normalized crack growth parameters were used. EIFS distributions based on normalized crack growth results need to be investigated further for a wide range of practical durability analysis situations.

The upper tail of the EIFSD is of most interest for durability analysis because the large initial flaws are more apt to cause crack exceedance problems than the smaller initial flaw sizes. The EIFSD can be force-fitted to the upper tail of the EIFS population, which might provide an even better

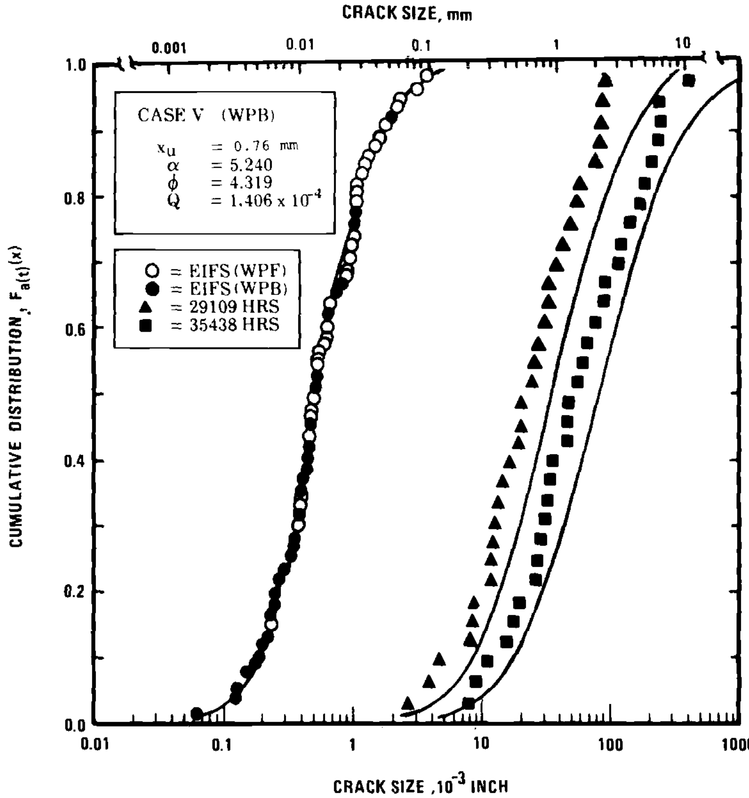

FIG. 8—*Correlation between predictions and test results for cumulative distribution of crack size at 29 109 and 35 438 flight hours for WPB data set (Case V: pooled EIFSs for WPF + WPB; unnormalized Q value).*

fit of the EIFSD to the tail area of most interest.[4] This aspect needs to be investigated further.

The EIFS pooling concepts and procedures for optimizing EIFS distribution parameters are promising for determining a reasonable EIFSD for practical durability analyses. Further research is needed to determine the EIFSD parameters based on pooled EIFSs for several fractographic data sets and to evaluate the accuracy and limits of the durability analysis predictions in the small-crack-size region [for example, <2.54 mm (0.10 in.)].

A parallel investigation to the one described herein [unpublished research by the first two authors (1985)] has been performed using the deterministic crack growth approach. The results of this investigation will be reported in due course. Based on the results for the stochastic and deterministic crack

[4] Lincoln, J. W., Wright-Patterson Air Force Base, OH, personal communication, 19 Nov. 1984.

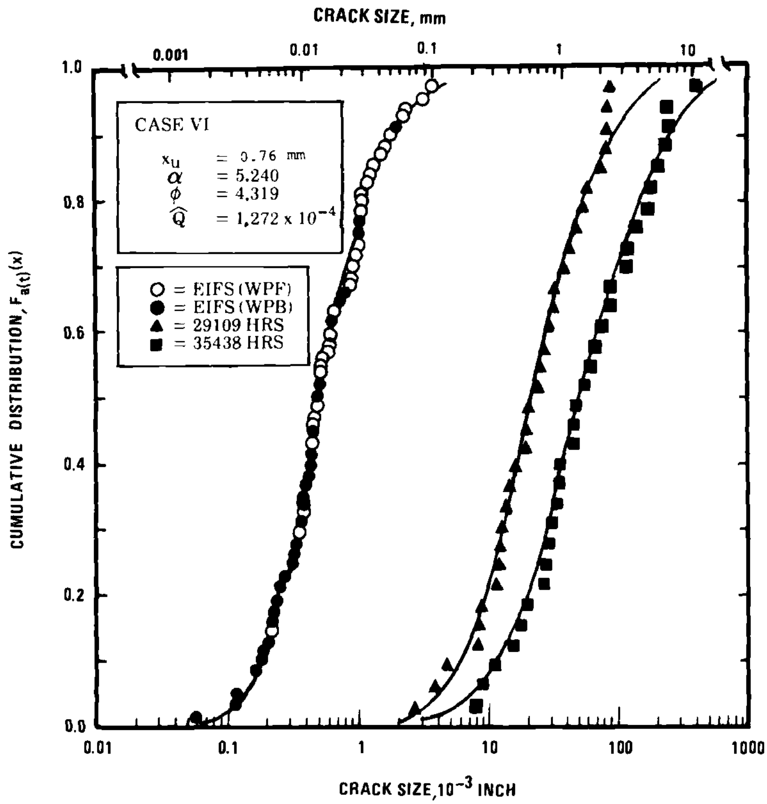

FIG. 9—*Correlation between predictions and test results for cumulative distribution of crack size at 29 109 and 35 438 flight hours for WPB data set (Case VI: pooled EIFSs for WPF + WPB; normalized* Q *value).*

growth approaches, the authors conclude that either approach is satisfactory for the durability analysis of aluminum alloys in the small-crack-size region. However, since the deterministic crack growth approach is mathematically simpler, this approach is recommended for use in the small-crack-size region. Further research is needed to show that the deterministic crack growth approach is also satisfactory for other alloys in the small-crack-size region. Also, the deterministic and stochastic crack growth approaches need to be investigated for durability analysis applications in the large-crack-size region.

Acknowledgment

This research was sponsored by the Air Force Wright Aeronautical Laboratories, Wright-Patterson Air Force Base, under Contract No. F33615-83-K-3226.

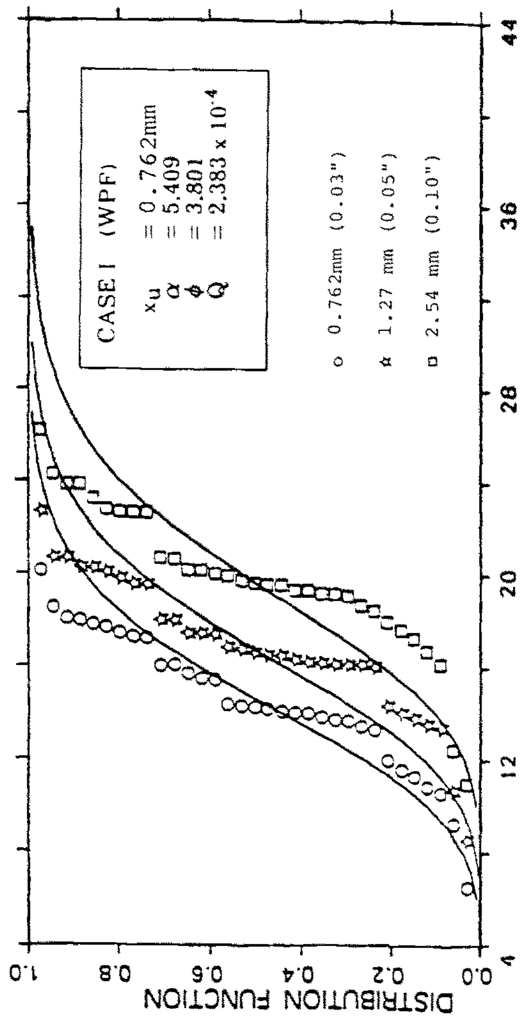

FIG. 10—*Correlation between predictions and test results for cumulative distribution of TTCI at 0.762, 1.27, and 2.54 mm for WPF data set (Case I: EIFSs for WPF; unnormalized Q value).*

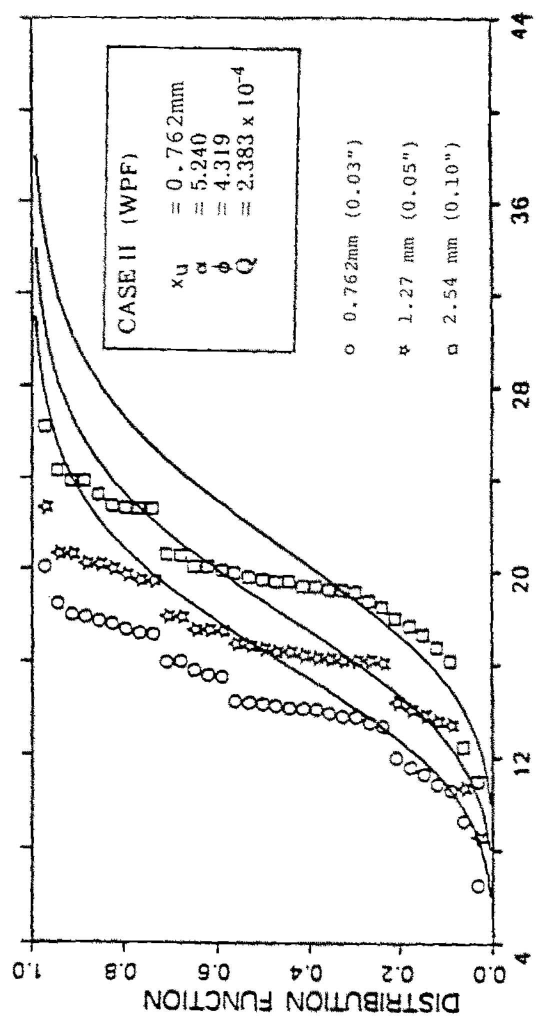

FIG. 11—*Correlation between predictions and test results for cumulative distribution of TTCI at 0.762, 1.27, and 2.54 mm for WPF data set (Case II: pooled EIFSs for WPF + WPB; unnormalized Q value).*

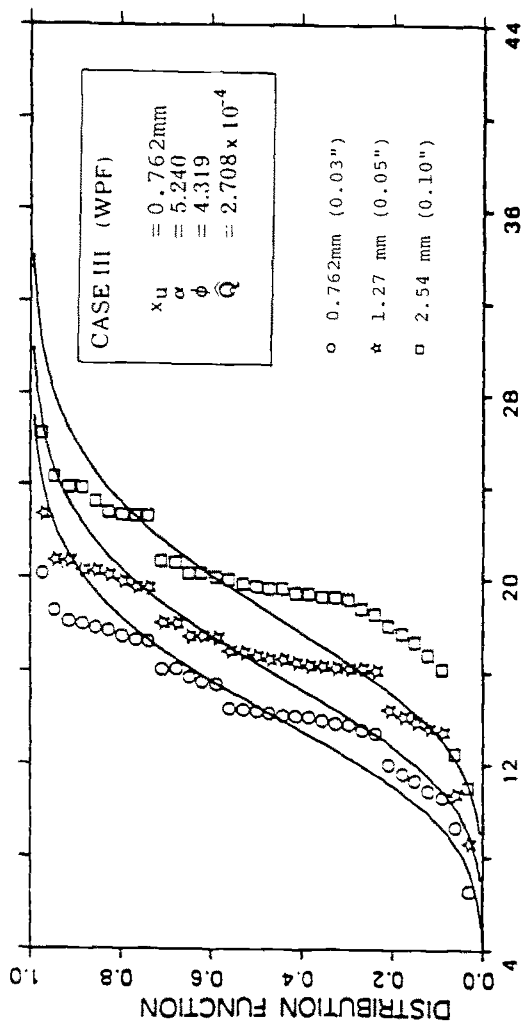

FIG. 12—Correlation between predictions and test results for cumulative distribution of TTCI at 0.762, 1.27, and 2.54 mm for WPF data set (Case III: pooled EIFSs for WPF + WPB; normalized Q value).

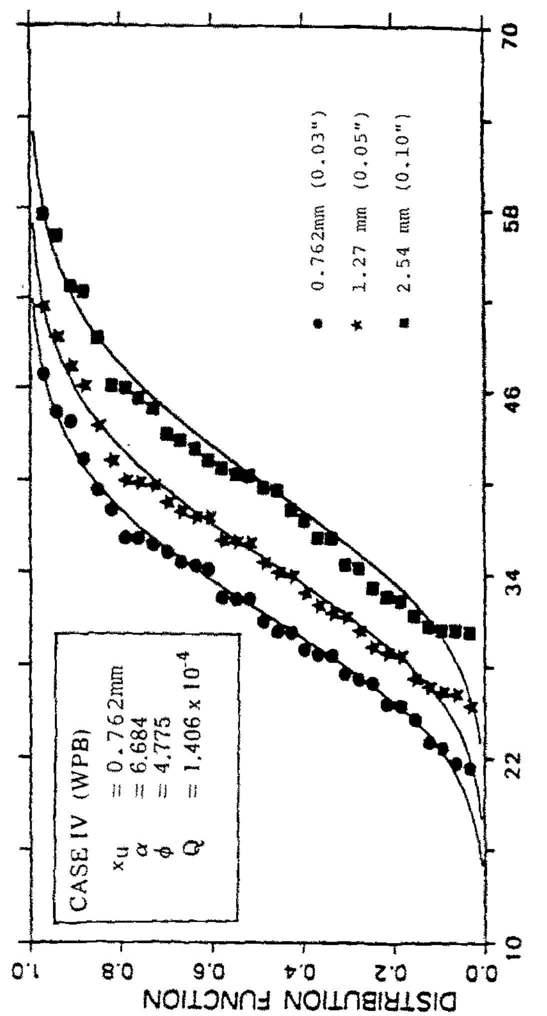

FIG. 13—*Correlation between predictions and test results for cumulative distribution of TTCI at 0.076, 1.27, and 2.54 mm for WPB data set (Case IV: EIFSs for WPB; unnormalized Q value).*

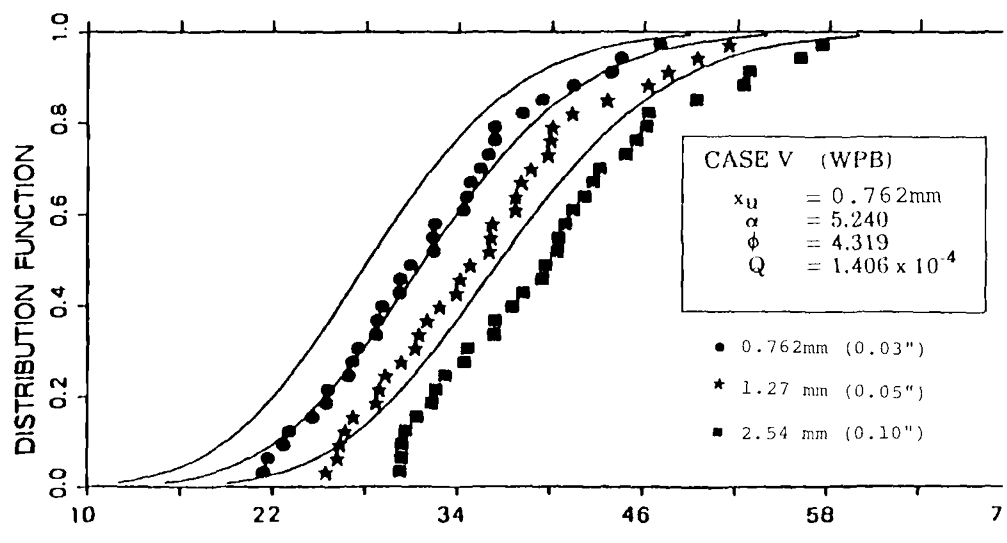

FIG. 14—*Correlation between predictions and test results for cumulative distribution of TTCI at 0.076, 1.27, and 2.54 mm for WPB data set (Case V: EIFSs for WPF + WPB; unnormalized Q value).*

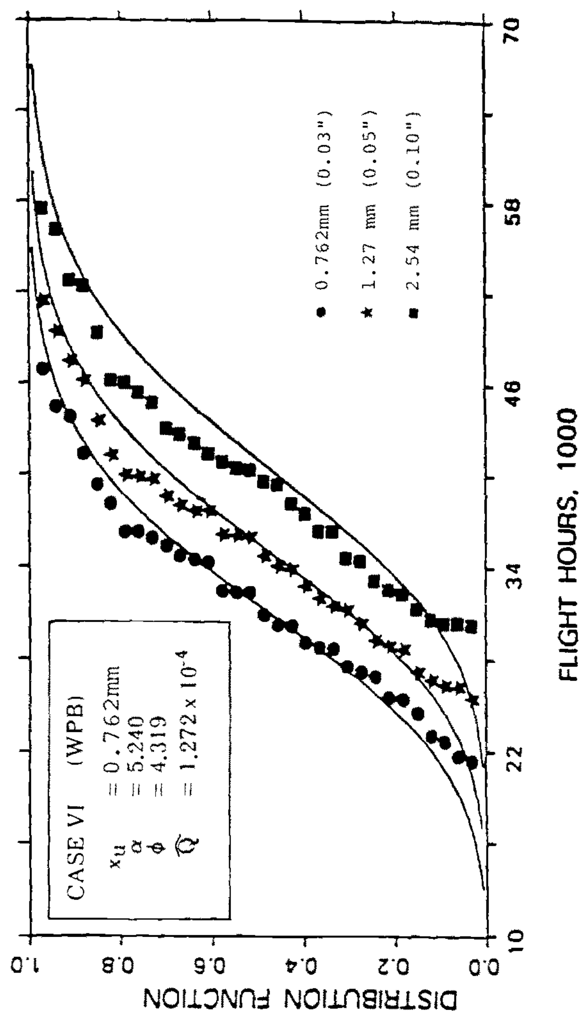

FIG. 15—*Correlation between predictions and test results for cumulative distribution of TTCI at 0.076, 1.27, and 2.54 mm for WPB data set (Case VI: pooled EIFSs for WPF + WPB; normalized Q value).*

References

[*1*] "Aircraft Structural Integrity Program," Military Standard MIL-STD-1530A, Air Force Aeronautical Systems Division, Wright-Patterson Air Force Base, OH, December 1975.

[*2*] "Airplane Strength and Rigidity Ground Tests," Military Specification MIL-A-8867B, Air Force Aeronautical Systems Division, Wright-Patterson Air Force Base, OH, 22 Aug. 1975.

[*3*] "Airplane Strength, Rigidity and Reliability Requirements; Repeated Loads and Fatigue," Military Specificaton MIL-A-8866B, Air Force Aeronautical Systems Division, Wright-Patterson Air Force Base, OH, August 1975.

[*4*] Manning, S. D., Yang, J. N., Shinozuka, M., and Garver, W. R., "Durability Methods Development, Volume I—Phase I Summary," AFFDL-TR-79-3118, Air Force Flight Dynamics Laboratory, Wright-Patterson Air Force Base, OH, September 1979.

[*5*] Manning, S. D., Flanders, M. A., Garver, W. R., and Kim, Y. H., "Durability Methods Development, Volume II, Durability Analysis: State of the Art Assessment," AFFDL-TR-79-3118, Air Force Flight Dynamics Laboratory, Wright-Patterson Air Force Base, OH, September 1979.

[*6*] Pendley, B. J., Henslee, S. P., and Manning, S. D., "Durability Methods Development, Volume III: Structural Durability Survey: State-of-the-Art Assessment," AFFDL-TR-79-3118, Air Force Flight Dynamics Laboratory, Wright-Patterson Air Force Base, OH, September 1979.

[*7*] Shinozuka, M., "Durability Methods Development, Volume IV—Initial Quality Representation," AFFDL-TR-3118, Air Force Flight Dynamics Laboratory, Wright-Patterson Air Force Base, OH, September 1979.

[*8*] Yang, J. N., Manning, S. D., and Garver, W. R., "Durability Methods Development, Volume V, Durability Analysis Methodology Development," AFFDL-TR-79-3118, Air Force Flight Dynamics Laboratory, Wright-Patterson Air Force Base, OH, September 1979.

[*9*] Shinozuka, M., "Durability Methods Development, Vol. VI—Documentation of Computer Program for Initial Quality Representation (Vol. IV), " AFFDL-TR-79-3118, Air Force Flight Dynamics Laboratory, Wright-Patterson Air Force Base, OH, November 1982.

[*10*] Manning, S. D. et al, "Durability Methods Development, Volume VII—Phase II Documentation," AFFDL-TR-79-3118, Air Force Flight Dynamics Laboratory, Wright-Patterson Air Force Base, OH, January 1984.

[*11*] Speaker, S. M. et al, "Durability Methods Development Volume VIII—Test and Fractography Data," AFFDL-TR-79-3118, Air Force Flight Dynamics Laboratory, Wright-Patterson Air Force Base, OH, November 1982.

[*12*] Norris, J. W., "Durability Methods Development, Volume IX—Documentation of Durability Analysis Computer Program," AFFDL-TR-79-3118, Air Force Flight Dynamics Laboratory, Wright-Patterson Air Force Base, OH, November 1982.

[*13*] Manning, S. D. and Yang, J. N., "USAF Durability Design Handbook: Guidelines for the Analysis and Design of Durable Aircraft Structures," AFWAL-TR-83-3027, Air Force Flight Dynamics Laboratory, Wright-Patterson Air Force Base, OH, January 1984.

[*14*] Yang, J. N. and Manning, S. D., "Statistical Distribution of Equivalent Initial Flaw Size," *Proceedings*, Annual Reliability and Maintainability Symposium, San Francisco, CA, 1980, pp. 112–120.

[*15*] Manning, S. D. and Smith V. D., "Economic Life Criteria for Metallic Airframes," *Proceedings*, 21st American Institute of Aeronautics and Astronautics Structures, Structural Dynamics, and Materials Conference, Part 1, 1980, Seattle, WA, pp. 504–511.

[*16*] Yang, J. N., "Statistical Estimation of Economic Life for Aircraft Structures," *Proceedings*, AIAA/ASME/ASCE/AHS 20th Structures, Structural Dynamics, and Materials Conference, 4–6 April 1979, St. Louis, MO, pp. 240–248; also in *Journal of Aircraft*, American Institute of Aeronautics and Astronautics, Vol. 17, No. 7, 1980, pp. 528–534.

[*17*] Yang, J. N., "Statistical Crack Growth in Durability and Damage Tolerant Analyses," *Proceedings*, AIAA/ASME/ASCE/AHS 22nd Structures, Structural Dynamics and Materials Conference, Part 1, Atlanta, GA, 6–8 April 1981, pp. 38–49.

[18] Manning, S. D., Garver, W. R., Kim, Y. N., and Rudd, J. L., "Durability Analysis—Format Requirements and Critique of Potential Approaches," *Proceedings*, American Society of Mechanical Engineers Failure Prevention and Reliability Conference, 1981, Hartford, CT, pp. 223–229.

[19] Rudd, J. L., Yang, J. N., Manning, S. D., and Garver, W. R., "Durability Design Requirements and Analysis for Metallic Airframes," *Design of Fatigue and Fracture Resistant Structures, ASTM STP 761*, American Society for Testing and Materials, Philadelphia, 1982, pp. 133–151.

[20] Rudd, J. L., Yang, J. N., Manning, S. D., and Yee, B. G. W., "Damage Assessment of Mechanically-Fastened Joints in the Small Crack Size Range," *Proceedings*, Ninth U.S. National Congress of Applied Mechanics, Symposium on Structural Reliability and Damage Assessment, Cornell University, Ithaca, NY, 21–25 June 1982, pp. 329–338.

[21] Rudd, J. L., Yang, J. N., Manning, S. D., and Yee, B. G. W., "Probabilistic Fracture Mechanics Analysis Methods for Structural Durability," *Proceedings*, Conference on the Behavior of Short Cracks in Airframe Components, AGARD-CP-328, Toronto, Canada, September 1982, pp. 10–1 through 10–23.

[22] "Advanced Durability Analysis," Report FZP-2233, Technical Proposal Prepared for U.S. Air Force Systems Command, Aeronautical Systems Division/PMRNA, General Dynamics, Fort Worth Division, Fort Worth, TX, 3 May 1984.

[23] Noronha, P. J. et al, "Fastener Hole Quality," AFFDL-TR-78-206, Air Force Flight Dynamics Laboratory, Vol. II, Wright-Patterson Air Force Base, OH, December 1978.

[24] Yang, J.N. and Donath, R. C., "Statistical Fatigue Crack Propagation in Fastener Holes Under Spectrum Loading," *Journal of Aircraft*, Vol. 20, No. 12, December 1983, pp. 1028–1032.

[25] Yang, J. N., Manning, S. D., Rudd, J. L., and Hsi, W. H., "Stochastic Crack Propagation in Fastener Holes," *Proceedings*, 26th AIAA/ASME/ASCE/AHS Structures, Structural Dynamics and Materials Conference, Orlando, FL, 15–17 April 1985, pp. 225–233, American Institute of Aeronautics and Astronautics Paper No. 85-0666; also in *Journal of Aircraft*, Vol. 22, No. 9, September 1985, pp. 810—817.

[26] Yang, J. N., Hsi, W. H., and Manning, S. D., "Stochastic Fatigue Crack Propagation with Applications to Durability and Damage Tolerance Analyses," AFWAL-TR-85-3062, Air Force Flight Dynamics Laboratory, Wright-Patterson Air Force Base, OH, February 1985.

[27] Lin, Y. K. and Yang, J. N., "A Stochastic Theory of Fatigue Crack Propagation," *AIAA Journal*, Vol. 23, No. 1, January 1985, pp. 117–124.

[28] Lin, Y. K. and Yang, J. N., "On Statistical Moments of Fatigue Crack Propagation," *Journal of Engineering Fracture Mechanics*, Vol. 18, No. 2, 1983, pp. 243–256.

[29] Virkler, D. A., Hillberry, B. M., and Goel, P. K., "The Statistical Nature of Fatigue Crack Propagation," *Journal of Engineering Materials and Technology, Transactions*, American Society of Mechanical Engineers, Vol. 101, 1979, pp. 148–152.

[30] Wood, H. A., Engle, R. M., Gallagher, J. P., and Potter, J. N., "Current Practice on Estimating Crack Growth Damage Accumulation with Specific Application to Structural Safety, Durability and Reliability," AFFDL-TR-75-32, Air Force Flight Dynamics Laboratory, Wright-Patterson Air Force Base, OH, January 1976.

[31] Tiffany, C. F., "Durability and Damage Tolerance Assessments of United States Air Force Aircraft," paper presented at American Institute of Aeronautics and Astronautics Structural Durability and Damage Tolerance Workshop, Washington, DC, 6–7 April 1978.

Gianni Nicoletto[1]

Experimental Characterization of Cracks at Open Holes and in Rounded-End Straight Attachment Lugs

REFERENCE: Nicoletto, G., "**Experimental Characterization of Cracks at Open Holes and in Rounded-End Straight Attachment Lugs,**" *Fatigue in Mechanically Fastened Composite and Metallic Joints, ASTM STP 927,* John M. Potter, Ed., American Society for Testing and Materials, Philadelphia, 1986, pp. 150–171.

ABSTRACT: The paper focuses on the application of the frozen-stress photoelastic technique to an assessment of various engineering solutions from the literature for several hole-related crack problems. Single corner, transitioning, and through-the-thickness cracks are examined. Remote tensile loading of a plate containing an open hole and 100% load transfer through a rigid pin in a rounded-end lug is considered.

Experimental evidence demonstrates the presence of stress intensity factor (SIF) gradients for every crack configuration. Good correlation with existing SIF solutions is found for the through-the-thickness configuration in lugs. Less conclusive are the comparisons with engineering estimates for corner cracks emerging from open holes and lug. The transitioning behavior of a part-through crack is also discussed. Finally, modeling aspects of three-dimensional fracture problems are examined.

KEY WORDS: damage tolerance, mechanical joints, part-through cracks, stress intensity factor, frozen-stress photoelasticity

Lug-type joints are widely used to connect major aircraft components. Such joints are characterized by 100% load transfer through a pin or a bolt. This design offers several advantages over other solutions—namely, simplicity, ease of assembly, and free pivoting around the pin axis, which prevents the transfer of local bending moments [*1*]. A disadvantage is the high stress concentration introduced by the hole and enhanced by the pin-bearing load. Fretting corrosion is expected in the region of sliding pin-lug contact. These drawbacks greatly affect the fatigue strength of lugs and suggest to the designer the adoption of low stress levels. Manufacturing and assembly operations may introduce pits or scratches that compromise further the fatigue resistance of various types of fasteners. The increasing interest in the initial quality of fastener holes for its impact on the durability of airframe structures is documented in Ref *2*.

[1] Researcher, Istituto di Meccanica Applicata alle Macchine, University of Bologna, Viale Risorgimento, 2, 40136 Bologna, Italy.

Since 1974 the U.S. Air Force has adopted damage tolerance requirements based on linear elastic fracture mechanics (LEFM) [*3*], which depend on the design concept and the degree of inspectability of the structure. Residual strength and crack growth life calculations for assumed initial damages of prescribed dimensions at the worst locations of a proposed design are included in the fatigue certification of airframe structures. Because of the low design stresses in lugs, a crack can be expected to grow slowly. Hence the lug joint may become a fail-safe joint on definition of inspection intervals [*4*].

Various authors have pointed out that one of the major shortcomings in the proposed use of crack growth analysis at the design level is the lack of reliable stress intensity factor (SIF) solutions for complex flaw configurations associated with natural cracks in thick-walled components (that is, plates with fastener holes, attachment lugs) [*5*]. Destructive teardown inspections of fatigued airframes have shown that the prevalent flaw shapes associated with fastener holes are the corner crack and the hole-wall crack [*2*].

The present paper deals with the hole-related crack problems shown in Fig. 1. Natural cracks were monotonically grown in epoxy specimens (Fig. 2) whose dimensions are specified in Table 1. Frozen-stress photoelastic techniques and LEFM stress tensor equations are used to evaluate SIFs at discrete locations along the crack fronts from the near-tip isochromatic fringes. Experimental SIFs for through-the-thickness and corner cracks emerging from open and pin-loaded holes are discussed. Only single cracks are examined. The experimental SIF estimates are correlated with various solutions developed for engineering fracture mechanics calculations. The

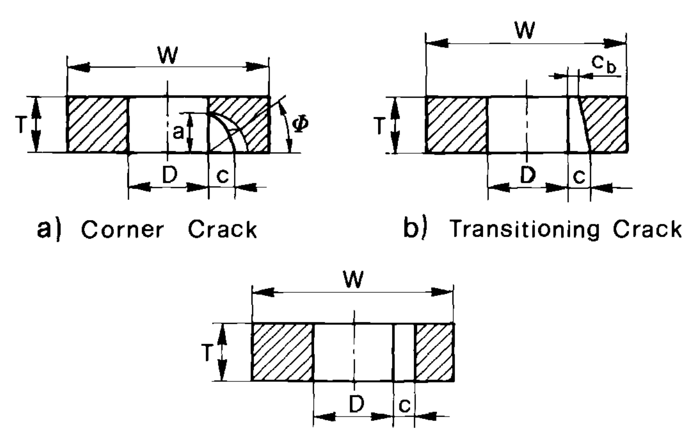

FIG. 1—*Types of flaw emerging from a hole:* (a) *corner crack;* (b) *transitioning crack;* (c) *through-the-thickness crack.*

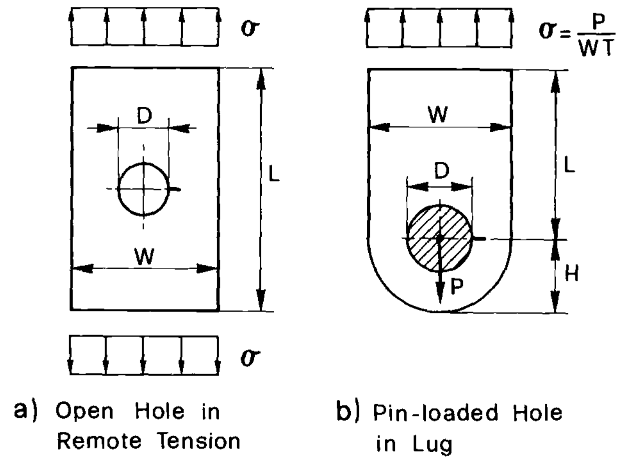

FIG. 2—*Types of hole loading:* (a) *open hole in a plate in remote tension;* (b) *pin-loaded hole in an attachment lug.*

transitioning behavior of a part-through crack is also discussed. Finally, aspects involved in three-dimensional fracture modeling are analyzed.

Experimental Methodology

Frozen-stress photoelasticity has been validated as a practical, accurate, and relatively inexpensive engineering design tool for a variety of complex cracked body problems [*6*]. It has been used for such diverse tasks as computer code verification [*7–8*] and assessment of recategorization criteria for embedded cracks included in design codes [*9*].

In the following section the experimental procedure, the SIF estimation method from photoelastic data, and the limitations of the technique are briefly reviewed.

Experimental Procedure

In applying the method, epoxy models are cast and machined to their final geometry (see Fig. 2 and Table 1). For the problem of a cracked lug,

TABLE 1—*Uncracked specimen dimensions.*[a]

Specimen Configuration	D, mm	D/T	W/D	L/W	W/H
Open hole in a plate (Fig. 2*a*)	18	1.0	3.0	3.0	. . .
Pin-loaded hole in lug (Fig. 2*b*)	30	2.0	2.5	1.5	2.0

[a]Key to terms:
D = hole diameter.
T = specimen thickness.
W = specimen width.
L = specimen length.
H = rounded end radius.

a rigid (that is, aluminum) pin was used for hole loading (Fig. 2*b*). A tiny starter crack is inserted at the desired location of the specimen by tapping with a sharp blade. The specimen is then inserted in a loading frame, placed in an oven and heated above stress-freezing temperature (that is, 150°C). The starter crack is monotonically grown to a depth of interest. Adequate dead loading is applied to the specimen at the beginning of the cooling portion of the stress freezing cycle.

At the end of the thermal cycle, natural flaw shapes are accurately recorded under $\times 10$ magnification using a profile projector. Slices 1 to 1.5 mm thick and perpendicular to the crack profile are removed at several locations where SIF estimates are sought.

SIF Extraction from Isochromatic Fringes

The extraction of an SIF estimate from each slice involves a combination of the isochromatic fringes and the near-tip, LEFM stress tensor equations. C. W. Smith's two-parameter method [*6*], based on the assumption that a LEFM-dominated zone exists in the vicinity of a crack tip, was used throughout the study.

The Mode I stress tensor in the case of a curved crack front has locally the following form

$$\sigma_{ij} = K(2\pi r)^{-1/2} f_{ij}(\Theta) + \sigma^{\circ}_{ij} \qquad (i, j = n, z) \tag{1}$$

where

K = the Mode I SIF,
r and Θ = polar coordinates centered at the crack tip, and
σ° = far-field stress contributions to the singular part of the stress field.

The z-axis coincides with the direction of the remote stress, while the n-axis lies on the z-plane and is locally orthogonal to the crack border.

The isochromatic fringes are related to the maximum in-plane shear stress, τ, by the stress-optic law

$$\tau = \frac{f^{\circ} N}{2t} \tag{2}$$

where

f° = photoelastic constant,
t = model thickness (that is, slice thickness), and
N = isochromatic fringe order.

Along the direction $\Theta = 90$ deg, Eqs 1 and 2 can be combined to yield in normalized form

$$\frac{K_{ap}}{K_{norm}} = \frac{K}{K_{norm}} + C\left(\frac{r}{a}\right)^{1/2} \tag{3}$$

where

$K_{ap} = \tau\,(8\pi r)^{1/2}$,
a = reference crack length, and
C = a constant.

The determination of the near-tip data (that is, fringe order versus relative distance from the crack tip) to be introduced in Eq 3 makes use of a projection microscope fitted with a transmission polariscope to analyze every slice. The Tardy compensation method for fractional fringe order determination [*10*] and $\times 10$ magnification are used to increase the number of data points retrieved. The data are fed into a microcomputer with a plotter for quick data elaboration. In a (normalized K vs. $\sqrt{r}$) diagram, the intercept with the y-axis of a straight line through the LEFM-dominated zone yields the SIF estimate [*11*].

Accuracy and Limitations

The large experience accumulated by many researchers suggests that the accuracy of the photoelastic SIF estimates can be reasonably expected to vary within ± 5 to 7% [*6,11*].

The frozen-stress photoelastic method has its own limitations in applicability to cracked body problems. The epoxy material displays grossly elastic and nearly incompressible mechanical behavior at temperatures above the stress freezing temperature.

Hence, photoelasticity cannot model plasticity-induced effects on crack growth, such as plastic zone size variations due to overloads and subsequent crack closure effects. Also, compressive residual stresses induced at fastener holes by manufacturing techniques (that is, mandrelizing) cannot be modeled.

Contact problems such as those for the pin-loaded lug of Fig. 2*b* are also difficult to model photoelastically because of the relative thermal dilations between the rigid (aluminum) pin and the epoxy lug. The actual pin/hole fit is not easily controlled. Contact conditions are also altered by the relative deformations of the low-modulus lug material and the aluminum pin. A study involving the use of a rather laborious finite difference procedure for stress separation was undertaken in order to check the real contact conditions in the photoelastic models. Unpublished results relative to an uncracked lug showed an effective 120-deg extension of the bearing area. Also, a camel-backed contact pressure distribution was found, as theoretically predicted in Ref *13* and recently verified by Hsu using the finite element (FE) method [*14*]. However, the reduction of the contact area and the highly different pin and lug material properties probably caused the observed higher contact pressure peaks. The experimental study confirmed that the presence of a through crack had an affect on the contact pressure distribution in the epoxy lug comparable to the numerical predictions of Ref *14* [*12*].

The author concludes that although only an approximated photoelastic modeling of the contact conditions in a structural joint is possible, the experimental contact conditions are still more realistic than those assumed in various analytical models that will be discussed later. It is expected that the effect of the boundary conditions on photoelastic SIF estimates is limited.

Photoelastic Characterization of Cracks at Holes

This section is divided as follows: Through-the-thickness crack configurations at holes are examined first, corner cracks are considered subsequently, and the transitioning crack behavior is finally analyzed. Each subsection deals separately with the cases of an open hole in a plate in tension and with the pin-loaded hole in a rounded-end attachment lug. For specimen dimensions and flaw configurations, see Figs. 1 and 2 and Table 1.

Through-the-Thickness Crack at a Hole

The rectilinear through-the-thickness crack configuration theoretically defines a bidimensional fracture problem, although recently, the actual three-dimensional implications of a straight crack intersecting a free surface have been under scrutiny of analysts and experimentalists [*15–16*]. Inspection of fracture surfaces reveals that rectilinear through cracks are never found in fracture specimens because of the constraint variation along the crack front. Plane strain conditions prevail in the inner portion of the crack, and plane stress is expected on the crack-free surface intersections. The macroscopic effect is a characteristically thumb-nailed flaw shape.

Open Hole in a Plate in Tension—The classical solution by Bowie [*17*] for a through-cracked hole in a infinite plate loaded in tension has been used to establish the accuracy of sophisticated and versatile techniques [*18*]. Extensive experimental verification of its validity has also been successfully carried out. However, if the plate is of finite width, a correction factor has to be applied to the Bowie solution. In Ref *19*, a photoelastic analysis of a through-cracked hole in a finite-width plate evidenced a good correlation when a correction factor proposed in Ref *20* was used.

Pin-Loaded Hole in Rounded-End Attachment Lug—A lug involves a complex stress distribution, and contact loading further complicates the analysis. When a through crack emerges from the hole in the plane orthogonal to the load direction, a mixed mode (that is, opening and sliding) crack loading occurs. The contribution of the Mode-II loading has been experimentally evaluated to be less than 20% [*21*] and is usually neglected in calculations [*18*]. A discussion of the Mode-II loading effect on crack growth may be found in Ref *12*.

Two photoelastic tests were performed to analyze through-the-thickness cracks in lugs. Through-the-thickness cracks were grown from starter corner cracks (A detailed description of these tests is reported elsewhere [*12*].) Experimental flaws displayed the characteristic thumb-nailing of fatigued through cracks. The photoelastic analysis identified that even in these cases, an SIF variation, although slight, occurs along the crack front. Lower, nearly constant SIFs were associated with the flaw interior; higher SIF values were reached at the free surfaces.

Due to the engineering significance of the problem, several investigators have proposed approximate SIF solutions for a through-the-thickness crack in a pin-loaded lug. Impellizzeri and Rich [*22*] compounded Bueckner's weight function for an edge crack and the finite element analysis of the uncracked lug. A finite width correction factor was also introduced. Newman [*20*] adopted a superposition of analytical solutions and correction factors to account for the lug geometry and the through-crack configuration. Kirkby and Rooke [*23*] also employed a superposition scheme of analytical solutions. Schijve and Hoeymakers [*4*] correlated crack growth data for thin through-cracked lugs with results of centrally cracked specimens of the same material thickness tested under identical conditions. Hsu [*14*] used the finite element method with the inclusion of a high-order crack-tip singularity element to determine pin-lug contact pressure distribution and SIFs for straight and tapered attachment lugs. Fujimoto and Saff [*24*] applied the slice synthesis method to study a variety of cracks at fastener holes.

In Table 2, a comparison of the previous solutions and the photoelastic results is presented. In order to account for the experimental SIF gradients, two SIF estimates are included for each crack length. The first (minimum) SIF is relative to the internal part of the flaw. The second (maximum) SIF is a free surface value. Hsu's results were obtained from a diagram [*14*] in which no appreciable difference with Newman's solution could be assessed for the crack depths considered.

Inspection of Table 2 reveals that all the solutions listed above fall in a relatively narrow band if the differences in their approaches are considered. Also, the correlation between photoelastic and engineering estimates for the through-cracked lug can be considered satisfactory on an overall basis.

The SIF gradients along the flaws, which were found in the photoelastic analysis and which may be physically explained in terms of constraint vari-

TABLE 2—*Comparison of the photoelastic stress intensity factors for two through-the-thickness cracks in lugs with solutions from the literature.*

	Relative Crack Length					
	$c/D = 0.21$	$c/D = 0.42$	Investigator	Ref, Year	Method[a]	W/D
Normalized Mode-I SIF, $\frac{K}{\sigma\sqrt{\pi c}}$	2.75	2.48	Impellizzeri-Rich	[22], 1976	EE	2.37
	2.60	2.31	Newman	[20], 1976	EE	2.40
	3.18	2.73	Kirkby-Rooke	[23], 1977	EE	2.56
	2.62	2.30	Schijve-Hoeymakers	[4], 1979	FCGC	2.40
	2.60	2.31	Hsu	[14], 1981	FEM	2.50
	2.92	2.52	Fujimoto-Saff	[24], 1982	SSM	2.37
	2.58 to 3.02	2.44 to 2.56	present author		FSP	2.50

[a]EE = engineering estimate; FCGC = fatigue crack growth correlation; FEM = finite element method; SSM = slice-synthesis method; FSP = frozen-stress photoelasticity.

ation, do, however, affect more accurate comparisons. The Hsu, Newman, and Schijve-Hoeymakers solutions yield almost identical SIF estimates, which correlate well with the minimum experimental SIF results observed in the specimen interior. Note, however, that if the surface experimental SIFs are used in the comparison, not only the Fujimoto-Saff solution but also the Kirkby-Rooke solution, which was commented on in Ref *4* as yielding systematically higher values, correlate well.

Corner Crack at Hole

Several reasons justify the interest in an accurate LEFM characterization of corner cracks at fastener holes. First, the damage tolerance requirements for aircraft structures prescribe that a corner crack (that is, quarter circular in shape and 1.27 mm in size) be assumed at a fastener hole as initial primary damage when the material thickness is greater than 1.27 mm [*25*]. A second reason stems from the observation that the portion of crack growth life occurring before back surface penetration can be in many cases the predominant portion of the entire life of the cracked component. This is especially true for thick-walled components such as lugs.

Another reason for characterizing corner cracks arises when the results of Ref *4* are considered; that is, the growth rates of corner cracks in lugs were significantly lower than those of through cracks. The use of the equivalent through-crack solution would result in overly conservative life estimates and it could be justified only if a "worst case" calculation is sufficient [*4*]. In addition, the analytical complexities associated with the corner crack problem render the available SIF solutions less proven than two-dimensional solutions. Part-through cracks involve bidimensional patterns of growth and substantial SIF gradients along the flaw border. Reference *5* conjectures that cracks in the presence of SIF gradients do not behave like through cracks, which are characteristic of standard fracture mechanics specimens. Also, according to Ref *5*, the controlling SIF is not yet demonstrated as being the peak or some function of the actual SIF distribution.

Open Hole in a Plate in Tension—In an experimental study [*11*], the SIF distributions of four corner cracks at open holes in plates of finite width were obtained. The observed flaw shapes were approximated by quarter ellipses. Their aspect ratios are shown in Fig. 3. The photoelastic results displayed relatively large SIF gradients along the flaw profiles, especially for the shallower cracks. The experimental SIFs correlated well with numerical results obtained by the finite element alternating method (FEAM) [*26*] for closely approximating quarter-elliptical flaws. No finite width effect could be singled out from the comparison.

In Ref *19* these experimental SIFs at the front surface and at the hole-crack intersections were also checked against previous photoelastic results

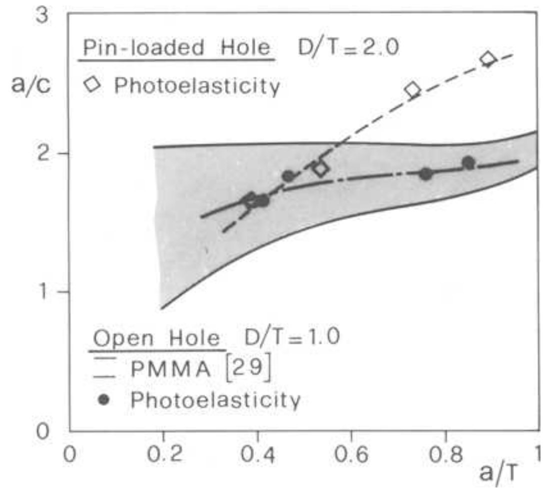

FIG. 3—*Quarter-elliptical aspect ratios for corner cracks.*

presented in Ref *27*. Only closely similar specimen and flaw geometries were considered. In these cases, the agreement between the two sets of photoelastic SIFs was within 8%.

These initial considerations on the verified accuracy of the photoelastic results help to compare the photoelastic results with the estimates obtained from several engineering solutions found in the literature; this comparison is presented in Fig. 4. The normalizing SIF used is given by the Bowie solution for a single through-the-thickness crack (that is, F_b is the Bowie function [*18*]). The photoelastic results are introduced as ranges, where the minimum SIF values are usually associated with the internal part of the flaw while the maximum SIF values are reached at the hole-crack intersection. Up to 30% SIF variation is found relative to an average SIF value. Solutions for wide plates were used in the correlation because, as previously pointed out in Ref *11*, no finite width effect on SIFs for the corner crack configuration could be singled out from the correlation with FEAM results.

The engineering solutions considered in the comparison include those of Hall and Finger [*20*], Shah [*28*], Newman [*20*], and Fujimoto and Saff [*24*]. Hall and Finger derived an empirical equation on the basis of residual strength tests of flawed specimens. They assumed that failure occurred when the standard fracture toughness (that is K_{Ic}) of the material was exceeded somewhere along the flaw. Even though the influence of the complex geometry is incorporated, the flaw aspect ratio was limited to $a/c < 1.0$. Shah used a Green's function approach to determine SIF starting from the stress distribution in the uncracked net section. Several correction factors had to be introduced to transform this solution for double embedded semicircular flaws at a hole into a solution for a single corner crack at a hole. Newman

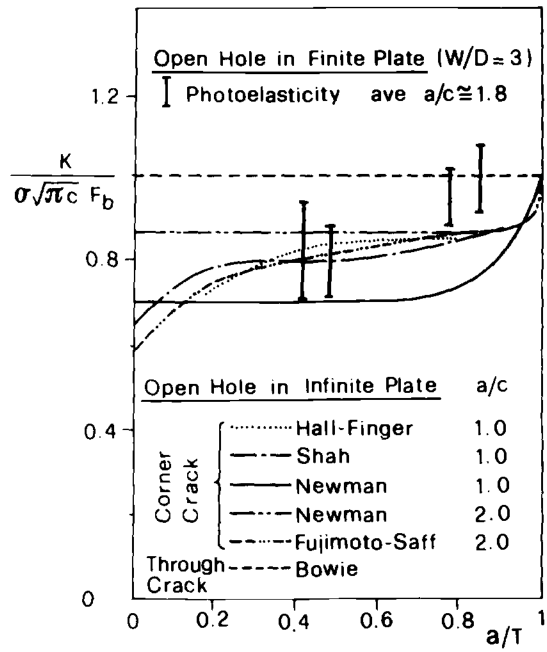

FIG. 4—*Comparison of photoelastic results with engineering solutions from the literature for corner cracks at an open hole.*

developed an empirical SIF equation for this corner crack problem. Recently, Fujimoto and Saff applied the slice synthesis method to several corner crack problems within a multidimensional crack growth prediction methodology. Note that the Fujimoto-Saff results shown in Fig. 4 were obtained from the original diagram [*24*] and that an a/c ratio of two was used in reducing their data.

Inspection of Fig. 4 reveals that all the solutions fall in a relatively narrow band which is bracketed by Newman's results for $a/c = 1$ and $a/c = 2$. The photoelastic results with their large SIF excursion along the flaw demonstrate that a single-value SIF correlation is difficult. For practical purposes, the solutions listed above are probably sufficiently accurate for engineering estimates of residual strength; however, the more versatile solutions have to be preferred. One of the limitations of several engineering solutions is the restriction of their applicability to a/c ratios less than 1.0; a/c ratios greater than 1.0, however, often are found when dealing with pure tensile loading, as is demonstrated by the results of a series of carefully monitored fatigue crack growth tests in polymethylmethacrylate (PMMA) discussed in Ref *29* and summarized in Fig. 3.

A final consideration is apparent from examination of Fig. 4: engineering and experimental estimates consistently predict lower SIFs than the Bowie through-crack solution. Reference *24* states that the bidimensional flaw shape evolution of a part-through crack represents, by itself, a mechanism of crack retardation.

Pin-Loaded Hole in a Rounded-End Attachment Lug—A series of frozen-stress photoelastic tests were run to investigate the effect of hole loading through a rigid pin on SIFs. SIF distributions for four crack configurations were obtained and are presented in Fig. 5. The magnified flaw shapes recorded during the tests are included in the same figure. They are characterized by higher a/c ratios of the approximating quarter of ellipse than the observed trend for the open hole case (see Fig. 3). A possible explanation of the differences of Fig. 3 is that there is a higher SIF reduction rate, with a crack depth, c, occurring at the crack-front surface intersection, for a loaded hole than for an open hole, as is presented in Figs. 6 and 7 of Ref *24*. This effect is related to the more severe stress gradient at a loaded hole than at an open hole. At the hole-crack intersection, the SIF variation with crack depth is expected to be less dramatic since the crack in both cases grows under constant far-field stress conditions.

As previously noted for corner cracks at open holes, marked SIF variations along the flaws are present. A comparison with open hole results demonstrates that the pin loading produces higher SIFs. In Ref *21*, several hundred percent increments in SIF were identified. If the present results are compared with the open hole results of Ref *11* at corresponding crack depths and positions along the crack profile the approximate increase in SIF is roughly 100%.

In Fig. 6, the photoelastic SIFs for the corner crack configurations are compared to the solutions for the through-the-thickness crack in a lug; these results were discussed in a previous section. As in Fig. 4, the presence of SIF gradients along corner flaws is included in the comparison by plotting a SIF range, in which the minimum SIF pertains usually to the internal part of the flaw and the maximum SIF occurs at the hole-crack intersection. The SIFs for transitioning cracks, also included, will be discussed in the next subsection. The front surface SIFs for a corner crack in a lug obtained by Fujimoto and Saff [*24*] are introduced in Fig. 6.

The through-cracked lug solutions yield higher SIFs than those for the corner crack configuration. In terms of applied SIF, this justifies the longer crack growth lives of corner cracked lugs, in comparison with through-cracked lugs, as reported in Ref *4*.

The photoelastic and the numerical data agree in describing an increasing SIF evolution with crack depth for corner cracks, which has to go through a maximum before coalescing with the decreasing SIF of a through crack.

Transitioning Crack Behavior

Analytical modeling of the corner crack evolution involves flaw shape assumptions. A quarter-elliptical approximation of a natural crack is nor-

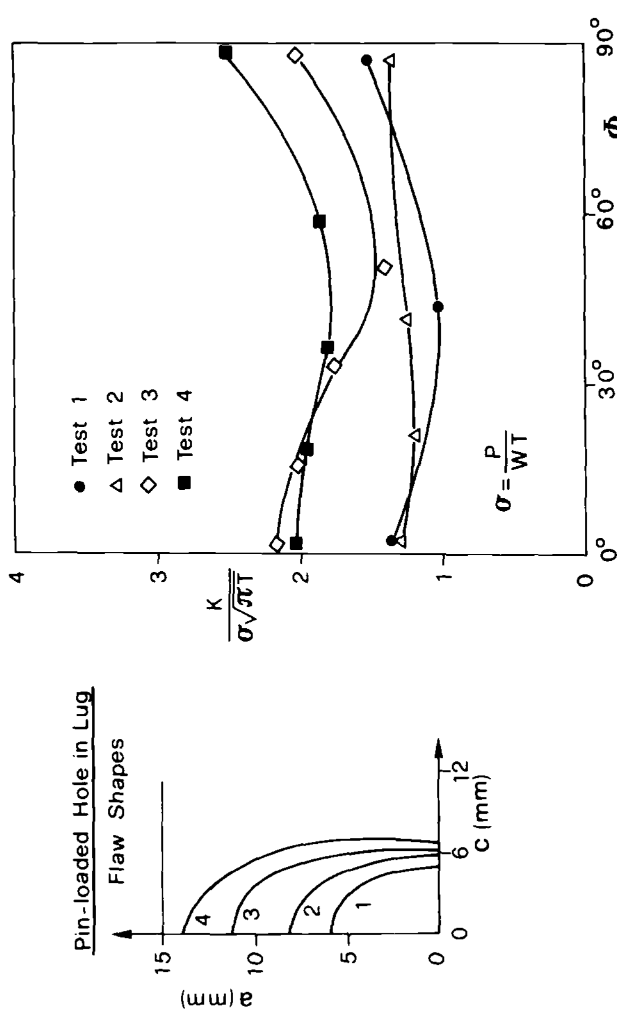

FIG. 5—*Observed flaw shapes and photoelastic SIF distributions for corner cracks at a hole in a lug.*

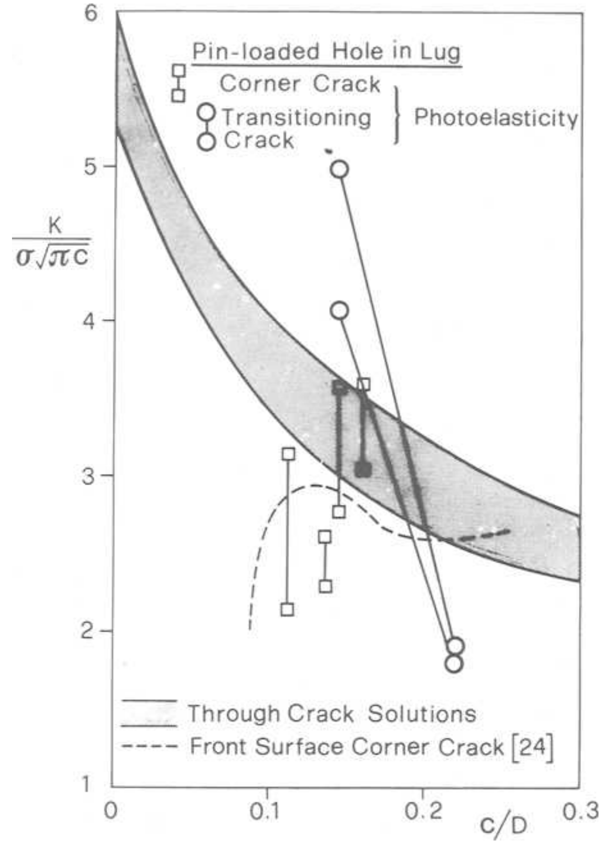

FIG. 6—*Comparison between photoelastic SIFs for corner cracks in a lug and engineering SIFs for a through-the-thickness configuration.*

mally accepted, and the accurate experimental observations of Ref *29* have provided its physical background. Self-similar crack growth (that is, it occurs when the a/c ratio is constant with increasing a/T) is another common assumption. Reference *24* demonstrates that a constant (in this case quarter-circular) shape assumption overestimates the cycles to breakthrough by a factor of two. A transitioning crack that involves the growth portion from back surface penetration to a stable through-the-thickness configuration is never self-similar if a quarter-elliptical schematization is maintained [*30*]. Several criteria have been proposed to characterize the transitioning behavior of part-through cracks (an example is in Ref *31*). Limited evidence, however, has been gathered on the actual transitioning behavior in terms of flaw shape evolution and SIFs.

Recently, this subject has been dealt with in Ref *29*. The investigators studied fatigue crack growth evolution at open holes in transparent PMMA

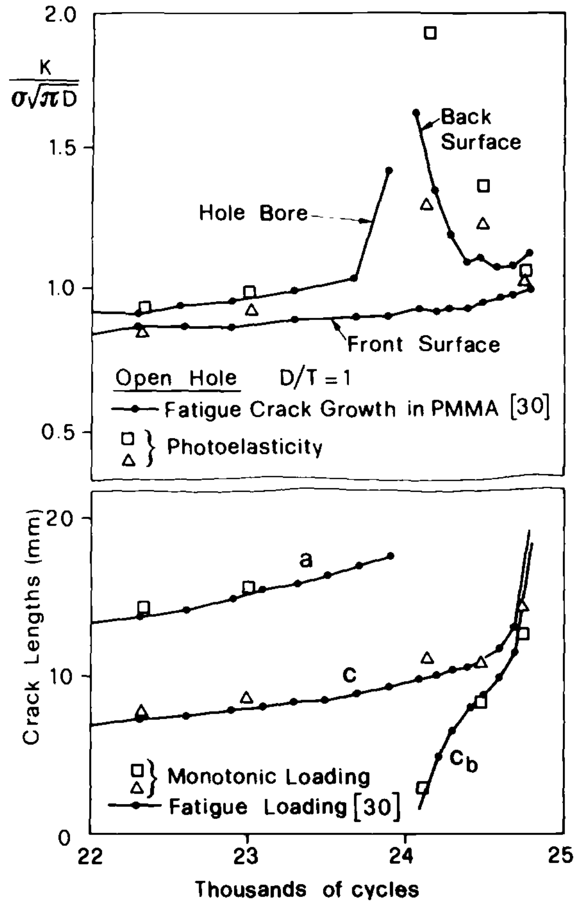

FIG. 7—*Crack growth patterns at an open hole in wide polymethyl methacrylate (PMMA) specimens and in finite epoxy specimens and corresponding free-surface SIFs during the transition from the corner to through the thickness.*

specimens. An accurate record of the crack dimensions they obtained with a photointerpreter/digitizer is shown in Fig. 7. The crack dimensions observed during the photoelastic study of geometrically identical (except in width) epoxy specimens are introduced in the same figure in order to define the corresponding points for the SIF comparisons presented in the upper part of the figure. Since no marked influence on flaw evolution parameters of the type of loading (that is, fatigue versus monotonic) or of the elastic material properties (Poisson's ratio of 0.34 for PMMA versus 0.49 for the epoxy resin above critical temperature) was previously assessed in Ref *11*, it was expected here that a fatigue and a monotonic crack under identical boundary conditions would go through similar crack configurations.

Inspection of Fig. 7 yields a comparison between corresponding SIF values at the two free surface intersections obtained by the crack growth rate correlation technique [29] and by frozen-stress photoelasticity. Note that both techniques evidence a peak in SIF occurring when the crack penetrates the back surface, which signals a highly unstable crack configuration. Accelerated growth rates ensue and a through-the-thickness configuration is reached in a limited number of cycles. The higher photoelastic SIFs after back surface penetration are probably due to the finite width of the epoxy specimens.

The validity of these observations for open holes are confirmed when SIFs obtained during the extensive photoelastic study of cracked lugs, reported in Ref *12*, are considered. In Fig. 8, front, back, and internal SIFs are plotted versus the hole and back surface depth of the flaw. The front and hole SIFs increase gradually up to back surface penetration when a drastic drop in the front SIF is countered by a less marked decrease in the back surface SIF. A steadily increasing SIF distribution for the transitioning portion of crack growth is reported in Ref *12* and is apparent in Fig. 6. When a stable (that is, through-the-thickness) configuration is regained, the front and back SIFs coalesce. Interestingly, the internal SIFs seem less affected by the transitioning process than the surface values.

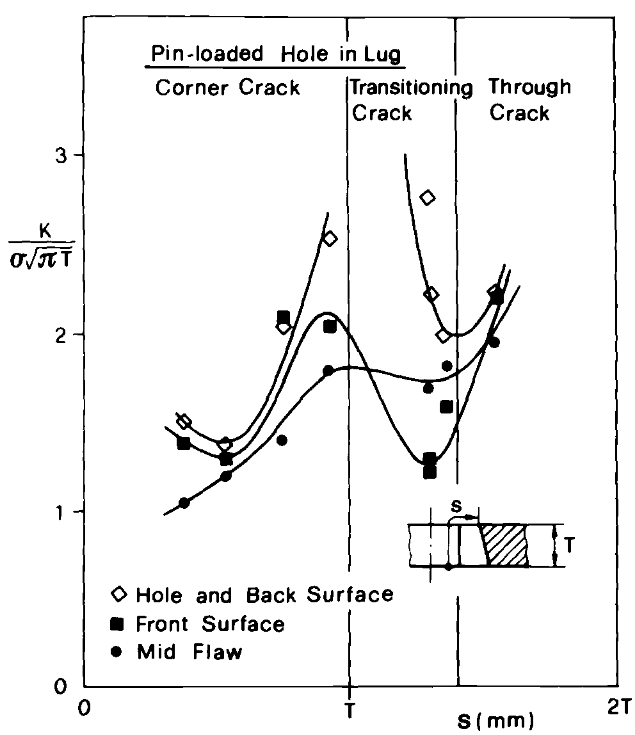

FIG. 8—*SIF evolution during the transition from the corner to through the thickness of a crack in a lug.*

From the previous observations, it is apparent that a transitioning criterion for a corner crack at a hole is analogous to the one included in Ref *31* for surface flaws. The entire crack growth life could be the sum of the corner crack growth life until breakthrough, and of the through-crack growth life from a depth equal to the plate thickness divided by the breakthrough aspect ratio until collapse.

Modeling Aspects of Three-Dimensional Fracture Problems

The practical significance of part-through cracks has been recognized for the past 20 years. However, the derivation of accurate SIF solutions needed in fracture calculations has been hindered by analytical complexities. Since only approximate engineering and numerical methods are applicable, experimental verification of the results is essential.

In 1976, a meeting of three-dimensional fracture specialists identified three "benchmark" types of flaws to be independently studied in great detail using a variety of numerical techniques [*32*]. Semielliptical surface flaws and quarter-elliptical corner cracks at open holes, both in plates under tension, were included, and flaw geometries were specified.

Since then, a greater effort probably has been devoted to the development of accurate SIF solutions for the semielliptical surface crack problem. In 1980, McGowan edited a paper [*33*] in which the numerical results for the benchmark crack geometries obtained with different techniques showed a remarkable agreement. A Schwartz alternating method, boundary integrals, and finite elements with either virtual crack displacement or crack-tip singular elements were assessed to yield SIF distributions that fell within a $\pm 3\%$ uncertainty band.

The results of this study demonstrated that powerful numerical techniques are now available for three-dimensional fracture analysis. However, the photoelastic results for surface flaws of C. W. Smith and Kirby [*7,8*] clarify that SIF values greatly depend on the flaw shape assumption, a prerequisite of the numerical techniques. An extensive experimental program demonstrated that natural shallow cracks were indeed semielliptical in shape, but that natural deep cracks deviated from the assumed semielliptical shape. Flexural loads had to be applied to approximate the crack aspect ratios specified by the benchmark geometries. These observations on flaw shape affected the SIF comparisons. One of the conclusions of Refs *7* and *8* is that some benchmark crack geometries recommended by the 1976 workshop could not be used for uniform tensile loading.

These considerations on modeling of surface flaws are significant for any part-through crack problem. In the following subsections two aspects involved in part-through crack analysis are discussed. First, local SIF variations due to natural flaw shape distortions are discussed. The impact on SIF of the aspect ratio assumption is finally analyzed.

Local Flaw Shape-SIF Interaction

In LEFM it is normally assumed that crack growth is controlled by the local SIF value. The photoelastic technique can give some insight on flaw evolution as related to local SIFs. In Ref *11* it was demonstrated that numerical and experimental results for open holes agree closely when the assumed and observed flaw shapes are similar (see the example in Fig. 9). The observed flaw and the approximating quarter ellipse of Test 3 are almost identical, and numerical and experimental SIF distributions are close. However, in practice, observations of postfailure fracture surfaces often display distorted flaw shapes. These flaws cannot be modeled numerically while photoelastic specimens sometimes present themselves in irregular flaw shapes. The recorded flaw shapes of some corner crack tests at open holes and fitted quarter ellipses are also shown in Fig. 9.

In Test 1, the natural flaw trails the fitted quarter ellipse in the interior; in Test 2 the natural flaw shape leads the fitted ellipse in the inner portion of the crack. When the photoelastic SIFs are compared to FEAM results [*18*] for an approximating flaw geometry, the downward concave SIF distribution indicates an increase in growth rate to be expected in the interior for Test 1. Conversely, for Test 2 a drop in the photoelastic SIF below the numerical results in the interior suggests a local decrease in crack growth. Similar observations were pointed out in Ref *34*.

It follows that an upward concave SIF distribution at the crack-free surface intersections and a nearly flat SIF distribution in the inner portion of the crack define a stable crack configuration with respect to the loading and geometrical boundary conditions (see Test 3).

Aspect Ratio Effect on Corner Crack SIFs

Extensive testing and accurate recording of the flaw shape evolution of corner cracks at open holes in fatigued PMMA specimens reviewed recently in Ref *29* have already been presented in Fig. 3. (Test 8 of Ref *29* is not included.) The shaded area defines the scatter band of observed fitted elliptical aspect ratios. In the same figure the aspect ratios observed during monotonic growth of cracks in epoxy demonstrates an accurate modeling of the corner crack at an open hole. Figure 3 defines a characteristic a/c ratio ranging from 1.5 to 2.0. In order to assess the influence of the flaw shape assumption on SIF distributions, the FEAM results for a corner crack of depth $a/t = 0.5$ and for various a/c ratios [*18*] are presented in Fig. 10. The numerical SIF distributions associated with $1.5 < a/c < 2.0$ display nearly constant, upwardly concave distributions, and photoelastic SIFs confirm the observation. The photoelastic SIF drop in the interior was addressed in the preceeding subsection. The numerical SIFs show steep SIF gradients for $a/c < 1.5$ or downward concave SIF distributions for $a/c > 2.0$. The author concludes that crack aspect ratios outside the previous a/c range are

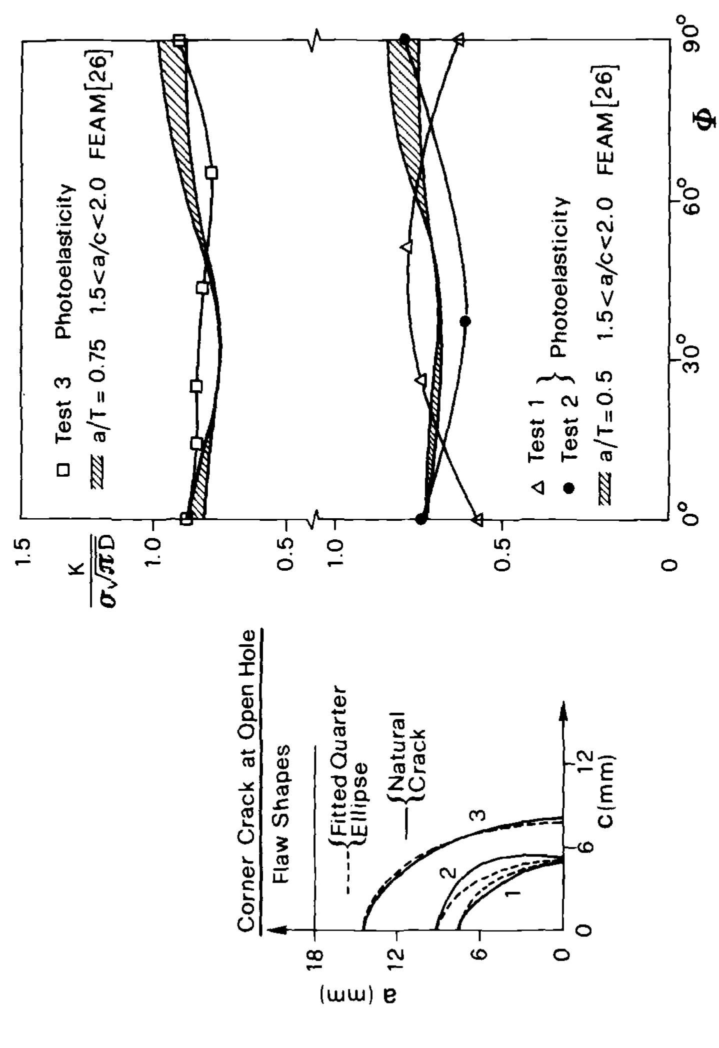

FIG. 9—*Local flaw shape distortions and corresponding SIF distributions.*

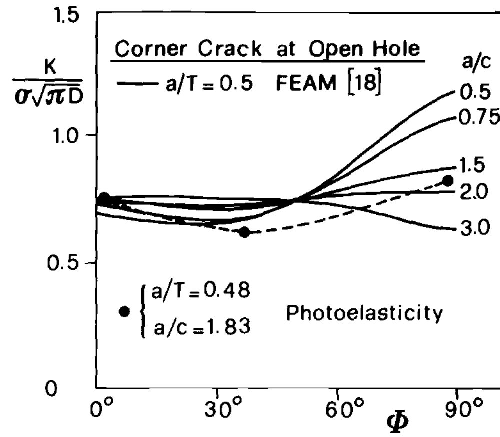

FIG. 10—*Aspect ratio effect on SIF distributions for a corner crack at an open hole.*

not associated with pure tensile loading. Also, steep gradients or downward concave SIF distributions may indicate a mismatch between the flaw aspect ratio and imposed boundary conditions.

These considerations and those previously included in the transitioning crack section confirm the validity of a multidimensional (that is, more than two free parameters) crack growth approach because it can be extended to non-self-similar propagation. Such an approach was developed in Ref *35* for corner cracks at holes. An SIF-based check of the flaw shape stability at each crack increment was also incorporated in a part-through crack growth prediction scheme.

Summary

In the present paper a series of frozen-stress photoelastic results have been presented and discussed. Corner, transitioning, and through-the-thickness cracks have been analyzed in terms of actual flaw shapes and corresponding SIF distributions. Single cracks at open holes and pin-loaded attachment lugs were examined.

One goal was to compare the experimental results with engineering solutions from the literature for the crack configurations considered. Through-crack behavior seems well-characterized by the existing solutions. The corner crack configuration presents additional difficulties essentially related to the observed SIF gradients along the flaw profiles. The transitioning behavior of a part-through crack has also been analyzed in terms of SIFs. This is particularly significant because this problem is not tractable with numerical methods since the crack growth is markedly non-self-similar.

Finally, aspects associated with modeling three-dimensional fracture problems have been discussed. The LEFM assumption of SIF-controlled local flaw evolution appears experimentally motivated. Although the experimental technique used throughout the work has its own limitations, it represents a powerful engineering tool for treating complex fracture problems, especially when non-self-similar crack growth patterns are involved.

Acknowledgments

The author wishes to acknowledge V. Taglioli, A. Petrucci, and the laboratory staff and facilities of the Istituto di Meccanica Applicata alle Macchine for assistance during the experiments.

References

[1] Schijve, J., "Lecture Notes on Fatigue, Static Tensile Strength and Stress Corrosion of Aircraft Materials and Structures," Report LR-360, Delft University of Technology, Delft, The Netherlands, October 1982.
[2] Wood, H. A., Rudd, J. L., and Potter, J. M., "Evaluation of Small Cracks in Aircraft Structures," *Some Considerations on Short Crack Growth Behaviour in Aircraft Structures,* AGARD-R-696, Advisory Group for Aerospace Research and Development, Neuilly sur Seine, France, 1983, pp. I/1 to I/11.
[3] Coffin, M. D. and Tiffany, C. F., *Journal of Aircraft,* Vol. 13, No. 2, 1976, pp. 93–98.
[4] Schijve, J. and Hoeymakers, H. W., *Fatigue of Engineering Materials and Structures,* Vol. 1, 1979, pp. 185–201.
[5] Anstee, R. E. W. and Edwards, P. R., "A Review of Crack Growth Threshold and Crack Propagation Rates at Short Crack Lengths," *Some Considerations on Short Crack Growth Behaviour in Aircraft Structures,* AGARD-R-696, Advisory Group for Aerospace Research and Development, 1983, pp. 2/1 to 2/12.
[6] Smith, C. W., *Optical Engineering,* Vol. 21, No. 4, 1982, pp. 696–703.
[7] Smith, C. W. and Kirby, G. C. in *Fracture Mechanics: Fourteenth Symposium—Volume I: Theory and Analysis, ASTM STP 791,* American Society for Testing and Materials, Philadelphia, 1983, pp. I/269–280.
[8] Smith, C. W. and Kirby, G. C. in *Proceedings,* 15th National Symposium on Fracture Mechanics, University of Maryland, College Park, MD, July 1982.
[9] Phang, Y. and Ruiz, C., "Recategorisation of Embedded Defects as a Single Embedded or Surface Defect," *Application of Fracture Mechanics to Materials and Structures,* Martinus Nijhoff, The Hague, The Netherlands, 1984, pp. 429–440.
[10] Kuske, A. and Robertson, G., *Photoelastic Stress Analysis,* Wiley, New York, 1974, pp. 112–114.
[11] Nicoletto, G., "Stress Intensity Distributions for Corner Cracks Emanating from Open Holes in Plates of Finite Width," *International Journal of Theoretical and Applied Fracture Mechanics,* Vol. 3, 1985.
[12] Nicoletto, G., "Stress Intensities for Cracks at Holes in Rounded-End Straight Attachment Lugs," *Engineering Fracture Mechanics,* Vol. 22, No. 5, 1985, pp. 829–838.
[13] Blok, H., "Inverse Problems in Hydrodynamic Lubrication and Design Directives for Lubricated Flexible Surfaces," *Proceedings,* Symposium on Lubrication and Wear, University of Houston, TX, 1963, p. 69.
[14] Hsu, T. M., *Journal of Aircraft,* Vol. 18, No. 9, 1981, pp. 755–760.
[15] Burton, W. S., Sinclair, G. B., Soleki, J. S., and Swedlow, J. L., *International Journal of Fracture,* Vol. 25, 1984, pp. 3–32.
[16] Epstein, J. S., "On the Variation of the First Classical Eigenvalue of Fracture Mechanics in Three Dimensional Transitory Stress Fields," Ph.D. dissertation, Virginia Polytechnic Institute and State University, Blacksburg, VA, 1983.
[17] Tada, H., Paris, P. C., and Irwin, G. R., *The Stress Analysis of Cracks Handbook,* Del Research Corp., Hellertown, PA, 1973.
[18] Smith, F. W. and Kullgren, T. E., "Theoretical and Experimental Analysis of Surface Cracks Emanating from Fastener Holes," AFFDL-TR-76-104, Air Force Flight Dynamics Laboratory, Wright-Patterson Air Force Base, OH, February 1977.

[19] Nicoletto, G., "Experimental Characterization of a Crack Emerging from a Circular Hole in a Plate in Tension," *Proceedings*, Assozione Nazionale per L'Analisi delle Sollecitazioni National Conference, University of Naples, Naples, Italy, 1984, pp. 289–299 (in italian).
[20] Newman, J. C. Jr., "Predicting Failure of Specimens with Either Surface Cracks or Corner Cracks at Holes," NASA TN D-8244, National Aeronautics and Space Administration, Washington, DC, June 1976.
pp. 63–73.
[21] Smith, C. W., Jolles, M., and Peters, W. H. in *Flaw Growth and Fracture; Tenth Conference, ASTM STP 631*, American Society for Testing and Materials, Philadelphia, 1977, pp. 190–201.
[22] Impellizzeri, L. F. and Rich, D. L. in *Fatigue Crack Growth Under Spectrum Loads, ASTM STP 595*, American Society for Testing and Materials, Philadelphia, 1976, pp. 320–336.
[23] Kirkby, W. T. and Rooke, D. P., "A Fracture Mechanics Study of the Residual Strength of Pin-Loaded Specimens," *Fracture Mechanics in Engineering Practice*, Applied Science Publishers, London, 1977, p. 339.
[24] Fujimoto, W. R. and Saff, C. R., *Journal of Experimental Mechanics*, Vol. 22, No. 4, 1982, pp. 139–146.
[25] Rudd, J. L., Hsu, T. M., and Wood, H. A. in *Part-Through Crack Fatigue Life Prediction, ASTM STP 687*, American Society for Testing and Materials, Philadelphia, 1979, pp. 168–194.
[26] Kullgren, T. E., Smith, F. W., and Ganong, G. P., *Journal of Engineering Materials and Technology*, Vol. 100, 1978, pp. 144–149.
[27] Smith, C. W., Peters, W. H., and Gou, S. F. in *Fracture Mechanics: Eleventh Conference, ASTM STP 677*, American Society for Testing and Materials, Philadelphia, 1979, pp. 431–445.
[28] Shah, R. C. in *Mechanics of Crack Growth, ASTM STP 590*, American Society for Testing and Materials, Philadelphia 1976, pp. 429–459.
[29] Grandt, A. F. and Macha, I. E., *Engineering Fracture Mechanics*, Vol. 17, No. 1, 1983, pp. 63–73.
[30] Grandt, A. J., Harter, J. A., and Heath, B. J., "The Transition of Part-Through Cracks at Holes into Through-the-Thickness Flaws," *Fracture Mechanics, ASTM STP 833*, American Society for Testing and Materials, Philadelphia, 1984.
[31] Rudd, J. L. in *Part-Through Crack Fatigue Life Prediction, ASTM STP 687*, American Society for Testing and Materials, Philadelphia, 1979, pp. 96–112.
[32] Hulbert, L. E., *International Journal of Fracture*, Vol. 13, 1977, pp. 87–91.
[33] McGowan, J. J., *Journal of Experimental Mechanics*, Vol. 20, No. 8, August 1980, pp. 253–264.
[34] Smith, C. W. and Nicoletto, G., "Experimental Stress Intensity Distributions by Optical Methods," *Defects, Fracture and Fatigue*, Martinus Nijhoff, The Hague, The Netherlands, 1983, pp. 325–336.
[35] Lof, C. J., "Lifetime Prediction Methods for Corner Cracks at Holes," *Behaviour of Short Cracks in Airframe Components*, AGARD-CP-328, 1983, Advisory Group for Aerospace and Development, Neuilly sur Seine, France, pp. 9/1 to 9/9.

John C. Ekvall[1]

Fatigue of Riveted Metallic Joints

REFERENCE: Ekvall, J. C., **"Fatigue of Riveted Metallic Joints,"** *Fatigue in Mechanically Fastened Composite and Metallic Joints, ASTM STP 927,* John M. Potter, Ed., American Society for Testing and Materials, Philadelphia, 1986, pp. 172–189.

ABSTRACT: Spectrum fatigue test results are presented on riveted lap joint and flush joint specimens made from 7075-T6 plate and extrusion and from 7091-T7E69 and IN9021 powder metallurgy (PM) aluminum alloys. For the lap joint specimens, the 7091-T7E69 PM plate material exhibited a shorter fatigue life than the 7075-T6 plate, 7091-T7E69 extrusion, and IN9021 extrusion materials. Crack growth rates were determined for the PM aluminum alloys from characteristic markings made on the fracture surfaces by the modified Minitwist fatigue loading spectrum. Fatigue life predictions were made for two types of 7075-T6 aluminum joints using the local stress-strain method of fatigue analysis. Finite element stress analyses were conducted to determine the local stress and strain at the fatigue critical location of the test specimens due to the spectrum of applied loads. Fatigue life predictions agreed with the test results within a factor of 1.22 for the two types of 7075-T6 specimens analyzed when accounting for the difference in fatigue properties of the materials with respect to grain direction.

KEY WORDS: riveted joints, aluminum alloys, finite element analysis, fatigue analysis, spectrum fatigue tests, fatigue life, fracture surface markings, crack growth rate, evaluation, powder metallurgy (PM)

Aluminum rivets are used extensively for joining members in aluminum aircraft structures. Good joint fatigue lives are obtained with rivets that expand to fill the fastener hole during installation. A proper installation imparts a small amount of residual stress in the sheet materials, which to a large extent alleviates variations in manufacturing hole quality. The rivet installation does not impart a large amount of residual stress, such as the split-sleeve cold working process, or a large amount of clamp-up, as with steel threaded fasteners with torque-off collars. Therefore, the effects of residual stress due to cold working or frictional restraint due to clamp-up are not considered in this paper.

Fatigue life predictions based on local stress and strain have been emerging since the late 1960s. These methods of analysis have been shown to be accurate for predicting the fatigue life of notched specimens by various investigators [*1*]. However, the methods of analysis have generally not been

[1] Research and development engineer, Lockheed-California Co., Burbank, CA 91520.

applied to predicting the fatigue life of mechanically fastened joints. This is because of the difficulty in accounting for the effects of residual stress due to cold working the hole, frictional restraint due to clamp-up, or fretting, which usually occurs in dry joints. This paper presents the fatigue test results of joints made from various aluminum materials and riveted with 7050-T73 and 2024-T31 alloy rivets. The joints were fabricated with a faying surface polysulfide sealant, and the fasteners were installed wet, which minimizes the effect of fretting fatigue, according to process bulletins of the Lockheed-California Co.

The local stress and strain at the fatigue critical location were determined for two types of aluminum joints using finite element analysis. Finally, fatigue life predictions were correlated with spectrum fatigue test results.

Fatigue Tests of Riveted Joints

Some fatigue tests were conducted to compare the fatigue properties of riveted joint specimens made from 7075-T6 aluminum plate and various powder metallurgy (PM) aluminum alloys. The geometries of the two types of specimens tested are shown in Fig. 1. The spliced joint specimens were made from 7075-T6 and 7091-T7E69 aluminum plate machined to 3.81-mm thickness and joined together with a 7075-T6 tee extrusion. The spliced joints were fastened with eight 4.76-mm-diameter 7050-T73 protruding head rivets with a 2D edge distance and a 4D spacing. The four-row lap joint specimens were made from four different aluminum alloys, 7075-T6 plate, 7091-T7E69 plate, 7091-T7E69 extrusion, and IN9021 extrusion. The materials were machined to 3.81-mm thickness and joined together with 4.76-mm-diameter DD (2024-T31) protruding head rivets at a 2D edge distance and 4D spacing. The joints were assembled with a faying surface sealant, and the fasteners were installed wet. The installation of the fastener expanded the diameter of the hole about 0.076 mm (0.003 in.).

Spectrum fatigue tests were conducted using the Minitwist (Modification A) spectrum loading sequence. The Minitwist fatigue loading spectrum [2], representative of the stresses in the wing lower surface of a transport aircraft, was modified (Modification A) by resequencing the 14 most severe flights, as shown in Table 1. Groups of 2 or 3 of the 14 most severe flights were spaced at 800 flight intervals within the basic 4000 flight spectrum. The relative severity of Flights A through E is indicated by the ratio of the maximum flight stress to the mean flight stress, S_{max}/S_m, in Table 1. Each group of severe flights was arranged in a low/high sequence. The flight groupings with the A, B, and C flights were arranged in a low/high sequence after the first application of the A flight. As shown in Ref *3*, this spectrum sequence provides characteristic markings every 800 flights on the fracture surface of 7075-T6 sheet and 7091-T7E69 plate materials, which aids in the post-failure examination of fatigue and crack growth test specimens. The

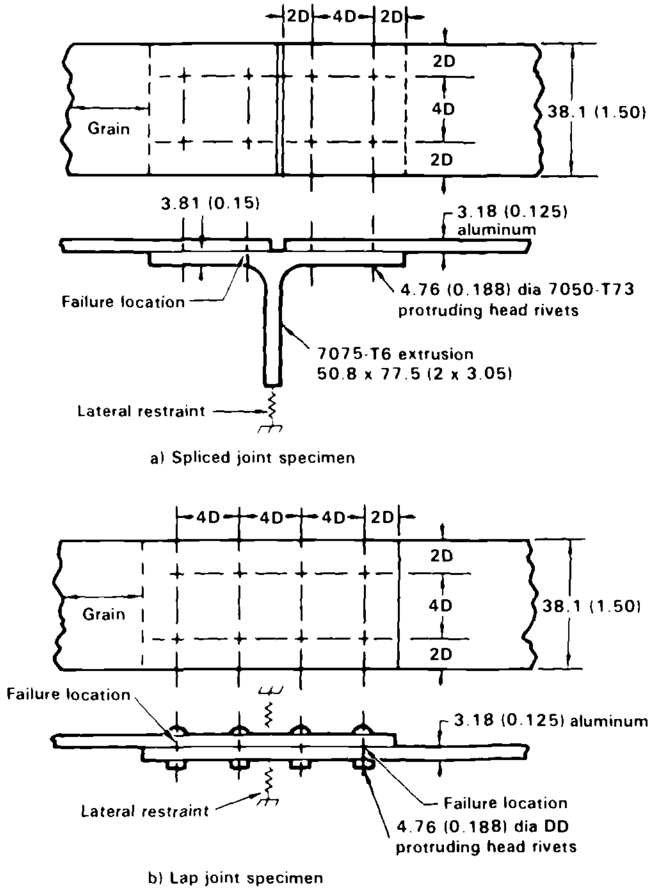

FIG. 1—*Design of mechanically fastened joint specimens: the fasteners were installed wet and assembled with a faying surface sealant; the dimensions are in millimetres (inches).*

TABLE 1—*Location of 14 most severe flights for Minitwist and Minitwist Modification A spectra.*

	Flight Number of Spectrum Sequence		
Type of Flight	Minitwist	Minitwist Modification A	$\frac{S_{max}}{S_m}$ Ratio[a]
A	1656	2800	2.60
B	2856	2001	2.50
C	501, 2926, 3841	401, 1201, 3601	2.30
D	106, 412, 689, 1099, 1653, 2682, 3360, 3835, 3894	399, 400, 1199, 1200, 1999, 2000, 2799, 3599, 3600	2.15
E	...	...	1.995

[a] S_{max} = maximum flight stress; S_m = mean flight stress.

author hoped that this spectrum sequence would also make characteristic markings on the fracture surface of the riveted joint specimens.

The results of the fatigue tests are given in Table 2. Both types of specimens were laterally restrained at the center of the joint, as shown in Fig. 1. The spliced joint specimens were tested at a 1-*g* stress of 62.1 MPa (9 ksi) and the lap joint specimens were tested at 1-*g* stress of 68.95 MPa (10 ksi). The spliced joint specimen failed in the 7075-T6 tee extrusion across the inside fastener row, as shown in Fig. 1*a*. The lap joint specimens failed in the sheet at the outside fastener row, either in the sheet next to the fastener heads or in the sheet next to the fastener bucktails.

As shown in Table 2, both spliced joint specimens failed in the 7075-T6 extrusion; therefore, no comparison can be made between the two plate materials. For the lap joint specimens, the 7091-T7E69 PM plate material exhibited a shorter fatigue life than the 7075-T6 plate, 7091-T7E69 extrusion, and IN9021 extrusion materials. Metallurgical examination indicated the 7091-T7E69 plate material was recrystallized, which may explain the poor fatigue test results. A large scatter was exhibited by both PM extrusion materials. Inclusions were noted at many places on the fracture surface of the IN9021 material, as shown in Fig. 2. An inclusion located in the vicinity of the fatigue origin would be a cause for early fatigue crack initiation. However, no inclusions were noted on the fracture surface of the 7091-T7E69 extrusion material.

The Minitwist (Modification A) spectrum made markings on the fracture surface of the PM aluminum materials, as shown in Fig. 3 for Specimen

TABLE 2—*Summary of fatigue tests conducted on mechanically fastened joint specimens.*

Joint Material	Specimen Type (see Fig. 1)	Flight 1-*g* Gross Area Stress, MPa[a]	Specimen No.	Failure Location[b]	Flights to Failure	Geometric Mean Flights
7075-T6 plate	spliced joint	62.10	A1	tee	9 199	10 176[c]
7091-T7E69 plate	spliced joint	62.10	B1	tee	11 257	. . .
7075-T6 plate	lap joint	68.95	A3	tail	53 185	42 269
			F1	head	50 788	
			F3	tail	29 991	
7091-T7E69 plate	lap joint	68.95	B2	tail	19 941	24 100
			B3	head	29 203	
7091-T7E69 extrusion	lap joint	68.95	C2	tail	80 011	37 400
			C3	tail	17 507	
IN9021 extrusion	lap joint	68.95	D2	tail	17 321	40 800
			D3	tail	96 055	

[a]Minitwist (Modification A) test spectrum. The end of each flight goes to -0.5 1-*g* flight stress.

[b]Failures at locations shown in Fig. 1 are as follows: head—failure in the sheet next to the fastener heads; tail—failure in the sheet next to the fastener bucktails; and tee—failure in the tee extrusion.

[c]Both specimens failed in the 7075-T6 tee extrusion.

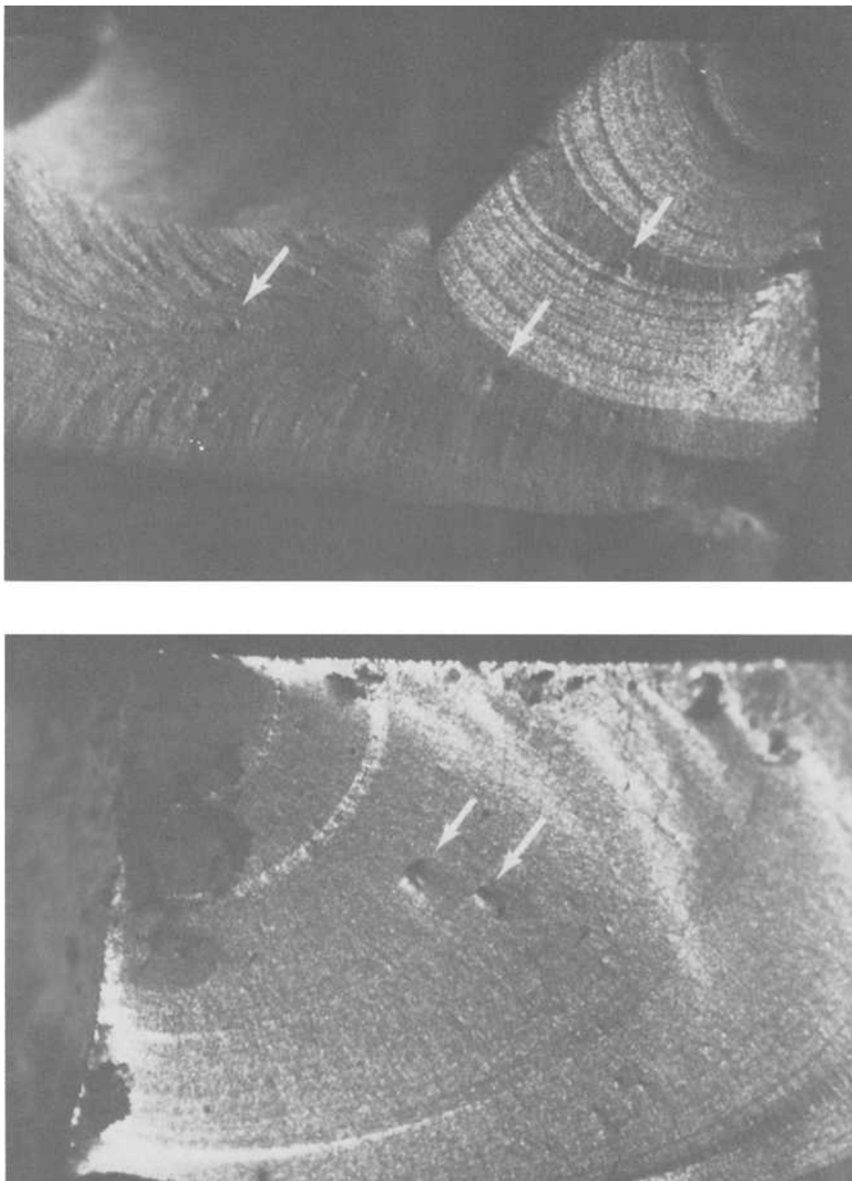

FIG. 2—*Inclusion noted by arrows on macrophotos at two locations on the fracture surface of IN9021 extrusion in Specimen D2 (magnification ×25).*

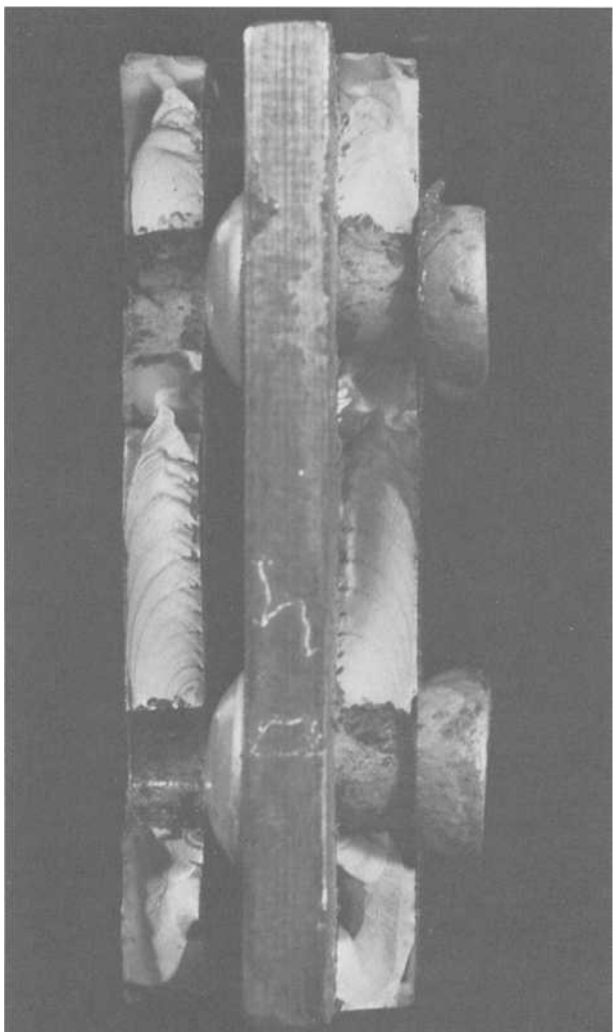

FIG. 3—*Fracture surface of Specimen D2 showing markings made by periodic growth flights spaced at 800 flight intervals.*

D2. These narrow markings are readily identifiable visually or under low magnification and are due to the growth flights spaced at 800 flight intervals. No markings were observed on the fracture surfaces of the 7075-T6 aluminum. The differences in marking characteristics between the two types of materials is attributed to microstructural features. The PM aluminum alloys have a very fine grain structure and the fracture surfaces are very smooth, including the raised markings made by the severe flights. The 7075-T6 aluminum has a much larger grain structure and the fracture surfaces have a rough jagged appearance. A slight mismatch between mating surfaces during compression loading will cause the fracture surfaces to rub and obliterate the markings on the 7075-T6 aluminum but not on the PM aluminum alloys.

Visual examination of the fracture surfaces was made to determine the number of flights of crack growth as indicated by the markings on the fracture surfaces. Table 3 presents a summary of the results, including the number of crack origins and the initial and final crack sizes of the largest crack observed on the fracture surface. The smallest observable marking was a semicircular corner crack approximately 0.5 to 0.8 mm long. Specimen D3 had some sealant near the origin which covered the fracture surface out to about 1.27 mm from the origin. These results indicate a crack growth life varying from about 6500 flights for 7091-T7E69 plate to about 11 000 flights for IN9021 extrusion. The fact that companion specimens had a different number of crack origins did not have a significant effect on the

TABLE 3—*Summary of crack growth measurements made on fracture surfaces of lap joint fatigue specimens.*

Specimen No.	No. of Crack Origins	Measurements of Largest Crack[a] Location[b]	Initial Crack Size, mm	Final Crack Size, mm	Flights of Crack Growth
A1	4	edge	. . .	4.3	. . .
		center		4.3	. . .
B1	4	edge	. . .	7.1	. . .
A3	4	center	. . .	12.5	. . .
F1	2	edge	. . .	6.4	. . .
F3	3	center	. . .	9.7	. . .
B2	4	center	0.56	8.4	6 741
B3	2	center	0.66	6.1	6 400
C2	2	edge	0.51	6.6	10 011
C3	3	edge	0.64	6.6	8 121
D2	3	center	0.41	10.9	10 321
D3	2	center	1.19	13.0	11 255

[a]The crack is measured on the faying surface from the edge of the fastener hole.
[b]The center crack is between the fastener holes. The edge crack is between the fastener hole and the edge of the specimen.

crack growth interval. Also, the large differences in fatigue lives between the specimens of the two PM extrusion materials is not due to differences in the crack growth rates.

Crack growth curves for the largest cracks in Specimens D2 and D3 are plotted in Fig. 4 based on measurements made of the markings on the fracture surface. The locations of the A and B flights were identified based on the pattern of the markings and their relationship to the flights associated with final failure. Both curves are relatively smooth continuous curves even though the A and B flights contain loadings significantly higher than those of the other flights (see Table 1). Although the A, B, and C grouping of flights produce characteristic markings, there is no indication of crack growth retardation after the application of the A or B flights in Fig. 4. This was also noted on the crack growth curves of 7075-T7E69 plate presented in Ref *3*, where crack growth measurements were made at closely spaced intervals. This is in agreement with McEvily [*4*], who noted a lack of detectable crack closure for IN9021 PM aluminum alloy even at threshold.

Finite Element Analysis

Finite element analyses were conducted for both joint specimens to determine the relationship between applied load and local stress at the failure location. The finite element model developed for the two joint specimens is shown in Fig. 5. The finite element models consisted of a series of bar elements connected at node points, which were offset at the fastener locations, as shown in Fig. 5. For the bypass load, the node is along the centroidal axis (center of gravity) of the plate. For load transfer, the node point is at the interface between the two plates.

The fasteners were modeled by three spring constants corresponding to the stiffnesses due to an axial load, a shear load, and a bending moment applied to the fastener. For calculating the spring constants, the fastener was modeled as a double cantilever beam fixed at the centerline of each plate. The equations for the cantilever beam fastener stiffnesses are

$$K_x = \frac{3EI}{L^3} + \frac{10AG}{9L} \tag{1}$$

$$K_y = \frac{AE}{L} \tag{2}$$

$$K_0 = \frac{2EI}{L^2} \tag{3}$$

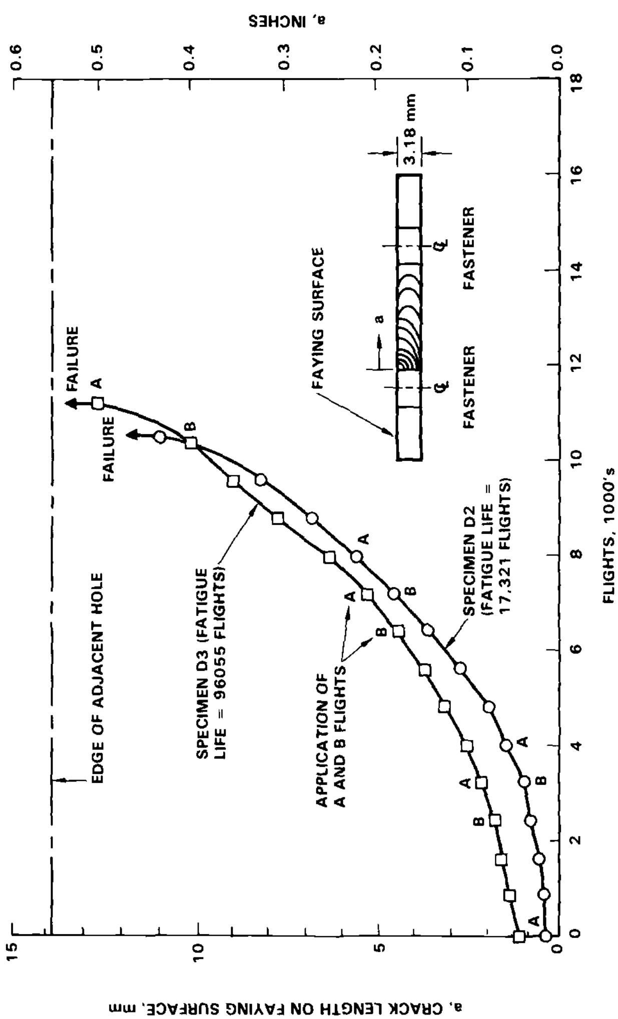

FIG. 4—*Crack growth between fastener holes for lap joint specimens made from IN9021 extrusion.*

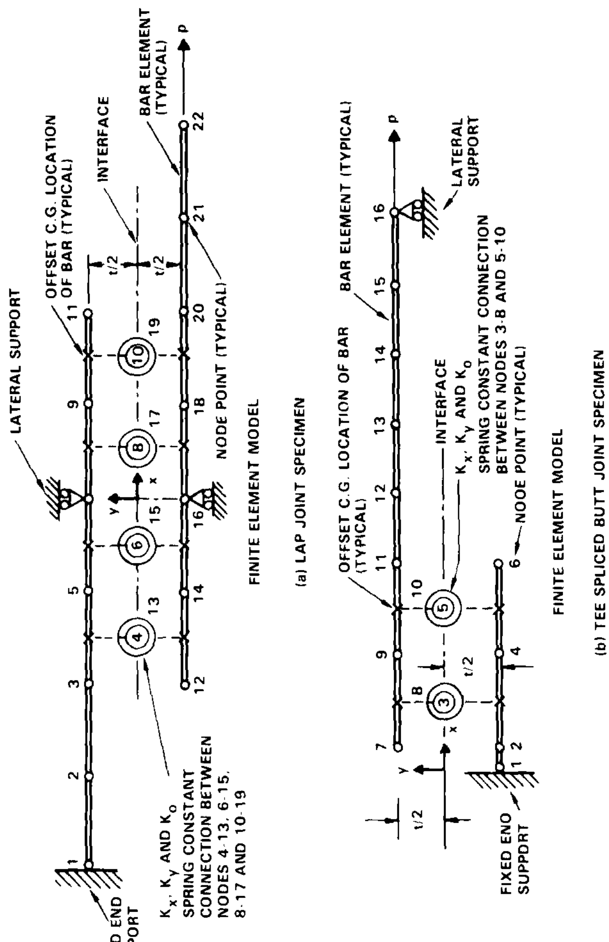

FIG. 5—*Finite element models of joint specimens.*

where

L = length,
A = circular cross-sectional area,
I = moment of inertia, and
E and G = material modulii.

The fastener stiffness K_x in Eq 1 includes the combined effects of bending and shear deformation due to a shear load where $^{10}/_{9}$ corresponds to a constant applicable to a circular cross section. The fasten stiffnesses K_y and K_0 in Eqs 2 and 3 represent the stiffnesses due to an axial load and a bending moment, respectively.

The finite element analysis was conducted using Calac-NASTRAN Rigid Format No. 4 Differential Stiffness Analysis [5]. The basic features of this analysis include large displacements, small strains, and elastic behavior of materials. The solution starts with the linear static analysis solution. The stiffness matrix is then modified for the next solution based on the output from the linear analysis. This iterative process is repeated after each analysis until the changes in the solution reach a specified error limit between the current solution and the previous solution. The results of the analysis account for the nonlinear response of the specimen as a function of the applied load.

The results of the finite element analysis were compared with the measured strains for the instrumented tee-joint specimen at an applied stress of 82.7 MPa (12 ksi). The average strains for back-to-back gages installed just outside of the joint agreed with the predicted average strain within 8%. This agreement between predicted strain and measured strain is not much larger than the error expected for strain gage measurements.

The relationship between applied load and peak stress was determined at the failure location for each joint test specimen. In order to compute the peak tension stresses, the output of the stresses from the finite element model was increased by (1) the ratio of gross area to net area (1.33), (2) the theoretical stress concentration factor, K_t, for the bypass load, and (3) the K_t value for the bending load in the plate. The K_t values were calculated from Ref *6*. For compression stresses, the bypass load was assumed to have a K_t of 1.0; that is, the fastener was assumed to be effective in transferring compression load across the fastener hole. The relationship between the peak stress at the edge of the critical fastener hole and the applied gross area stress is shown in Fig. 6.

The finite element model predicted the correct failure locations, shown in Fig. 1 for both specimens. The maximum tensile stresses were found at the interface of the first fastener row for the lap joint and at the interface of the second fastener row for the spliced joint. The load transfer was also the highest at these two failure locations; that is, 30% for the lap joint and

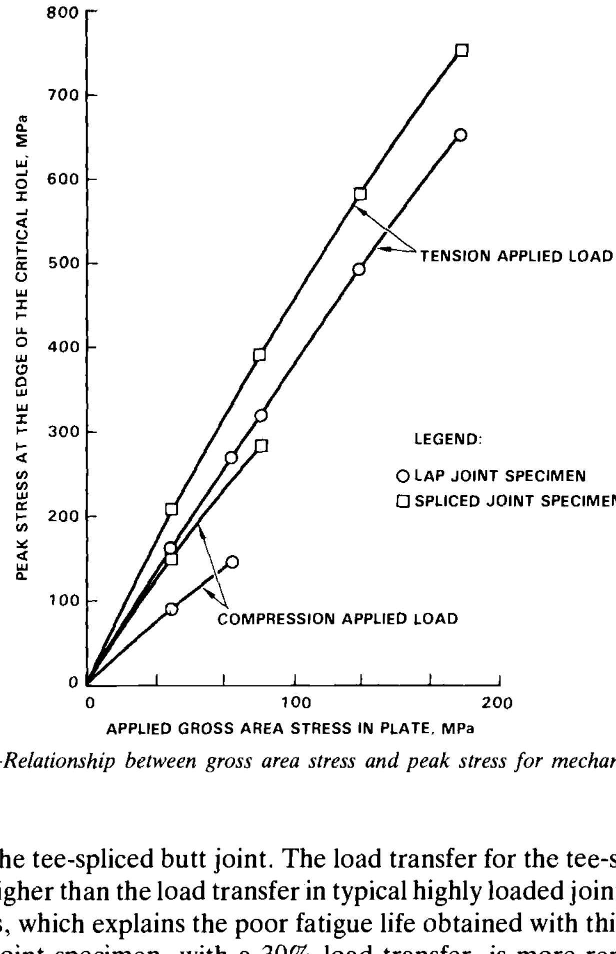

FIG. 6—*Relationship between gross area stress and peak stress for mechanically fastened joints.*

54% for the tee-spliced butt joint. The load transfer for the tee-spliced joint is much higher than the load transfer in typical highly loaded joints in aircraft structures, which explains the poor fatigue life obtained with this specimen. The lap joint specimen, with a 30% load transfer, is more representative of the amount of load transfer at highly loaded fasteners in aircraft structures.

Fatigue Analysis

Fatigue analyses of the two joint specimens were conducted using the method of analysis presented in Ref *7* and illustrated in Fig. 7. The fatigue life prediction method of analysis is based on the local stresses and strains at the fatigue critical location. Local stress and strain are calculated using the cyclic stress-strain properties of the material and Neuber's rule [*8*]. The stress cycle is expressed in the form of an effective stress using Walker's equation [*9*]. The fatigue allowables are determined from *S-N* and spectrum tests conducted on notched coupons. Spectrum test data on aluminum alloys [*7*] indicate that the fatigue allowable curve needs to be reduced beyond

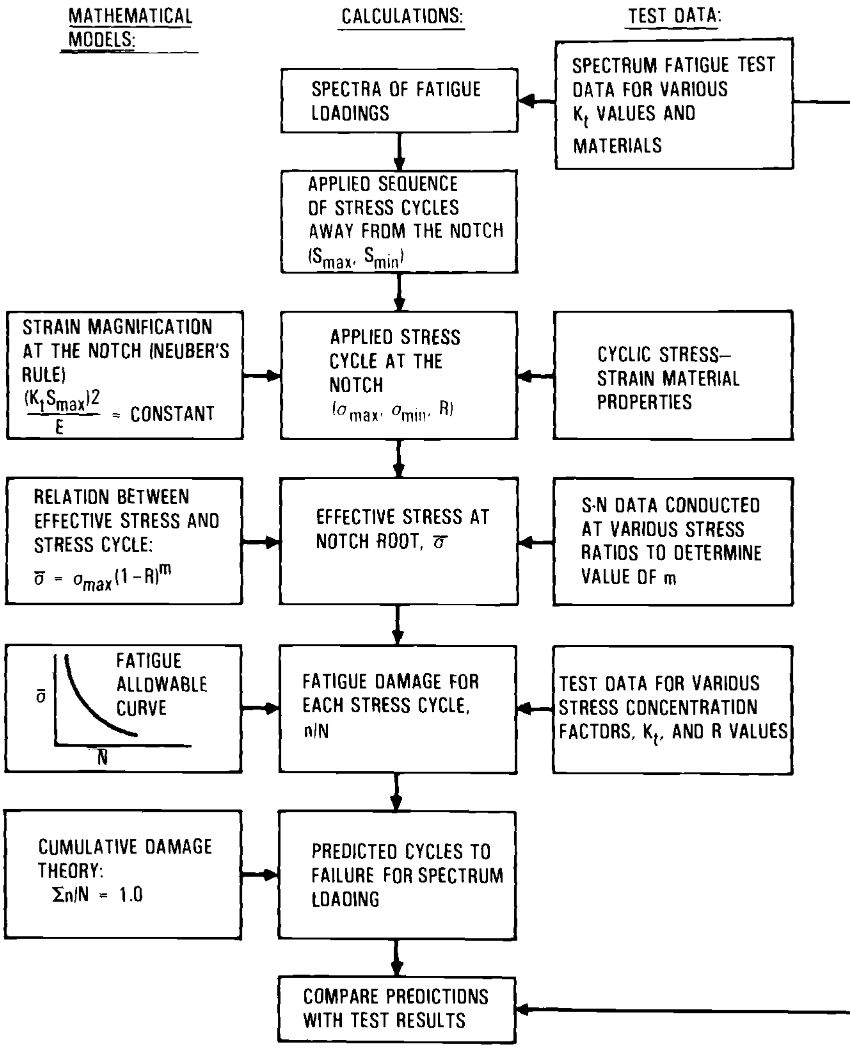

FIG. 7—*Local effective stress fatigue analysis methodology.*

10^5 cycles. Predictions using this reduced allowable curve and Miner's rule provided correlations with flight-by-flight spectra tests conducted on notched coupons [7] within a factor of 2.0. Correlations between Palmgren-Miner's fatigue life predictions and spectrum test results of 7075-T6 notched coupons differ by more than a factor of 3.0 [7].

A computer program based on the analysis method shown in Fig. 7 was used to predict the fatigue lives for the joint specimens that failed in 7075-T6 material. The fatigue allowables shown in Fig. 8 [7] are based on *S-N* and spectrum fatigue tests of specimens fabricated in the longitudinal grain direction of 7075-T6 aluminum. For the analysis of flight-by-flight spectrum test results, the lower curve in Fig. 8 is applicable. The value of the empirical material exponent, m, in Walker's equation for this material is 0.425. The Minitwist (Modification A) spectrum was converted to local effective stresses at the fatigue critical location using the relationships given in Fig. 6. The computerized analysis was conducted on a cycle-by-cycle basis for the exact 4000 flight sequence of cycles applied to the test specimens.

The fatigue allowables in Fig. 8 are directly applicable to the lap joint specimens since the failures occurred in the longitudinal grain direction of the sheet material. For the lap joint specimens, the predicted fatigue life was 38 674 flights, in comparison with the geometric mean life of 42 269 flights (Table 2), which differs by a factor of 1.09.

The spliced joint specimens failed in the transverse grain direction of the extrusion. Some test data from Ref *10* are used to account for differences in the fatigue properties with respect to grain direction of the material. Spectrum fatigue tests were conducted on notched (K_t = 2.7) 7075-T6510 extrusion specimens tested in both grain directions. The spectrum, shown schematically in Fig. 9, is representative at the wing root on the lower surface of a transport aircraft. The 184-flight block contains air loadings, ground loadings, and mean-to-mean ground/air/ground loadings applied in a low/high sequence.

The test results, plotted in Fig. 10, were geometric mean lives of 31 416 flights for the specimens tested in the longitudinal grain direction and 19 252 flights for four specimens tested in the transverse grain direction. These data indicate that the fatigue life is 1.63 times longer in the longitudinal grain direction than in the transverse grain direction. Applying this factor to the mean life of the spliced joint specimens gives 16 586 flights, which is in contrast to a predicted value of 20 272 flights or a difference factor of 1.22.

Conclusions

1. Riveted lap joints made from 7091-TE69 plate material exhibited a shorter fatigue life than joints made from 7075-T6 plate, 7091-T7E69 extrusion, and IN9021 extrusion materials.
2. Metallurgical examination indicated the 7091-T7E69 material was recrystallized, which probably explains the poor fatigue test results for this material.
3. Many inclusions were noted in the fracture surfaces of the IN9021 extrusion specimens.
4. The Minitwist (Modification A) fatigue loading spectrum provided visually identifiable markings on the fracture surfaces of 7091 and IN9021 PM aluminum alloys at intervals of 800 flights. Markings on the fracture

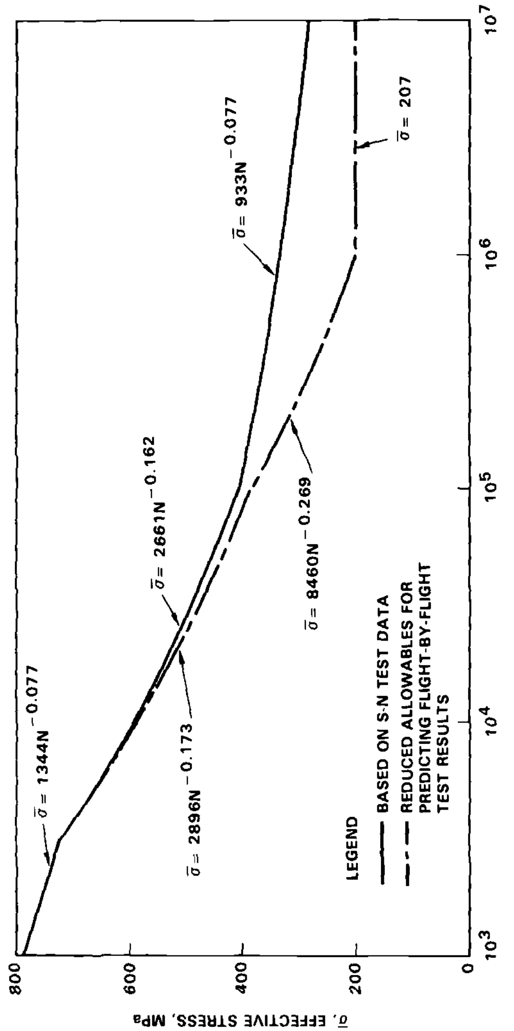

FIG. 8—*Fatigue allowables curves for 7075-T6 aluminum in the longitudinal grain direction with a notch radius of 3.18 mm.*

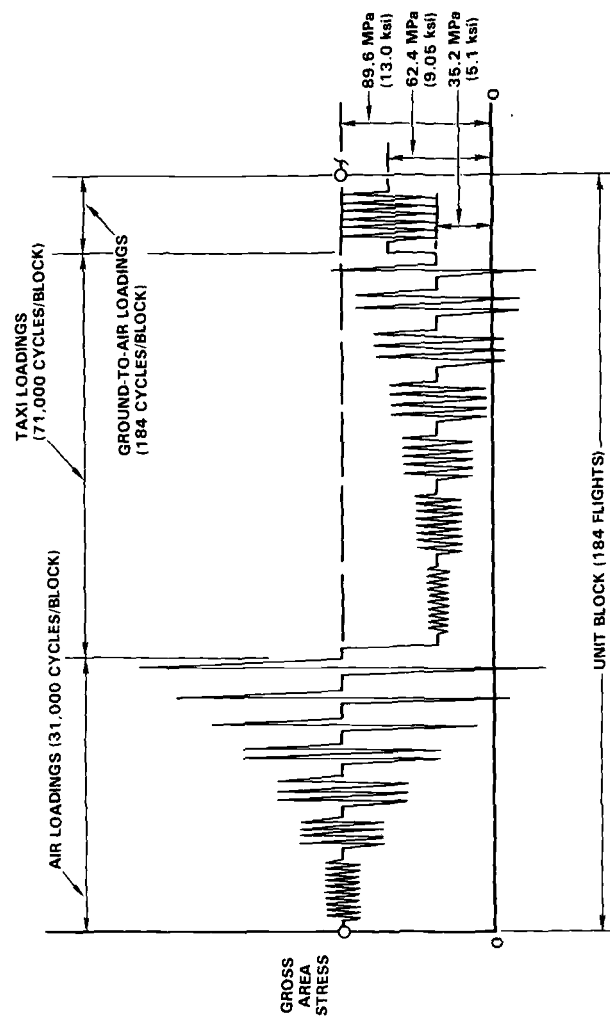

FIG. 9—*Schematic representation of the 184-flight block loading sequence.*

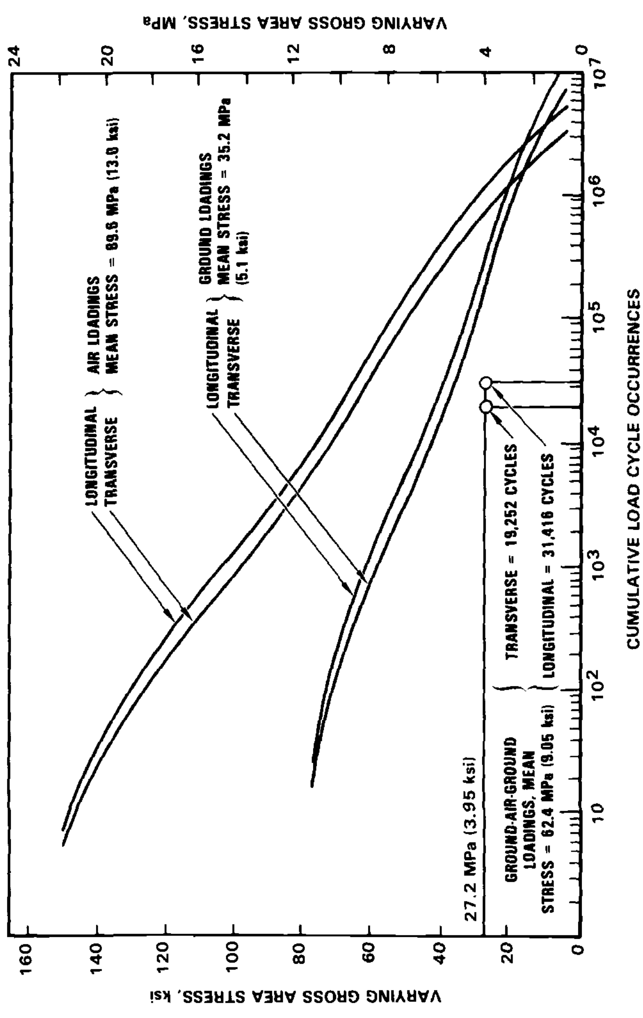

FIG. 10—*Mean spectrum fatigue test results for notched* (K_t = *2.7) 7075-T6 extrusion tested in the longitudinal and transverse grain directions.*

surfaces of 7075-T6 plate were obliterated during compression loading by rubbing contact between the mating surfaces. Contact between mating surfaces of the PM aluminum alloys did not affect the markings because the fracture surfaces were very smooth.

5. Fatigue life predictions for 7075-T6 aluminum using the local stress-strain method of fatigue analysis for two types of joint specimens correlated with the Minitwist (Modification A) spectrum fatigue test results within a factor of 1.22 when accounting for the difference in fatigue properties of the material with respect to grain direction.

Acknowledgments

The author would like to express his appreciation for the contributions of the following people who contributed to the results presented in this paper: L. Bakow for the design of the test specimens and modification of the Minitwist spectrum, W. P. Renslen for conducting the fatigue tests, M. Khaled for conducting the finite element analysis of the test specimens, L. Young and M. McMasters for assisting in the development of the fatigue analysis methodology, and W. E. Hart for the fractographic evaluation of the failed specimens.

References

[1] "Fatigue Under Complex Loading: Analyses and Experiments," *SAE Advances in Engineering*, Vol. 6, 1977.

[2] Lowak, H., de Jonge, J. B., Franc, J., and Schütz, D., "MINITWIST, Shortened Version of TWIST," National Aerospace Laboratory (NLR), Amsterdam, The Netherlands, 1 May 1979.

[3] Ekvall, J. C., Bakow, L., and Brussat, T. R., "Periodic Loading Sequences for the Systematic Marking of Fatigue Crack Fracture Surfaces," *Proceedings* AGARD Conference No. 376, Fatigue Crack Topography, AGARD-CP-376, Advisory Group for Aerospace Research and Development, Sienna, Italy, November 1984, pp. 10–1 to 10–9.

[4] McElvily, A. J., "Annual Report on the Fatigue of Powder Metallurgy Alloys for the Period 1 December 1981 to 30 November 1982," USAF Grant No. AFOSR 81-0046, Air Force Office of Scientific Research, Washington, DC, January 1983.

[5] *CALAC-NASTRAN Structural Analysis Manual*, LR 24062, Lockheed-California Co., Burbank, CA, revised 1 Feb. 1978.

[6] Peterson, R. E., *Stress Concentration Factors*, Wiley, New York, 1974.

[7] Ekvall, J. C., Young, L., and McMaster, M. D., "Fatigue Life Prediction Based on Local Effective Stress," *Proceedings*, Fatigue '84: Second Conference on Fatigue and Fatigue Thresholds, University of Birmingham, 3–7 Sept. 1984, Vol. 2, Engineering Materials Advisory Services Ltd., U.K., 1985.

[8] Neuber, H., "Theory of Stress Concentration for Shear Strained Prismatic Bodies With Arbitrary Non-Linear Stress-Strain Law," *Journal of Applied Mechanics*, December 1961.

[9] Walker, E. K., "The Effect of Stress Ratio During Crack Propagation and Fatigue Life," *Effects of Environment and Complex Load History on Fatigue Life, ASTM STP 462*, American Society for Testing and Materials, Philadelphia, January 1970, pp. 1–14.

[10] Urzi, R. B., "Fatigue Properties of Several Corrosion Resistant High Strength Aluminum Alloys," LR 19578, Lockheed-California Co., Burbank, CA, 28 Dec. 1966.

Michael A. Landy,[1] *Harry Armen, Jr.,*[2]
and Harvey L. Eidinoff[2]

Enhanced Stop-Drill Repair Procedure for Cracked Structures

REFERENCE: Landy, M. A., Armen, H., Jr., and Eidinoff, H. L., **"Enhanced Stop-Drill Repair Procedure for Cracked Structures,"** *Fatigue in Mechanically Fastened Composite and Metallic Joints, ASTM STP 927,* John M. Potter, Ed., American Society for Testing and Materials, Philadelphia, 1986, pp. 190–220.

ABSTRACT: A repair technique for cracked structures that consists of stop drilling the crack tip is examined. This repair procedure is enhanced by cold expanding the stop-drill hole and by installation of an interference-fit fastener. An experimental and analytical investigation of the effectiveness of the enhanced stop-drill procedure is presented. The analysis consists of elastic-plastic stress analysis utilizing the finite element approach to determine residual stress distributions, stress intensity factors around the stop-drill holes due to cold expansion, and stress intensity factors along the fatigue crack paths followed by crack initiation and crack growth life predictions. Comparisons of the life predictions and fatigue test data are also presented. The results indicate that cold expansion and interference-fit fastener installation improve the fatigue performance of stop-drill holes through crack tips by factors ranging from 3 to 20.

KEY WORDS: fatigue, fracture mechanics, cold working, stop-drill, fatigue enhancement, interference-fit fastener (IFF)

Fatigue cracks in airframe structures have always raised serious concern. While not as technically acceptable as reworking or replacement of the cracked structure, stop drilling at the crack tip is commonly used as an interim repair procedure. Typically, this procedure involves drilling a hole at the tip of the crack to reduce the stress concentration and, hopefully, to retard further crack growth. Unfortunately, cracks often quickly reinitiate from the stop-drilled hole (Fig. 1) because of relatively high stress concentration of this notch geometry. Also, there are incidents where the stop-drill hole is not accurately located, leaving the crack tip in the structure and permitting crack growth to continue. These circumstances necessitate further repair, increased aircraft downtime, and increased maintenance costs.

[1] Engineering manager, Fatigue Technology, Inc., Seattle, WA, 98188.
[2] Group head and Engineering specialist, respectively, Structural Mechanics, Grumman Aerospace Corp., Bethpage, NY, 11714.

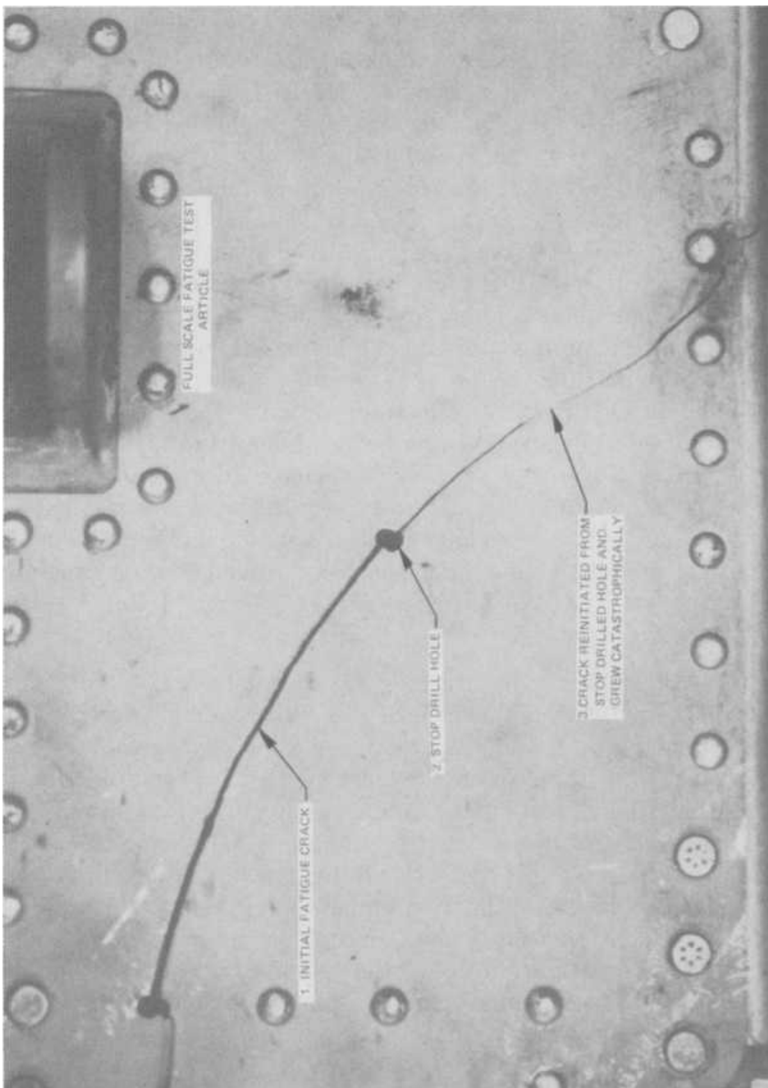

FIG. 1—*Typical stop-drill repair situation.*

Furthermore, a serious safety problem can develop if excessive crack growth occurs prior to the next scheduled inspection.

An enhanced stop-drill repair procedure has been developed [1] to increase the fatigue crack reinitiation life and crack propagation life at the stop-drill hole. The enhanced procedure consists of stop drilling the crack tip and then cold expanding (cold working) the stop-drill hole. Further fatigue enhancement is achieved by inserting an interference fit fastener in the stop-drill hole. If the fatigue crack originated at a fastener hole, the fastener hole should also be given the same fatigue enhancement treatment since another fatigue crack could be initiated at this location.

An experimental and analytical program was carried out to quantify the fatigue life improvement that the fatigue enhancement introduces to the stop-drill repair. Fatigue tests of specimens having an enhanced stop-drill repair configuration were performed. These tests measured fatigue life for variations in the amount of cold expansion, amount of fastener interference, different structural materials, constant amplitude and fatigue load spectrum cycling, and even the effect of the stop-drill hole missing the crack tip. The primary material used in the investigation was 7075-T651 aluminum alloy plate. A multistep analytical procedure was developed to predict the magnitude of the residual stresses resulting from cold expansion of the hole, to predict the crack initiation life, and to predict the crack propagation life. The analytical procedure provided good correlation with the test data and can be used to predict the life of enhanced stop-drilled cracked structures.

Description of Problem

The stop-drill problem is illustrated in Fig. 2. A fatigue crack initiates at a fastener hole in a structure that experiences cyclic loading. After the crack becomes sufficiently large and is detected, a hole is drilled so that the crack tip is removed. This stop-drill hole reduces the stress concentration at the crack tip. Under additional fatigue cycling, a fatigue crack will initiate on the stop-drill hole circumference opposite the original fatigue crack if the principal applied stress is perpendicular to the crack. If the stop-drill hole is cold expanded, the crack initiation life and the subsequent crack propagation life are increased considerably. Further enhancement of the fatigue life can be effected by inserting an interference fit fastener in the stop-drill hole. The same enhancement procedures can be applied to the fastener hole, thus increasing its fatigue life.

Experimental Program

A test program was organized to quantify the life improvement introduced by the enhanced stop-drill repair procedure. Parameters for investigation included: (1) the effect of the amount of applied cold expansion, (2) the effect of fastener interference, and (3) the effect of missing the crack tip

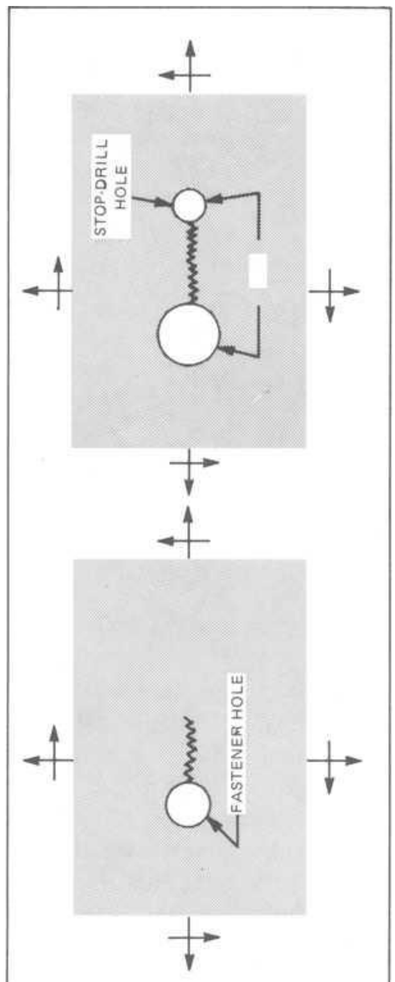

FIG. 2—*Description of the stop-drill problem.*

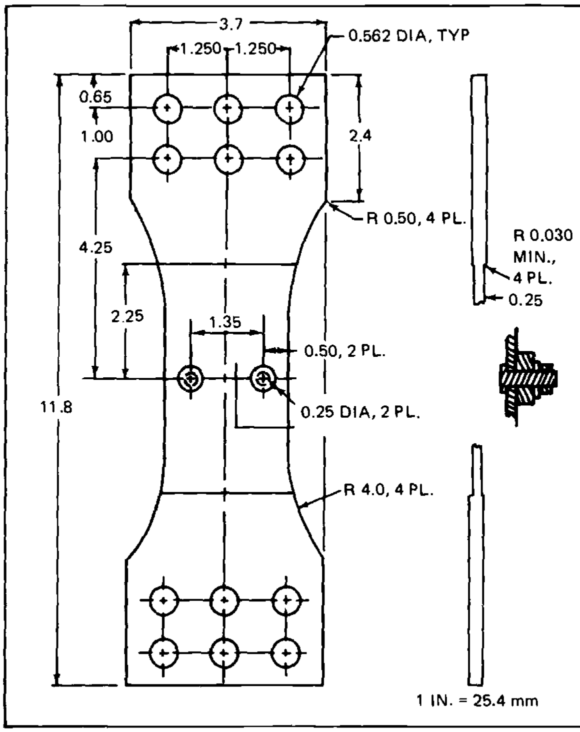

FIG. 3—*Fatigue test specimen—slotted hole. PL indicates the centerline. The dimensions are in inches (1 in. = 25.4 mm).*

during stop drilling. The baseline material selected for the study was 7075-T651 aluminum alloy.

A test specimen was designed to simulate a crack in a structural panel with a stop-drill hole located at or near the crack tip. This specimen (Fig. 3) has a thin [0.30-mm (0.012-in.)] slot representing a fatigue crack that is 34.29 mm (1.35 in.) long and perpendicular to the loading direction. A 6.35-mm-diameter (0.25-in.) hole at each end of the slot represents the stop-drill hole. The edge margin was maintained at a ratio of $e/D = 2.0$ (distance from the center of the hole to the edge of the part/hole diameter) with reference to the nominal final hole diameter. The nominal specimen thickness was 6.35 mm (0.25 in.). The static tensile properties and results of chemical analysis of the 7075-T651 plate used for the experiments are presented in Tables 1*a* and 1*b*.

Cold-expanded (CX) specimens were prepared by reaming pilot holes to the appropriate starting hole diameter. The holes were then cold expanded, final reamed, and fitted with a steel fastener, where applicable. The fasteners used were protruding-head, straight-shank Hi-Lok fasteners installed with various amounts of interference. Cold expansion was accomplished by

TABLE 1a—*Material properties of 7051-T561 alloy.*[a]

Material	Yield Strength (0.2% Offset), ksi	Ultimate Tensile Strength, ksi	Elongation (in 0 to 7-in. gage length), %
7051-T561 alloy	79.3	84.7	10.0

[a]Conversion factors: 1 ksi = 6.9 MPa; 1 in. = 25.4 mm.

drawing an oversized mandrel through the stop-drill hole, using a prelubricated stainless steel split sleeve. Non-cold-expanded (NCX) specimens were prepared by final reaming pilot holes to the required size and fitting fasteners, where applicable. When the fasteners were fitted, a backup block was used between the back of the specimen and the nuts to preclude fretting failures.

For investigating the effect of missing the crack tip during stop drilling, specimens were precracked so as to obtain sharp, natural cracks emanating from the stop-drill holes. Starter notches were cut into the sides of both pilot holes with a travel wire electrical discharge machine. The specimens were then cycled under decreasing load until cracks had initiated and grown to the appropriate length. The holes were then cold expanded and final reamed (enhanced stop-drill repair), or final reamed (standard stop-drill repair), so as to leave 1.27 or 2.54-mm (0.050 or 0.100-in.) sharp cracks, as required.

All the specimens were cycled to failure in closed-loop, electrohydraulic fatigue test machines, under load control, in laboratory air at ambient temperature. Loads were applied to achieve the stated stress level, based on the net cross-sectional area of the specimen—the gross area less the area of the holes and slot. Constant-amplitude loads were generated by digital function generators. The test machines and associated electronics are calibrated semiannually, with a standard traceable to the National Bureau of Standards. Test results in terms of log mean cycles to failure are plotted in Figs. 4 and 5.

Figure 4 illustrates the effect of cold expanding the stop-drill holes. The figure shows that the fatigue life is increased from 5000 to 122 000 log mean cycles to failure by cold expansion alone. This is a factor of over 20 on life. Further fatigue enhancement can be achieved by installation of interference-

TABLE 1b—*Chemical analysis of 7051-T561 alloy, in weight percent.*

Material	Cu	Si	Fe	Mn	Mg	Zn	Cr	Ti	OE[a]	OET[b]	Al
7051-T561	1.57	0.08	0.23	0.048	2.54	5.47	0.21	0.06	0.15	0.15	balance

[a]Other elements.
[b]Other elements, total.

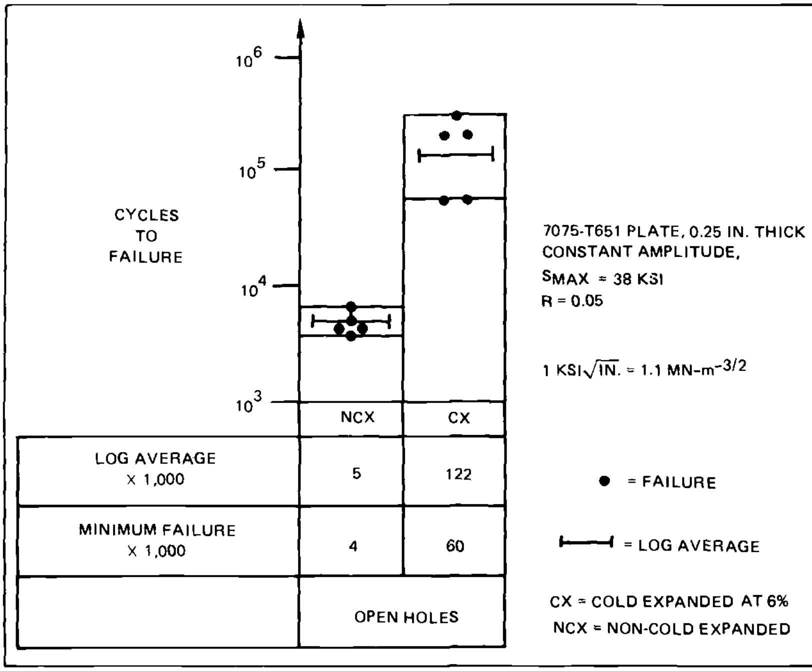

FIG. 4—*Effect of cold expansion on the fatigue life of open-hole specimens.*

fit fasteners (IFF) after cold expanding the stop-drill holes. As shown in Fig. 5, installing neat fit or slight clearance fit fasteners increases the fatigue life to about 400 000 log mean cycles to failure. Groups of five specimens, each having fasteners with interference levels of 0.0381 and 0.076 mm (0.0015 and 0.0030 in.) were also fatigue tested. These specimens were tested to be between 1 million and 2.7 million cycles, and no failures were observed. This combination of CX and IFF increased the fatigue life by a factor of over 200 times in comparison with a standard, nonenhanced stop-drill hole.

Analytical Program

A multistep analytical procedure was employed to predict the fatigue life of the cracked, stop-drilled structure. The procedure consisted of the following sequence of analyses: (1) an elastic-plastic finite element analysis (FEA) to determine the residual stress distributions resulting from cold expansion of the stop-drill holes, (2) calculation of stress intensity factors (SIF) for applied and residual stresses, (3) calculation of life to crack initiation, and (4) calculation of crack growth life. The total life is the sum of the predicted crack initiation and crack propagation lives. The procedure used here is similar to the procedure used in an earlier study [2] of the fatigue behavior of round cold-expanded holes.

Assumptions that are central to the analytical procedure include the following:

1. Crack initiation life is cyclic life to create a 0.254-mm-radius (0.01-in.) corner crack at the stop-drill hole.
2. Crack propagation life is life to grow a 0.254-mm-radius (0.01-in.) corner crack to fracture.
3. Superposition of residual and applied stress intensity factors is valid:

$$K_{\text{total}} = K_{\text{applied loads}} + K_{\text{residual}} \tag{1}$$

4. Crack growth is governed by K_{total}.
5. K_{residual} distribution is a function of the residual stress distribution in the cracked structure.

Stress Analysis of Cold Expanded Holes

Cold expansion is treated by means of a two-dimensional elastic-plastic finite element analysis program [3] in which an incremental solution algorithm based on the residual force method [4] is used. The hole cold expansion process is simulated by enforcing appropriate constraint conditions for those nodes on the hole circumference and prescribing that the hole expand radially in a uniform manner to a diameter, D, corresponding to an initial

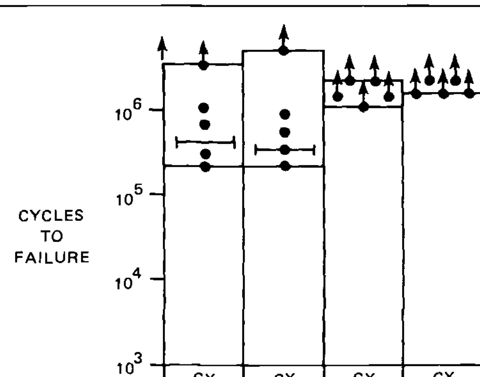

LOG AVERAGE × 1,000	404	389	N/A	N/A
MINIMUM FAILURE × 1,000	241	237	N/A	N/A
NOMINAL FASTENER INTERFERENCE IN.	-0.001	0.000	0.0015	0.0030

7075-T651 PLATE, 0.25 IN. THICK
CONSTANT AMPLITUDE,
S_{MAX} = 38 KSI
R = 0.05

FILLED HOLES, 0.0015 IN. FASTENER INTERFERENCE
PROT HEAD 1/4 HILOCKS

● = FAILURE
↑ = NO FAILURE
├┤ = LOG AVERAGE
CX = COLD EXPANDED AT 6%
NCX = NON-COLD EXPANDED
1 KSI$\sqrt{\text{IN.}}$ = 1.1 MN-m$^{-3/2}$

FIG. 5—*Effect of cold expansion plus interference-fit fasteners on fatigue life.*

expansion defined by

$$i(\%) = \frac{\overline{\mathrm{D}} - \mathrm{D}}{\mathrm{D}} \times 100 \tag{2}$$

where D and $\overline{D}$ are the original and maximum expansion hole diameters, respectively. The nonlinear stress-strain behavior of the material is characterized by the three-parameter Ramberg-Osgood equation.

At this point the plate has experienced elastic deformation and its behavior is governed by the following equilibrium equation written in matrix form,

$$[K]\{u\} = \{F\} + \{Q\} \tag{3}$$

The applied nodal load vector, F, represents a set of forces corresponding to the uniform radial expansion of the stop-drilled hole. The vector is determined from the prescribed radial-displacement constraint conditions and reflects the asymmetric character of the local stiffness of the cracked stop-drilled hole. The vector Q is the set of nodal forces developed from the prevailing plastic strains present in the structure. The plastic strains are treated in much the same manner as initial (thermal and lack-of-fit) strains.

The residual stresses corresponding to a springback from the cold expansion are determined by removing the multipoint constraint conditions previously imposed during the radial expansion of the hole. At the relaxed (springback) state, the governing equation becomes

$$[K]\{u_r\} = \{Q\} \tag{4}$$

where the elastic stiffness matrix, $[K]$, and the plastic residual load vector, Q, differ from their counterpart representations in Eq 3 to account for the additional independent nodal degrees of freedom (DOF) resulting from the release of the multipoint constraints. The vector of residual displacements, u_r, is then used to establish corresponding levels of residual stresses, strains, and changes in energy level.

A finite element idealization of the stop-drill slotted specimen is shown in Fig. 6. To take advantage of symmetry about two axes, only one quarter of the specimen was modeled, implying a crack at each of the two stop-drill holes. The model has 446 members with 684 nodes and 1413 DOF. In the region around the stop-drill hole, where large stress gradients and plastic stresses were expected, eight-noded isoparametric quadrilateral finite elements were employed. Away from the slotted hole region, four noded quadrilateral finite elements were deemed adequate and were used. The stresses and strains in the eight-noded elements are determined at a set of two-by-two Gaussian quadrature points within the element and then ex-

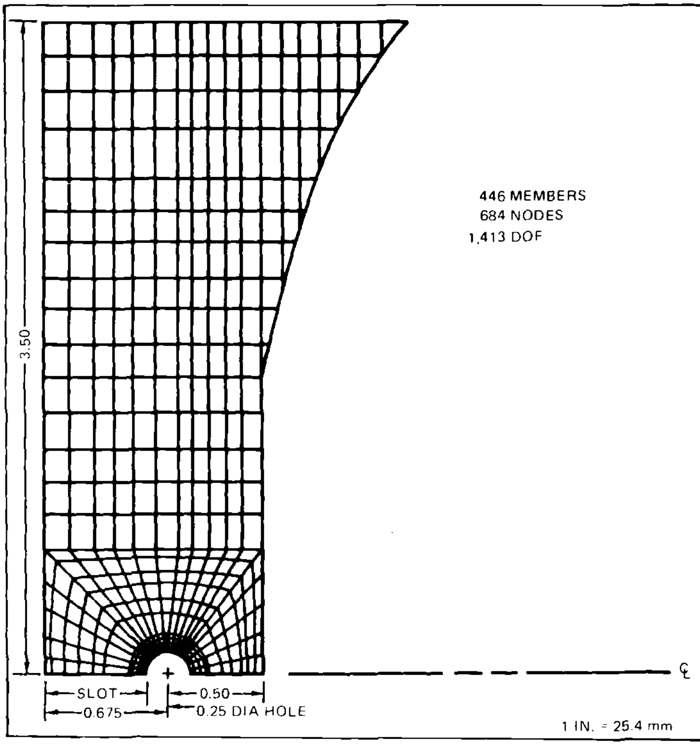

FIG. 6—*Finite element idealization.*

trapolated to the nodal locations. For the four-noded elements, only the centroidal values of stress and strain are considered.

Circumferential (hoop) stresses along the x-axis during and following the cold expansion process, determined by the elastic-plastic FEA, are presented in Fig. 7. It is along this path that a fatigue crack will initiate and grow. Also shown in Fig. 7 are the same stress distributions for cold expanding a round hole. A 4.5% mandrel interference level was used for both the slotted and round holes. Note that the residual stress distributions for both geometries are similar, but that the slotted configuration has residual compressive stresses extending out to a greater distance from the edge of the hole than the round configuration. Since the compressive residual stress increases crack growth life, it is expected from this result that the slotted configuration will have superior crack growth life for crack lengths greater than about 1.27 mm (0.05 in.). The opposite may be true for cracks smaller than 1.27 mm (0.05 in.). At the edge of the hole ($x = 0$), the residual compression stress is slightly higher for the round hole configuration.

Residual stresses along the crack path (x-axis) are about the same for both round and slotted configurations, but this is not true around the cir-

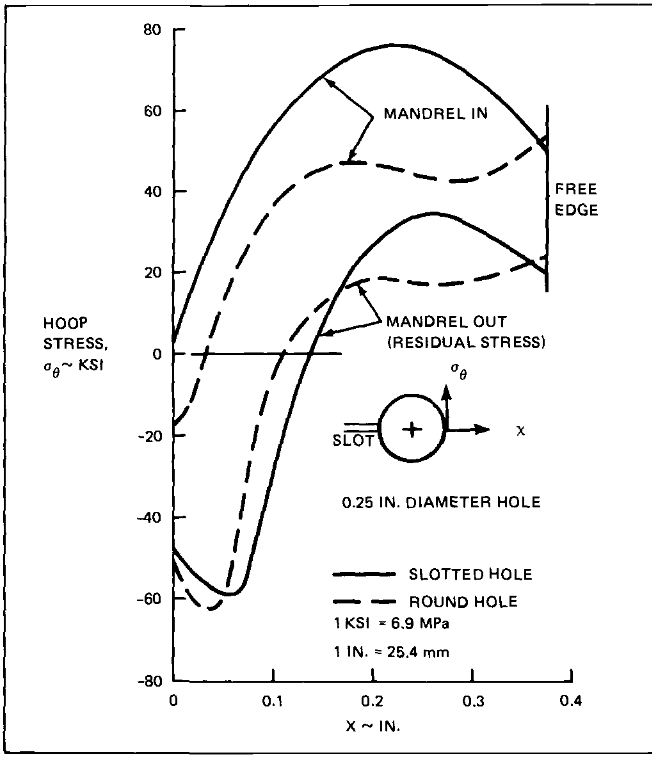

FIG. 7—*Stresses during cold expansion of 4.5%.*

cumference of the hole. Presented in Fig. 8 are hoop stresses around the circumference of the hole for both the round and slotted configurations. It can be observed that the cold expanded round hole configuration produces residual compressive hoop stress that is fairly constant all around the circumference, but the slotted hole produces residual compressive hoop stresses that vary from a maximum near the x-axis to zero at the slot which is at $\theta = 180$ deg. This result shows that the cold expansion is generally less effective for the slotted hole, that is, produces smaller hoop stresses. However, along the x-axis where fatigue cracks initiate, the cold expansion is very effective and produces high residual compressive stresses along the crack path.

The effect of varying the mandrel interference on residual stresses is shown in Fig. 9. Increasing the mandrel interference does not affect the magnitude of the maximum compressive residual stress, but significantly increases the size of the compressive residual stress region. This is beneficial. However, to achieve static equilibrium, the compressive residual stress must be balanced by tensile residual stresses farther away from the hole. In this case, tensile residual stresses remain at the free edge, and their magnitude

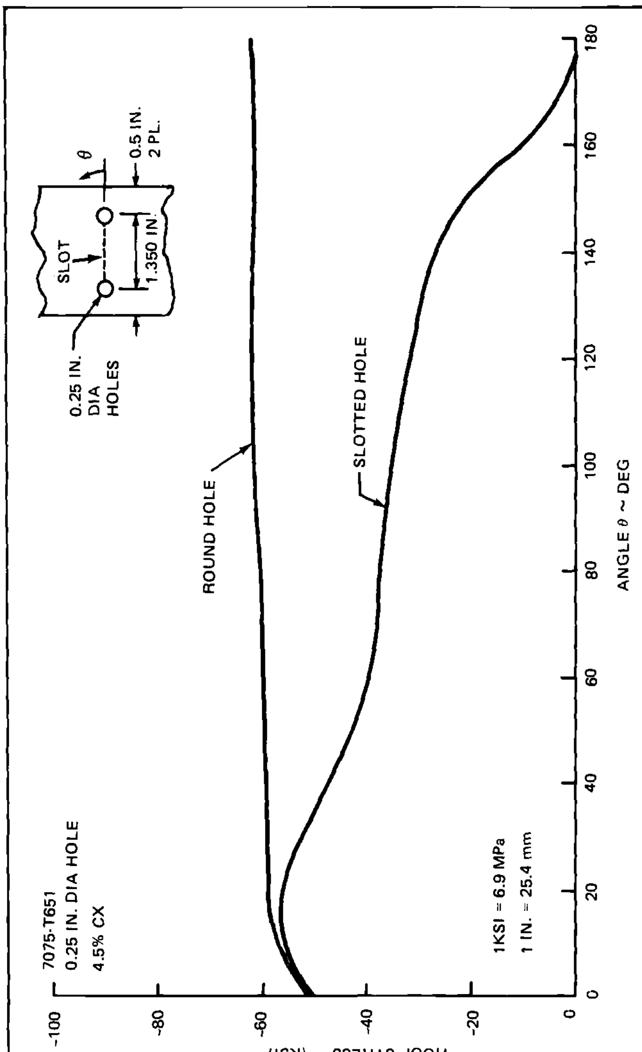

FIG. 8—*Circumferential distribution of hoop stress at the edge of the hole (after the constrains are released).*

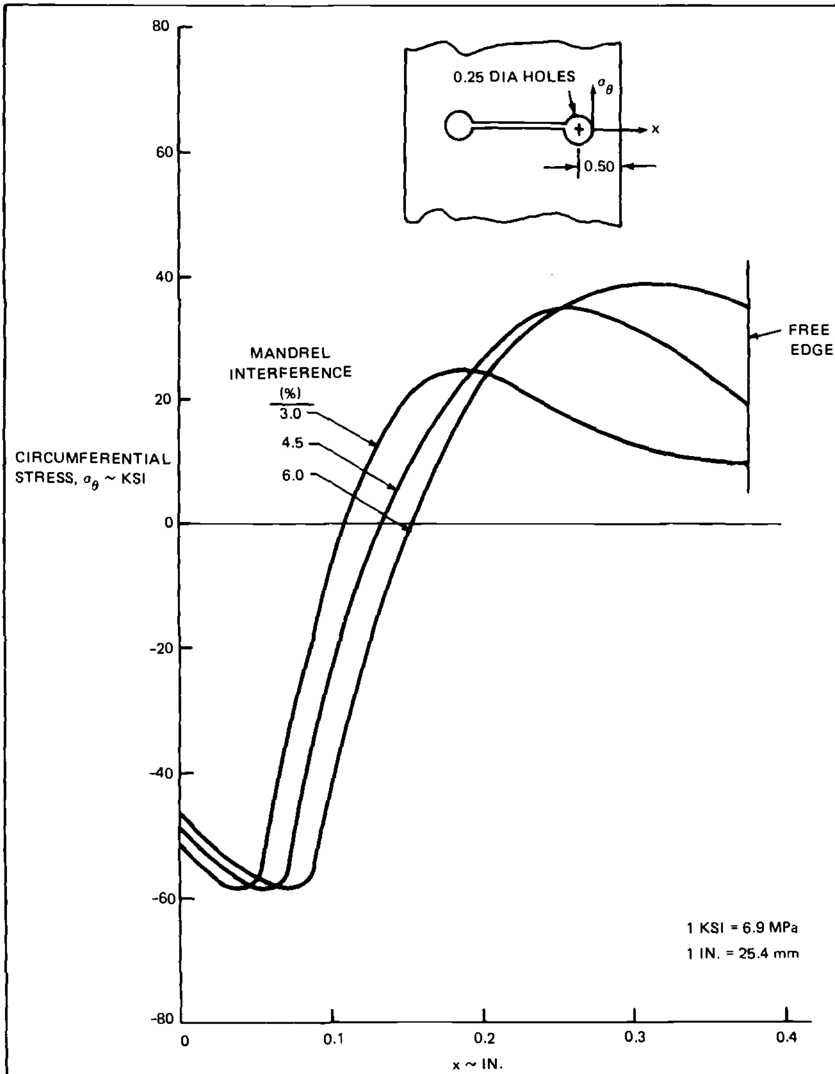

FIG. 9—*Residual stresses due to cold expansion of a slotted-hole specimen.*

increases with increasing mandrel interference. These tensile residual stresses along the free edge offer potential sites for stress corrosion cracking if subjected to an aggressive environment.

Residual strains resulting from the cold expansion of the slotted hole specimen were measured by the moiré fringe technique [5]. A moiré grid was bonded to a test article prior to cold working. Mandrel expansion of 5.5% was employed. Radial and tangential (hoop) strains were measured along radial lines from the hole centerline at 0, 90, and 180 deg, and the test data are shown in Fig. 10. The largest residual strains occur at 0.0 deg, followed by lower strains at 0 = 90 deg, and negligible strains at 180 deg. This variation is consistent with the elastic-plastic FEA. A comparison of the FEA predictions with tangential strain measurements along the 0 = 0 deg (x-axis) line is presented in Fig. 11. Correlation of the analysis and test data is reasonably good, with the predictions showing 20% higher values close to the edge of the hole.

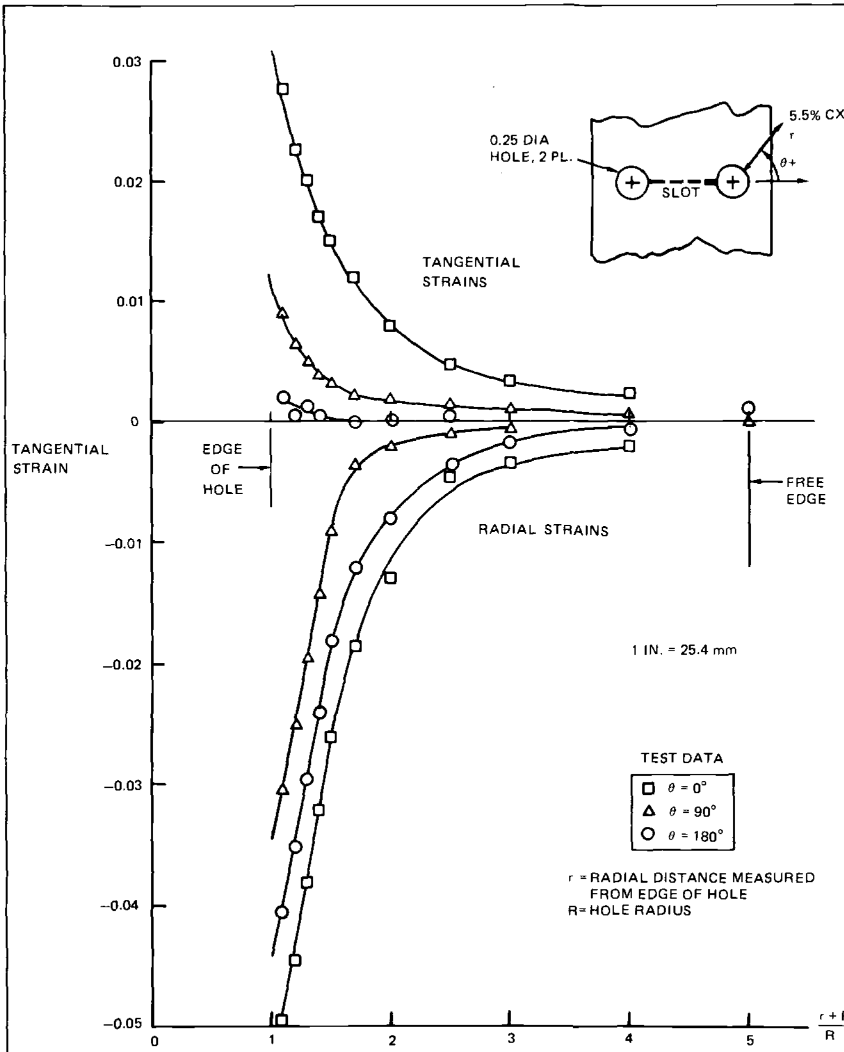

FIG. 10—*Measured strain distributions for a slotted hole.*

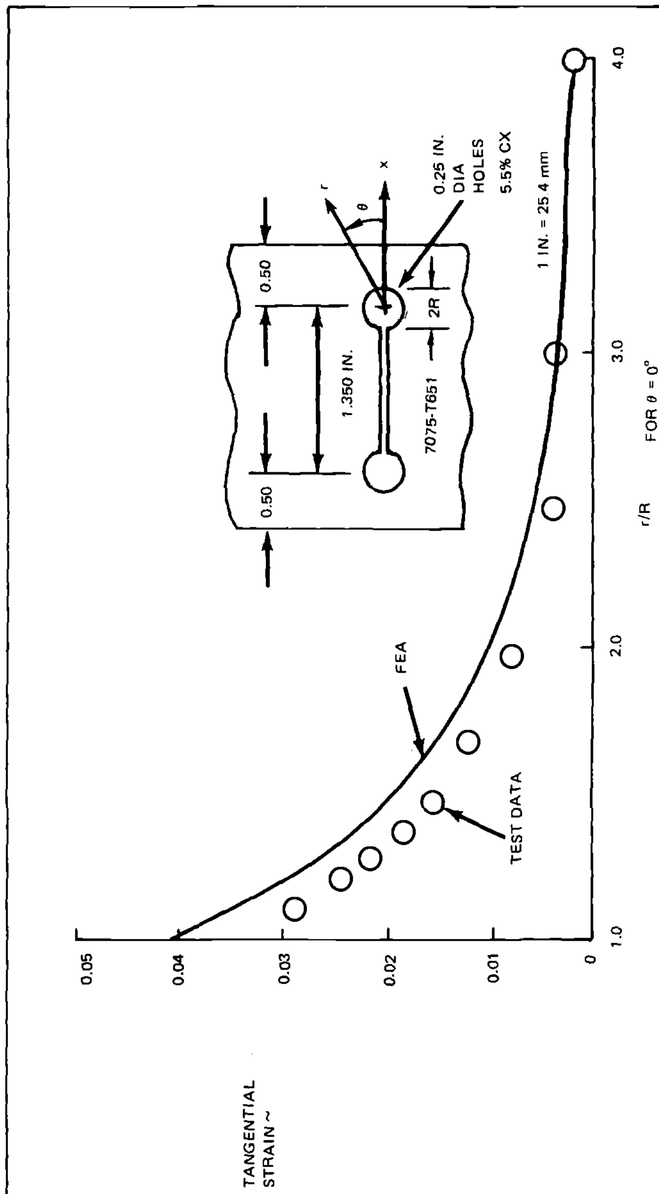

FIG. 11—*Tangential strain for a stop-drilled specimen.*

Stress-Intensity Factor Analysis

Stress intensity factors (SIFs) were calculated for the slotted hole specimen by means of the energy release rate technique [*6*]. In this approach, a crack is introduced along the *x*-axis and the total potential energy is calculated by

$$\pi = -½\{u\}^T\{P\} \tag{5}$$

where

π = total potential energy,
$\{u\}$ = vector of generalized nodal displacement, and
$\{P\}$ = vector of generalized nodal forces.

The energy release rate per unit thickness, G, is obtained by

$$G = \left\{\frac{\partial\pi}{\partial c}\right\} = \frac{1}{2}\left\{\frac{\partial u}{\partial c}\right\}^T\{P\} \tag{6}$$

where c is the crack length.

For small changes in crack length, where the crack grows from c to $(c + \Delta c)$, the Eq 6 can be approximated by

$$G = \frac{\Delta\pi}{\Delta c} = \frac{1}{2}\frac{(W - W_0)}{\Delta c} \tag{7}$$

where W is the potential of the applied external loads. For situations where the crack opening mode (Mode I) is dominant, the value of the energy release rate may be directly related to the stress intensity value by

$$G = \frac{K_I2}{E^*} \tag{8}$$

where

$$E^* = \left\{\begin{matrix} E\text{, plane stress} \\ E/(1 - \nu^2)\text{, plane strain}\end{matrix}\right\}$$
K_I = stress intensity factor.

The finite element model of the slotted hole specimen used for the stress analysis was also employed for the SIF analysis. SIFs were calculated by the energy release rate approach for applied remote tensile stress and the results are shown in Fig. 12. Also shown in Fig. 12 are SIFs for an elliptical hole in a finite width strip where the ellipse has the same major axis length and root radius as the slotted hole. The elliptical hole values are com-

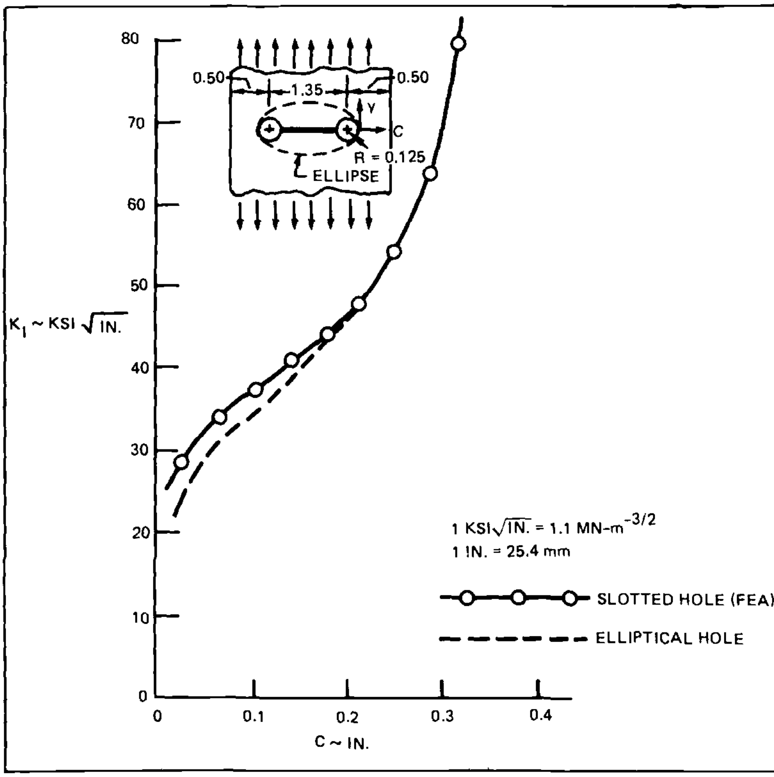

FIG. 12—K_I *for a slotted-hole specimen* (S_{NET} = *38 ksi*).

pounded from a solution for an elliptical hole [7] and a finite width correction. It can be observed in Fig. 12 that for crack lengths less than 5.08 mm (0.20 in.), the slotted SIF has slightly higher values than the elliptical hole configuration, and for larger crack lengths, the SIFs are identical.

Stress-Intensity Factors by Residual Energy Release Rate

Stress intensity factors for the applied fatigue loads (see Fig. 12) were obtained by elastic energy release rate analysis. In order to account for the residual stresses resulting from cold expansion of the stop-drill hole, a linear elastic fracture mechanics (LEFM) superposition procedure was employed. In this procedure, the presence of the cold expansion residual stresses gives rise to a residual SIF, denoted K_R. This SIF is used to establish an effective stress intensity factor, K_I, expressed as the sum

$$K_I = K_\infty + K_R \tag{9}$$

where K_∞ is the SIF caused by the applied loading in the absence of residual stresses. The effective SIF is then used with a crack growth rate equation to predict fatigue crack growth life. This procedure has been previously used [*2,8–10*], and good correlation with test data was shown.

In the previous studies associated with cold expansion [*2,8–10*], the residual SIFs were calculated by a weight function method [*11*]. This approach implicitly assumes that the residual stress pattern generated from the cold expansion procedure remains constant as the crack propagates from the edge of the cold-expanded worked hole. This, of course, is not correct. To circumvent the aforementioned shortcoming, a procedure involving the residual energy release rate, G_R, is used to establish values K_R that reflect the changing nature of the residual stresses as the crack length increases. This energy release rate is the result of prescribing the residual stresses to be zero on a new crack surface as it is formed.

Within the framework of finite element methods, the values of energy release rates for linear elastic behavior are determined from the changes in the potential energy per unit of crack extension. Values of G_R are determined in the same manner, with the condition that the potential energy at the residual state (relaxed configuration after cold expansion) must be written in the absence of an applied load as

$$\pi = \tfrac{1}{2}\{\tilde{u}\}^T[\tilde{K}]\{\tilde{u}\} - \{\tilde{u}\}^T\{\tilde{Q}\} \tag{10}$$

where $\{\tilde{u}\}$, $\{\tilde{Q}\}$, and $\{\tilde{K}\}$ correspond to the residual displacements, plastic load vector, and stiffness matrix, respectively. These quantities are determined in the absence of the applied load and in the presence of a crack. Their values will change as a function of the crack length in the structure. The values of G_R (per unit thickness) can be determined from

$$G_R = \frac{\Delta\pi}{\Delta c} \tag{11}$$

where$\Delta\pi$ is the change in potential energy with respect to a change in crack length, Δc.

To demonstrate the applicability of this procedure to a cold expansion situation, the residual energy release rate technique was applied to the problem of a centrally located round hole in a rectangular plate, as shown in Fig. 13. A comparison of the results for K_R from the weight-function method and the residual energy release rate method is also shown in this figure. The results indicate that for relatively short crack lengths (less than half of the radius), the two analytical procedures yield similar values of K_R. However, as the crack length increases, the values of K_R from the residual energy release rate are considerably smaller than corresponding values determined from the weight function method. The differences in the results are directly related to the changing residual stress distributions that develop as the crack length increases. These changing patterns are illustrated in Fig. 14, where the residual stresses for several different crack lengths can be

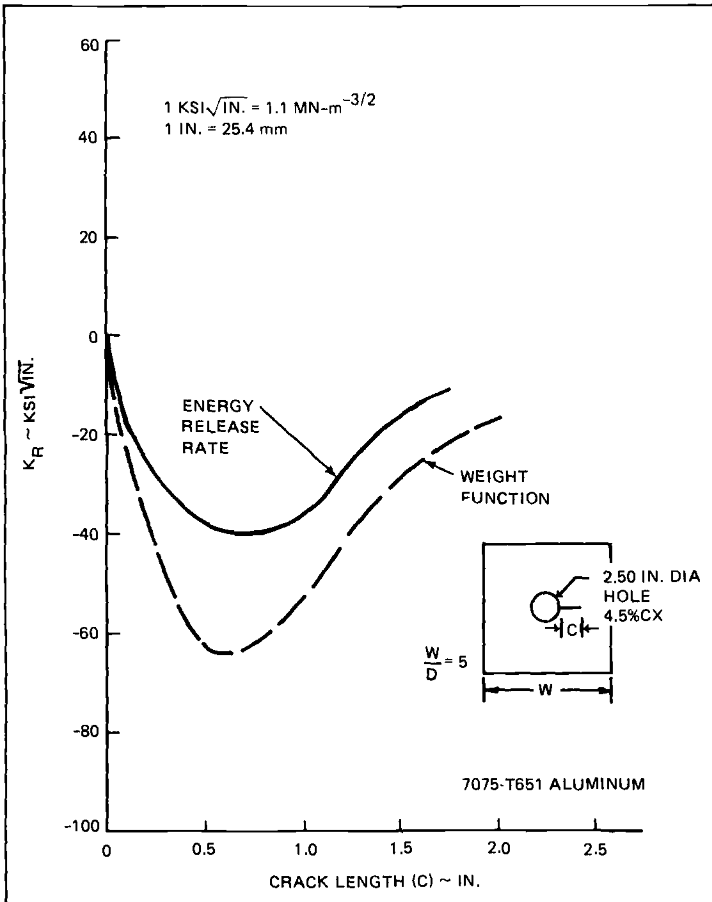

FIG. 13—*Residual stress intensity factor (energy release rate versus weight function).*

compared with the uncracked case. These changing residual stress patterns reflect the self-equilibrating condition that must be enforced across the net section where the crack propagates.

The residual energy release rate procedure was next used to determine residual SIFs for the slotted hole specimen, and the results are presented in Fig. 15. For comparison, residual SIFs for this configuration were calculated by the weight function technique, using the residual stress distributions from Fig. 9 but with a weight function for a round hole. Even though the latter residual SIFs are in error, they indicate the general relationship between energy release rate and weight function predictions. The two approaches give similar values for small crack lengths and deviate from one another at larger crack lengths with the weight function method giving unconservative residual SIFs over a large range of crack lengths.

Life Prediction

Fatigue life predictions were made by using a two-step analytical procedure that considers life to crack initiation and crack propagation life. Life to crack initiation is defined as life to create a 0.254-mm (0.010-in.) corner crack at the stop-drill hole. The life to crack initiation analysis methodology is the local strain approach [*12*]. The method uses strain life and cyclic stress-strain test data, tracks the stress and strain histories at the notch, and

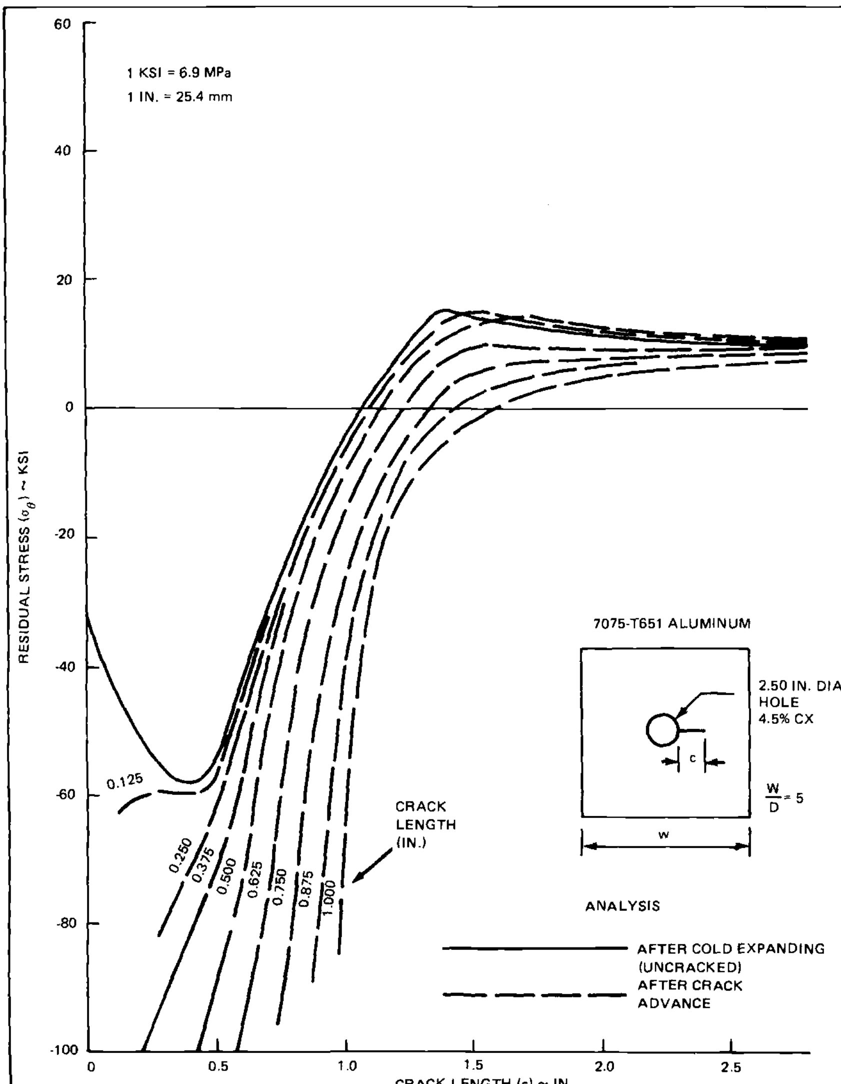

FIG. 14—*Residual stress distributions as functions of the crack length after cold expansion.*

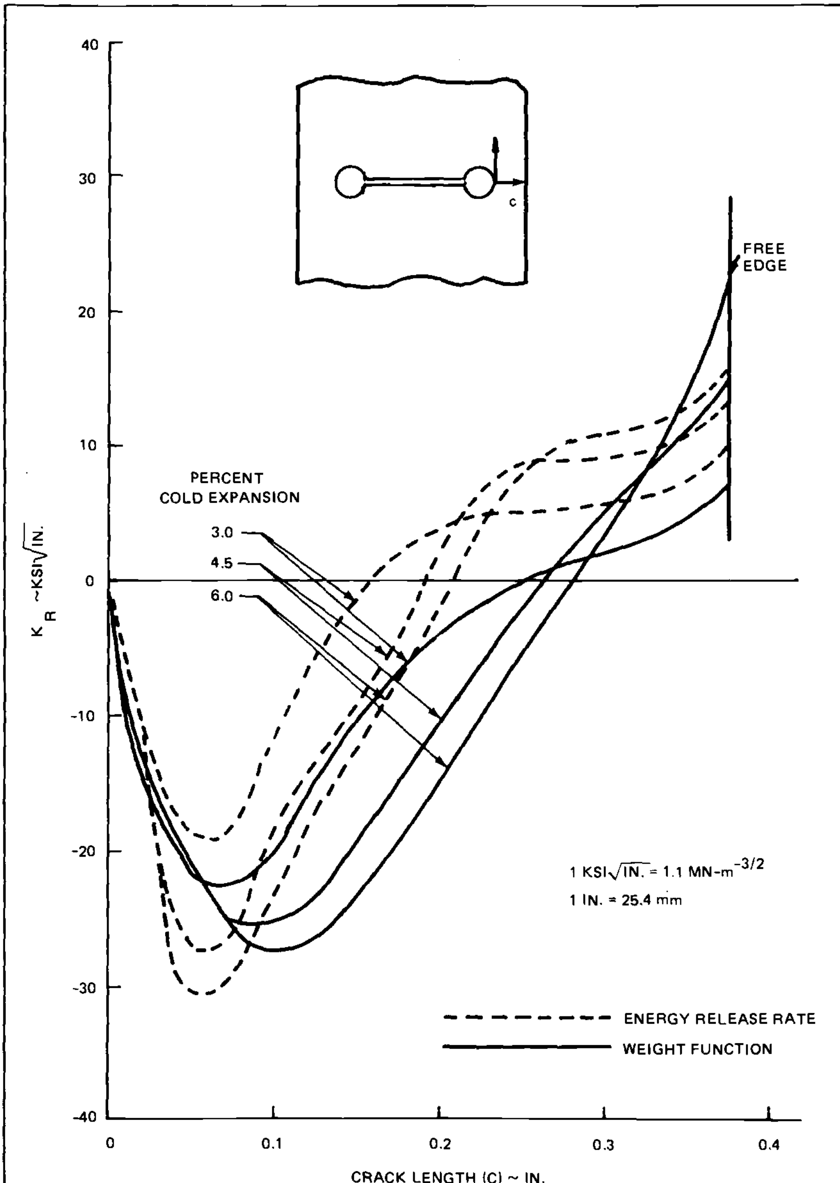

FIG. 15—*Residual stress intensity factors—slotted hole.*

uses Miner's cumulative damage rule. Crack propagation life is determined by using LEFM procedures.

Fatigue Life to Crack Initiation Analysis

The local strain approach was employed to predict life to crack initiation, with the specific methodology outlined in Ref *12*. This approach is based on cumulative damage analysis that accounts for prior load history. Stresses and strains at a notch root are tracked for all applied maximum and minimum loads in a fatigue spectrum. Cyclic and hysteresis stress-strain curves and a Neuber effective stress concentration factor are part of this process. A rainflow cycle counting scheme evaluates the calculated local strain history obtained at the notch to form half cycles and full cycles (closed hysteresis stress-strain curves) corresponding to constant-amplitude cycling. Damage is calculated by entering constant amplitude strain-life curves determined by correlating smooth ($K_T = 1.0$) fatigue specimen test data. The test data were correlated to the lower edge of strain versus life to failure of the specimen, as given in Ref *13*. The strain-life test data are obtained for fully reversed fatigue cycling (stress ratio = -1.0). Mean stress effects are accounted for in the damage calculation by a correction factor that calculates an equivalent fully reversed strain amplitude. Finally, crack initiation life is determined by linear summation of damage, that is, by Miner's rule.

The fatigue life to crack initiation methodology also accounts for the effects of initial stress and strain at the notch root due to cold expansion. These initial stresses and strains are taken from the elastic-plastic FEA of the cold expansion process. For the cases examined here, these initial conditions were significant, increasing the crack initiation lives by factors of 2 to 5 when compared with predictions made in their absence. In addition to finding stresses and strains, the FEA found that the elastic stress concentration factor, K_T, for the slotted specimen is 3.25.

Fatigue Crack-Growth Analysis

Crack growth predictions were made with a rate equation of the following form [*14*], which is based on the crack closure concept

$$\frac{dc}{dN} = C' \left[\left(\frac{1 - C_f}{1 - R} \right) \Delta K \right]^n \tag{12}$$

where C' and n are empirical constants and $C_f = C_f(\mathrm{R})$ is the closure factor [*14*]. This equation describes the crack-growth rate behavior as a function of the stress ratio, R. The empirical constants were found by correlating crack-growth rate test data from Ref *15*.

The stress intensity factors K_{max} and K_{min} were calculated for each cycle by superposition of the applied and residual stress intensity factors, as described by Eq 1. Thus

$$K_{max} = K_{max}^{appl} + K_R \tag{13a}$$

$$K_{min} = K_{min}^{appl} + K_R \tag{13b}$$

The residual SIFs were calculated by the residual stress energy release rate procedure. The cracks were assumed to initiate and grow as quarter-circular corner cracks. Therefore, the SIFs were adjusted to have the proper shape factor and magnification factors for the plate configuration. This same procedure was followed in previous investigations [*2,10*]. The crack growth was calculated by linear summation on a cycle-by-cycle basis.

The spectrum load interaction effects on crack growth were predicted using a multiparameter yield zone (MPYZ) model [*16*] that utilizes Eq 12. This model uses an effective stress approach to predict the following load interaction effects: (1) crack growth retardation during load cycles following overloads, (2) crack growth acceleration during the application of overloads, (3) acceleration during load cycles following underloads and compression loads, and (4) acceleration during load cycles following underloads and compression loads.

Comparison of Analytical and Experimental Results

The fatigue lives to failure, N_f, were determined by adding together the life to crack initiation and the crack propagation life. The results are shown in Fig. 16 for NCX and CX slotted holes subjected to constant-amplitude cycling. In the NCX hole case, the predictions are accurate at the lower stress levels and somewhat conservative at the higher stress levels. Three levels of cold expansion were considered: 3, 4.5, and 6%. The analytical predictions are good at the higher stress levels and slightly nonconservative at the lowest stress level.

The results for a maximum cyclic stress of 262 MPa (38.0 ksi) (net) with a cold-expanded hole are presented in Fig. 17 as a plot of crack length versus cycles. This figure illustrates the two-step fatigue life approach. It shows that the crack initiation life prediction is conservative, and the crack propagation life is slightly unconservative. The unconservatism in the crack growth analysis may be due to some additional plastic stress redistribution as the crack propagates that is not accounted for or due to the treatment of the mandrel as a rigid body during the cold expansion analysis. Actually, the mandrel is an elastic body which contracts slightly as it is pulled through the hole. Accounting for this contraction will reduce the initial residual stresses and will be the subject of a future investigation.

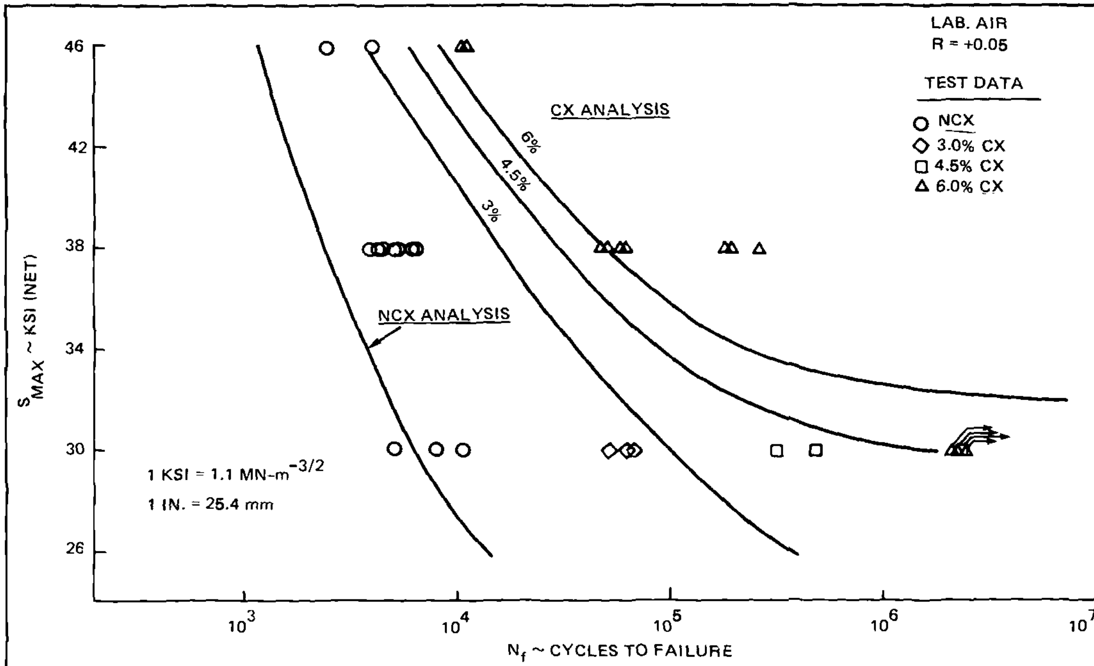

FIG. 16—*Effect of cold expansion on the fatigue life of stop-drilled holes ~7075-T651.*

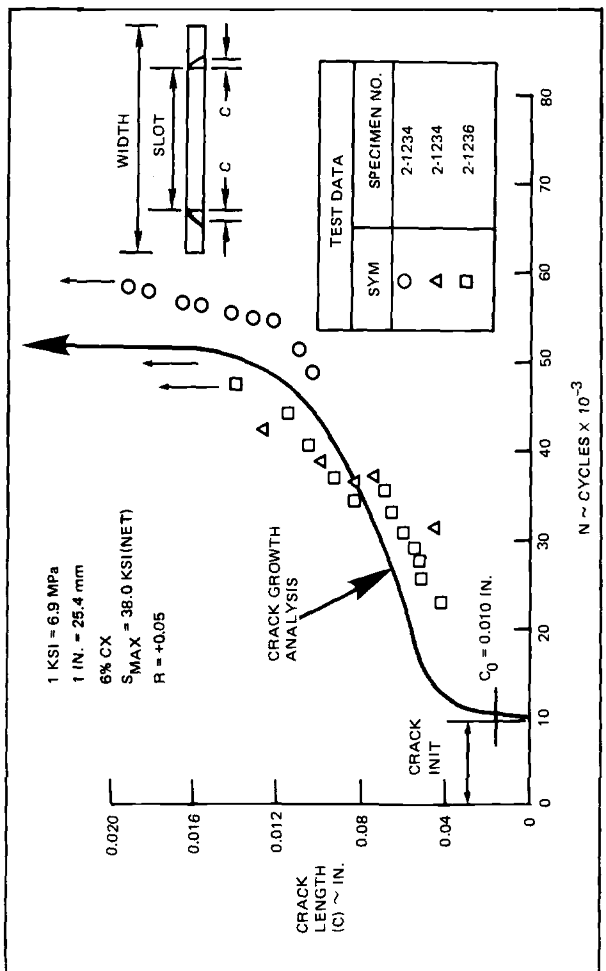

FIG. 17—Crack growth life of a cold-expanded slotted hole of 7075-T651 alloy.

The effect of adding fasteners to the cold-expanded slotted hole specimens is shown in Fig. 18. Here, test data are shown for the clearance-fit, neat-fit, and interference-fit fastener configurations. All of these specimens were cold expanded to a 6% mandrel interference level. Note that the addition of fasteners increases the total fatigue life and that increasing the level of interference further increases the fatigue life. For comparison, slotted hole specimens that are not cold expanded (NCX) are also shown. An analytical prediction is also presented in Fig. 19 by a line connecting predictions for cold-expanded slotted holes and cold-expanded slotted holes with neat-fit fasteners. The predictions are conservative but indicate the same trend in life shown by the test data.

The same analysis procedure that was used for constant-amplitude fatigue cycling was applied to a fatigue spectrum case, and the results are presented in Fig. 19 along with cold-expanded and non-cold-expanded test data. The fatigue spectrum is a randomized flight-by-flight simulation of a fighter aircraft wing lower cover. For the non-cold-expanded slotted hole, excellent correlation of the test data is achieved by the analysis. In the cold-expanded case, the tests were discontinued after about 20 000 flight hours. Inspection of the specimens revealed no measurable cracks. Predicted life for the test specimens is about 80 000 flight hours.

Tests were performed to investigate the behavior of the cold-expanded stop-drill hole in the event that the crack tip is not removed by the hole but remains in the structure. In these test specimens, holes were drilled leaving crack tips 1.27 and 2.54 mm (0.050 and 0.100 in.) beyond the edge of the hole. The stop-drill holes were then cold expanded to 6% mandrel interference. The results are presented in Fig. 20, where it is shown that the fatigue lives of these specimens are still comparable to cases in which the crack tip was removed. These tests are especially significant, as they indicate that the enhanced stop-drill procedure is almost as effective even if the stop-drill hole fails to remove the crack tip and leaves up to a 2.54-mm (0.10-in.) crack beyond the stop-drill hole.

Conclusions

A combined experimental and analytical investigation into the performance of an enhanced stop-drill repair procedure for cracked 7075-T651 aluminum structure has been carried out. The enhancement consists of cold expanding the stop-drill hole and installation of interference-fit fasteners. Experiments included measurements of residual strains and fatigue testing of a slotted hole specimen that was representative of stop-drill repair configuration. Analytical techniques used included elastic-plastic finite element analysis to predict residual stress and strain distributions introduced by cold expansion of the holes, the energy release rate approach to calculate applied load stress intensity factors, and the residual stress energy release rate

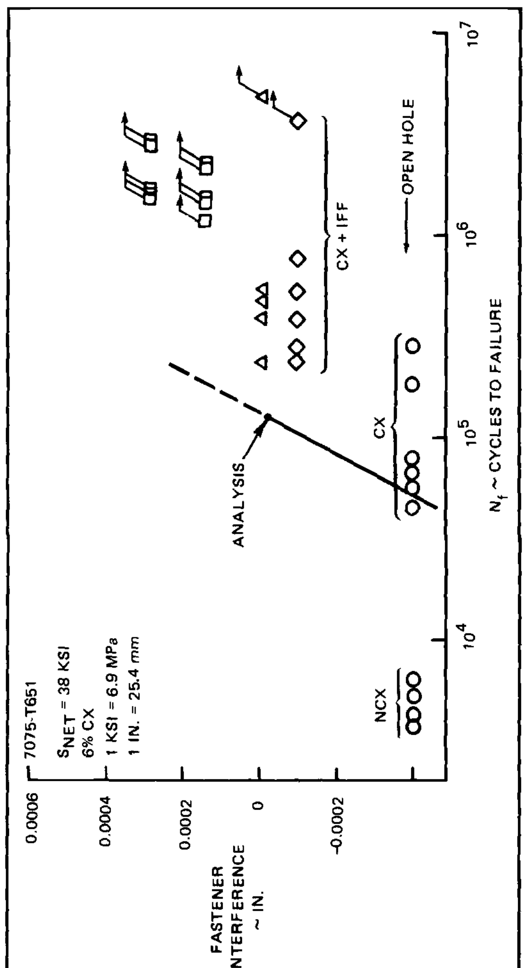

FIG. 18—*Effect of the fastener interference on the fatigue life of cold-expanded stop-drilled holes.*

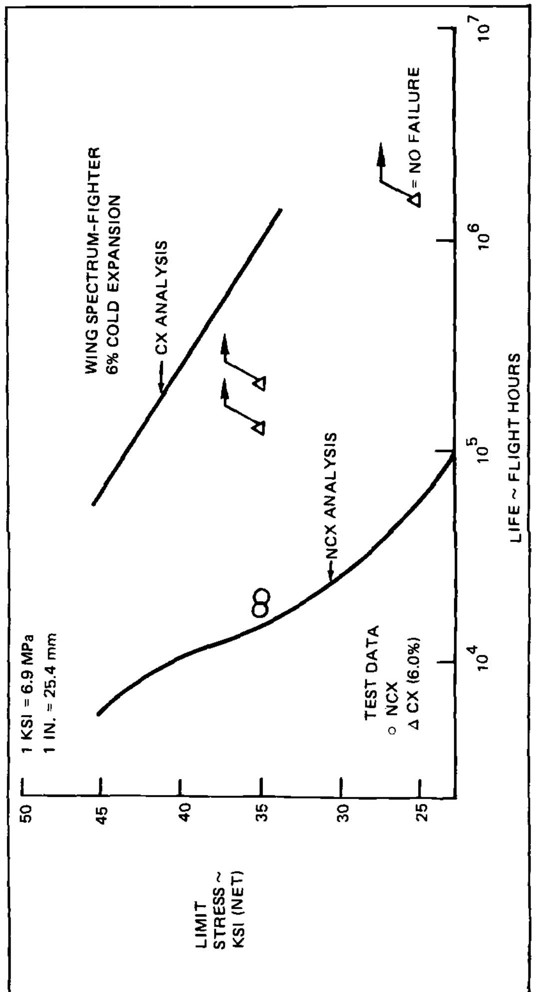

FIG. 19—*Fatigue life of a slotted specimen subjected to spectrum loading.*

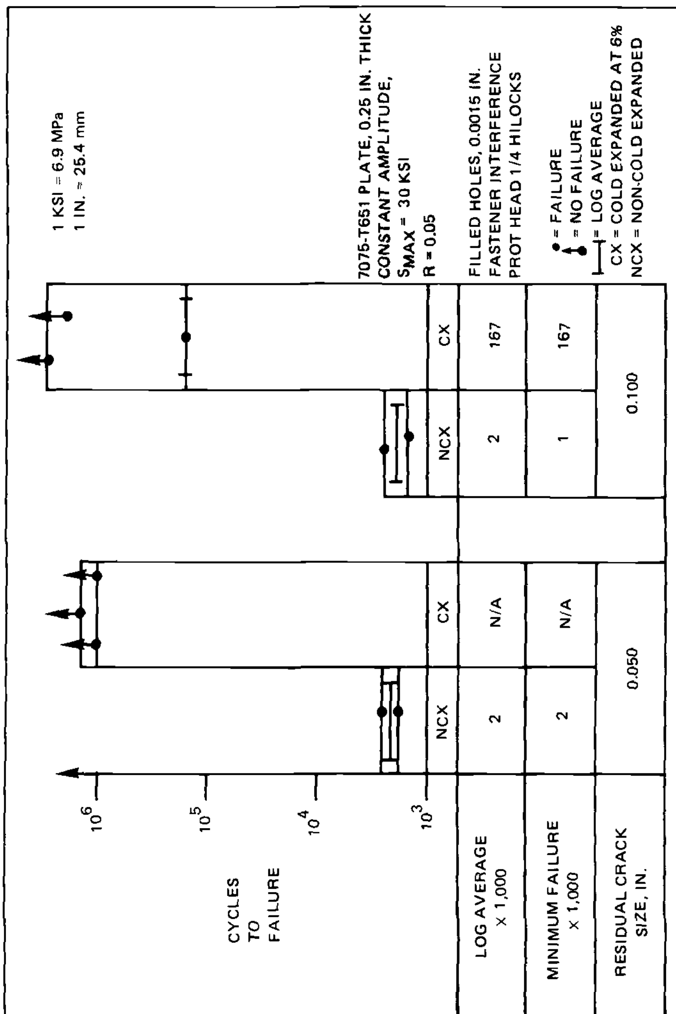

FIG. 20—*Effect of not removing the crack tip on the fatigue life.*

approach to calculate residual stress intensity factors. In addition, linear superposition of applied and residual stress intensity factors was employed for fatigue crack growth life predictions. Total fatigue lives were calculated by a two-step procedure, consisting of life to crack initiation plus crack propagation life.

From the results presented, the following can be stated:

- Cold expansion of a stop-drill hole increases the fatigue life by an order of magnitude in 7075-T651 aluminum alloys.
- The addition of an interference-fit fastener to a cold-expanded stop-drill hole further enhances the fatigue life to two orders of magnitude.
- The multistage analysis procedure provides reasonable correlation with test data.
- The enhanced repair procedure provides an order-of-magnitude improvement in the fatigue life even if the stop-drill hole misses the crack tip.
- The analytical procedure needs to be evaluated for other materials and fatigue spectra.

References

[1] Landy, M. and Champoux, R. L., "Enhanced Stop-Drill Repair Using Split Sleeve Cold Expansion," Report No. 4198-1, Fatigue Technology, Inc., Seattle, WA, 16 July 1984.

[2] Armen, H., Levy, A., and Eidinoff, H. L., "Elastic-Plastic Behavior of Coldworked Holes," *Journal of Aircraft*, American Institue of Astronautics and Aeronautics Vol. 21, No. 3, March 1984, pp. 193–201.

[3] Pifko, A., Levine, H. S., and Armen, H., Jr., "PLANS—A Finite Element Program for Nonlinear Analysis of Structures." *Theoretical Manual*, Vol. 1, NASA CR-2568, National Aeronautics and Space Administration, Washington, DC, November 1975.

[4] Armen, H. and Pifko, A., "Computer Techniques for Plasticity," *Pressure Vessels and Piping: Design Technology—A Decade of Progress*, S. Y. Zamrik and D. Dietrich, Eds., American Society of Mechanical Engineers, New York, 1982, pp. 601–616.

[5] Horsch, F. J. and Schwarz, R. C., "A Moire Fringe Data Handling System for Application in an Industrial Laboratory," *Proceedings*, Sixth International Conference of Experimental Stress Analysis, European Permanent Committee for Stress Analysis/Society for Experimental Stress Analysis, Munich, West Germany, September 1978.

[6] Zatz, I. J., Eidinoff, H. L., and Armen, Jr. H., "An Application of the Energy Release Rate Concept to Crack Growth in Attachment Lugs," AIAA Paper No. 81-0491, presented at the 21st Structures, Structural Dynamics, and Materials Conference, American Institute of Aeronautics and Astronautics, Atlanta, GA, April 1981.

[7] Newman, J. C., Jr., "An Improved Method of Collocation for the Stress Analysis of Cracked Plates with Various Shaped Boundaries," NASA TN D-6376, National Aeronautics and Space Administration, Washington, DC, August 1971.

[8] Cathey, W. H. and Grandt, A. F., Jr., "Fracture Mechanics Consideration of Residual Stresses Introduced by Coldworking Fastener Holes," *Journal of Engineering Materials and Technology*, Vol. 102, January 1980, pp. 85–90.

[9] Impellizeri, L. F. and Rich, D. L., "Spectrum Fatigue Crack Growth in Lugs," *Fatigue Crack Growth under Spectrum Loads, ASTM STP 595*, American Society for Testing and Materials, Philadelphia 1976, pp. 320–336.

[10] Rich, D. L. and Impellizeri, L. F., "Fatigue Analysis of Coldworked and Interference Fit Fastener Holes," *Cyclic Stress-Strain and Plastic Deformation Aspects of Fatigue Crack*

Growth, ASTM STP 637, American Society for Testing and Materials, Philadelphia, 1977, pp. 153–175.

[*11*] Bueckner, H. F., "A Novel Principle for the Computation of Stress Intensity Factors," *Zeitschrift für Angewandte Mathematik und Mechanik,* Vol. 50, No. 9, 1979, pp. 529–546.

[*12*] Friedman, R., "Grumman Local Strain Method for Predicting Fatigue Life," Report No. ADR20-11-81.2, Grumman Aerospace Corp., Bethpage, NY, November 1981.

[*13*] Manson, S. S. and Hirschberg, M. H., "Fatigue Behavior in Strain Cycling in the Low and Intermediate Cycle Range," *Proceedings,* Tenth Sagamore Army Materials Research Conference, Sagamore, NY, 13–16 Aug. 1963.

[*14*] Bell, P. D. and Creager, M., "Crack Growth for Arbitrary Spectrum Loading," AFFDL-TR-74-129, Air Force Flight Dynamics Laboratory, Wright-Patterson Air Force Base, OH, October 1974.

[*15*] Hudson, C. M., "Effect of Stress Ratio on Fatigue Crack Growth in 7075-T6 and 2024-T3 Aluminum Alloy Specimens," NASA TN D-5390, National Aeronautics and Space Administration, Washington, DC, August 1969.

[*16*] Johnson, W. S., "Multi-Parameter Yield Zone Model for Predicting Spectrum Crack Growth," *Methods and Models for Predicting Fatigue Crack Growth Under Random Loading, ASTM STP 748,* American Society for Testing and Mateials, Philadelphia, 1981, pp. 85–102.

Heimo Huth[1]

Influence of Fastener Flexibility on the Prediction of Load Transfer and Fatigue Life for Multiple-Row Joints

REFERENCE: Huth, H., "**Influence of Fastener Flexibility on the Prediction of Load Transfer and Fatigue Life for Multiple-Row Joints,**" *Fatigue in Mechanically Fastened Composite and Metallic Joints, ASTM STP 927,* John M. Potter, Ed., American Society for Testing and Materials, Philadelphia, 1986, pp. 221–250.

ABSTRACT: An improvement of the accuracy of fatigue life prediction methods used for multiple-row riveted or bolted joints can be expected only if the rivet load distribution is considered during design and fatigue analysis. To calculate the individual load transfer and the bypassing load the fastener flexibility must be taken into account. Semiempirical formulas for the calculation of fastener flexibility existing in the literature turn out to be not exact or at least not applicable for a wider range of joint geometries. This unsatisfactory situation was the reason for performing an extensive experimental investigation during which fastener flexibilities for a wide range of joints of practical interest were determined.

The effects of primary joint parameters, such as the plate material, clamping length, and diameter and material of the fastener, as well as the effects of secondary parameters, such as the clamping force, condition of the faying surfaces, and fit and type of head of the fastener, were investigated through specific variations. For this purpose load-deformation measurements under quasi-static and flight-by-flight loading conditions were performed using single- and double-shear specimens with known load transfer.

A formula for fastener flexibility, valid for riveted and bolted metallic and graphite/epoxy joints, was derived from the test results and proved to be significantly superior to those found in the literature. This formula for load transfer calculations of multiple-row fatigue loaded joints was used to predict accurately the measured values of load transfer. This improvement also leads to a better fatigue life prediction. The load transfer measurements showed a quasi-linear relationship between the applied load and the total load transfer which was little affected by fatigue loading, although the load transferred by bearing was not constant. By measuring bearing loads and local strains close to fastener holes in a multiple-row joint the author shows that with increasing friction the bearing stress and the local strains decreased. The redistribution of loads or the changes in the mechanisms of load transfer result in a relief of the fatigue critical location. Since these changes of the local stress situation cannot be predicted, the application of fatigue life prediction methods on the basis of local strains must lead to inaccurate results.

[1] Research engineer, Fraunhofer-Institute fuer Betriebsfestigkeit (LBF), Darmstadt, West Germany.

KEY WORDS: fastener flexibility, load transfer, riveted joint, bolted joint, single-shear joint, double-shear joint, fatigue life estimation, Falstaff sequence, graphite/epoxy, aluminum alloy, deformation measurements

By far, most of the fatigue cracks occurring in aircraft structures originate at holes of shear loaded fasteners. This is due mainly to the inaccuracy of fatigue life prediction methods used for multiple-row riveted or bolted joints. The three main causes for this inaccuracy are the following:

1. The damage accumulation hypothesis itself is inaccurate.
2. The design data are not appropriate.
3. Mistakes are made during stress analysis.

The aim of this investigation was to show how the last two problems can be alleviated. For this purpose it is essential to determine and correctly consider the forces/stresses acting in a joint. As shown in Fig. 1 for the last fastener of a single-shear joint, the stresses result from these forces:

(*a*) the bypassing force, F_{BP},
(*b*) the bearing force, F_{BR}, and
(*c*) the forces transferred by friction, F_{FR}.

The last two forces sum up the total load transferred at that fastener location, F_{LT}. If this force, often also referred to as rivet force, is related to the applied external force, F_0, one talks of the "load transfer." Although it is well known that the amount of load transfer has a superior influence on

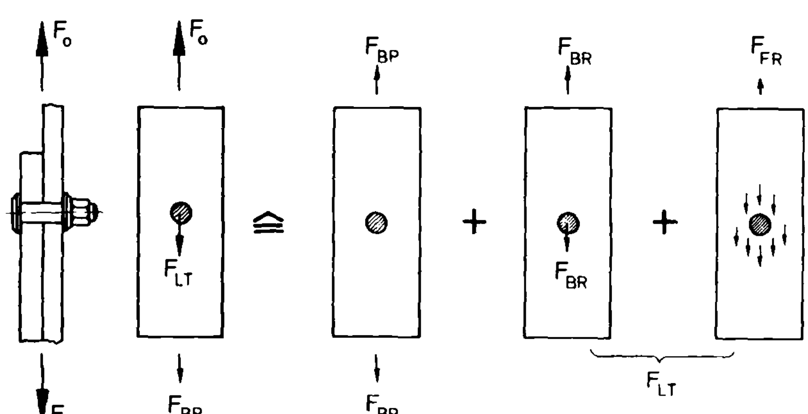

FIG. 1—*Definition of forces acting in a joint.*

the fatigue life of a multiple-row joint, surprisingly few results of investigations can be found in the literature [*1–3*]. For example, the *S-N* curves for single-shear riveted joints derived from test results reported in Ref *1* are shown in Fig. 2. The amount of load transfer was varied from 22 to 100% by changing the number of rivets from 10 to 1. It can be seen that in the region of practical interest (0.2 < LT < 0.5) there is a factor of 10 on the fatigue life.

Load transfer or the distribution of rivet loads in a multiple-row joint depends not only on the number of rivets used but even more on the fastener flexibility. If the rivet loads are to be calculated, using, for example, a mathematical model developed in Refs *4* and *5* and extended in Ref *6*, the stiffness of flexibility of the rivets has to be considered. As shown schematically in Fig. 3, the fastener flexibility has a more or less pronounced influence, depending on the type of joint in question.

In the aircraft industry a number of semi-empirical formulas for the calculation of fastener shear flexibility have been developed [*7–10*]. In most cases they were derived from a rather limited number of static tests. A comparison of the different formulas has been presented in Refs *11* and *12*. The results were disappointing since the scatter was rather large and, furthermore, a comparison of test results of flight-by-flight loaded specimens showed large differences in fastener flexibilities.

This unsatisfactory situation was the reason for performing an extensive experimental investigation during which fastener flexibilities for a wide range of joints of practical interest were to be determined.

Experimental Determination of Fastener Flexibilities

The following parameters were expected to affect the deformation behavior and thus also the fastener flexibility. The primary parameters (dealing with geometry and materials) are the following:

(*a*) Young's modulus of the plate materials,
(*b*) clamping length,
(*c*) fastener diameter,
(*d*) fastener material, and
(*e*) single- or double-shear configuration.

The secondary parameters (dealing with installation) are these:

(*a*) clamping force,
(*b*) fit of the fastener,
(*c*) type of fastener head, and
(*d*) condition of the faying surfaces.

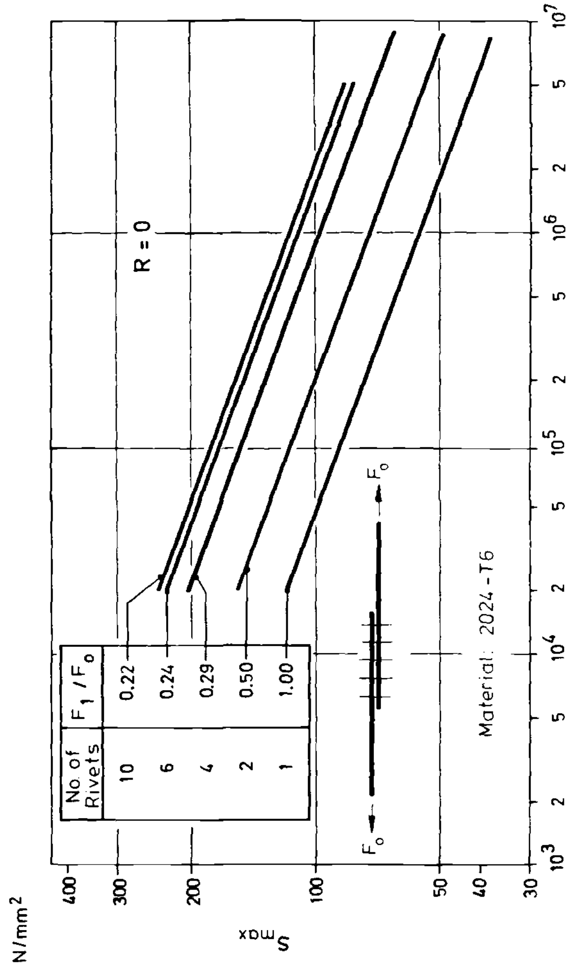

FIG. 2—*Influence of load transfer on the fatigue behavior of single-shear riveted joints* [1].

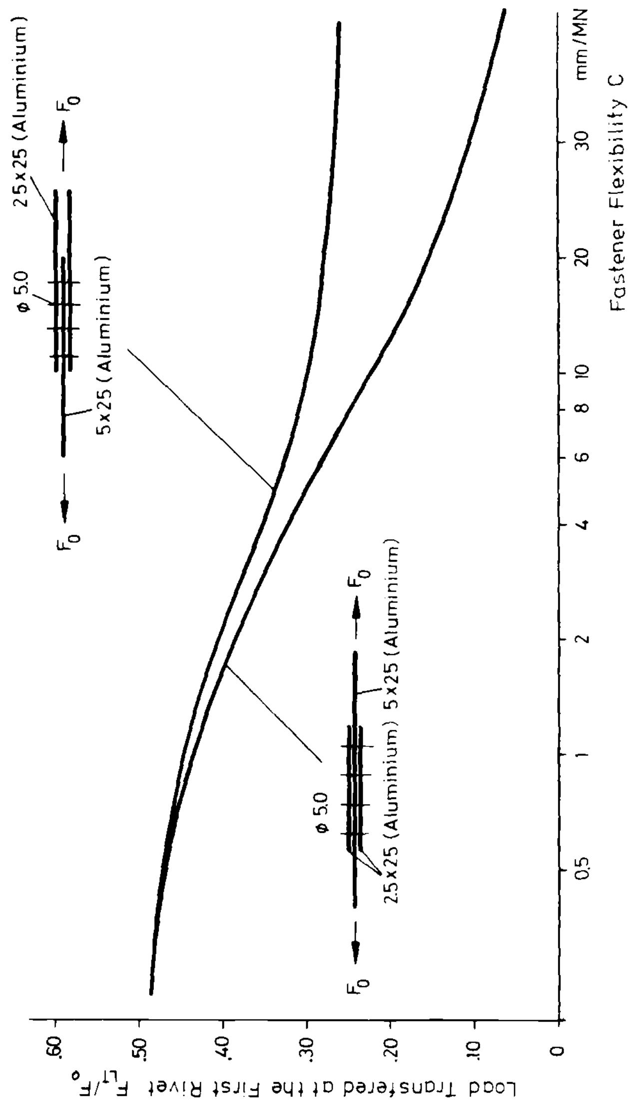

FIG. 3—*Influence of fastener flexibility on load transfer (schematic).*

TABLE 1*a*—*Investigation of Specimens ISS01 and IDS01 of Group I (bolted metallic joints).*

Parameters	Single Shear ISS01	Double Shear IDS01
Primary		
plate materials	2024 T3	2024 T3
fastener material	Ti-6Al-4V	Ti-6Al-4V
clamping length	10 mm	10 mm
bolt diameter	5.0 mm	5.0 mm
Secondary		
type of head	flush head	protruding head
faying surfaces	PRC[a]	PRC[a]
fastener fit	interference fit	interference fit
clamping force	normal (high)	normal (high)

[a] PRC stands for antifretting compound.

In addition, the following three groups of joints of practical interest were defined:

Group I—bolted metallic joints.
Group II—riveted thin-sheet metallic joints.
Group III—bolted graphite/epoxy joints.

Specimens

For each group, two types of basic specimens, single-shear (SS) with 100% and double-shear (DS) with 50% load transfer, were defined using the most common combination of parameters. All other specimens differed by variation of only one primary or secondary joint parameter in the range of practical interest. This is shown in Tables 1*a* and 1*b* for the bolted metallic joints. In all, 45 different specimens were manufactured and tested.

TABLE 1*b*—*Investigation of further specimens of Group I (bolted metallic joints).*[a]

	Single Shear Specimens		Double Shear Specimens	
Parameter V	Results	Specimen No.	Results	Specimen No.
Plate materials	7075 T73	ISS02		
	Ti-6Al-4V	ISS03	Ti-6Al-4V	IDS03
Fastener material	steel	ISS12	steel	IDS10
Clamping length, mm	5.0	ISS05	4.5	IDS05
	20.0	ISS06	15.0	IDS06
			20.0	IDS07
Bolt diameter, mm	6.35	ISS10	6.35	IDS09
	8.0	ISS09	8.0	IDS08
Type of head	protruding head	ISS11	...	...
Faying surfaces	without PRC	ISS04	without PRC	IDS04
Fastener fit	clearance fit	ISS13	clearance fit	IDS11
Clamping force	low	ISS14	low	IDS12

[a] Additional specimens with blind bolts (ISS15 and IDS13) were tested.

The manufacturing details for Group I include the following: Three different plate materials (2024 T3, 7075 T73, and Ti-6Al-4V alloys) were used; the plate thickness varied between 1.0 and 10.0 mm. For most specimens the sealing compound PR 1436 was applied to the faying surfaces. The fasteners (NAS and Hi-Lok bolts) were installed with interference fit (25 to 30 μm) using normal clamping forces.

The specimens of Group II were made of 2024 T3 clad material using solid rivets and PR 1436.

For the graphite/epoxy specimens of Group III the material T 300/C 914 was used in two lay-ups—Laminate II $(O_2/\pm45/O_2/\pm45/\overline{90})_s$ and isotropic $(0/\pm45/90/0/\pm45/90)_s$—with nominal thicknesses of 2.1, 4.2, and 6.3 mm. Here the NAS bolts were installed with clearance fit, and a shim of 0.2 mm thickness (Hysol EA 934 ± 50% aluminum powder) was applied to the faying surfaces.

The actual dimensions for those specimens used to investigate the influences of the primary joint parameters, and further details, are listed in Tables 2 and 3.

Test Procedure

Since an experimental determination of the individual deformations due to shear, bending, and bearing loads is not possible, an integral value of the total deformation was measured using a strain-gage-equipped extensometer, as shown in Fig. 4. The elastic deformations of the specimen segments within the gage length, ℓ_0 ($\Delta\ell_1$ and $\Delta\ell_2$), were eliminated by electric compensation, thus the load-δ-curves could be recorded directly.

One specimen of each type was used for quasi-static measurements, being cyclically loaded at $R = 0$ with a stepwise increasing upper load until fracture; thus the elastic-plastic load-deformation curves were obtained.

A second specimen was used to measure the deformations and changes of the deformation behavior under Falstaff loading [13]. For these measurements a relatively short artificial flight (11 cycles) was deduced from the Falstaff sequence (see Fig. 5), comprised of load levels 3 to 29 ($\overline{R} = -0.24$). This extra measuring flight was applied as Flights 1 and 2 prior to the Falstaff sequence. After 600 and 6000 flights, the measurements were repeated. Test stress levels were chosen so that a fatigue life of about 12 000 flights could be reached. In some cases, fatigue cracks developed in the single-shear specimens before reaching 6000 flights. For the double-shear specimens, this stress level of $\overline{\sigma}_0 = 172.5$ N/mm^2 resulted in somewhat unrealistic high bearing stresses. Thus several tests were repeated using two thirds of this value.

Test Results

From the test results, that is, the recorded load-deformation curves (see the example in Fig. 6), some general phenomena can be derived. The load-

TABLE 2—*Details for the double-shear specimens (variation of primary joint parameters).*

Specimen No.	Materials		Dimensions, mm			Fasteners		Results of the quasi-stat. tests			Fastener Flexibilities, mm/MN: Falstaff-tests	
	1	2	t_1	t_2	w	d	Type	FM	F_{ult}, N	$C_{2/3}$	C_F	$\overline{C_F}$
IDS01	2024T3	2024T3	5.1	2.5	25	5.0	A 1	X/Y2	22,400	9.6	9.0	5.2
IDS03	Ti6Al4V	Ti6Al4V	5.4	2.5	25	5.0	A 1	Z	29,800	7.0	6.6	4.6
IDS05	2024T3	2024T3	2.5	1.0	25	5.0	A 1	X/Y2	9,800	13.2	12.0	5.0
IDS06	2024T3	2024T3	5.1	5.1	25	5.0	A 1	X/Y1	24,500	8.6	8.2	5.4
IDS07	2024T3	2024T3	10.1	5.1	25	5.0	A 2	Z	31,120	8.3	7.1	3.6
IDS08	2024T3	2024T3	5.1	2.5	40	8.0	A 1	X2	36,980	6.9	6.4	3.8
IDS09	2024T3	2024T3	5.1	2.5	32	6.35	A 1	X2	29,250	8.6	8.1	7.7
IDS10	2024T3	2024T3	5.1	2.5	25	5.0	B 1	XY/2	23,175	8.6	7.9	6.0
IDS13	2024T3	2024T3	5.1	2.5	25	4.8	B 3	X2	22,075	-	8.3	11.2
IIDS01	2024T3	2024T3	2.0	1.0	24	4.8	C 1	X2	8,100	17.8	14.2	12.6
IIDS02	2024T3	2024T3	4.0	2.0	24	4.8	C 1	Z	10,400	10.4	8.2	5.0
IIDS03	2024T3	2024T3	2.0	2.0	24	4.8	C 1	X/Y1	8,750	13.4	-	-
IIDS04	2024T3	2024T3	2.0	1.0	16	3.2	C 1	Z	4,130	18.8	17.2	12.0
IIIDS01	CFRP (lam II)	CFRP (lam II)	4.5	2.1	25	5.0	A 1	X2	17,970	15.7	14.8	5.4
IIIDS02	CFRP isotropic	CFRP isotropic	3.8	1.95	25	5.0	A 1	X2	18,940	17.5	15.8	7.4
IIIDS03	CFRP (lam II)	2024T3	4.4	2.5	25	5.0	A 1	X/Y1	17,080	13.8	11.4	3.4
IIIDS10	CFRP (lam II)	CFRP (lam II)	6.4	4.4	25	5.0	A 1	XY1	28,160	11.1	12.0	3.6

Types of Fasteners:
A = Titanium Bolt
B = Steel Bolt
C = Aluminum Rivet

1 = Protruding Head
2 = Flush Head
3 = Blind Bolt with Prot. Head
4 = Blind Bolt with Flush Head

Failure Modes (FM):

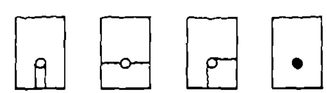
X Y X/Y Z

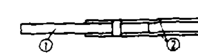

TABLE 3—*Details for the single-shear specimens (variation of primary joint parameters).*

Specimen No.	Materials		Dimensions, mm			Fasteners		Results of the quasi-stat. tests		Fastener Flexibilities, mm/MN	Falstaff-tests	
	1	2	t_1	t_2	w	d	Type	FM	F_{ult}, N	$C_{2/3}$	C_F	$\overline{C_F}$
ISS01	2024 T3	2024 T3	5.1	5.1	25	5.0	A 2	Z	28,655	24.1	22.0	10.1
ISS02	7075 T3	7075 T3	4.9	4.8	25	5.0	A 2	Z	27,970	25.2	22.4	11.6
ISS03	Ti6Al4V	Ti6Al4V	5.3	5.3	25	5.0	A 2	Z	29,800	15.2	19.4	10.8
ISS05	2024 T3	2024 T3	2.5	2.5	25	5.0	A 2	Z	15,060	36.0	26.0	11.6
ISS06	2024 T3	2024 T3	10.1	10.1	25	5.0	A 2	Z	32,380	20.6	19.0	13.4
ISS09	2024 T3	2024 T3	5.1	5.1	40	8.0	A 2	Z	>47,800	15.8	13.1	6.3
ISS10	2024 T3	2024 T3	5.1	5.1	32	6.35	A 2	Z	43,155	20.6	20.6	20.2
ISS12	2024 T3	2024 T3	5.1	5.1	32	6.35	B 2	Z	50,210	18.0	15.8	10.9
ISS15	2024 T3	2024 T3	5.1	5.1	25	4.8	B 4	Z	31,815	22.8	24.0	37.0
IISS01	2024 T3	2024 T3	2.0	2.0	24	4.8	C 2	Z	7,700	32.0	28.5	12.4
IISS02	2024 T3	2024 T3	4.0	4.0	24	4.8	C 2	Z	10,600	20.8	19.0	11.8
IISS04	2024 T3	2024 T3	2.0	2.0	16	3.2	C 2	Z	4,080	56.0	55.2	57.6
IISS09	2024 T3	2024 T3	2.0	2.0	24	4.0	C 2	Z	8,250	40.2	36.5	33.6
IIISS01	CFRP (lam II)	CFRP (lam II)	4.5	4.5	25	5.0	A 2	X1	22,020	33.2	30.5	8.0
IIISS02	CFRP isotropic	CFRP isotropic	3.8	3.8	25	5.0	A 2	Y1	19,210	38.6	33.2	8.8
IIISS07	CFRP (lam II)	CFRP (lam II)	4.4	4.4	40	8.0	A 2	Z*	41,740	23.7	21.2	6.8
IIISS08	CFRP (lam II)	CFRP (lam II)	2.2	2.1	25	5.0	A 2	X1/Z	13,104	42.5	52.5	19.8
IIISS09	CFRP (lam II)	CFRP (lam II)	6.4	6.4	25	5.0	A 2	X1	27,030	21.0	28.8	7.6

Types of Fasteners:
A = Titanium Bolt
B = Steel Bolt
C = Aluminum Rivet

1 = Protruding Head
2 = Flush Head
3 = Blind Bolt with Prot. Head
4 = Blind Bolt with Flush Head

Failure Modes (FM):

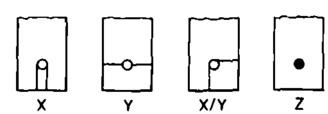

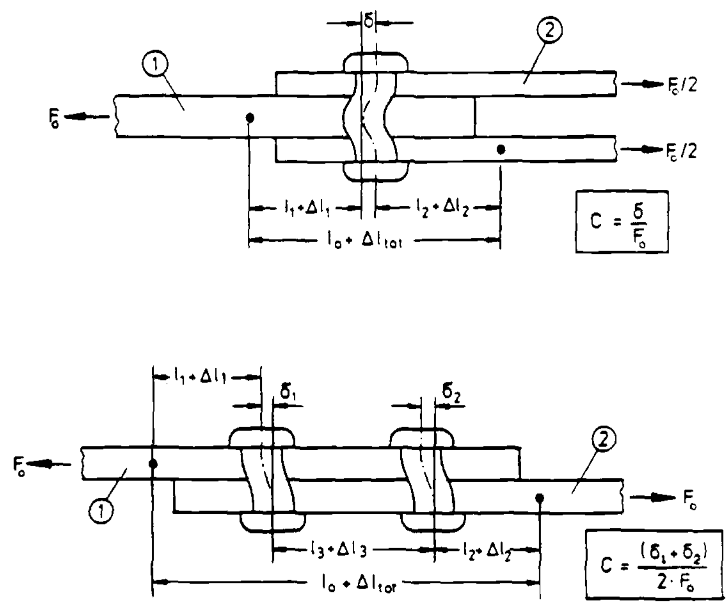

FIG. 4—*Deformations in single- and double-shear specimens.*

deformation curves under static loading (enveloping curve) show a somewhat unexpected behavior since no linear relationship, even in the region of elastic deformations, was recorded. The exceptions are some of the curves recorded with riveted specimens (Group II), probably because of their lower clamping forces. The unloading and reloading curves, however, show a linear behavior with nearly unchanging slope. Having been loaded to a certain amount of permanent deformation, the slope changes only insignificantly until final fracture.

The typical appearance of hysteresis curves recorded during flight-by-flight loading is the following: Due to the rather high but nevertheless realistic stress level, pronounced plastification effects occur during the first flight. The hysteresis loops of the second flight are already much more narrow: with an increasing number of flights their areas increase, while the deformation amplitude gets smaller. The sometimes drastic changes of shape and area are caused by the changing conditions of friction and plastic deformations of the fastener holes. It can be observed, however, that the slope of the linear part of the hysteresis does not change very much. As shown in Fig. 7, the slope of the connecting line between the maximum and minimum of the 0 to 5 g loop, $\overline{C}_F$, is strongly influenced by fatigue loading, whereas the slope of the linear part, C_F, is not. A complete presentation of the test results is given in Ref *14*.

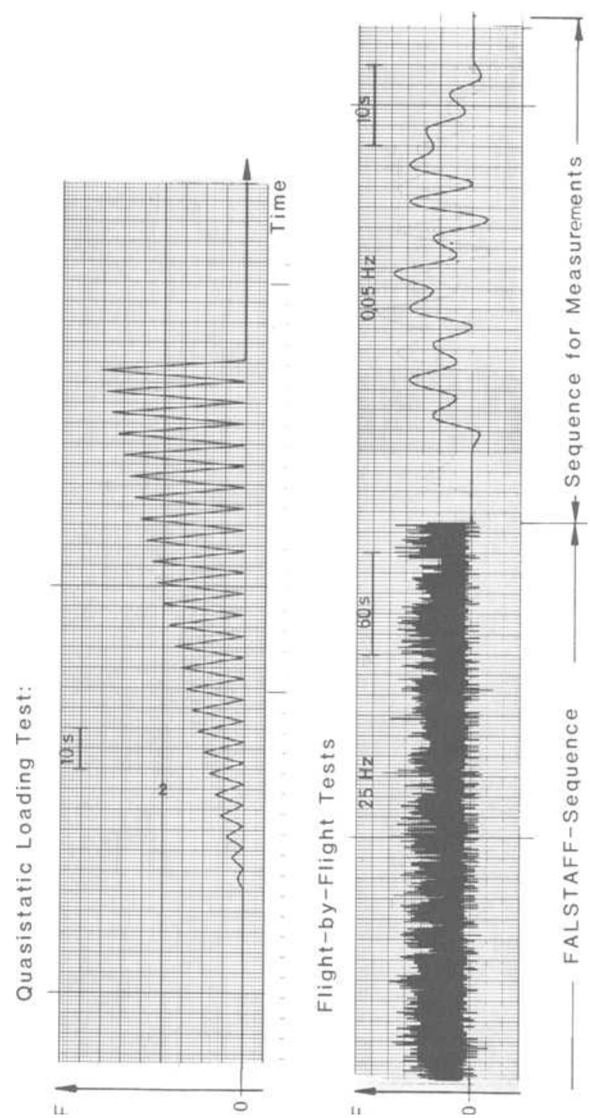

FIG. 5—*Loading sequences used during displacement measurements.*

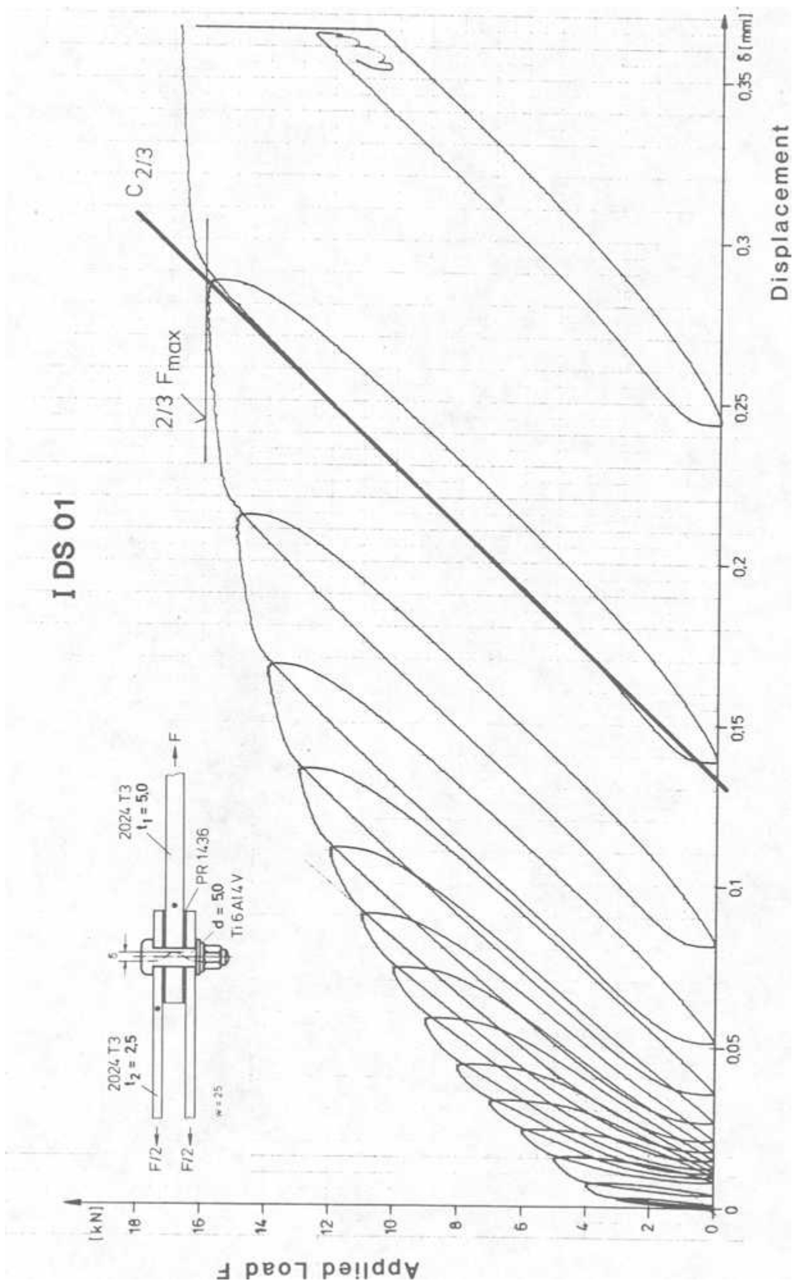
I DS 01
C 2/3
2/3 F max
2024 T3
t1 = 5,0
2024 T3
t2 = 2,5
PR 1436
d = 5,0
Ti 6 Al 4 V
F
F/2
F/2
Applied Load F
[kN]
18
16
14
12
10
8
6
4
2
0
0
0,05
0,1
0,15
0,2
0,25
0,3
0,35
δ [mm]
Displacement

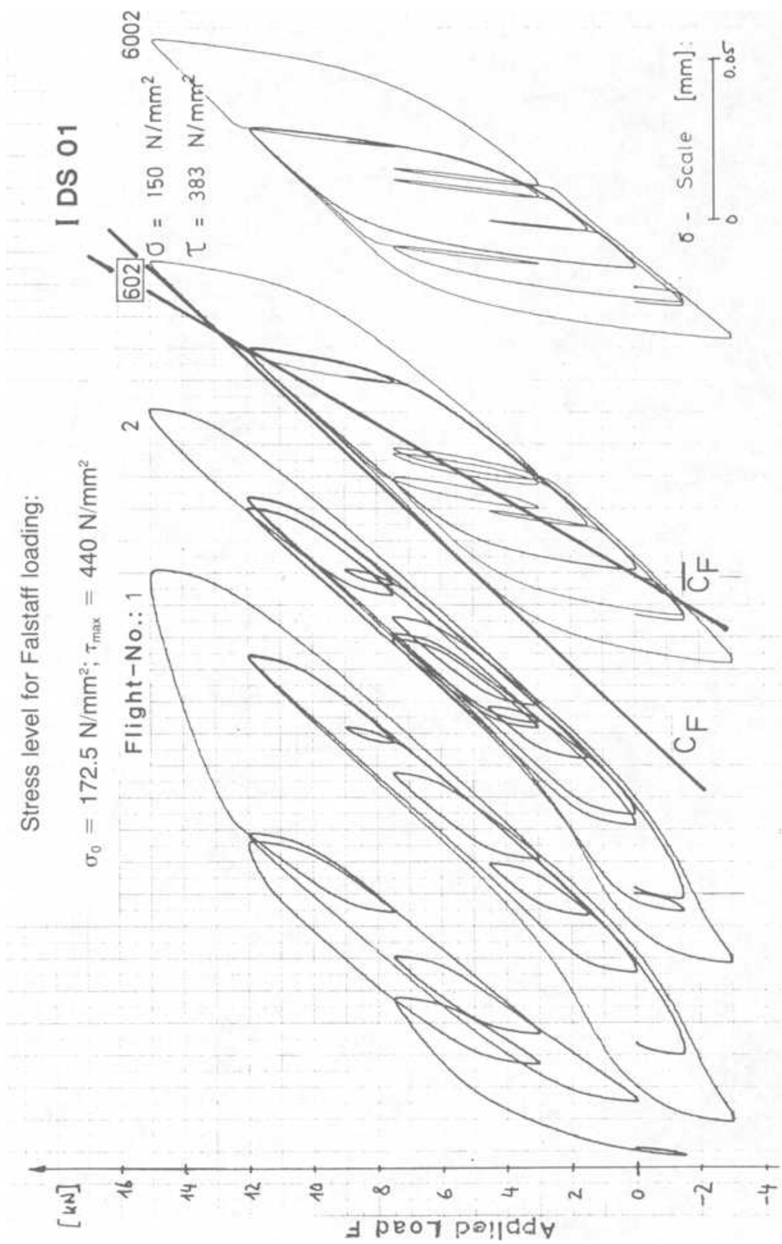

FIG. 6.—*Evaluation of load-displacement recordings (definition of fastener flexibility).*

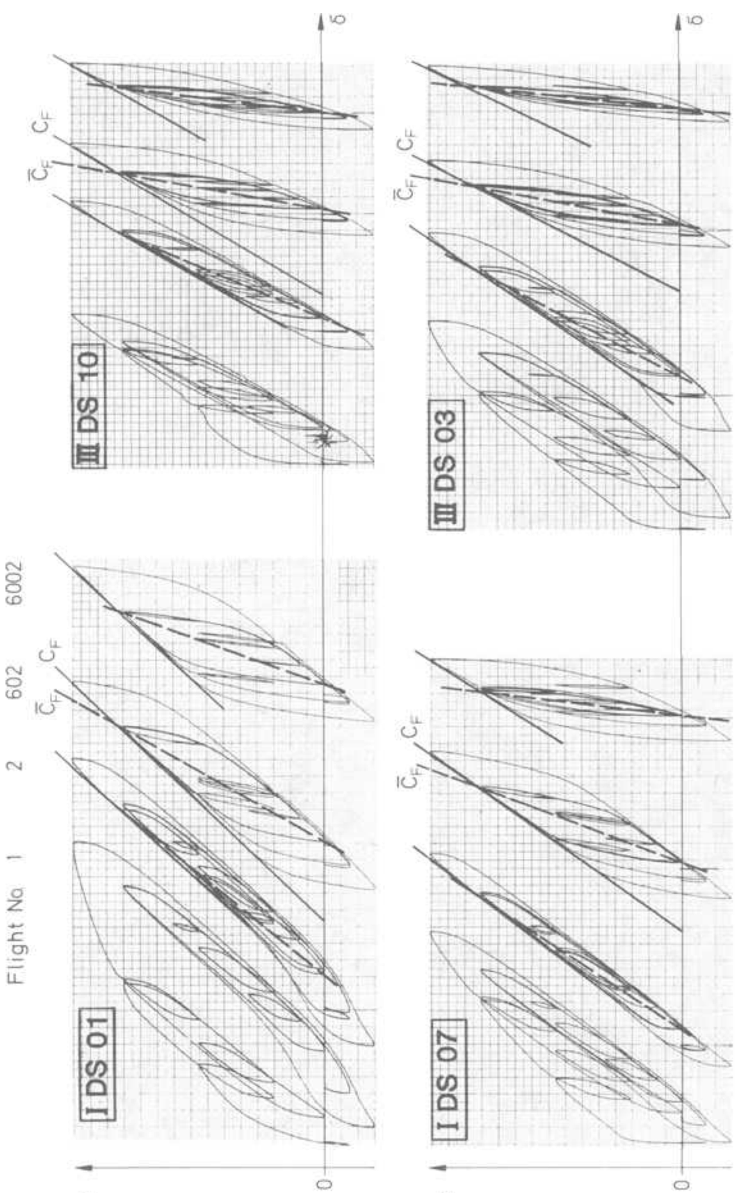

FIG. 7.—*Influence of flight-by-flight loading on fastener flexibility* C_F *and* $\bar{C}_F$ *(double-shear specimens).*

Since these C_F values are in most cases identical with the $C_{2/3}$ values of the quasi-static tests (see Fig. 6), the author concludes that these values represent characteristic quantities related to the fastener flexibility of the individual joints.

An equation containing all primary parameters was set up and fitted to the above-mentioned test results, producing a new formula for fastener flexibility:

$$C = \left(\frac{t_1 + t_2}{2d}\right)^a \frac{b}{n}\left(\frac{1}{t_1E_1} + \frac{1}{nt_2E_2} + \frac{1}{nt_1E_3} + \frac{1}{2nt_2E_3}\right) \tag{1}$$

The bracket on the right side comprises the flexibility resulting from bearing loads, while the left part contains portions due to fastener bending and shear. It was necessary to use different Constants a and b for the three groups of joints under consideration:

Group I—bolted metallic joints	$a = 2/3$; $b = 3.0$
Group II—riveted metallic joints	$a = 2/5$; $b = 2.2$
Group III—bolted graphite/epoxy joints	$a = 2/3$; $b = 4.2$

Equation 1 is valid for single-shear ($n = 1$) and double-shear ($n = 2$) joints.

In order to compare the accuracy in predicting fastener flexibilities, the following three equations (for single shear) were chosen from the literature:

Tate and Rosenfeld [*4*]:

$$C = \frac{1}{t_1E_1} + \frac{1}{t_2E_2} + \frac{1}{t_1E_3} + \frac{1}{t_2E_3} + \frac{32(t_1 + t_2)(1 + \nu)}{9E_3\pi d^2} + \frac{8(t_2^3 + 5t_2^2t_1 + 5t_2t_1^2 + t_1^3)}{5E_3\pi d^4} \tag{2}$$

Boeing [*7*]:

$$C = \frac{2^{(t_1/d)^{0.85}}}{t_1}\left(\frac{1}{E_1} + \frac{3}{8E_3}\right) + \frac{2^{(t_2/d)^{0.85}}}{t_2}\left(\frac{1}{E_2} + \frac{3}{8E_3}\right) \tag{3}$$

Douglas [*10*]:

$$C = \frac{5}{d \cdot E_3} + 0.8\left(\frac{1}{t_1E_1} + \frac{1}{t_2E_2}\right) \tag{4}$$

The results of comparative calculations and their comparison with the presented test results are shown in Figs. 8 through 11. For the double-shear case, equations from the literature predict values that are too high, which would lead to an overestimation of fatigue life. For single-shear specimens, the opposite tendency can be noticed.

Load Transfer Measurements and Calculations

In order to test the applicability of the derived Eq 1 for fastener flexibility, load transfer measurements with several different multiple-row joints were performed. Thus, the possible improvements in load transfer calculation were to be demonstrated. Thirteen different types of strain-gage specimens—four examples are shown in Fig. 12—were used for load transfer measurements. The load transfer at the first fastener ranged between 15% and 45%. Special attention was paid to a correct positioning of the strain gages, since strain distributions across the width of the specimen, as shown on Fig. 13, were expected and had to be taken into account.

For some specimens, the measurements were repeated after the application of some 600 flights of the Falstaff loading sequence. For lap joints, the fatigue loading does not result in changes of load transfer and fastener load distribution, as shown on Fig. 14. Moderate changes are recorded for reinforcement specimens (Types II.1 and II.2), but in general a quasi-linear relationship between the transferred load and the applied load is obtained.

Comparisons between the calculated and measured load transfer values resulted in good agreement (Fig. 15). The application of the so-called Boeing and Douglas formulas (Eqs 3 and 4) during load transfer calculations for the specimens investigated led in some cases to errors of 40%, as shown on Fig. 16. From available fatigue test results it can be concluded that such errors in load-transfer predictions would result in a 400% error for the predicted fatigue life.

Mechanisms of Load Transfer

In order to clarify the discrepancies between the results of the deformation measurements that show a distinct influence of fatigue loading on the deformation behavior and the results of the load-transfer measurements where this influence does not appear, some additional tests were performed. A double-shear specimen with three fasteners (Fig. 17) was prepared to measure load transfer, the local strain at a fastener hole, the bearing load, and the displacement (that is, fastener flexibility) simultaneously. The total load transfer was measured using three strain gages positioned between two fasteners, and the load transferred by bearing was measured using an instrumented steel bolt. The results obtained are shown on Fig. 18. It can be seen that all curves except that of the total load transfer show a clear

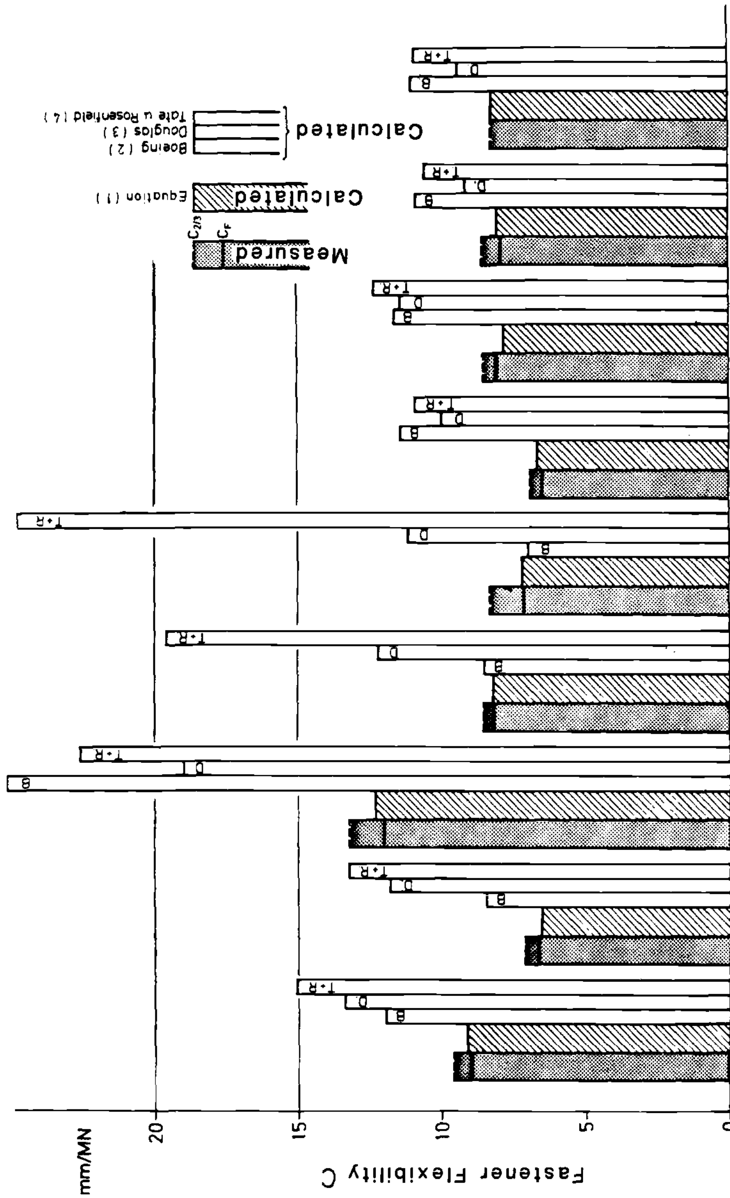

FIG. 8—*Comparison of measured and calculated fastener flexibilities for bolted double-shear specimens.*

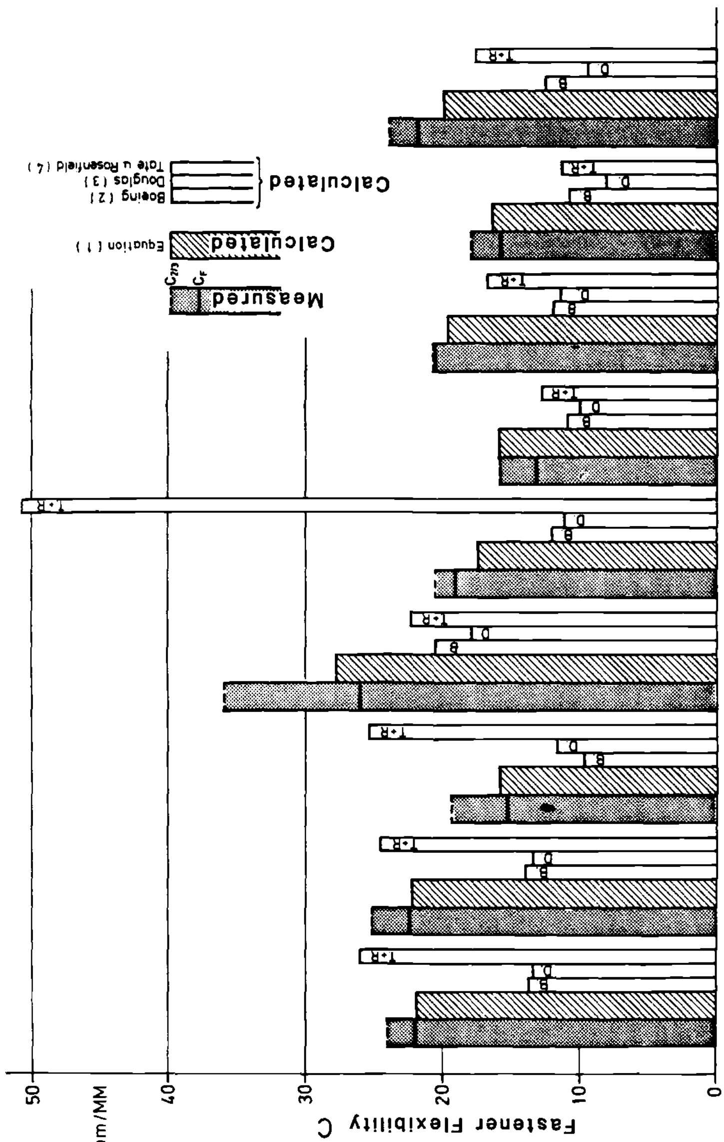

FIG. 9—*Comparison of measured and calculated fastener flexibilities for bolted single-shear specimens.*

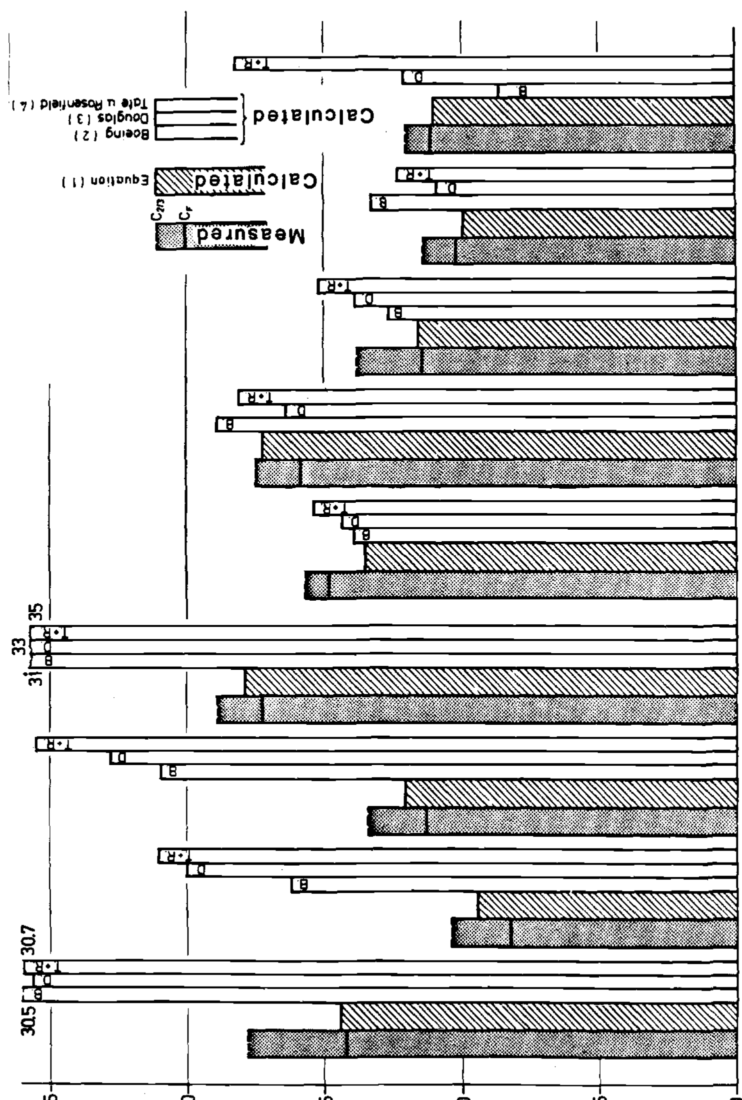

FIG. 10—*Comparison of measured and calculated fastener flexibilities for riveted metallic and bolted graphite/epoxy double-shear specimens.*

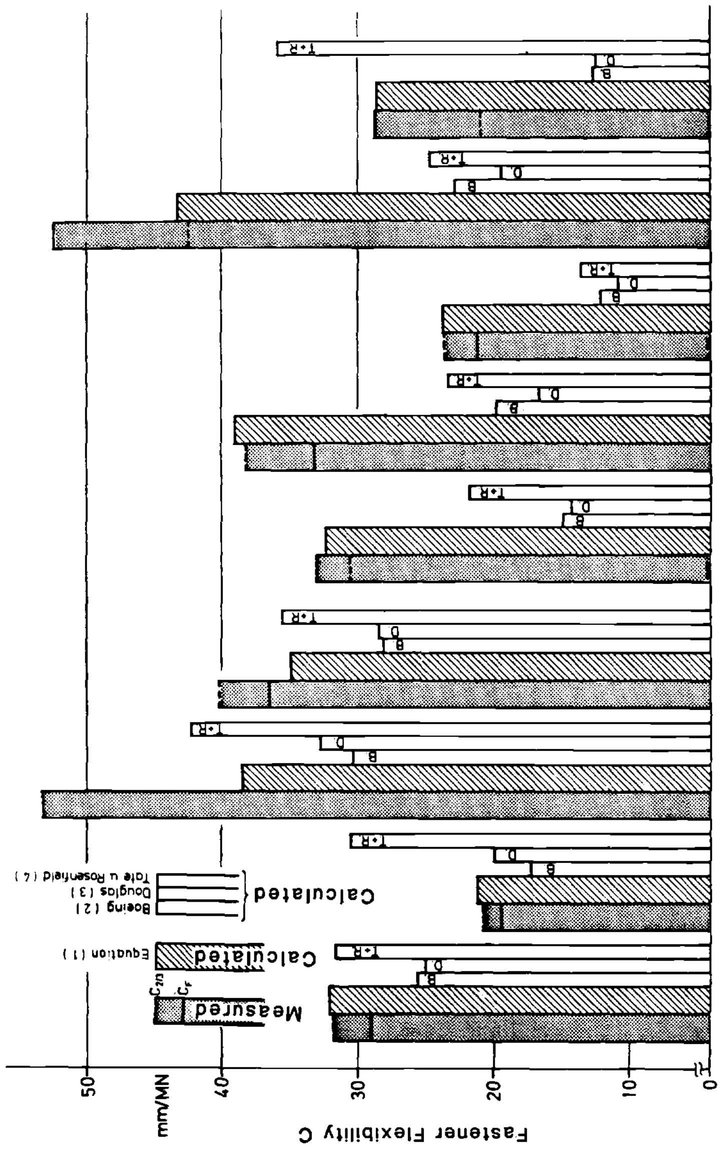

FIG. 11—*Comparison of measured and calculated fastener flexibilities for riveted metallic and bolted graphite/epoxy single-shear specimens.*

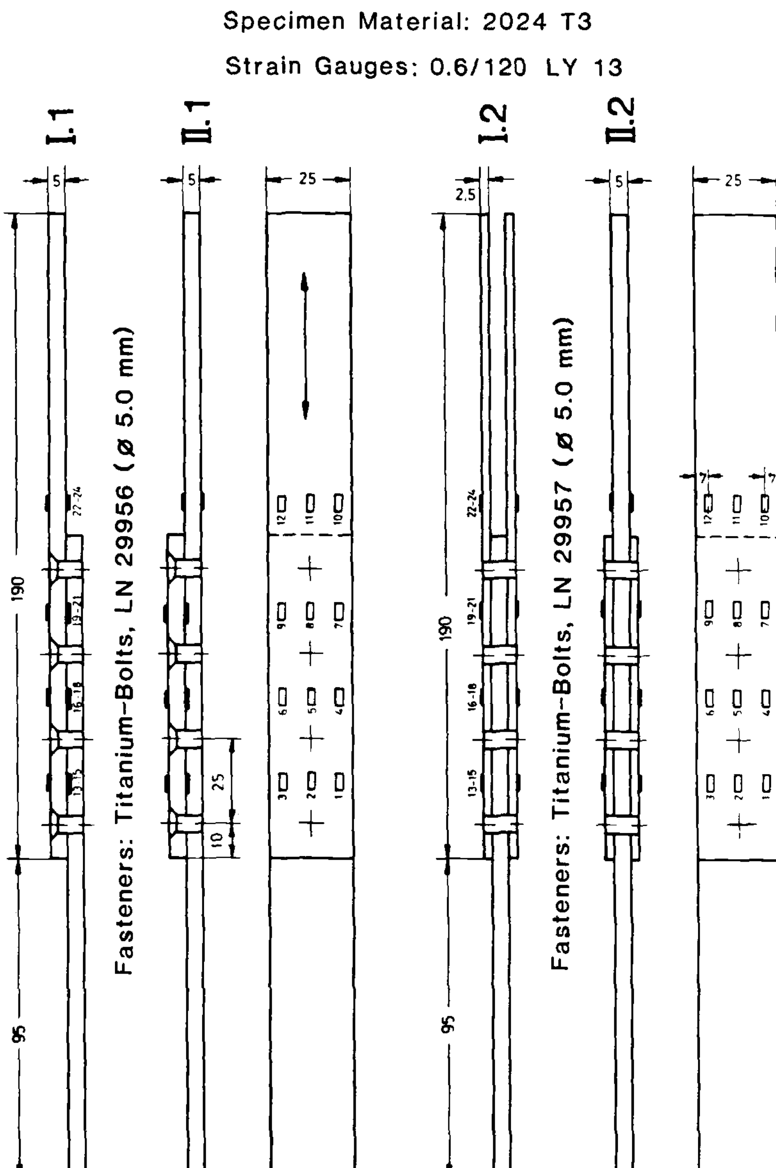

FIG. 12—*Examples of multiple-row joints used for load-transfer measurements.*

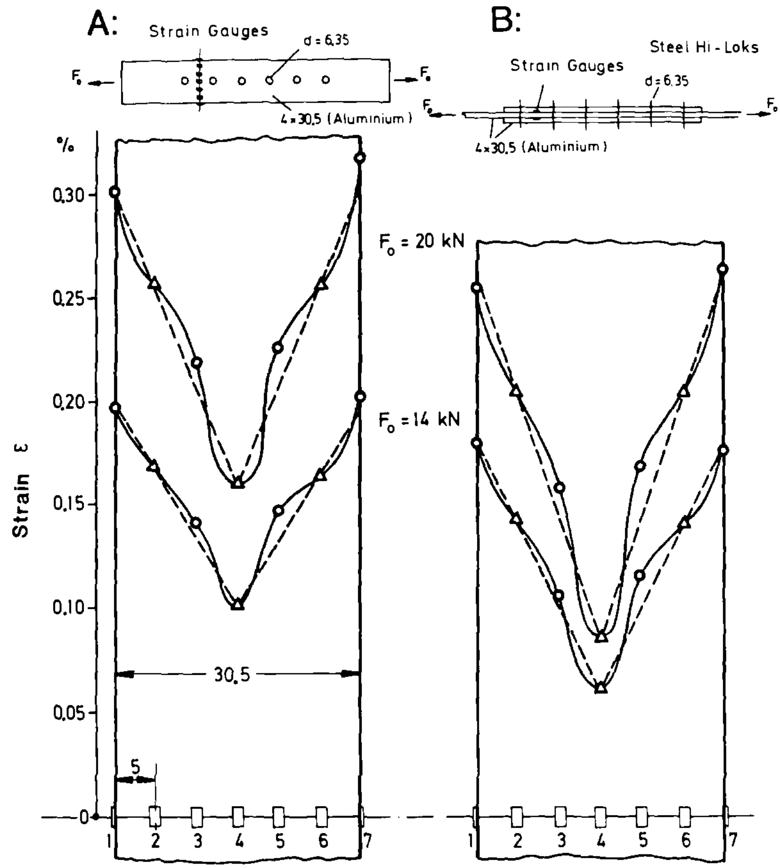

		$\bar{\varepsilon}$ [%]	S [N/mm²]	F_0 [N]
A	—— 12 Str. Gauges	0.231	161.5	19,702
	– – – 3 Str. Gauges	0.230	161.0	19,642
	from F_0/A_{Gross}	–	163.9	20,000
B	—— 12 Str. Gauges	0.1732	121.2	14,791
	– – – 3 Str. Gauges	0.1730	121.1	14,770

Δ: Recommended Strain Gauges Positions

FIG. 13—*Experimental determination of load transfer from measured strain distributions.*

nonlinear behavior. The recorded changes of slope occur at about the same level of applied load.

Taking into account the results of the fastener flexibility measurements—in particular, the changes of the hysteresis loops with increasing number of flights—the following statements about the mechanisms of load transfer can be made. The linear and unchanging correlation between the applied load and the total load transfer results from the fact that changes in frictional forces (that is, an increasing part of the load transferred by friction) are

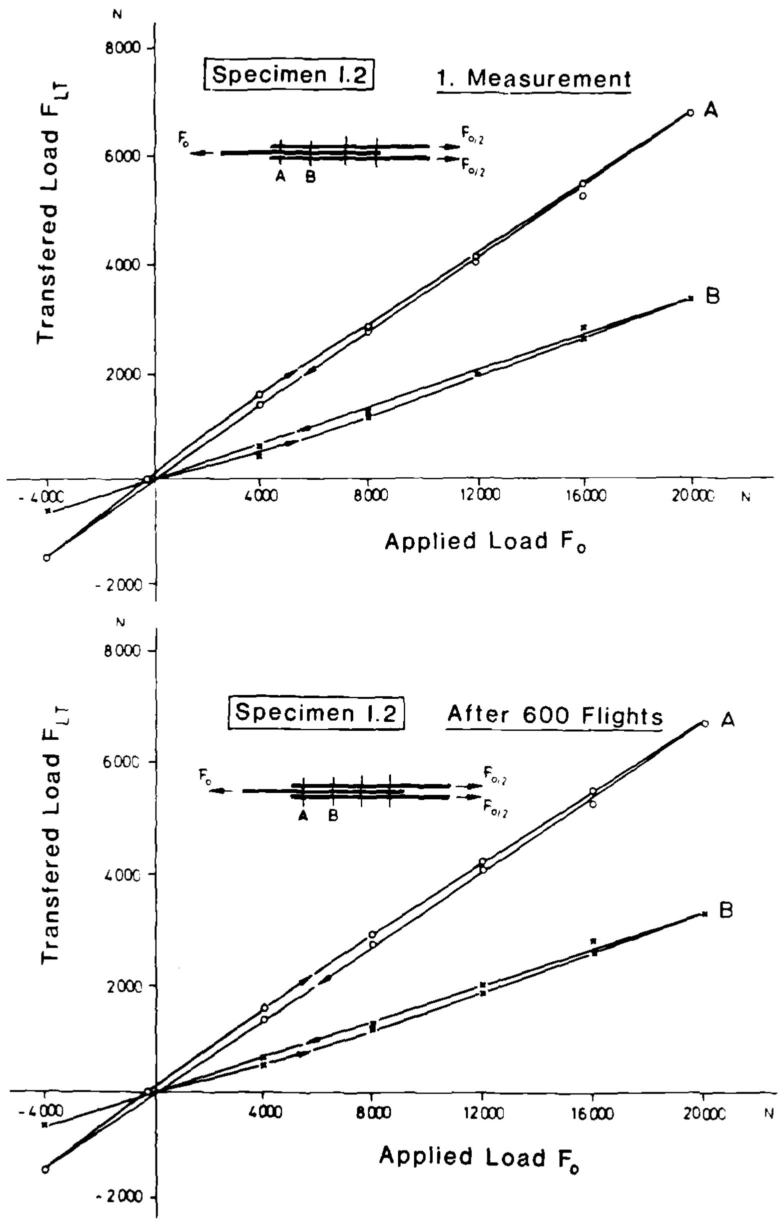

FIG. 14—*Influence of applied load and fatigue loading on the load transfer in a double-shear joint.*

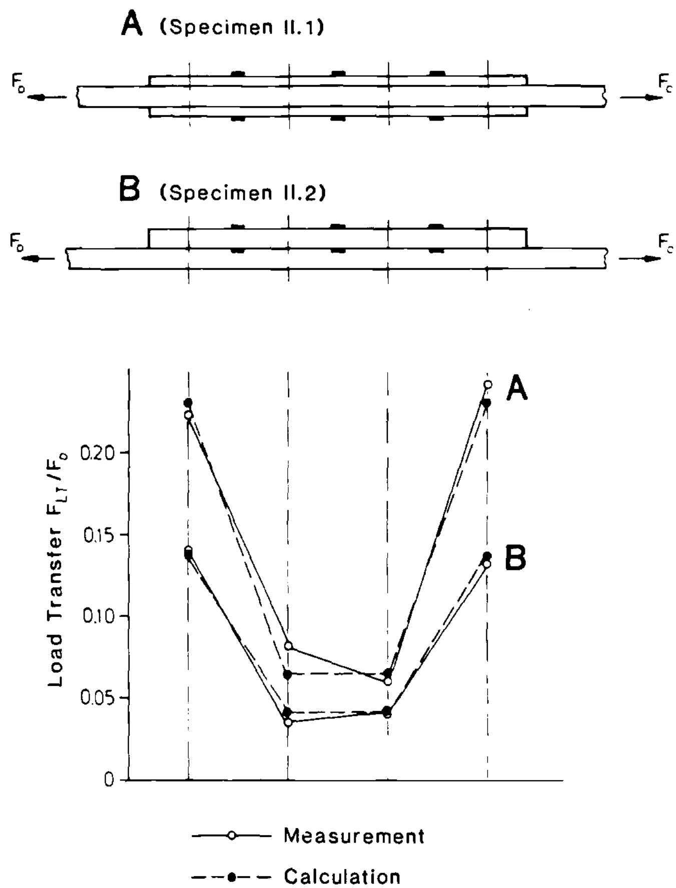

FIG. 15—*Distribution of fastener loads in four-row joints.*

accompanied by a decrease in the bearing load. This is illustrated schematically by the left sketch in Fig. 19.

Frictional forces, depending on clamping force and changing as a result of fatigue loading, also influence the notch root strains, as shown in the right sketch of Fig. 19. With increasing friction, the contribution from the bearing load to the local strain, and thus the total notch root strain, decreases. Redistributions of loads or changes in the load transfer mechanisms result in a relief of the critical volume of material at the edge of the fastener hole. Since the development and the effects of these changes cannot be predicted, the fatigue life cannot be accurately predicted using local stresses.

The following procedure is recommended for the fatigue life prediction of multiple-row joints. The distribution of fastener loads for the joint in question is to be calculated by taking into account the joint parameters and

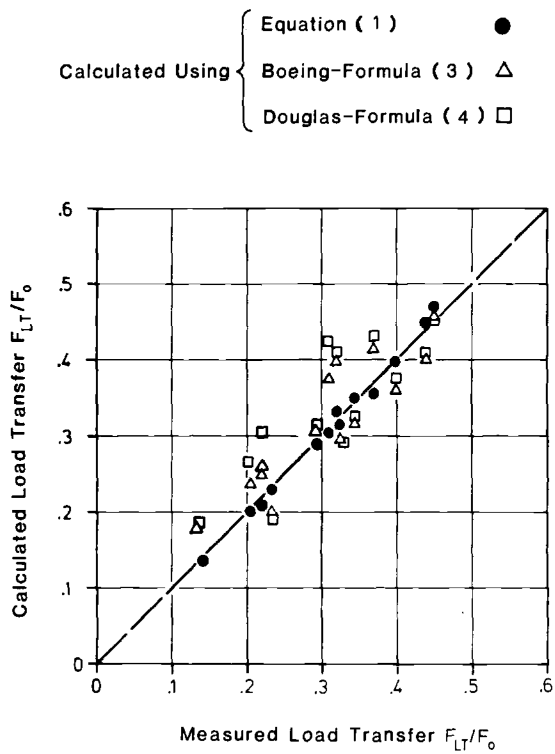

FIG. 16—*Comparison of measured and calculated load-transfer values for 13 different specimens.*

gross stresses. Then the respective stresses due to bypassing loads and the assumed bearing loads are determined. As shown before, a further calculation of local stresses or strains must be regarded as useless. More attention must be paid to the selection of the correct design data. These should be a set of life curves established for joint specimens of different load-transfer conditions and materials, using standardized flight-by-flight loading sequences. Influences on the fatigue behavior resulting from fastener installation parameters, secondary bending, the type of joint, and so on, are to be accounted for by experimentally determined correction factors. Finally, the relative miner's rule [*15*] can be used to account for the differences between the actual stress spectrum and the test spectrum of the design data.

Summary

The results of this investigation can be summarized as follows:

1. The influence of flight-by-flight loading on the deformation behavior and fastener flexibility of single- and double-shear joints is shown.

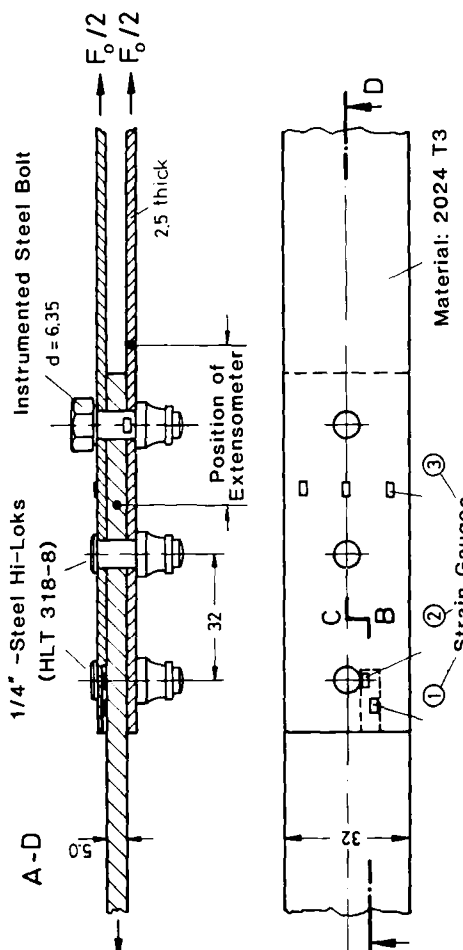

FIG. 17—*Specimen for load and deformation measurements.*

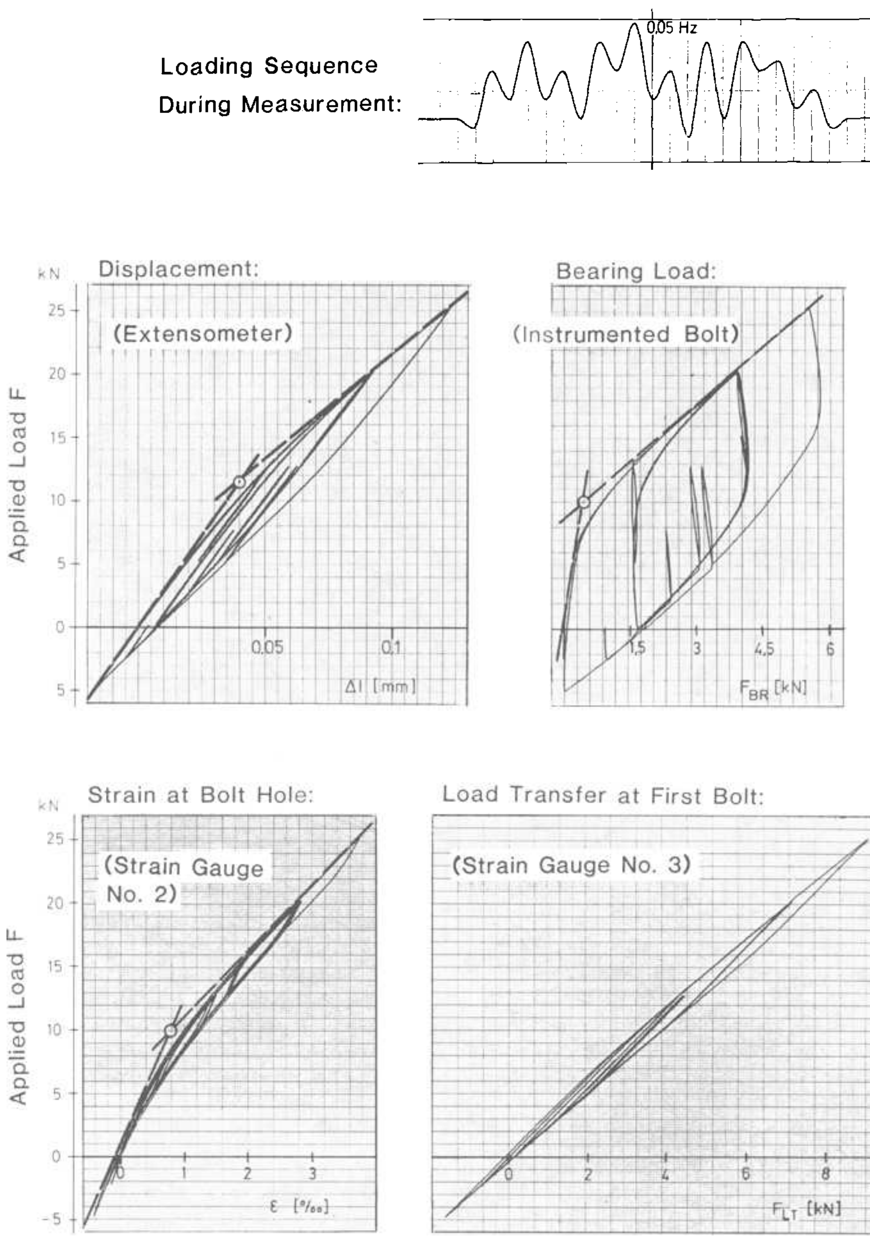

FIG. 18—*Measured loads and deformations in a double-shear joint.*

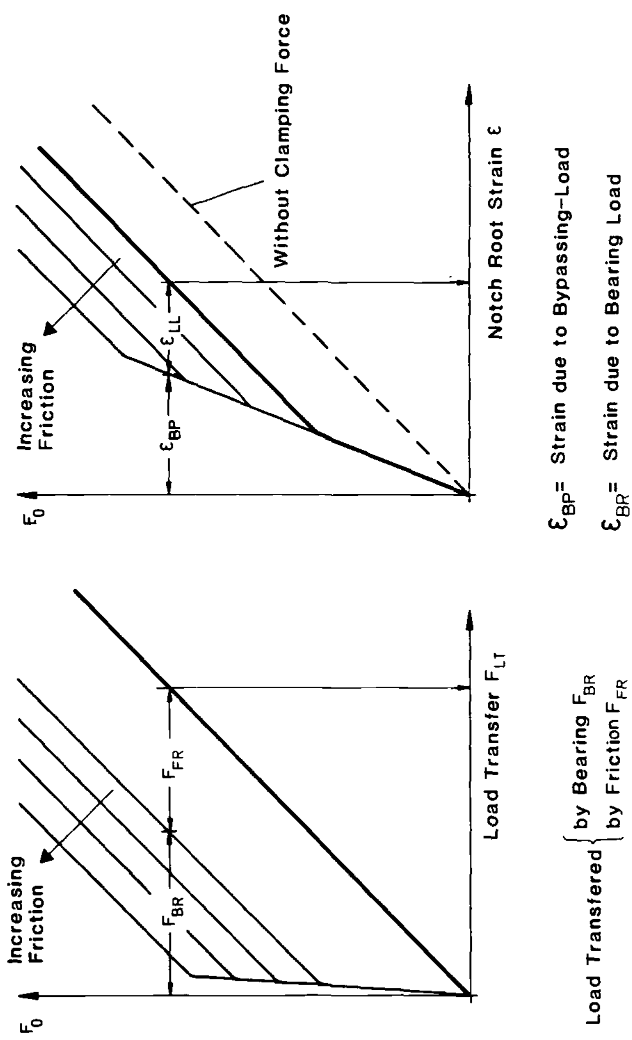

FIG. 19—*Mechanism of load transfer and its influence on notch root strain.*

2. A method for the evaluation of load-deformation curves is developed and a suitable definition of fastener flexibility to be used for loads transfer calculations of fatigue loaded joints is found.

3. For lap joints, the value of fastener flexibility can be regarded as a constant, since the total load transfer is independent of the stress level and the number of applied flights.

4. A new formula for fastener flexibility is derived. The use of this formula leads to improved load-transfer prediction and consequently also to improvements in fatigue life predictions for multiple-row joints.

5. The improved accuracy in load-transfer prediction will also have positive effects in the field of design and optimization of shear loaded joints.

6. From test results it can be concluded that the application of so-called local strain concepts for fatigue life predictions cannot be used successfully for joints.

7. The author suggests that to improve the accuracy in predicting the fatigue life of joints, fatigue data (*S-N* curves or life curves) incorporating stresses due to load transfer, bearing loads, and bypassing loads, together with a relative miner's rule, should be used.

References

[1] Bürnheim, H. "Beitrag zur Frage der Zeit- und Dauerhaltbarkeit der Nietverbindungen," dissertation, Technische Hochschule Darmstadt, Darmstadt, Germany, 1944.

[2] Jarfall, L., "Steel Bolts in Aluminum Plate: Fatigue Performance/Fastener Flexibility, FFA Report Hu-1369, Flygtekniska Försöksanstalten, Stockholm, Sweden, 1978.

[3] Franz, J. and Schütz, D., "Zur Lebensdauerabschätzung von Fügungen mit schubbeanspruchten Befestigungselementen unter Berücksichtigung der Lastübertragung," BMVg-FBWT 79-11, LBF, Darmstadt, Germany, 1979.

[4] Tate, M. B. and Rosenfeld, S. J., "Preliminary Investigation on Loads Carried by Individual Bolts in Bolted Joints," NACA TN-1051, National Advisory Committee for Aeronautics, Washington, DC, 1946.

[5] Vogt, F., "The Load Distribution in Bolted or Riveted Joints in Light-Alloy Structures," NACA Technical Memorandum No. 1135, National Advisory Committee for Aeronautics, Washington, DC, 1947.

[6] Franz, J., "Zur Spannungsanalyse von genieteten und geklebten Fügungen sowie von Sandwichplattenstreifen unter äußeren Lasten und Temperaturbeanspruchungen," LBF-Forschungsbericht FB-152, Darmstadt, Germany, 1980.

[7] Unpublished reports of the Boeing Co., Renton, WA.

[8] Barrois, W., "Stresses and Displacements Due to Load Transfer by Fasteners in Structural Assemblies," *Engineering Fracture Mechanics*, Vol. 10, Pergamon Press, 1978, pp. 115–176.

[9] Unpublished report of the Grumman Aerospace Corp.

[10] Swift, T., "Development of the Fail-Safe Design Features of the DC-10 in *Damage Tolerance in Aircraft Structures ASTM STP 486,* American Society for Testing and Materials, Philadelphia, 1971, pp. 164–214.

[11] Jarfall, L., "Review of Some Swedish Work on Fatigue of Aircraft Structures During the Period of May 1975 to April 1977," FFA Technical Note HE-1918, presented at the International Committee on Aeronautical Fatigue, Conference, Darmstadt, Germany, 1977.

[12] Jarfall, L., "Shear Loaded Fastener Installations," 12th International Committee on Aeronautical Fatigue, Symposium, Toulouse, France, 1983.

[13] Lowak, H., Schütz, D., Hück, M., and Schütz, W., "Standardisiertes Einzelflugprogramm für Kampfflugzeuge—FALSTAFF," IABG Report No. TF 568/LBF Report No. 3045, LBG, Darmstadt, Germany, 1976.
[14] Huth, H., "Zum Einfluß der Nietnachgiebigkeit mehrreihiger Nietverbindungen auf die Lastübertragungs- und Lebensdauervorhersage," LBF Report No. FB-172, dissertation, Technische Universität München, Munich, Germany, 1984.
[15] Schütz, W., "The Fatigue Life Under Three Different Load Spectra—Test and Calculations," AGARD CP-118, Symposium on Random Load Fatigue, Advisory Group for Aerospace Research and Development, Lyngby, Denmark, 1972.

Ramaswamy L. Ramkumar[1] *and Eric W. Tossavainen*[1]

Strength and Lifetime of Bolted Laminates

REFERENCE: Ramkumar, R. L. and Tossavainen, E. W., **"Strength and Lifetime of Bolted Laminates,"** *Fatigue in Mechanically Fastened Composite and Metallic Joints, ASTM STP 927*, John M. Potter, Ed., American Society for Testing and Materials, Philadelphia, 1986, pp. 251–273.

ABSTRACT: An extensive experimental program was conducted to investigate the effects of various parameters on the strength and lifetime of bolted laminates. The tested joint specimens were composite-to-metal joints where a single fastener transferred the load from one plate to the other. The various test variables were the bolted plate geometry, laminate lay-ups, stacking sequences and thicknesses, fastener material, diameter, fastener head type (protruding or countersunk), fastener torque, joint configuration (single lap or double lap), load type (tensile or compressive under static and fatigue loading conditions), and test environment conditions (room or ambient temperature and dry; elevated temperature and wet). All the laminates were fabricated using AS1/3501-6 graphite/epoxy prepreg material.

Static tests reproduced the general trends reported in the literature for the effects of plate edge distance and plate width on the strengths of laminates and the corresponding failure modes. Constant-amplitude fatigue tests were conducted at a frequency of 10 Hz, maintaining a constant minimum-to-maximum cyclic load ratio. The effect of the maximum cyclic load amplitude, as a fraction of the corresponding static strength, on the number of cycles to failure was recorded. Hysteresis plots, hole diameter, and fastener torque loss measurements were also obtained during fatigue. The obtained results complement data available in the literature.

KEY WORDS: bolted joints, composite-to-metal joints, single shear, double shear, graphite/epoxy, static tests, constant-amplitude fatigue, environmental effects, hysteresis plots, hole elongation

This paper summarizes the effects of many variables on the strength and lifetime of laminates that are bolted to metallic plates using a single fastener [*1*]. The test laminates were fabricated using nonwoven AS1/3501-6 graphite/epoxy material. Their lay-ups ranged from a highly fiber-dominated lay-up (70/20/10) to a fairly matrix-dominated lay-up (30/60/10), where the numbers in parentheses indicate the percentages of 0, ±45, and 90-deg plies in the laminate (Table 1). The laminate geometries were varied to study

[1] Engineering specialist and engineer, respectively, Northrop Corp., Aircraft Division, One Northrop Ave., Hawthorne, CA 90250.

TABLE 1—*Test laminate lay-ups.*

Laminate No.	No. of Plies	% of 0-Deg, ±45-Deg, and 90-Deg Fibers	Stacking Sequence
1	20	50/40/10	$[(45/0/-45/0)_2/0/90]_s$
2	20	70/20/10	$[45/0/-45/0_3/90/0_3]_s$
3	20	30/60/10	$[45/0/-45/0/45/90/-45/0/45/-45]_s$
4	20	50/40/10	$[0_3/\pm45/0_2/\pm45/90]_s$
5	20	70/20/10	$[0_3/\pm45/0_4/90]_s$
6	20	30/60/10	$[(\pm45)_3/0_3/90]_s$
7	20	50/40/10	$[90/\pm45_2/0_5]_s$
8	20	70/20/10	$[90/0_2/45/0_4/-45/0]_s$
9	20	30/60/10	$[0/\pm45/0/\pm45/90/\pm45/0]_s$
10	40	50/40/10	$[(45/0/-45/0)_2/0/90]_{2s}$
11	60	50/40/10	$[(45/0/-45/0)_2/0/90]_{3s}$
12	40	70/20/10	$[45/0/-45/0_3/90/0_3]_{2s}$
13	60	70/20/10	$[45/0/-45/0_3/90/0_3]_{3s}$
14	40	30/60/10	$[45/0/-45/0/45/90/-45/0/45/-45]_{2s}$
15	60	30/60/10	$[45/0/-45/0/45/90/-45/0/45/-45]_{3s}$

the effects of fastener hole diameter, D, edge distance, E, and width, W, on the laminate strength and the corresponding failure modes (Fig. 1). The metallic plates were designed to ensure colinearity of the load path in the bolted plates away from the fastener location and to preclude metal failure (Fig. 2).

Static tests were conducted under room-temperature, dry (RTD) and elevated-temperature, wet (ETW) conditions. Under compressive loading, a lateral stabilization fixture was used to prevent gross buckling of the test section. A special loading fixture was used to transfer a specified fraction of the total applied load to the fastener. A clip gage was used to measure the relative displacement of the bolted plates across the fastener (joint displacement). A plot of the applied load versus the joint displacement yielded the joint stiffness. Strain gages were mounted on selected test specimens to obtain strain data. The fastener/plate displacement was selectively recorded using a low-kilovolt radiography.

Tension-tension ($R \simeq 0$), compression-compression ($R \rightarrow -\infty$), and tension-compression ($R = -1$) constant-amplitude fatigue tests were conducted at 10 Hz. The effect of the maximum cyclic stress amplitude, and the corresponding bearing stress at the fastener location, on the number of cycles to failure was recorded. In cases where excessive hole elongation occurred, the maximum cyclic bearing stress amplitude was plotted against the number of cycles required to cause prescribed hole elongations. Hysteresis plots were generated for this purpose.

The reader is referred to Ref *1* for additional test details. The results reported in this paper are complementary to those generated in Ref *2*, and are a significant addition to the data currently available in the literature.

Static Test Results

The effect of the fastener diameter on the tensile response of a 20-ply, 50/40/10 lay-up (Laminate 1 in Table 1) is presented in Fig. 3. The composite-to-aluminum load transfer was effected by protruding head steel fasteners, in a single-lap configuration, under RTD conditions. It is apparent that the gross tensile strength and the bearing strength of the laminate decrease when the fastener diameter is increased. A similar trend is also observed under static compression.

The effect of specimen width (W/D ratio) on the tensile response of a 50/40/10 lay-up (Laminate 1 in Table 1) with $E/D = 3$ is shown in Fig. 4. The load, P, at failure and the bearing strength increase as W/D increases from a small value to approximately six. Beyond $W/D = 6$, the bearing strength remains relatively unchanged. When $W/D \leq 4$, the failure mode is primarily a net section failure across the hole (Mode 7 in Fig. 5). For $W/D > 4$, the failure mode is primarily a partial or a total shear-out of the laminate (Modes 1 or 2 in Fig. 5). Similar results are obtained for the 70/20/10 and 30/60/10 lay-ups (Laminates 2 and 3, respectively, in Table 1). For $W/D > 4$, the 30/60/10 laminate fails in a local bearing mode (Mode 3 in Fig. 5). Under compressive loading, the results follow the trend observed under tension (see Ref *1*). This includes tests on 70/20/10 and 30/60/10 laminates under 103°C (218°F) wet conditions.

The effect of specimen edge distance (E/D ratio) on the tensile response of 50/40/10 and 70/20/10 laminates with $W/D = 6$ is presented in Figs. 6 and 7. The results for the 30/60/10 laminate are similar to those in Fig. 6 (see Ref *1*). The bearing strength of all the lay-ups increases as E/D increases to a value of 4 or 5, beyond which the bearing strength is relatively invariant (Figs. 6 and 7). The 50/40/10 lay-up exhibits a shear-out mode of failure (Mode 1 in Fig. 5) where E/D is less than or equal to 3. For $E/D > 3$, the laminate exhibits a local bearing mode of failure (Mode 3 in Fig. 5). The 70/20/10 lay-up exhibits a total shear-out mode of failure (Mode 2 in Fig. 5) for E/D values below 5. The high percentage of 0-deg plies in this lay-up causes the shear-out mode to preempt the bearing mode of failure, observed in lay-ups with smaller percentages of 0-deg plies, when $E/D > 3$. Consequently, the increase in the shear-out area with an increase in E/D results in an increase in the bearing and gross strengths beyond $E/D = 3$. The 30/60/10 lay-up exhibits a cleavage type of failure (Mode 6 in Fig. 5) when $E/D = 1.5$. But for $E/D = 3$ and 5, failure is induced by local bearing. Therefore, the bearing and gross strengths for this laminate are relatively invariant beyond $E/D = 3$.

Joint eccentricity effects are addressed by comparing single-lap test results with double-lap test results. Significant bolt bending effects could be introduced by the eccentricity in the load path in a single-lap (single-shear) test configuration. Figure 8 compares the single-lap and double-lap tension test

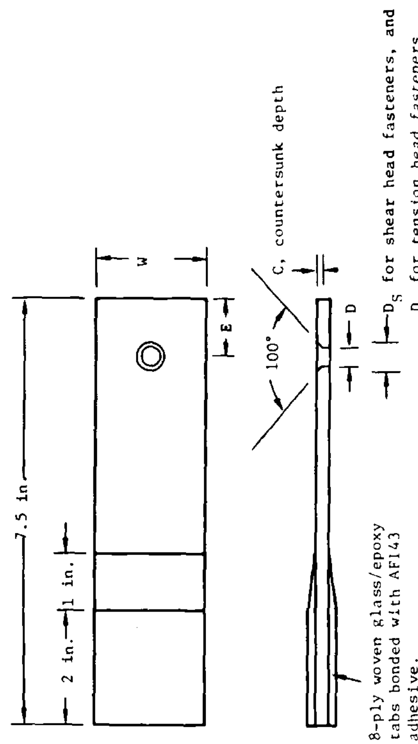
W
E
7.5 in
2 in.
1 in.
100°
C, countersunk depth
D
D_S for shear head fasteners, and
D_T for tension head fasteners
8-ply woven glass/epoxy
tabs bonded with AF143
adhesive.

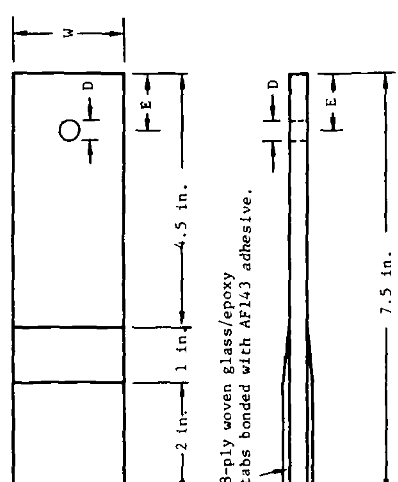
W
D
E
4.5 in.
1 in.
2 in.
7.5 in.
8-ply woven glass/epoxy
tabs bonded with AF143 adhesive.

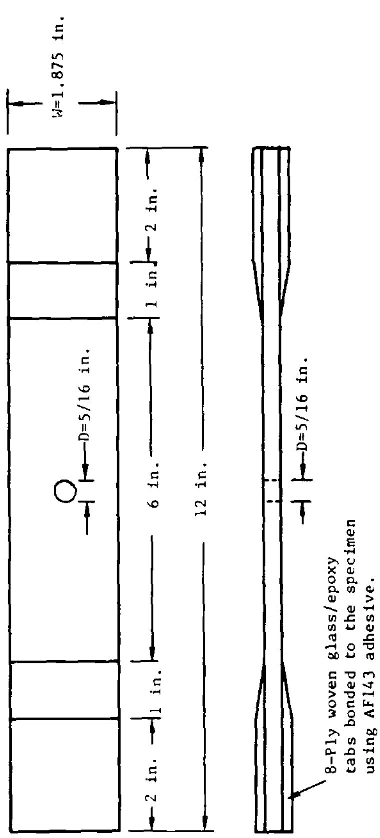

FIG. 1—*Specimen geometries for the various tests (1 ksi = 6895 MPa; 1 in. = 25.4 mm; 1 lb · in. = 0.113 N · m).*

ALUMINUM BLOCK TYPE	D	W	E	t_1	t_2	L	a
A	.250	1.500	1.8	0.31	0.73	6.60	1.8
B	.313	1.875	1.8	0.31	0.73	6.60	1.8
C	.500	3.000	1.8	0.31	0.73	6.60	1.8
D	.750	4.500	2.0	0.31	0.73	7.50	2.5
E	.313	0.625	1.8	0.31	0.73	6.60	1.8
F	.313	1.250	1.8	0.31	0.73	6.60	1.8
G	.313	2.500	1.8	0.31	0.73	6.60	1.8
H	.500	3.000	2.0	0.50	1.22	7.00	2.0
I	.750	4.500	2.5	0.68	1.69	9.00	2.5
J	.313	1.875	2.0	0.16	--	6.00	--

All dimensions in inches (in.= .0254 m)

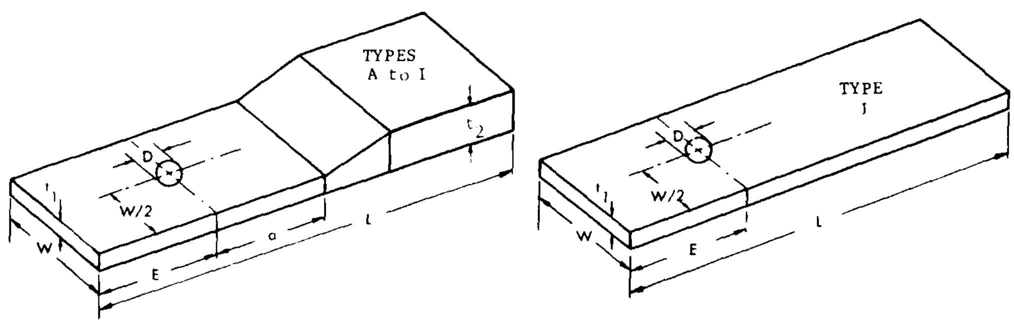

FIG. 2—*Metal plate dimensions for single- and double-shear tests (1 ksi = 6895 MPa; 1 in. = 25.4 mm; 1 lb · in. = 0.113 N · m).*

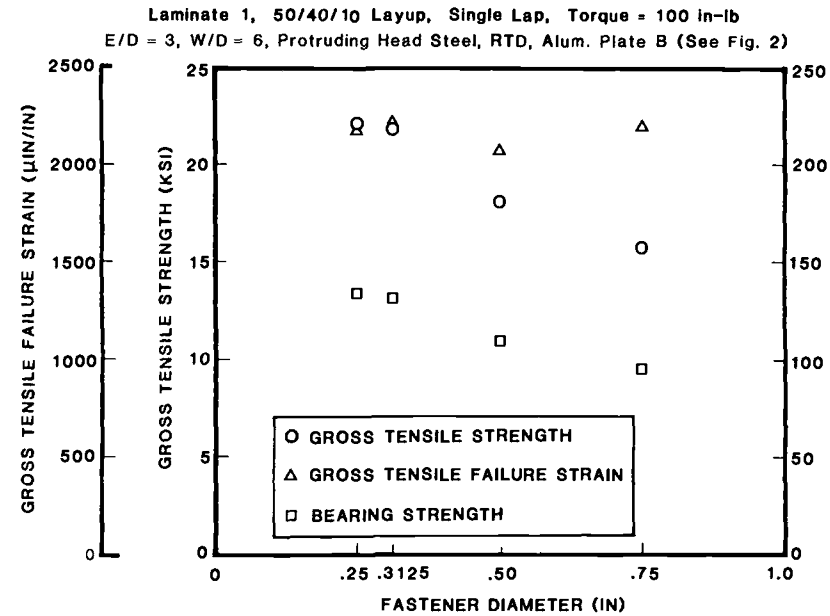

FIG. 3—*Effect of fastener size on the tensile response of 50/40/10 laminates in single shear (1 ksi = 6895 MPa; 1 in. = 25.4 mm; 1 lb · in. = 0.113 N · m).*

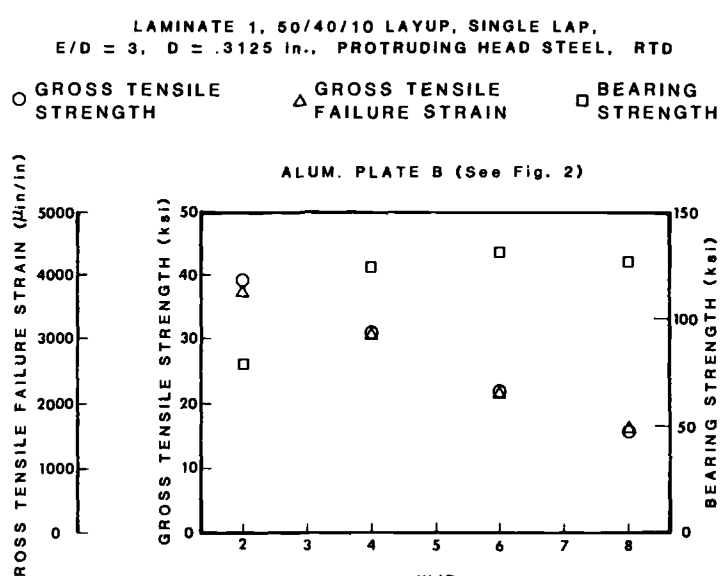

FIG. 4—*Effect of specimen width on the tensile response of 50/40/10 laminates in single shear (1 ksi = 6895 MPa; 1 in. = 25.4 mm; 1 lb · in. = 0.113 N · m).*

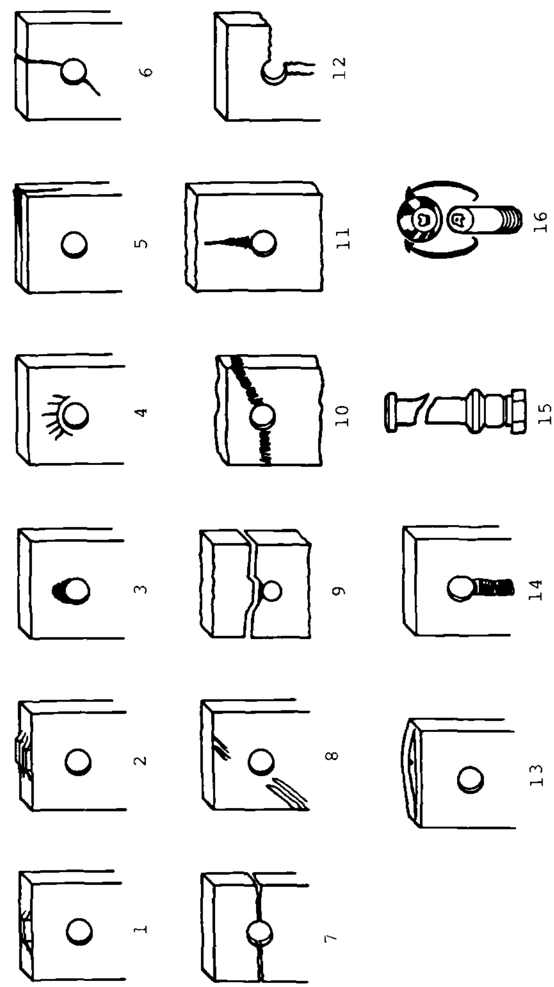

FIG. 5—*Various failure modes and corresponding mode identification numbers (see Refs 1 and 2).*

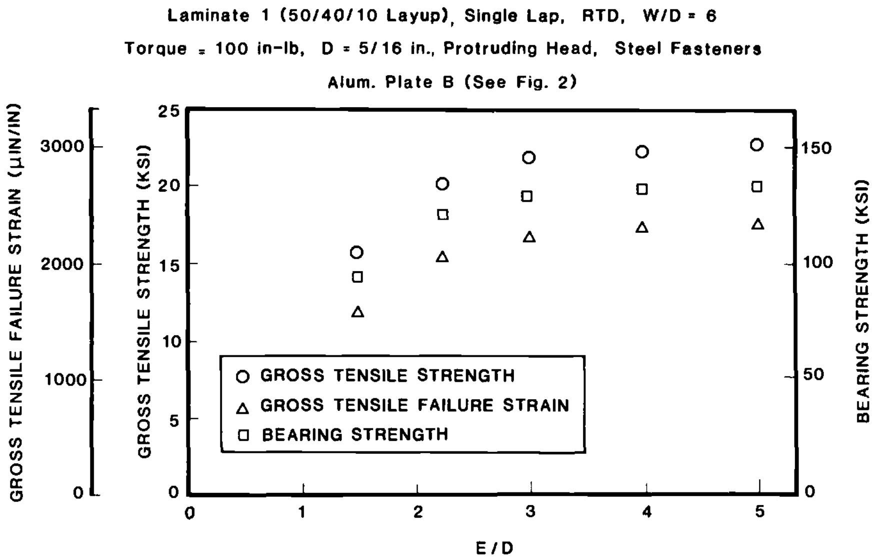

FIG. 6—*Effect of edge distance on the tensile response of Laminate 1 (1 ksi = 6895 MPa; 1 in. = 25.4 mm; 1 lb · in. = 0.113 N · m).*

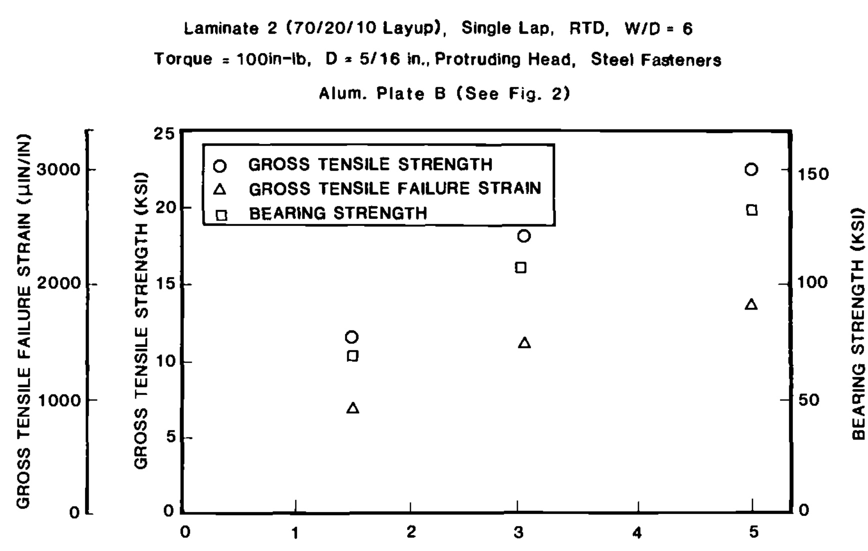

FIG. 7—*Effect of edge distance on the tensile response of Laminate 2 (1 ksi = 6895 MPa; 1 in. = 25.4 mm; 1 lb · in. = 0.113 N · m).*

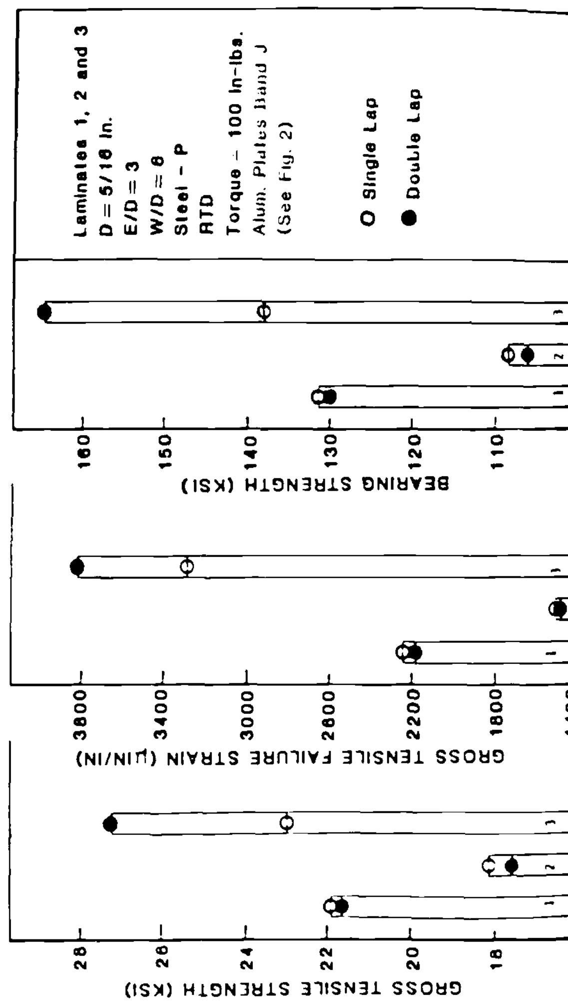

FIG. 8—*Comparison of the tensile response under single- and double-shear test configurations (1 ksi = 6895 MPa; 1 in. = 25.4 mm; 1 lb · in. = 0.113 N · m).*

results for Laminates 1, 2, and 3 (see Table 1) with $E/D = 3$, $W/D = 6$, and $D = 0.3125$ in. The large axial stiffness of the aluminum plates causes Laminates 1 and 2 to be relatively unaffected by the change from a single-shear to a symmetric double-shear test configuration. Laminate 3, on the other hand, exhibits a 17% increase in the gross tensile and bearing strengths in a double-shear configuration. The gross compressive and bearing strengths of Laminate 1 increase by approximately 20% when the test configuration changes from single shear to double shear (see Ref *1*).

An increase in the fastener torque increases the friction between the composite and metal coupons and increases the rotational constraint at the fastener head and nut locations. Consequently, an improvement in the load-carrying capacity of the joint is anticipated. Figure 9 indicates that there is very little improvement under tension for Laminate 1 in a single-shear configuration. Under compressive loading, however, the bearing strength increases by approximately 30% when the fastener torque is changed from 0 (finger-tight) to 22.6 N · m (200 lb · in.) (Fig. 10).

Three fastener materials (steel, titanium, and aluminum) were tested in the program. The fasteners were either of the protruding head type (P) or the countersunk type—the 100-deg shear head (Csk-S) and the 100-deg tension head (Csk-T). All the aluminum fasteners suffered shear and tension failures (Modes 15 and 16 in Fig. 5), and the tension head steel and titanium fasteners suffered tension failures in a single-shear configuration. Figure 11 indicates that steel fasteners yield larger strengths in comparison with ti-

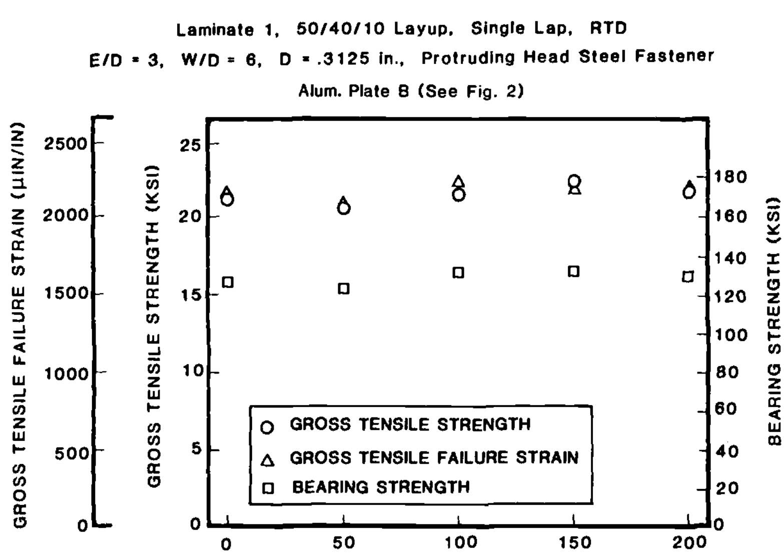

FIG. 9—*Effect of fastener torque on the tensile response of a 50/40/10 laminate in single shear (1 ksi = 6895 MPa; 1 in. = 25.4 mm; 1 lb · in. = 0.113 N · m).*

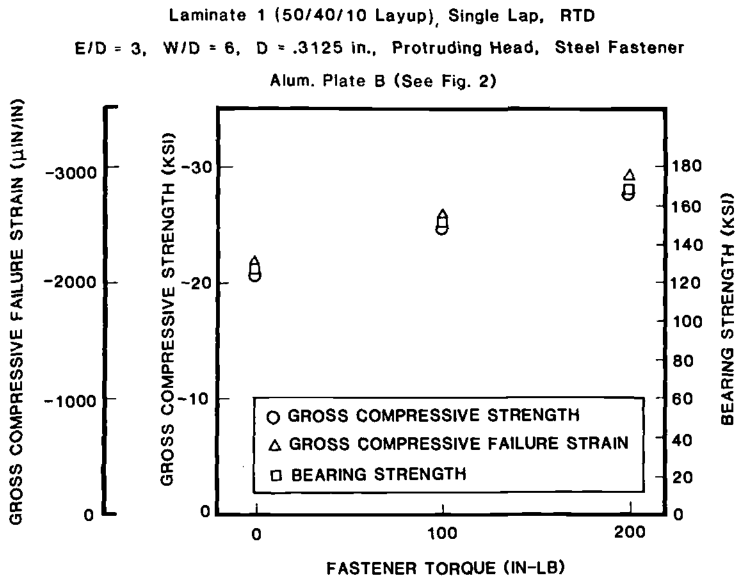

FIG. 10—*Effect of fastener torque on the compressive response of Laminate 1 (1 ksi = 6895 MPa; 1 in. = 25.4 mm; 1 lb · in. = 0.113 N · m).*

tanium fasteners, and protruding head fasteners yield larger strengths than 100-deg tension head fasteners, which yield larger strengths than 100-deg shear head fasteners.

Selected test specimens were preconditioned to absorb near-equilibrium level moisture under 95% relative humidity conditions and were subsequently tested under room temperature RTW or 103°C (218°F) conditions. Figure 12 indicates that the RTW and 103°C (wet) strengths are lower than the RTD strengths. Similar results were obtained under compressive loading (see Ref *1*).

Figure 13 presents the effect of changing the stacking sequence on the tensile response of 20-ply, 50/40/10 lay-ups. Grouping together all the 0, ±45, and 90-deg plies (Laminate 7 in Table 1) causes a loss in the gross tensile and bearing strengths that is approximately 10%. Similar results were obtained for 70/20/10 and 30/60/10 laminates (see Ref *1*).

An increase in the thickness of a laminate in a single-lap configuration introduces additional load eccentricity and bolt flexibility effects. Reference *1* contains results from tests on 20-ply and 60-ply laminates with 50/40/10 lay-ups. The thicker laminate yields strength values that are approximately 5% lower than those for the 20-ply laminates.

A summary of the effect of laminate lay-up (percentages of 0, ±45, and 90-deg plies) on the tensile and compressive response of 20-ply laminates in single shear is presented in Figs. 14 and 15, respectively. In every case, the percentage of 90-deg plies is maintained to be 10%. Under tensile

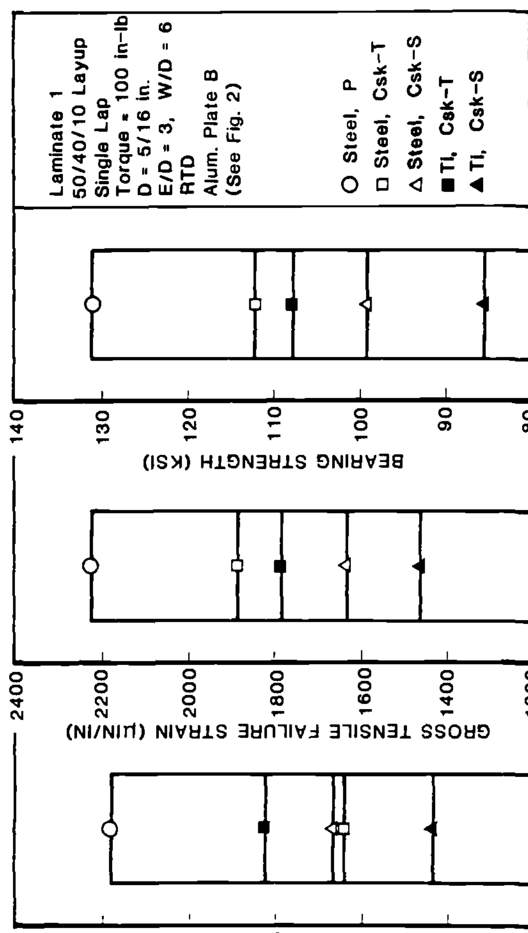

FIG. 11—*Effect of fastener material and countersink on the tensile response of Laminate 1 (1 ksi = 6895 MPa; 1 in. = 25.4 mm; 1 lb · in. = 0.113 N · m).*

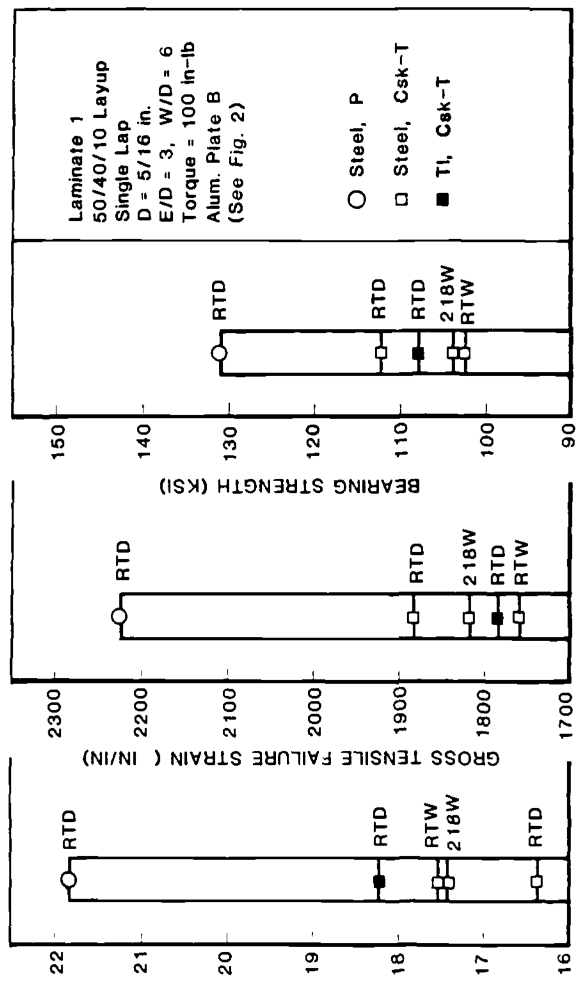

FIG. 12—*Effect of environment on the tensile response of Laminate 1 (1 ksi = 6895 MPa; 1 in. = 25.4 mm; 1 lb · in. = 0.113 N · m).*

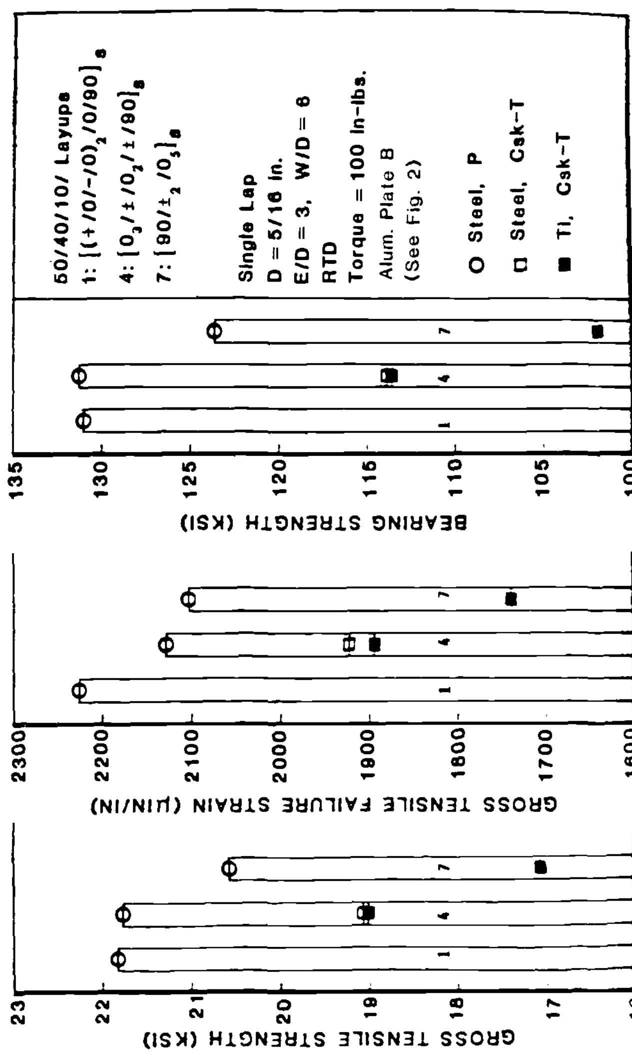

FIG. 13—*Effect of stacking sequence on the tensile response of 50/40/10 laminates in single shear (1 ksi = 6895 MPa; 1 in. = 25.4 mm; 1 lb · in. = 0.113 N · m).*

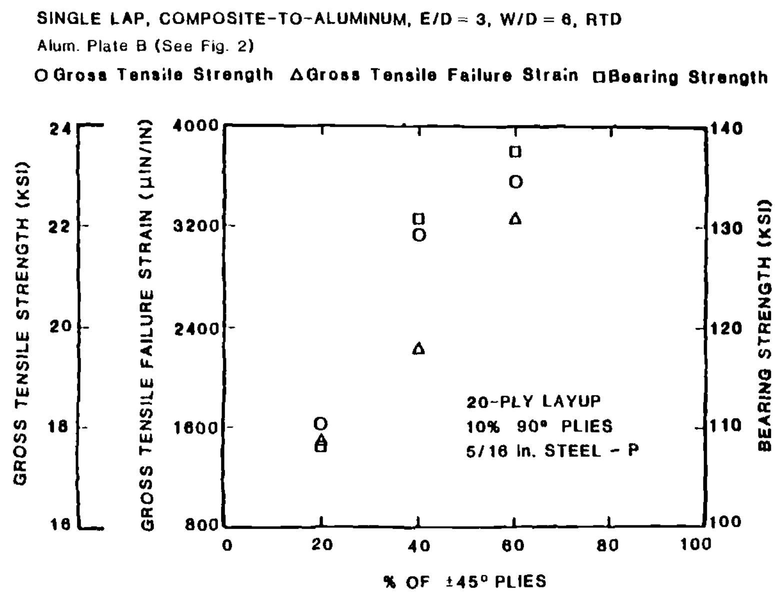

FIG. 14—*Effect of laminate lay-up on the tensile response of 20-ply laminates in single shear (1 ksi = 6895 MPa; 1 in. = 25.4 mm; 1 lb · in. = 0.113 N · m).*

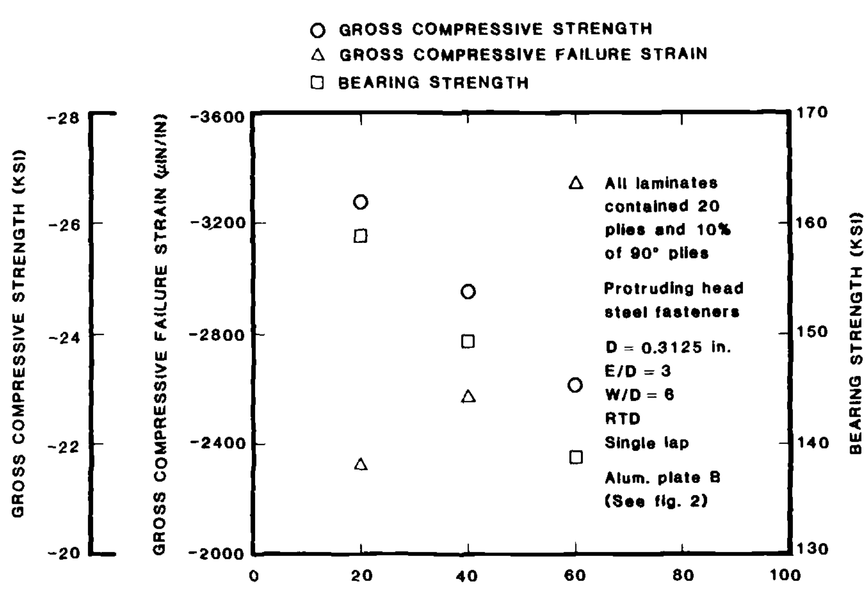

FIG. 15—*Effect of lay-up on the compressive response of 20-ply laminates (1 ksi = 6895 MPa; 1 in. = 25.4 mm; 1 lb · in. = 0.113 N · m).*

loading, the strengths increase with the percentage of ±45-deg plies. For 20 and 40% of ±45-deg plies, failure is induced by shear-out. For 60% of ±45-deg plies, failure is induced by local bearing. Under compressive loading, E/D has no effect on the failure mode or the strength of the laminates. In this case, all the lay-ups fail in a local bearing mode, and the strengths decrease with an increase in the percentage of the ±45-deg plies (Fig. 15). When other failures are precluded, the bearing strength increases with an increase in the percentage of 0-deg plies.

The results discussed above correspond to full-bearing situations in which the total applied load is transferred from one member to another via a fastener. In practical bolted structures, an isolated fastener location is generally subjected to in-plane loads on either side of the fastener. In this case, the fastener load is the difference between the magnitudes of the load on either side of the fastener, to satisfy equilibrium requirements. To simulate this situation in single fastener tests, a special loading fixture was used in the program (see Ref *1*).

The effect of the bolt bearing stress on the gross tensile strength of Laminate 1 is presented in Fig. 16. The gross tensile strength and the failure

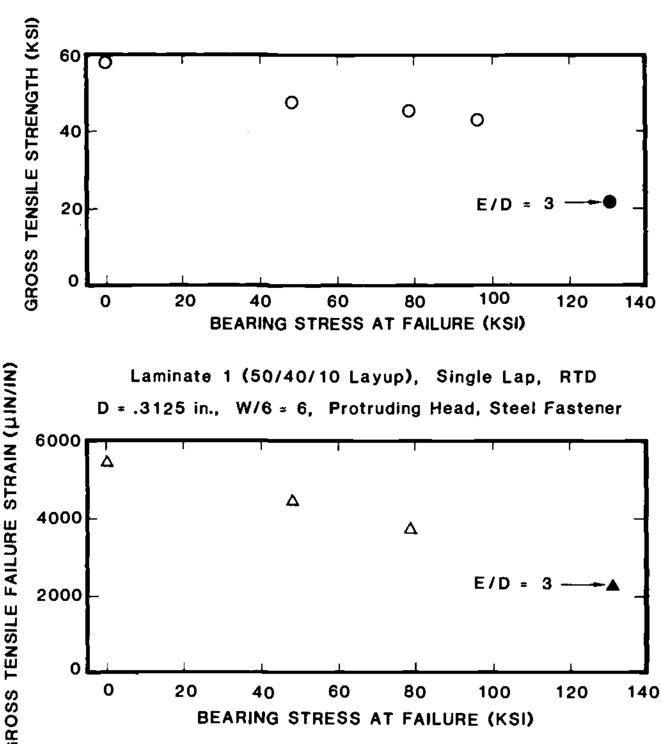

FIG. 16—*Interaction between the gross tensile strength or failure strain and the bearing stress at failure for Laminate 1 (1 ksi = 6895 MPa; 1 in. = 25.4 mm; 1 lb · in. = 0.113 N · m).*

strain decrease when the fastener bearing stress is increased from 0 to nearly 690 MPa (100 ksi). This corresponds to a variation in the bolt-to-total-load ratio from 0 to nearly 0.375. A net section failure occurs in Laminates 1 and 3 when bolt loads are up to 0.375 times the total load. In Laminate 2, the failure mode switches from the net section to the local bearing when the bolt-to-total-load ratio increases from 0.287 to 0.375 (see Ref *1*). The bearing mode of failure determines the maximum value for the fastener load. Figure 16 indicates that the gross tensile strength may be assumed to decrease in a linear fashion with the bearing stress until the failure mode switches from the net section to the local bearing. Results from the full-bearing tests are also included in the figures (identified by points with $E/D = 3$).

The effect of compressive loading on the interaction between the gross strength and the bolt bearing stress, for Laminate 1, is shown in Fig. 17. The gross strength is relatively unchanged when the bolt bearing stress is

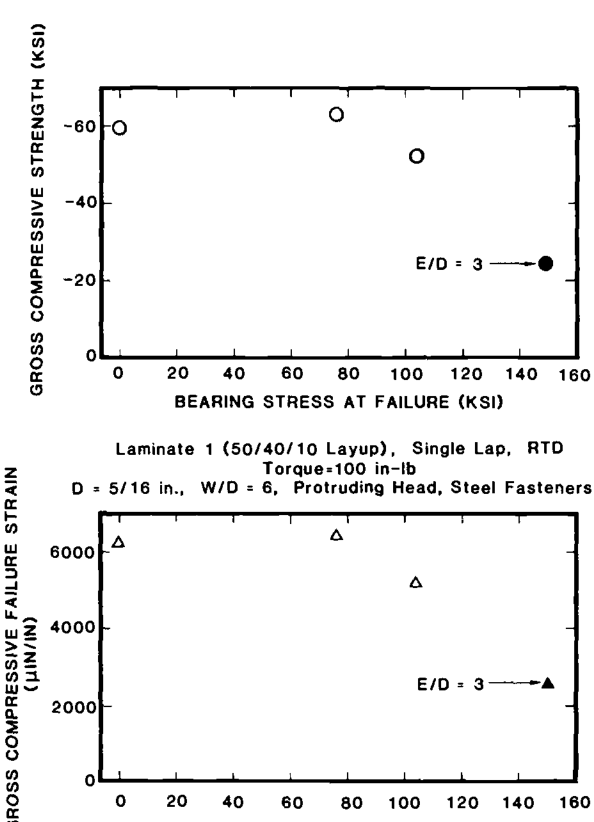

FIG. 17—*Interaction between the gross compressive strength or failure strain and the bearing stress at failure for Laminate 1 (1 ksi = 6895 MPa; 1 in. = 25.4 mm; 1 lb · in. = 0.113 N · m).*

below 557 MPa (80 ksi) for Laminates 1 and 2, and below 414 MPa (60 ksi) for Laminate 3 (see Ref *1*). Beyond this bearing stress value, the gross strength decreases until the failure mode switches from the net section to the local bearing. Net section failure occurs in Laminates 1 and 2 for bolt-to-total-load ratios below 0.33. In Laminate 3, local bearing failure occurs at a bolt-to-total-load ratio of 0.33, and net section failure occurs at lower values (see Ref *1*).

The negligible effect of bolt bearing stresses [below 414 to 557 MPa (60 to 80 ksi) in magnitude] on the gross compressive strength of laminates is believed to be due to the reduced local stress concentrations that result when the fastener provides an effective load path in the plane of the laminate. In contrast, bolt bearing stresses increase the stress concentrations at the fastener location under tensile loading.

Fatigue Test Results

Constant-amplitude fatigue tests were conducted at a frequency of 10 Hz. The minimum-to-maximum cyclic stress ratio, R, was selected to be zero for tension-tension fatigue, $-\infty$ for compression-compression fatigue, and -1 for fully reversed tension-compression fatigue tests. Unless otherwise specified, fatigue tests were conducted with 7.9-mm-diameter (5⁄16-in.), protruding-head, steel fasteners, torqued to 11.3 N · m (100 lb · in.), under RTD conditions. The composite specimens had E/D and W/D values of 3 and 6, respectively, and were bolted to aluminum plates in a single-lap configuration. During fatigue, hysteresis curves were generated, and hole elongation data were obtained from these curves.

Specimens that failed within a million cycles of the imposed loading were assumed to have suffered fatigue failure. In cases where fatigue failure was induced by hole elongation, the number of cycles to failure was dependent on the extent of hole elongation. Specimens that survived a million cycles of the imposed loading were referred to as "run-out" specimens.

Tension-tension ($R = 0$) fatigue tests on composite-to-metal joints yield the results shown in Fig. 18. Tests on composite-to-aluminum joints resulted in net section fatigue failures in the aluminum plates. Subsequently, aluminum was replaced by steel, and the results in Fig. 18 were obtained. Fatigue failures correspond to partial or total shear-out failures in the composite part, with negligible bearing-induced hole elongation. Tension-tension fatigue has a negligible effect on the lifetime of 50/40/10 laminates bolted to steel plates in a single-lap configuration. Maximum cyclic bearing stresses below 90% of the static bearing strength result in a "run-out" situation. Similar results have been reported by others for tests in a double-lap configuration (see Ref *2*).

In the fully reversed ($R = -1$) fatigue situation, failures are induced by local bearing and excessive hole elongation. Hole elongation is computed

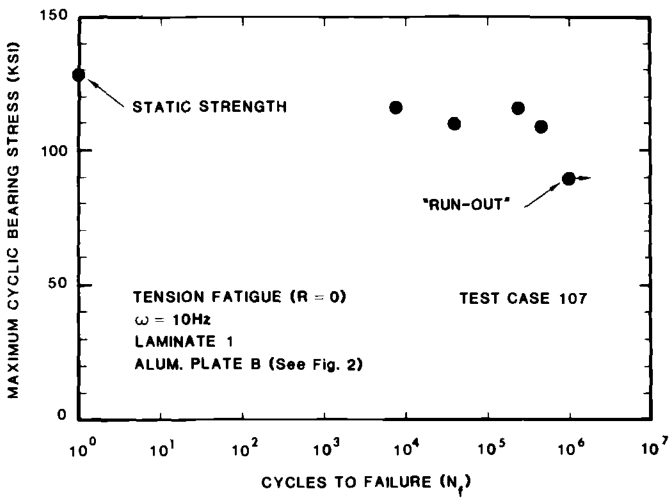

FIG. 18—*Effect of tension fatigue* (R = *0*) *on Laminate 1 in single shear* (*1 ksi = 6895 MPa; 1 in. = 25.4 mm; 1 lb · in. = 0.113 N · m*).

as a percentage of the original hole diameter, and its variation with the number of fatigue cycles is dependent on the imposed cyclic bearing stress. Figure 19 presents the variation of hole elongation with fatigue cycles when 50/40/10 laminates are bolted to aluminum. The different curves in Fig. 19 correspond to different maximum cyclic bearing stress values. The results in Fig. 19 are used to generate Fig. 20, which plots the maximum cyclic

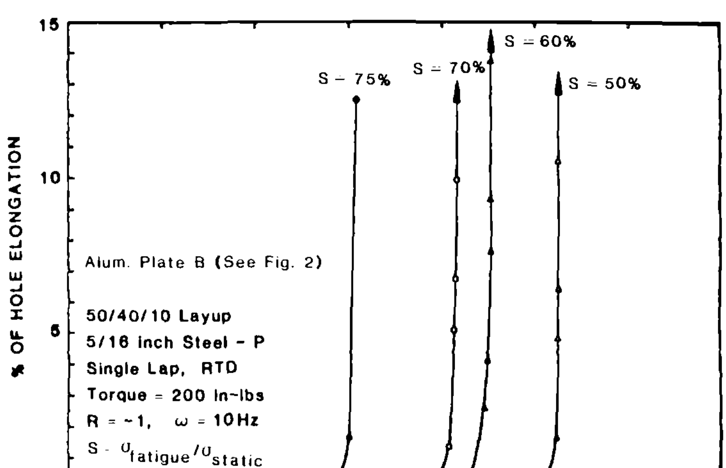

FIG. 19—*Effect of maximum cyclic bearing stress on the hole elongation rate for Laminate 1 under* R = *−1 loading* (*1 ksi = 6895 MPa; 1 in. = 25.4 mm; 1 lb · in. = 0.113 N · m*).

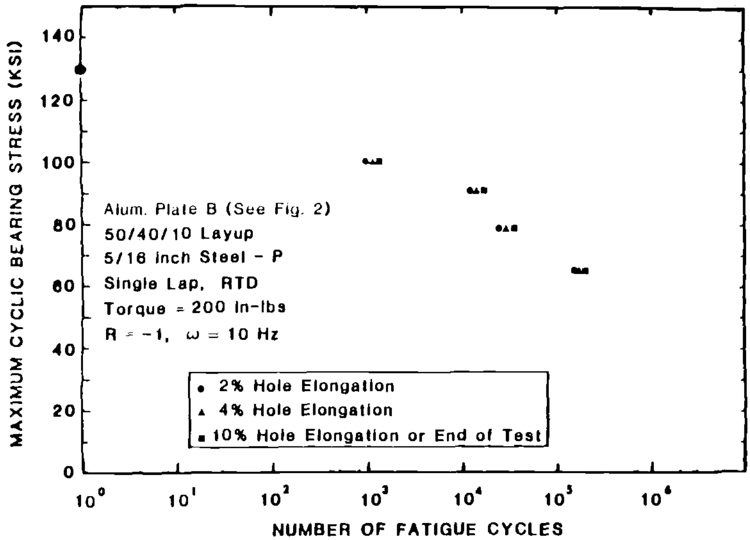

FIG. 20—*Effect of maximum cyclic bearing stress on the number of* R = −*1 fatigue cycles needed to cause specified hole elongations in Laminate 1 (1 ksi = 6895 MPa; 1 in. = 25.4 mm; 1 lb · in. = 0.113 N · m).*

bearing stress versus the number of fatigue cycles required to induce 2, 4, and 10% (end-of-test value) of hole elongation in 50/40/10 laminates. Figures 19 and 20 indicate that hole elongation increases abruptly beyond 1 to 2%. Or, once the bearing mode of failure is precipitated, hole elongation increases from a low value (1 to 2%) to a prohibitive value (<10%) within a few cycles. When a reversed ($R = -1$) cyclic load is applied in a load-controlled test setup, cyclic impulse loads are imposed on diametrically opposite hole locations. This worsens with hole elongation, resulting in the accelerated hole elongation rates beyond 1 to 2%.

Compression fatigue ($R \rightarrow -\infty$) tests on composite-to-aluminum single-lap joints yielded the results presented in Fig. 21. When the maximum cyclic bearing stress value is below 85% of the static bearing strength, the 50/40/10 laminate does not suffer any fatigue failure. Otherwise, fatigue failure is induced by local bearing and shear-out on the compression side of the hole.

Fully reversed ($R = -1$) fatigue tests were also conducted to quantify the effects of fastener torque and head type, environment, load eccentricity, and laminate lay-up (see Ref *1*). A comparison parameter was identified to be the threshold bearing stress, which is the maximum cyclic bearing stress value below which fatigue failures do not occur for a million cycles.

Tests corresponding to Figs. 19 and 20 were conducted at an initial fastener torque level of 22.6 N · m (200 lb · in.). Reference *1* contains results that correspond to initial torque levels of 0 and 11.3 N · m (100 lb · in.). A comparison of the three sets of results indicates that, at low torque levels,

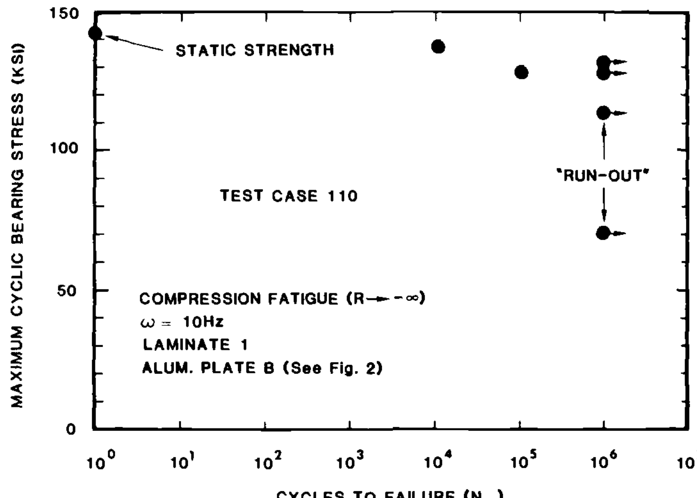

FIG. 21—*Effect of compression fatigue* (R → −∞) *on Laminate 1 in single shear* (*1 ksi = 6895 MPa; 1 in. = 25.4 mm; 1 lb · in. = 0.113 N · m*).

hole elongation increases relatively gradually, whereas at high torque levels, hole elongation change is very abrupt.

When 100-deg tension head steel fasteners replaced the protruding head steel fasteners in $R = -1$ tests on composite (50/40/10 laminate)-to-aluminum single-lap joints, some of the tension head fasteners suffered tensile failure (Mode 16 in Fig. 5). Tests in which fastener failures did not occur yielded a lower threshold bearing stress than those for protruding head fasteners. Tests attempted with 100-deg tension head titanium fasteners resulted in fastener failures (Mode 16 in Fig. 5).

On 50/40/10 laminate-to-aluminum single-lap joints, $R = -1$ tests were conducted under RTD and 103°C (wet) conditions, setting the initial torque value at 11.3 N · m (100 lb · in.). A comparison of the results (see Ref *1*) indicates that the 103°C (wet) threshold bearing stress [approximately 241 MPa (35 ksi)] is lower than the RTD value [approximately 310 MPa (45ksi)].

The effect of load eccentricity was studied by comparing single-lap and double-lap $R = -1$ test results on 50/40/10 laminates (see Ref *1*). The threshold bearing stress was determined to be approximately the same for both test configurations. The large axial stiffness of the metal plates used in the single-lap tests is believed to be the reason for this.

On 50/40/10, 70/20/10, and 30/60/10 lay-ups, (Laminates 1, 2, and 3 in Table 1, respectively), $R = -1$ tests were conducted after the lay-ups had been bolted to aluminum plates in a single-lap configuration. Protruding head steel fasteners 7.9 mm (5⁄16 in.) in diameter were used on Laminates 1 and 3, and 7.9-mm-diameter (5⁄16 in.), 100-deg tension head steel fasteners were used on Laminate 2. All the tests were conducted under RTD conditions, with an initial fastener torque of 11.3 N · m (100 lbs · in.). A comparison of the test results for the three laminates (see Ref *1*) indicates that although the static bearing strengths are different for the three lay-ups [586 to 896 MPa (85 to 130 ksi)], their million-cycle threshold bearing stress amplitudes are approximately equal [276 MPa (40 ksi)].

Conclusions

A summary of test results from Ref *1* was presented to illustrate the effects of many joint parameters on the strength and lifetime of bolted AS1/3501–6 graphite/epoxy laminates. Static test results quantified the effect of these joint parameters on the strength of various laminate lay-ups and their corresponding failure modes. Fatigue tests quantified the threshold bearing stresses under various loading conditions (*R* values). The threshold bearing stress is a fraction of the corresponding static bearing strength. Below the threshold bearing stress, fatigue failure and excessive hole elongation are precluded for a million fatigue cycles. Results presented in this paper, additional results in Ref *1*, and those available in Ref *2* provide an adequate data base to quantify the effect of significant joint parameters on the strength and lifetime of AS1/3501–6 graphite/epoxy laminates. The presented results corroborate the general design practices currently used by the industry in designing mechanically fastened laminated components. They also include data that will enable further qualification of a few existing design guidelines.

Acknowledgment

The results presented in this paper were generated in a Northrop/AFWAL program (Contract F33615-82-C-3217). The authors gratefully acknowledge the support offered by the AFWAL technical monitors Dr. V. B. Venkayya and Capt. M. Sobota.

References

[*1*] Ramkumar, R. L. and Tossavainen, E. W., "Bolted Joints in Composite Structures: Design, Analysis and Verification; Task I Test Results—Single Fastener Joints," AFWAL-TR-84-3047, Air Force Wright Aeronautical Laboratories, Wright-Patterson Air Force Base, OH, August 1984.

[*2*] Garbo, S. P. and Ogonowski, J. M., "Effect of Variances and Manufacturing Tolerances on the Design Strength and Life of Mechanically Fastened Composite Joints." Vol. 1, AFWAL-TR-81-3041, Air Force Wright Aeronautical Laboratories, Wright-Patterson Air Force Base, OH, April 1981.

P. K. Mallick,[1] *R. E. Little,*[1] *and J. W. Dunham*[1]

Fatigue of Bolted Continuous Fiber Sheet Molding Compound Composite-Metal Joints

REFERENCE: Mallick, P. K., Little, R. E., and Dunham, J. W., **"Fatigue of Bolted Continuous Fiber Sheet Molding Compound Composite-Metal Joints,"** *Fatigue in Mechanically Fastened Composite and Metallic Joints, ASTM STP 927,* John M. Potter, Ed., American Society for Testing and Materials, Philadelphia, 1986, pp. 274–288.

ABSTRACT: Load-controlled tension-tension cyclic tests on continuous fiber sheet molding compound (CSMC) composite-metal bolted joints have been performed. The test results show that both failure mode and stress-life data depend strongly on whether the width of the specimen is larger or smaller than the clamped area. Based on the observed failure modes in a single bolt pattern, a stress-life model is proposed. Limited data for multiple bolt patterns are reasonably consistent with the failure model.

KEY WORDS: continuous fiber sheet molding compound (CSMC) composites, bolted joint, specimen width, bearing damage, fretting fatigue, bolt pattern

With the concurrent development of high-fiber-content sheet molding compounds (SMC) and compression molding technology in recent years, fiber-reinforced plastic composite has become a viable alternative material in the automotive industry. However, just as in aerospace structures, the attachment of composite automotive components (either within a subassembly or to the vehicle) is still an issue of great concern. The load-carrying capacity of the composite material continues to be severely limited by the weakness at the attachment.

Although adhesive bonding is generally recognized as a better method of attachment for fiber-reinforced plastic composites, there are a great many applications where bolted joints are preferred for quick disassembly of components for inspection, repair, or replacement. In the aerospace industry, emphasis has been placed on developing new and special fastening technology to accommodate the weakness of composite-metal or composite-

[1] Associate professor, professor, and graduate student, respectively, Department of Mechanical Engineering, University of Michigan—Dearborn, Dearborn, MI 48128.

composite bolted joints. Automotive applications, on the other hand, still rely upon commercially available standard fasteners, principally because of their lower cost and easy availability.

The present work involves the first stage of a continuing study of the fatigue performance of a bolted lap joint between a steel plate and compression-molded continuous-fiber SMC composite sheet material. The bolted joint was obtained by clamping the two materials with standard toolmaker studs and nuts. The objective of this paper is to investigate the failure modes and to generate appropriate stress-life data (*S-N* curves), as influenced by clamping pressure (tightening torque) and joint dimensions.

Experimental Procedure

Material

The material used in this study is a continuous fiber sheet molding compound (CSMC) composite, commercially designated CSMC C40R30. Each ply of this material contains 40% by weight of unidirectional continuous (C) E-glass fibers in a layer with 30% by weight of randomly oriented (R) chopped (25-mm-long) E-glass fibers. The matrix is a vinyl ester resin.

Flat plates were compression molded with four plies of CSMC C40R30 molding compound. The ply stacking sequence was (CR)/(CR)/(RC)/(RC), where C represents the continuous fiber side and R represents the random fiber side of each ply. The nominal thickness for the molded plates was 3.7 mm. The resin burnoff test showed a variation in fiber distribution of between 67 and 70% by weight across the transverse (flow) direction of the molded plate. Constant-width specimens were cut in the longitudinal (0 deg) direction of the continuous fibers from these plates.

Test Method

Load-controlled tension-tension cyclic tests [maximum-to-minimum-stress ratio (R) = 0.25] were performed in a Sonntag fatigue testing machine, equipped with a 5-to-1 load multiplying fixture (Fig. 1). The frequency of cycling was 30 Hz, and no significant temperature rise was observed during cyclic testing.

The CSMC specimens, with a 6.63-mm-diameter (d) centric hole at each end (Fig. 2), were bolted to 12.7-mm-thick steel plates by means of hardened steel (toolmaker) studs and flanged nuts, forming a simple lap-type joint. As illustrated in Fig. 2*c*, the end plates were designed to make the loading axis coincide with the specimen axis so that the specimen was loaded in tension. The lever-arm effect of the 5:1 loading fixture causes a maximum slope of approximately ±0.2 deg at the bottom grip. The resulting bending effect on the specimen is negligible because of its high compliance. The diameter of the steel studs was 6.35 mm. The edge distance, e, was 25.4 mm,

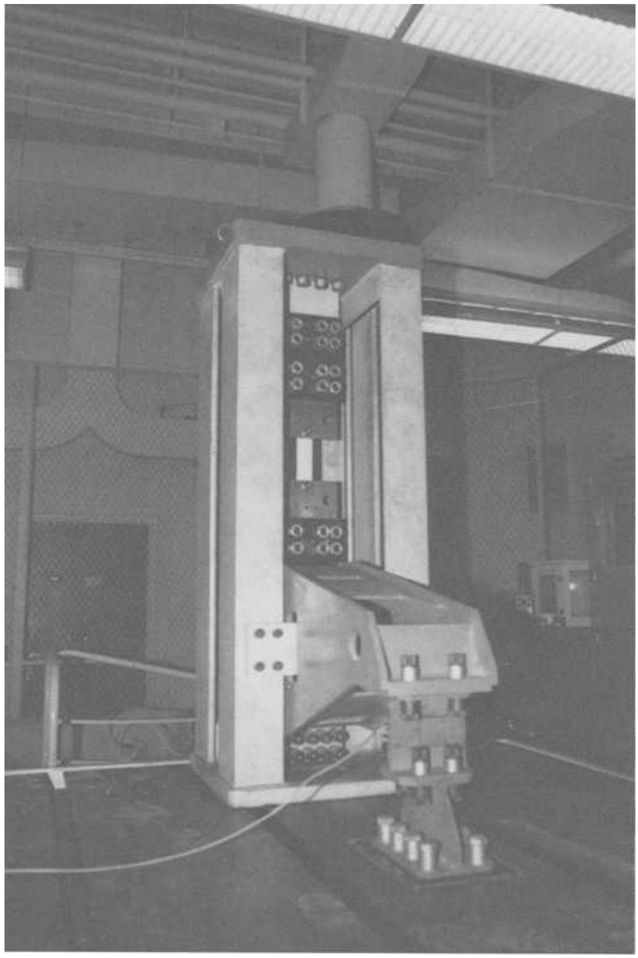

FIG. 1—*Test setup for cyclic testing of bolted joints.*

so that e/d = 3.8 for all tests. The washer diameter of the flanged nuts was 15.9 mm. The clamping pressure on the specimens was varied by tightening the nuts to two different torque levels, namely, 16.9 and 22.6 N · m. Except for a few cases, there was no significant decrease in clamping torque during the cyclic tests.

Two different groups of specimen width, w, were tested. Group I consisted of specimens wider than the washer diameter, ranging from w = 19 mm to w = 50.8 mm. In preliminary cyclic tests, it was observed that the life of the joint in these specimens was controlled by bearing failure. It was concluded from these tests that to induce fatigue failure at the joint in a reasonable short life (less than about 10^6 cycles), the net nominal tensile stress must at least equal the nominal bearing stress at the hole. To create this condition, the width of the specimen cannot be greater than twice the diameter of the hole, namely, for $d = 6.63$ mm, $w \leq 13.26$ mm. For the joint configuration involving Group II specimens, the test specimens were narrower than the washer diameter, with a width of 12.7 mm.

Results

Static Tests

The ultimate tensile strength, averaged for 13 CSMC specimens tested in the direction of continuous fibers (0 deg), was 524 MPa (75 980 psi). In conventional pin-bearing tests, bearing faiiure was observed at e/d ratios

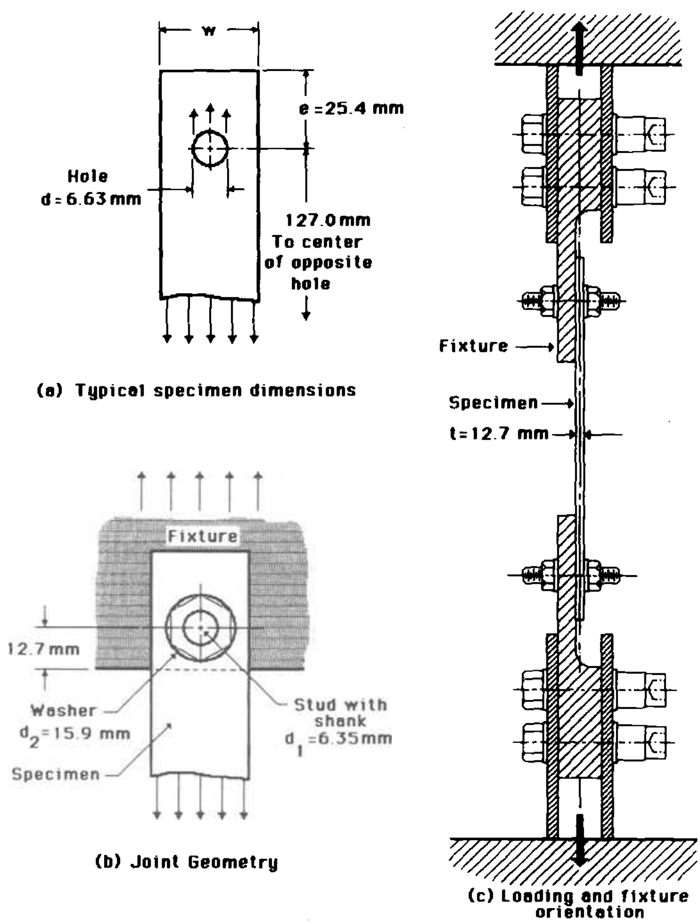

FIG. 2—*Specimen dimensions, joint geometry, and loading and fixture orientations used in the cyclic tests.*

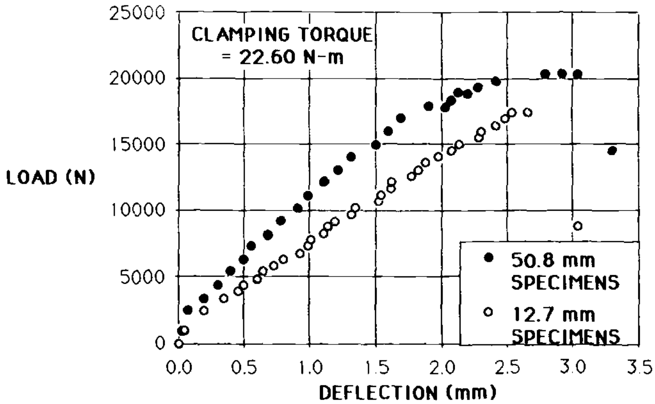

FIG. 3—*Typical load-deflection curve obtained in Sonntag static tests.*

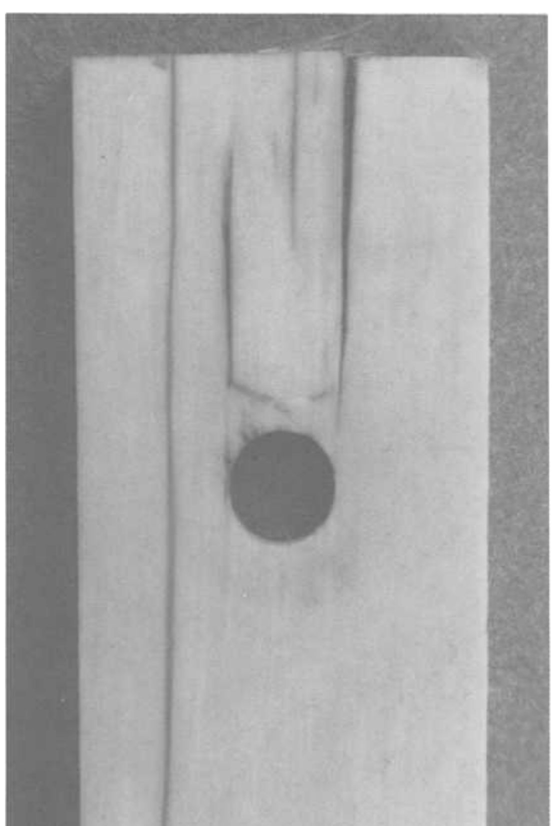

FIG. 4—*Static failure mode in Group I specimens.*

equal to or greater than 3. The average pin bearing strength, based on six 25.4-mm-wide specimens with $e/d = 3$, was 385 MPa (55 790 psi). For smaller e/d ratios, failure occurred by shear-out.

Static tests were also conducted on specimens with the joint geometry shown in Fig. 2, employing only the preloading mechanism of the Sonntag machine. Typical load-deflection diagrams obtained in these tests are shown in Fig. 3. For Group I specimens (widths larger than the washer diameter), the bearing failure was followed by shear cracks at the edges of the hole (Fig. 4). For Group II specimens (widths smaller than the washer diameter), failure was also initiated by shear cracks at the edge of the hole. At high clamping torques (11.3 N · m and higher), Group II specimens failed when the longest shear crack reached the end of the specimen (Fig. 5). At low clamping torques, however, failure in Group II specimens was caused by bearing damage.

Bearing strength is plotted in Fig. 6 as a function of clamping torque for Sonntag static test data. These data show that the bearing strength for CSMC composites increases somewhat with increasing clamping torque. Similar

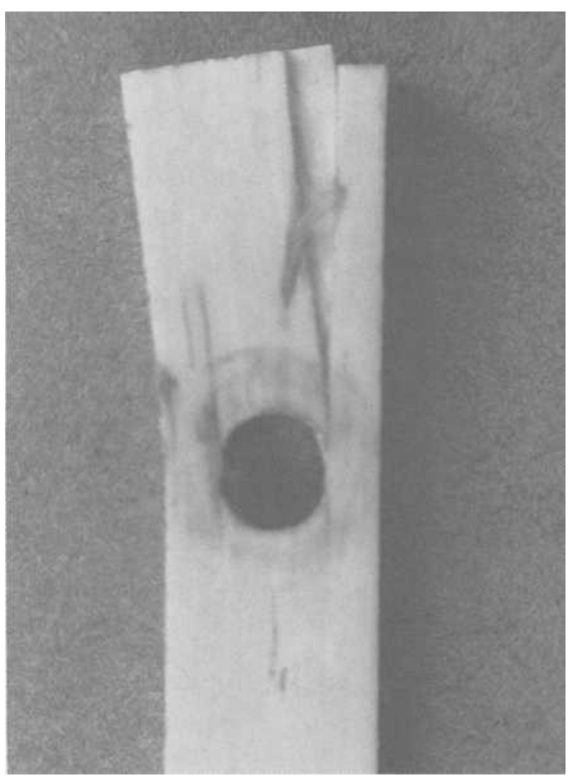

FIG. 5—*Static failure mode in Group II specimens.*

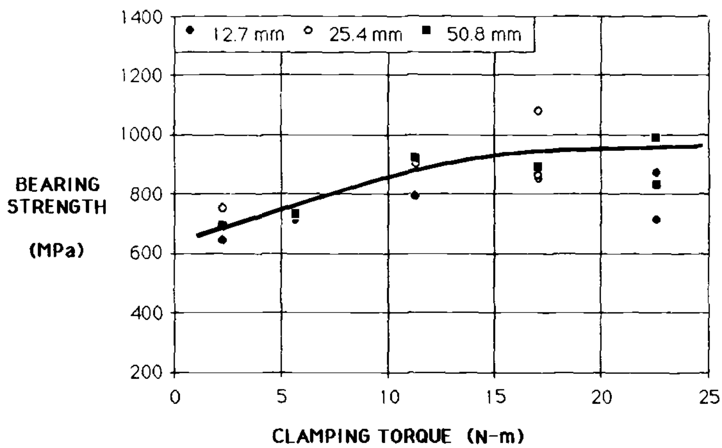

FIG. 6—*Static bearing strength versus clamping torque for CSMC-steel bolted joints.*

results were reported by Stockdale and Matthews [*1*] as well as by Crews [*2*], who attributed improved bearing strength to higher frictional resistance against slip provided by the clamping pressure.

Cyclic Tests

Failure Modes—For Group I specimens (widths larger than the washer diameter), bearing failure dominates at high maximum loads even at the higher clamping torque (22.6 N · m) (Fig. 7). Clearly, the clamping torque did not prevent axial slip of the specimen relative to the studs. These results are consistent with those of Crews [*2*], who also found that the hole elongation takes place earlier and at a greater rate as the clamping torque is reduced.

At lower maximum loads, there was no evidence of bearing failure in Group I specimens. Instead, a fatigue (tensile) crack was initiated by fretting on the faying (back) surface of the specimen (Fig. 8). This semicircular crack was located well inside the perimeter of the washer. Specimen failure resulted from the extension of this crack to the edges of the specimen. There was no evidence of crack or any other damage on the front (nut) side of the specimen.

For Group II specimens (widths smaller than the flange diameter), failure was initiated with the appearance of microscopic edge cracks near the faying (back) side of the specimen adjacent to the steel plates, schematically shown in Fig. 9*a*. These cracks were loaded in the clamped area (between the bolt hole diameter and the nut flange diameter) on the interior side of the attachment. With an increasing number of cycles, more and more edge cracks appeared and joined together to create a damage zone near the back side of the specimen (Fig. 9*b*).

This damage zone extended from the back surface to nearly the midsurface of the specimen and ended at the edge of the bolt hole. From the appearance of fretting in this damage zone, it was evident that specimen failure did not occur immediately after the formation of the damage zone. Failure started with the tensile rupture of the fibers in the remaining section of the thickness (Fig. 9*b*). However, because of high compressive stresses just underneath the flange, the crack did not run across the hole. Instead, it was diverted parallel to the fibers as it approached the front surface of the specimen. The crack emanated from the edge of the hole and progressed toward the edge of the flange, where it was diverted again to run around the periphery of the flange (Fig. 9*c*).

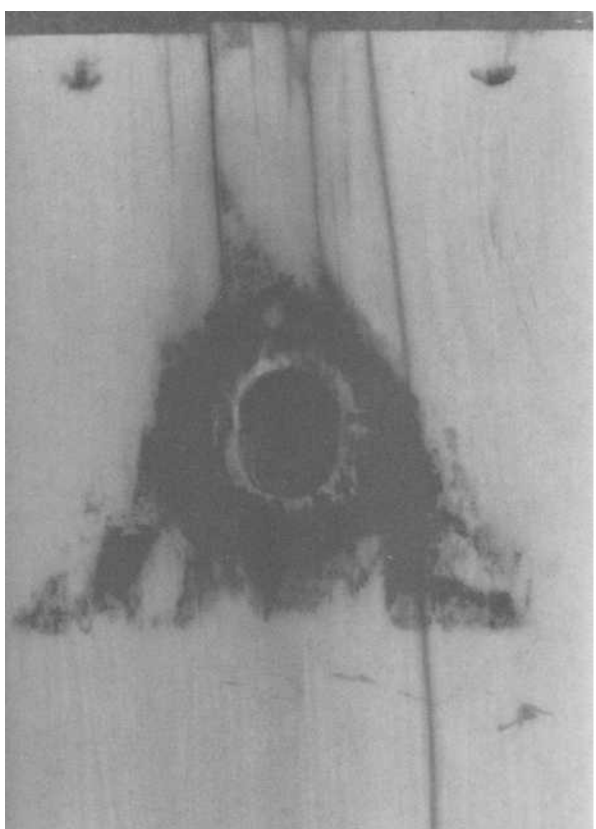

FIG. 7—*Bearing failure at high maximum loads in cyclic tests with Group I specimens.*

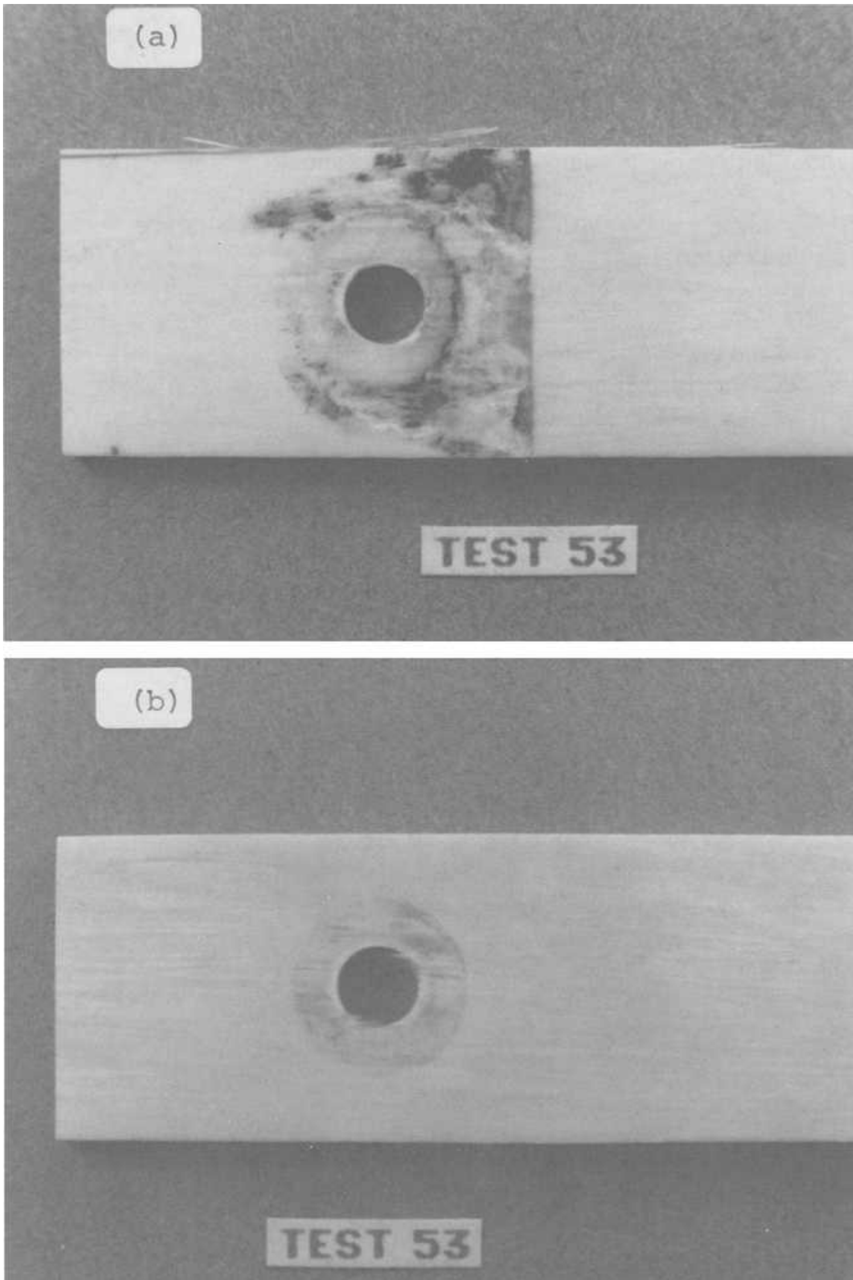

FIG. 8—*Fretting Fatigue Crack at low maximum loads in cyclic tests with Group I specimens:* (a) *faying surface,* (b) *front surface.*

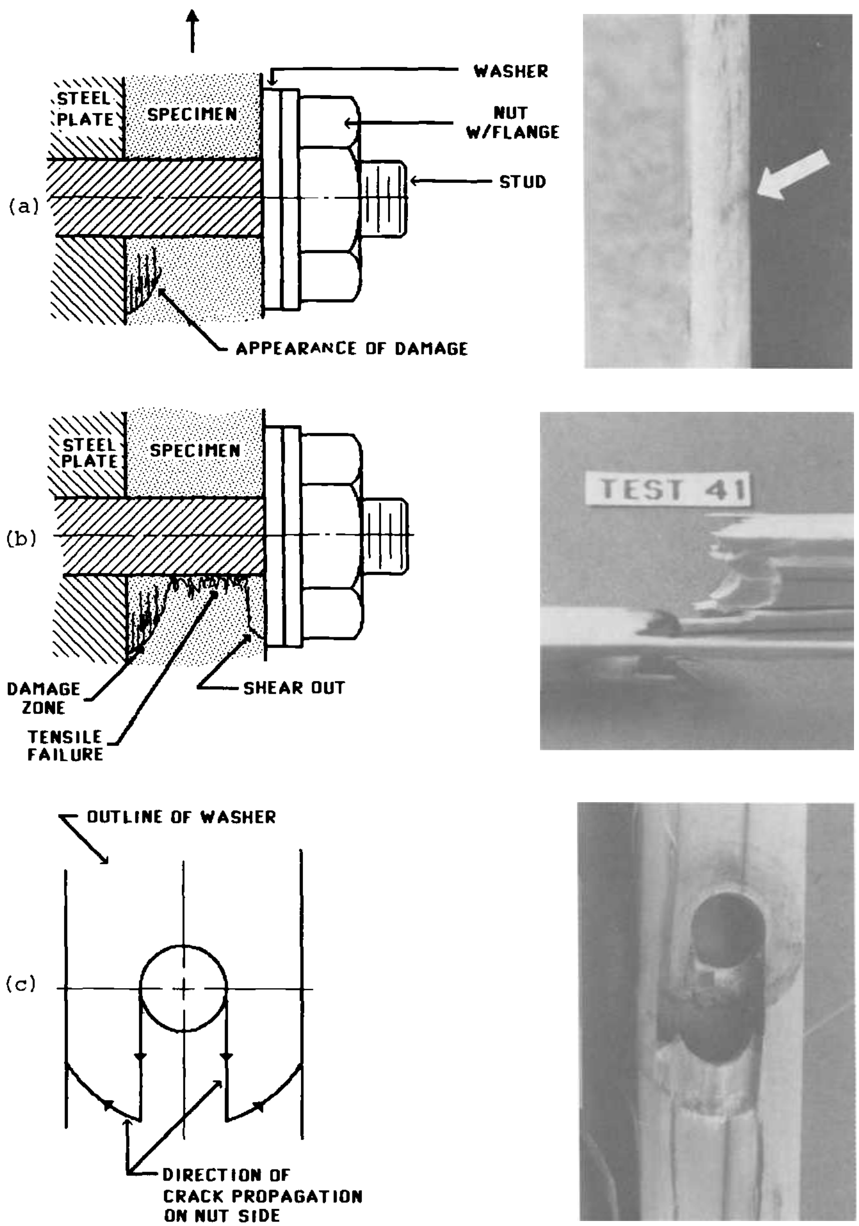

FIG. 9—*Schematic representation of fretting fatigue failure in cyclic tests with Group II specimens.*

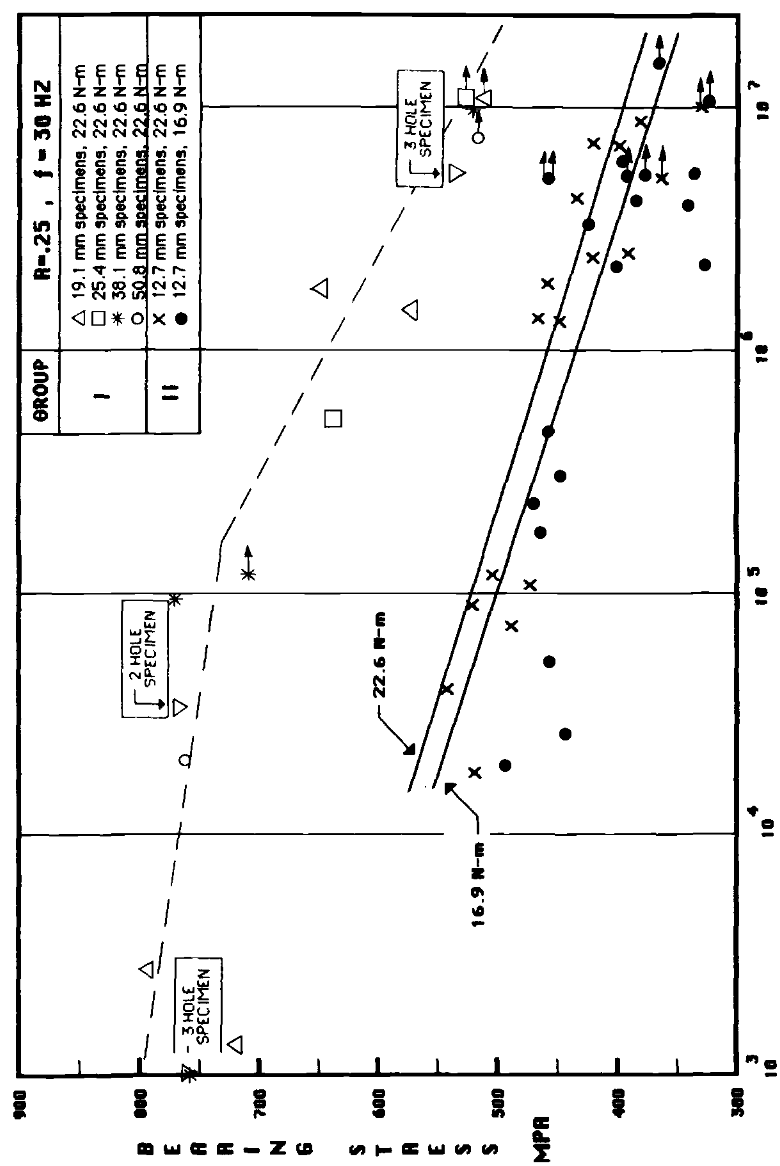

FIG. 10—*Bearing stress-life data for CSMC-steel bolted joints.*

Stress-Life Data—Figure 10 shows the bearing stress as a function of log life for all specimens tested cyclically in this study. In Group I specimens, bearing stresses lower than half the static bearing strength did not cause failure up to 10^7 cycles. On the other hand, higher bearing stresses caused rapid failure of the specimen. Although the data for Group I specimens are limited, it appears that the bearing stress-life diagram is approximately the same for all widths greater than the washer diameter.

Fatigue tests for Group II specimens were replicated at most stress levels. Thus, the data for these specimens are sufficiently large to warrant statistical analysis. Median straight-line *S-N* curves were established by maximum likelihood analysis [*3*], in which a homoscedastic (uniform variance, that is, independent of the stress amplitude used in testing) log-normal life was assumed. All specimens were bolted identically at each end; that is, each end had the same probability of failure. Yet only one end (either top or bottom) failed in testing, thereby generating one failure value and one suspended value. The *S-N* curve for 16.9-N · m clamping torque pertains to 14 failure values and 22 suspended values, while that for 22.6-N · m clamping torque pertains to 15 failure values and 19 suspended values. Each ordinary datum point plotted in Fig. 10 corresponds to one failure value and one suspended value, whereas each datum point with an arrow corresponds to two suspended values, namely, to both ends of the specimen. The median *S-N* curves lie above most of the data because of the large number of suspended values, especially the *S-N* curve for 16.9-N · m clamping torque. One way to rationalize this behavior is to argue that if all of the suspended tests could be continued to failure, the present median *S-N* curve is the best (present) estimate of the subsequent resulting median *S-N* curve.

Discussion of the Statistical Analysis—Since the fatigue life in this study exhibits such marked scatter, even the data for the Group II specimens in Fig. 10 are too meager to discern the actual shape of the *S-N* curve. We have adopted a linear *S-N* curve and assumed a homoscedastic variance, simply because we have no solid basis to support a more sophisticated model. This limitation further highlights the need for a larger sample size in testing of composites and for replication (at least two specimens) at various stress amplitudes. Moreover, the specimen design employed in this study generates a suspended value for each failure value, thereby providing additional (needed) statistical information. The authors strongly recommend that other investigators either avoid the use of a modified specimen in which only one end is likely to fail (that is, a "one-ended" specimen), or ignore the suspended values associated with "two-ended" specimens.

Discussion

Depending on the level of the cyclic load, failure of CSMC-metal bolted joints is due either to bearing or to fretting-initiated fatigue. The *S-N* diagram based on bearing stress can be divided into the two distinct regions shown schematically in Fig. 11. Since bearing failure dominates at shorter lives, reduced clamping pressure may have a detrimental effect on the life of the joint. At longer lives, however, fretting-initiated fatigue failure controls the strength of the joint, and clamping pressure, above a certain minimum value, has a relatively small effect in this region. For the design purposes, it is necessary to establish the critical bearing stress that divides the two regions of this failure model.

Fatigue cracks in both Group I and Group II specimens were initiated by fretting; however, there was a distinct difference in the location and propagation of these cracks. In Group I specimens, fatigue cracks were initiated at the faying surface and propagated outward from the center to the specimen edges. In Group II specimens, fatigue cracks were initiated at the edges of the specimen and propagated inward. Accordingly, Group II specimens exhibit lower fatigue strengths than Group I specimens. This difference between the fatigue strengths of Group I and Group II specimens indicates the desirability of keeping machined edges in low stress areas whenever practical.

Although the two-segment *S-N* curve for Group I specimens in Fig. 10 is based on limited data and is, therefore, merely faired rather than established by statistical analysis, it provides a basis to "predict" the failure mode

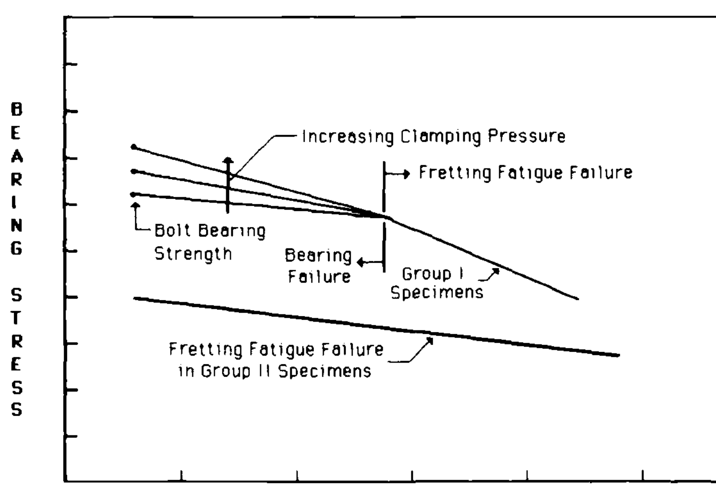

FIG. 11—*Failure model for CSMC-steel bolted joints.*

and strength of multiple (two or three) bolt joint patterns. To verify this hypothesis, three multiple-hole specimens (Fig. 12) were tested in the same manner as the single-hole specimens. Figure 12 presents the data for these multiple-bolt joints which, for practical purposes, fall on the single-bolt joint *S-N* curve (Fig. 10). From limited experiments with multiple-bolt patterns, it appears that large margins, as well as large transverse and back pitches, are required to obtain multiple-bolt joint strengths comparable to single-bolt joint strengths.

Future Work

Good design dictates that margins, as well as transverse and back pitches, be reduced as much as possible to make a compact joint. Moreover, the minimum practical tightening torque should be used without sacrificing the joint strength significantly. Accordingly, these parameters should be established by testing a relatively broad spectrum of joint geometries and materials.

Since bearing stress dictates failure, it is also imperative that ways to improve the bearing strength and to reduce fretting on the faying surface be studied. It would appear prudent to study various inserts and special washers to improve the strength of joints formed by standard fasteners.

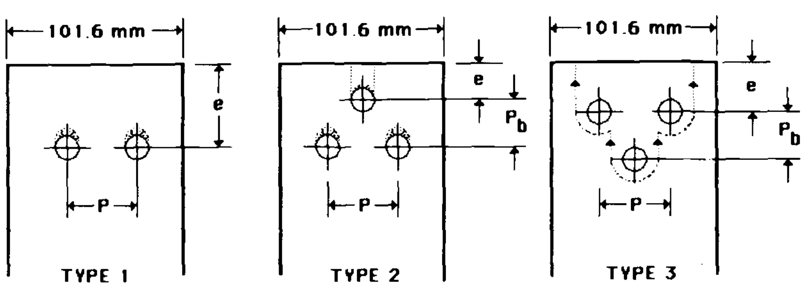

TYPE	e (mm)	p (mm)	Pb (mm)	Smax (MPa)	N	COMMENT
1	38.1	25.4	–	758	30,000	BEARING FAILURE
2	12.7	25.4	25.4	758	1,000	BEARING FAILURE AND SHEAR OUT AT THE TOP HOLE
3	38.1	25.4	25.4	517	5,335,000	FATIGUE FAILURE

R = 0.25, f = 30 HZ, CLAMPING TORQUE = 22.60 N-m

FIG. 12—*Failure in two- and three-hole CSMC-steel bolted joints:* (a) *appearance of damage,* (b) *propagation of crack through thickness,* (c) *shear type crack on the front surface.*

References

[*1*] Stockdale, J. H. and Matthews, F. L., "The Effect of Clamping Pressure on Bolt Bearing Loads in Glass Fibre Reinforced Plastics," *Composites*, January 1976.
[2] Crews, J. H., "Bolt-Bearing Fatigue of a Graphite/Epoxy Laminate," *Joining of Composite Materials, ASTM STP 749*, American Society for Testing and Materials, Philadelphia, 1981.
[*3*] Little, R. E., "Review of Statistical Analysis of Fatigue Life Data Using One-Sided Lower Statistical Tolerance Limits," *Statistical Analysis of Fatigue Data, ASTM STP 744*, American Society for Testing and Materials, Philadelphia, 1981.

Author Index

Subject Index

C

M

N

P

R

S

ISBN 0-8031-0927-X